Inversion of OBC seismic data for P- and S-wave velocities.

Guy R. Hall

Declaration

I hereby declare that this thesis has been composed by myself and the work described is entireley my own unless explicitly stated otherwise in the text.

Guy Hall
Edinburgh
September 2003

Abstract

This thesis describes a new method for deriving a shared-earth velocity model for P-P and P-SV reflections measured with ocean bottom cable (OBC) data.

The data have the potential to reveal lithological and fluid information about the rocks in the subsurface. The S waves recorded on OBCs are usually SV waves that have been converted on reflection of downgoing P-waves from the source. Conventional processing of OBC data separates the P-waves and SV-waves on the basis of particle motion: P-waves on the vertical component and SV-waves on the horizontal components. The P-waves are then processed in the conventional way, using procedures based on common mid-point (CMP) gathers that have been well established for decades and are very successful in determining subsurface structure. The SV waves are conventionally processed in a similar procedure, based on common- conversion point (CCP) gathers, that requires the P-wave to S-wave velocity ratio, γ, to be known a priori; initially this must be guessed. The result of processing these two data sets is two seismic time sections: one a P-wave section and the other a converted wave section. By subjectively correlating events in these two sections it is possible to estimate the S-wave velocities. This may lead to further iterations in the converted wave processing.

My aim is to remove the need for any guesswork in the estimate of γ and to eliminate the subjective correlation step.

The basic earth model underlying my approach is of discrete homogeneous isotropic elastic layers separated by interfaces at which reflections occur. I invert the reflection travel times of common-shot gathers or common-receiver gathers to find the layer velocities and the positions of the interfaces *in depth*, working from the top downwards. I start with a travel time inversion scheme developed by Guangpin Li that assumes the interfaces are plane, but locally dipping. This gives an initial estimate of the ray paths and the interfaces. We then assume that the interfaces can be described as locally parabolic which gives better inversion results. For the P-wave data, the P-wave velocities and the interface geometry are the output of the inversion. These P-wave velocities, but not the interface geometry, are used for the converted-wave inversion, the output of which is S-wave velocities and interface geometry. The interface geometry must be the same for both inversions: this shared-earth model is the criterion for determining which converted-wave reflections correspond with the P-wave reflections.

I have developed a processing flow based around this inversion scheme, that requires a number of new steps, including separation of P-waves and S-waves, manually picking travel time curves in shot gathers, and parameterising the picked data using cubic polynomials. The output of the processing flow are P- and S-wave interval-velocity in depth models that can be used for pre-stack depth migration. The processing scheme I develop is very simple compared with traditional schemes for generating interval-velocity depth models. Tests of the model building

flow on both P-P and P-SV synthetic data yield good results. However, the initial model affects the final result and it is clear that, in some cases, the inversion drives the solution to a local, rather than a global, error minimum. I propose a brute-force solution for this problem: give the inversion a range of velocities in any layer and for each velocity find the minimum-error interface; then choose the velocity that gives the least error.

I apply the new processing flow to real data provided by Shell from the Guillemot field in the North Sea. The results are good, but there are still small errors in the velocity model which I attribute to limitations in the way we have chosen to parameterise the earth. These errors can be reduced by updating the velocity field based on the residual moveout of reflection events in the migrated common image gathers. The method needs to be extended to layers that may have vertical and horizontal gradients.

Acknowledgments

This thesis is the product of four years work. Throughout that time I have been influenced greatly by my supervisors Anton Ziolkowski and David Taylor. I must thank Anton for seeding many ideas and guiding my work. Anton has taught me a lot about the seismic method and signal processing, and more generally how to aproach scientific problems. Anton has also worked hard to help me improve this document from what was simply an amalgamation of work I had done, into this more coherent thesis. Thanks are due to do David whose practical help in computing matters and interesting discussions have been greatly appreciated; all the work generating the finite difference dataset took many months and I would never have been able to do it myself.

Guangpin Li and I have collaborated for the duration of the INSPIRE project. Without his work on travel time inversion this thesis would have been a very different body of work. It has been a pleasure working with Guangpin who has taught me a huge amount about ray-tracing, and whose integrity is an example to us all, thankyou.

Shane and Justin deserve special mention for putting up with a whole host of inane questions about computers; without them I would have brought whole computer systems to their knees inumerable times over the last few years! Magi deserves a special mention in the computer section; while a fellow student he has provided much guidance on matters UNIX and Latex, and has put quite a few hours into educating me, thanks.

My family have always been there, either in person, or at the end of a phone line. Thank you for putting up with years of ‘it’s nearly finished’ and keeping my spirits up through the inevitable low points. Sergei Zatsepin and Geoffrey Boulton have always kept in mind my need for salt water, thanks. Too many friends to list have been great to me over the last few years whether we have shared time in bars, in the air, or at sea, you all know who you are; thanks for the general life support you have provided.

I am eternally indebted to early help from Jannette Jeanette Mayall with my English and my Godfather, Rory, without whose maths coaching I would probably not have even passed my A' level. Two teachers who stand out from my past are Mrs Shorey and Mr Dunthorne, thanks for showing me that it can be done.

I would like to thank my sponsors, initially my study was funded by NERC. I have more recently been supported by the INSPIRE project under whose auspicies I have worked for the last year. Sponsors of the INSPIRE project are the Department of Trade and Industry, Shell exploration UK and ExxonMobil exploration company. Interesting discussions have invariably resulted from the sponsors meetings and have provided much food for thought. I must also mention Margaret who has always been there to coordinate us all.

Contents

List of Figures

Notations and Conventions

Abreviations and mathematical notation commonly used in the thesis are defined in this section.

Abreviations

Abreviation	Meaning
OBC	Ocean Bottom Cable
4C	Four component
CMP	Common mid point
CCP	Common conversion point
ACCP	Asymptotic common conversion point
NMO	Normal Moveout
P-P	Pure mode P-wave reflection
P-S	Converted wave reflection made up of a downgoing P-wave and an upcoming S-wave
RMS	Root Mean Squared
DMO	Dip moveout
PSTM	Pre stack time migration
PSDM	Pre stack depth migration
MVA	Migration velocity analysis
CIG	Common image gather

Symbols

Symbol	Meaning	Dimensions
x	Horizontal coordinate	m
z	Vertical coordinate	m
v_p	Compressional wave velocity	m/s
v_s	Shear wave velocity	m/s
γ	Ratio of v_p/v_s	
$t(0)$	Zero offset travel time	s
$t(x)$	Travel time of an event at offset x	s
α	Velocity of a P-wave (isotropic)	m/s
β	Velocity of an S-wave (isotropic)	m/s
λ	Fluid incompressibility	N/m^2
μ	Shear modulus	N/m^2
ρ	density	Kg/m^3
v_{stack}	stacking velocity	m/s
v_{rms}	RMS velocity	m/s
v_x	horizontal component of particle velocity	m/s
v_z	vertical component of praticle velocity	m/s

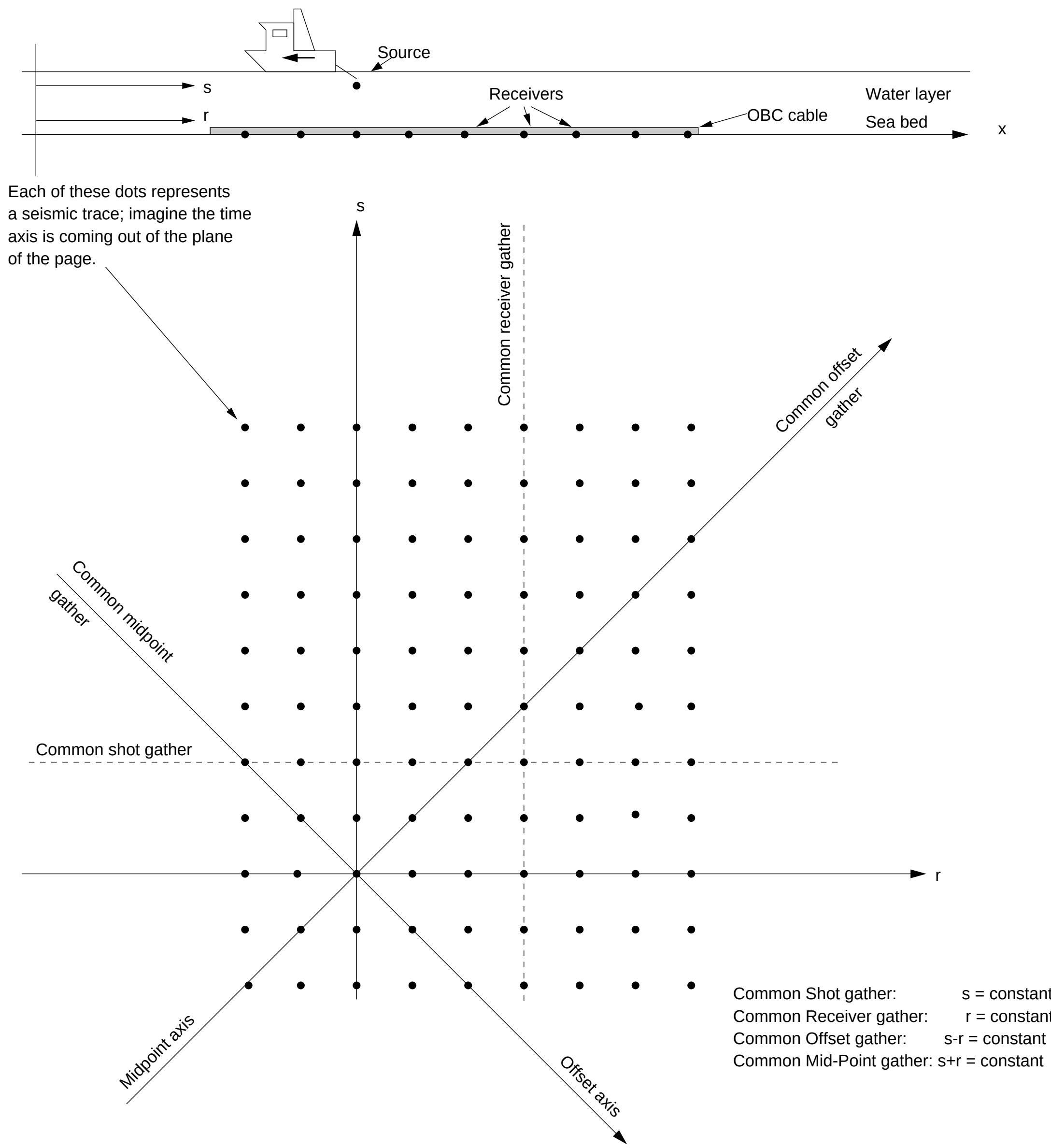

Figure 0.1. The relationship between source and receiver coordinate and the common-midpoint, common-source, common-receiver and common-offset gathers are displayed graphically.

Chapter 1

Introduction

1.1 Review of previous work and definition of the problem

The earliest 'controlled source' seismology was begun by Robert Mallet in the mid 19th Century (Mallet, 1848). Developments in theory and technique by the 1920s allowed number of groups to start using seismic reflections with a view to describing subsurface geology (Udden, 1920). However it is not untill the advent of multiple coverage and digital processing in the 1950's that the processing of seismic data bears much resemblance to what is used by the petroleum industry today (Sheriff & Geldart, 1995). With the correct processing, records of energy reflected from the sub-surface are used to delineate subsurface geological structure. A very important part of the processing involves determining the seismic velocity. Only when we know how fast the energy travels through the different volumes of rock in the subsurface can a sharp, focused, and correctly positioned image of the subsurface be generated. The processed seismic sections are of great value to geologists trying to locate potential hydrocarbon reserviors. The main focus of effort in marine seismic exploration, both in terms of research and field acquisition, has been invested in pure mode pressure wave (P-wave) reflection seismology. Traditionally, marine P-wave data are acquired using the combination of an impulsive energy source to generate P-waves in the water column and a 'streamer' many kilometres long with pressure sensors distributed along it which detect the resulting wavefield. In most situations P-wave reflection data are good at defining the location of prominent, P-wave reflecting, interfaces which can be interpreted by geologists.

Research into reflection seismology using the shear wave (S-wave) mode has been going on since the 1960's (Garotta, 2000). S-wave propagation is insensitive to certain physical properties of rocks which affect P-waves. By analysing S-wave data alongside P-wave data we are able to gain more information regarding the nature of the rocks in the subsurface than by analysing P-waves alone. There is the potential to differentiate certain lithologies based on the absolute values of velocity and the ratio of P- and S-wave velocities (Berg, 1997; Michelena *et al.*, 2001). At sea when all the instrumentation is in the water column, it is not possible to generate or record S-waves directly as they do not propagate in fluids. Fortunately, when a P-wave is reflected at an interface, energy is divided between reflected and transmitted P- and S-waves, see Figure 1.1(a). With sensors on the sea floor it is possible to measure both mode converted S-waves and pure mode P-wave reflections at the same time. The work in this thesis is concerned with a particular type of mode-converted wave, in which mode conversion occurs at the reflection point. The result is a ray path whose downgoing leg is a P-wave and whose upgoing leg is an S-wave, see Figure 1.1(b). Mode converted P-SV waves have been collected and processed by the exploration industry for about the last twenty years (Stewart *et al.*, 2002). Sucessful uses of the data include imaging through gas clouds and imaging low P-wave impedence boundaries. The data, however, have greater potential and *"this will only be acheived when fully compatible (depth and amplitude) P and PS sections are obtained" (Garotta, 2001).*

Both P-P and P-S data can be moveout corrected and stacked to make time sections, the vertical scales of which are two-way-travel time. S-waves travel more slowly than P-waves. The arrival time of a reflection event from a particular reflecting interface on the converted wave stacked section is later than that of a pure mode P-P reflection event from the same interface on the P-wave stacked section. This discrepancy in arrival times complicates the comparison of P-wave and converted wave data. The correlation between events with different arrival times on the two sections is needed to derive the

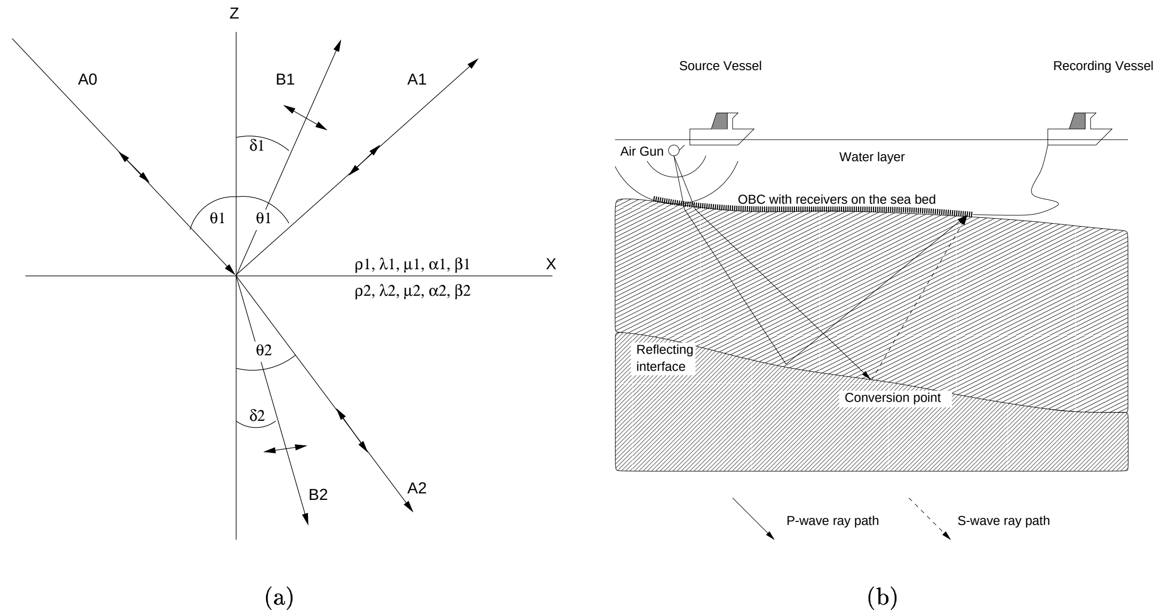

Figure 1.1. Figure (a) shows how energy is partitioned at an interface between two isotropic solids. Figure (b) shows a schematic of the OBC acquisition geometry, it is able to measure directly both P-wave and mode converted S-waves.

$v_p : v_s$ ratio is ambiguous and hard to quantify. The earth has coordinates of depth not time, and it is possible to generate depth velocity models and seismic images from P-wave and converted wave seismic data. If this can be done with sufficient accuraccy both P-wave and converted-wave sections share a single common earth model which is consistent with both datasets.

The processing of P-SV data has been shoe-horned to follow as closely as possible the processing flow used for P-P data. The issues with this stem from different velocities of P- and S-waves. This causes two big problems. The first is that, because of Snell's law, the ray path of a converted wave is asymmetric. Even in the case of plane horizontal layers the common mid-point approximation is completley invalid for converted waves. Even the correct gathering of traces for velocity estimation is non-trivial. Binning converted wave traces into common conversion point gathers needs a value for the $v_p : v_s$ ratio, which is something we do not know at this very first step in the processing flow (Thomsen, 1999). The other big problem that comes from the difference in P- and S-wave velocity is that P-P and P-S events reflected and converted at a given interface arrive at the earth's surface at different times.

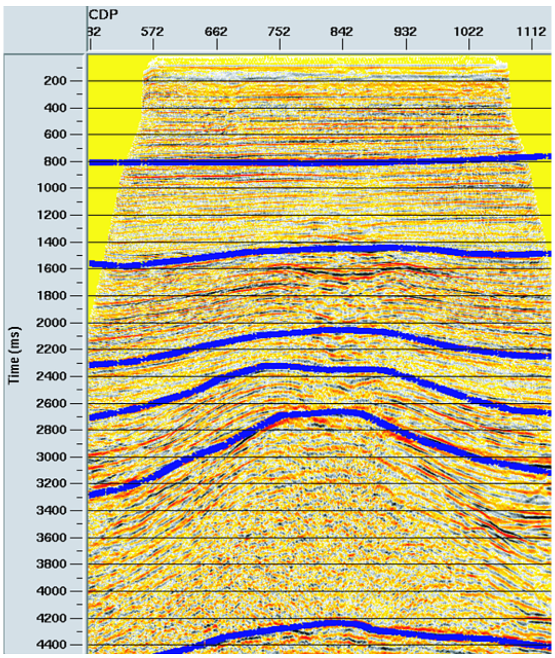

(a)

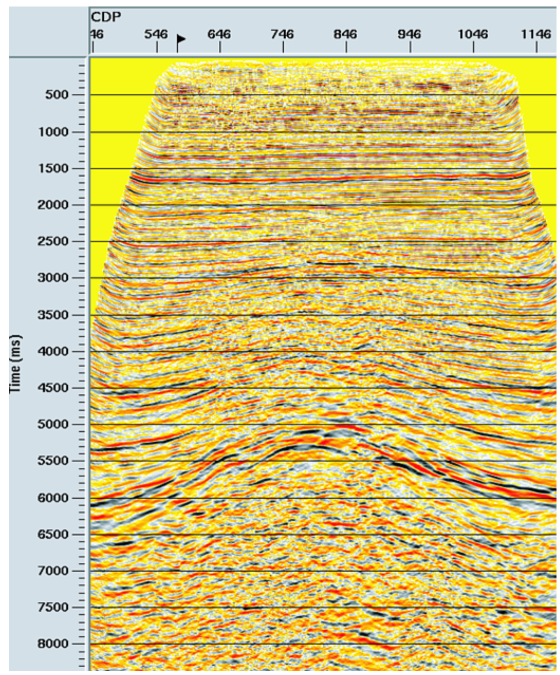

(b)

Figure 1.2. Figure (a) is a P-P stacked section and (b) is a P-SV stacked section. Some events have been picked on the P-P data, it is not possible to tell with any degree of confidence which event on the P-SV section corresponds with the picked events on the P-P section. The images provided by Fabio Mancini, who also processed the data.

Joint inversion is what is required to get the most out of the P-P and P-S data recorded using multicomponent sensors. Many current processing schemes eg: MacLeod *et al.* (1999); Pope *et al.* (2000); Mancini *et al.* (2003) rely on event correlation in the post stack time domain. This step is subjective and there is no test to determine whether the correlation is correct, see Figure 1.2. All combined P-P and P-S processing flows that use CCP binning really need to know the $v_p : v_s$ ratio before they start, which is not possible. They make up for this with a number of iterative steps as the estimates of the velocity ratios are improved, making the processing flow rather complicated, see Figure 1.3(b). After all this processing there are four results: a P-wave stacking velocity field; a conventional P-P stack; a converted wave stacking velocity field; and a P-SV stack. The two stacked sections have different vertical axes, which are the P-P and P-SV two-way travel times, which makes comparison of the two datasets difficult. It is possible to go one step further and look at the data in depth which should make the comparison between the two sections easier (Garotta *et al.*, 2002). To do this the stacking velocities must be converted to interval velocities, usually using a Dix type inversion. The depth-velocity models can then be used for depth migration. This leads to two sections that at least have the same vertical and horizontal coordinates. The converted wave velocity field is a mixture of two things, the downgoing P-wave velocity and the upgoing S-wave velocity. From this mixture somehow the S-wave velocity has to be found: If you know the S-wave velocity independently the problem is easy to solve. But we don't, the upshot of this is that to convert the two (P-P and P-SV wave) stacking velocity fields to depth-interval velocity fields required for depth imaging we must rely on the subjective event correlation step (Herrenschmidt *et al.*, 2001). Many more complicated joint velocity inversion schemes require P-P and P-SV events to be paired before depth conversion (Grechka *et al.*, 2002), or rely on event correlation at some other stage during the velocity determination process (Mikhailov *et al.*, 2001).

1.2 My contribution

In this thesis I present a method for deriving P- and S-wave velocities from seismic data. Working in a 2D environment we assume curved interfaces and an isotropic

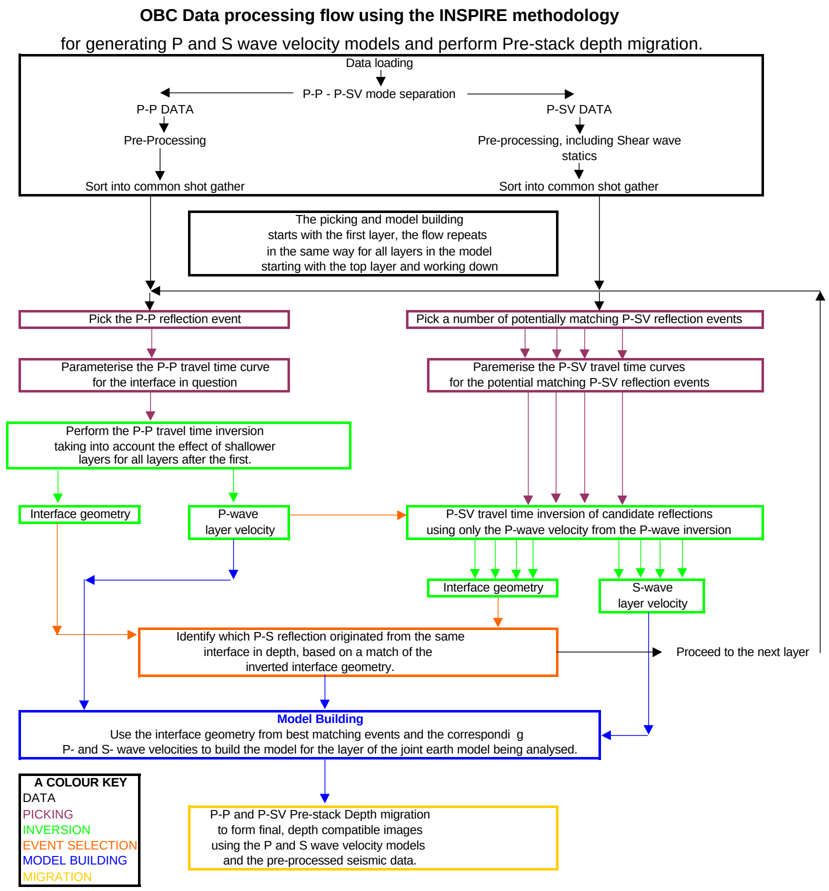

(a)

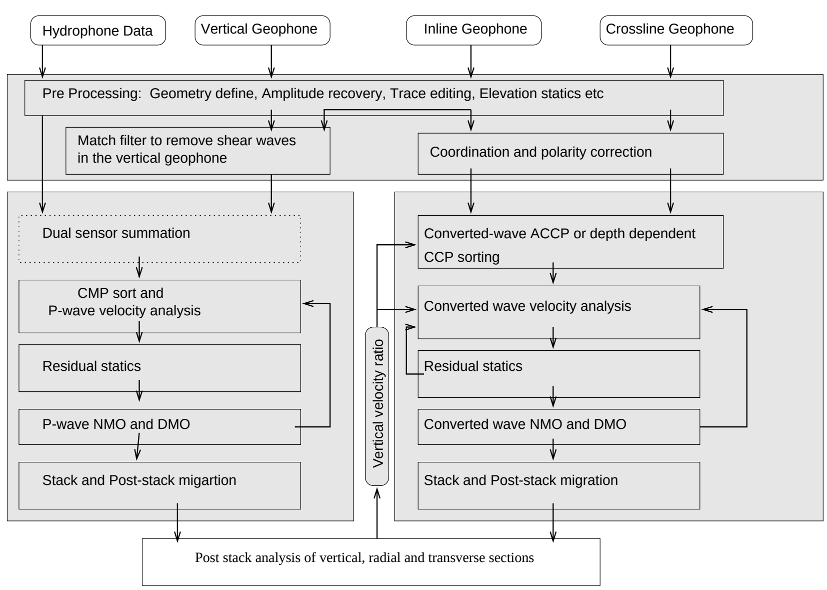

(b)

Figure 1.3. Figure (a) shows the steps in the processing flow that I have developed, (b) shows a more traditional P-P flow inspired scheme, requiring a number of updates and resulting in two incompatible time sections.Figure (b) is taken from Yuan (2001)

velocity distribution within each layer and invert directly for interval velocity and reflector geometry. I define velocities in terms of layers with boundaries at which there are impedence contrasts giving reflections. These reflections are the the raw data that define the model. By working in common-shot or common-receiver gathers we do not make any assumptions regarding physical parameters such as the $v_p : v_s$ velocity ratio (γ) when processing the data. I have developed a processing flow that is based around the travel time inversion method of Guangpin Li (2002). The output depth-velocity model is ideal for use in conjunction with pre-stack-depth-migration. The processing flow that I have developed uses many pre-existing tools and ideas from other well established areas of seismic data processing. I have put these parts together in a way that I believe is new and original.

1.3 Layout of this thesis

This thesis shows how I developed a method that applies a travel time inversion scheme to the problem of processing multicomponent seismic data. I outline the previous work in the field of seismic data processing of OBC data. The real OBC data set I am using has problems that I solve by developing special-purpose filters. The methodology I have developed for inversion of real data for P- and S-wave velocites, and structure, employs a travel time inversion scheme developed by Guangpin Li *et al.* (2002) within the University of Edinburgh's INSPIRE project. I have developed a method to acquire travel time data from the seismic records to input into the inversion. I then go on to test my picking and model building techniques on a finite difference synthetic dataset before applying it to the real data set.

The contents of each chapter are summarised below. Short summaries of the chapter contents are repeated in italics on the first page of each chapter.

Chapter 2

In this chapter I discuss the background on which my work rests. I talk about both P-P and P-SV wave data and current methods of processing to derive images of the subsurface. I outline the limitations of some of the processing techniques currently available. I conclude that when investigating P-P and P-SV data it is desirable to work in the depth domain as this is the only truly common domain for both P-P and P-SV datasets. We should try to quantify or avoid event correlation. At present this is a subjective step and hard to do unless there are structural features - and even then there is no way to check, using the data, if the correlation is correct.

Chapter 3

In this chapter I introduce the real dataset on which I test our methods. The data have a problem with contamination caused by coupling between the horizontal inline and vertical geophones and in this chapter I show how this contamination is suppressed using a predictive least-squares filter.

Chapter 4

In this chapter I discuss the method of travel time inversion developed by Guangpin Li (Li *et al.*, 2002) that is used to define a local 2-D velocity structure. The inversion initally assumes iso-velocity layers and plane dipping interfaces. The errors are unacceptably high (up to 24% in places) and we have to include interface curvature in the inversion. We then assume that interfaces can be described by a second order polynomial in x and the results are improved; average errors in velocity are reduced to less than five per cent.

Chapter 5

We saw in the previous chapter how it is possible to determine local velocity models using travel time inversion. The input data for the inversion are travel time curves and in this chapter I discuss methods of parameterising travel time curves seen in seismic data. I also discuss which events to pick, and show an example with a plane horizontal layered model where travel time inversion is used to identify the correct P-SV event to match a P-P reflection event.

Chapter 6

The inversion is a ray based inversion method, and in previous chapters I have tested the method using only synthetic data generated by ray tracing. In this chapter I apply my processing methodology to P-P and P-SV data from a 2-D synthetic dataset generated using finite difference code. I also show a method of joining up the results from many inversions to build a 'survey wide' velocity model out of a number of local inversion results.

Chapter 7

Up to now all the tests using the picking, inversion and model building have been applied to synthetic data of one sort or another. In this chapter I show the application of the new methodology to the real dataset that was introduced in Chapter 3.

Chapter 8

Here I conclude that it is possible to use travel time inversion to process seismic data. The models we can invert are not very complex yet, but in a stratified earth with moderate dip and curvature the route from data to a depth model suitable for migration is simple. Picking reflection travel times is a bottleneck which takes too long at present. An efficient picking routine is required. Further work includes improving the picking and travel time parameterisation, the comunication between the data and the inversion and reducing the effects of layer curvature on velocity determination.

Chapter 2

Background

In this chapter I discuss the background on which my work rests. I discuss both P-P and P-SV wave data and current methods of processing to derive images of the subsurface. I outline the limitations of some of the processing techniques currently available. I conclude that when investigating P-P and P-SV data it is desirable to work in the depth domain as this is the only truly common domain for both P-P and P-SV datasets. We should try to quantify or avoid event correlation, at present this is a subjective step and hard to do unless there are structural features - and even then there is no way to check, using the data, if the correlation is correct.

2.1 Seismic Waves

The seismic reflection method is used for exploration of the earth's crust. Analysis of seismic waves that have travelled through the earth can lead to information on geological structure, seismic velocity distribution, lithology and pore fluid presence. This information is used by the petroleum industry for hydrocarbon exploration and monitoring of production. There are many different sorts of seismic waves. In this thesis

I consider a subset of seismic waves which travel through a medium and are known as body waves. These can be separated broadly into two different types: compressional, or P-waves and shear, or S-waves. When analysed together the different properties of these wave types lead to a great deal of information about the nature of the subsurface.

In the following section I consider body waves in isotropic media.

2.1.1 P-waves

P-waves are compressional waves whose particle motion is parallel to the direction of propagation of the wave. The speed with which a P-wave travels is given by α in equation 2.1

$$\alpha = \left(\frac{\lambda + 2\mu}{\rho}\right)^{1/2}, \tag{2.1}$$

where λ and μ are known as *Lamé's constants* or *elastic constants* with μ being the 'shear modulus' and λ the 'fluid incompressibility', ρ is the density (Sheriff & Geldart, 1995).

2.1.2 S-waves

S-waves are shear waves. Their particle motion has two degrees of freedom. Those whose particle motion is in the plane containing the incident ray and the normal to the interface are known as SV waves, SH waves have particle motion perpendicular to this plane. When referring to S-waves, unless I specify otherwise, I will be considering the SV mode. This mode is usually the more energetic in the situations encountered in this thesis. S-waves travel with velocity β given in equation 2.2,

$$\beta = \left(\frac{\mu}{\rho}\right)^{1/2}. \tag{2.2}$$

Because Lamé's constants are always positive, α is always greater than β. The velocity of an S-wave ranges from 0 to $(1/\sqrt{2})$ of α the P-wave velocity in a given medium. A fluid, by definition, does not support shear stress; μ is zero, and so S-waves do not propagate in fluids. (Sheriff & Geldart, 1995)

2.1.3 Reflection and Conversion

When energy is incident on an interface between two solids with different elastic properties, energy is both transmitted across the interface, and reflected back away from the interface. Energy is partitioned between reflected and transmitted P- and S-waves, even if the incident wave is a P-wave. For the case of a P-wave normally incident on an interface, the reflection amplitude is directly proportional to the change in acoustic impedance (the product of velocity and density) across the boundary. Figure 2.1 shows the waves generated by a P-wave incident on a solid-solid boundary. As the incident angle of the wave θi changes, so does the proportion of energy that is transmitted, reflected or undergoes mode conversion. The exact figures for partitioning of energy at an interface are given by the Zoeprittz equations, (Zoeppritz, 1919). In the example shown in Figure 2.2, note that below about 33^o angle of incidence the P-wave reflected energy decreases with increasing incidence angle. The S-wave has zero reflectivity at normal incidence and the reflected amplitude increases up to about 33 degrees. At the critical angle the pattern of reflected amplitude becomes more complex. For most reflection data that we will work with, we are dealing with reflections with incident angles below the critical angle. In the earth density and velocity contrasts are generally small and so *'usually appreciably less than 1% of the energy is reflected at any interface'* (Sheriff & Geldart, 1995). Exceptions to this are the sea floor, and the sea surface where a large portion of the energy can be reflected.

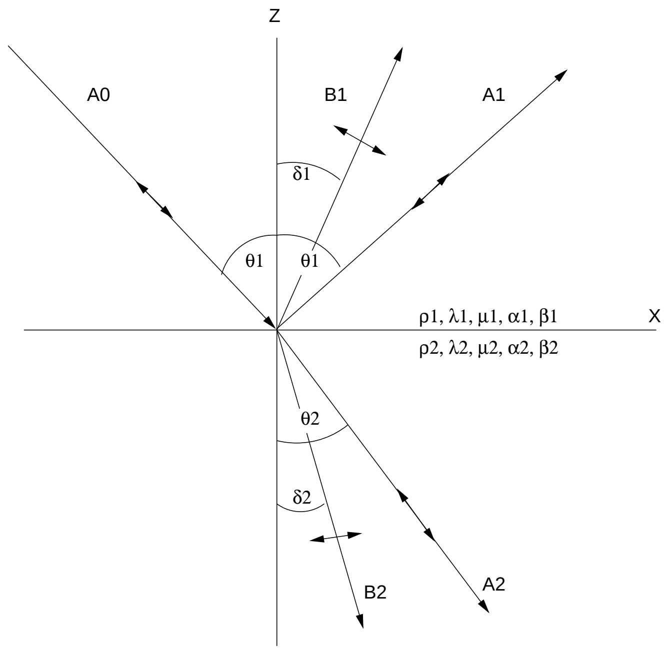

Figure 2.1. Waves generated at an interface between to isotropic solids by an incident P-wave. A's refer to P-waves, and B's to SV waves. The arrows indicate particle motion polarities.

When a wave, which starts off as a P-wave at the source, is reflected from an interface and returns to the surface as a mode-converted S-wave it is known as a P-SV or sometimes C-wave. I will refer to these 'converted waves' as P-SV waves.

Snell's law governs the angles of reflection and refraction. It relates the sine of the angle of incidence or reflection of a wave to the velocity of the medium:

$$\frac{\sin\theta 1}{\alpha 1} = \frac{\sin\delta 1}{\beta 1} = \frac{\sin\theta 2}{\alpha 2} = \frac{\sin\delta 2}{\beta 2} = p, \tag{2.3}$$

where α and β are the P and S-wave velocities, and θ and δ are the angles of incidence as in Figure 2.1. p is the component of slowness of each ray parallel to the interface. For a given incident wave slowness *parallel to the interface* does not change on reflection or transmission.

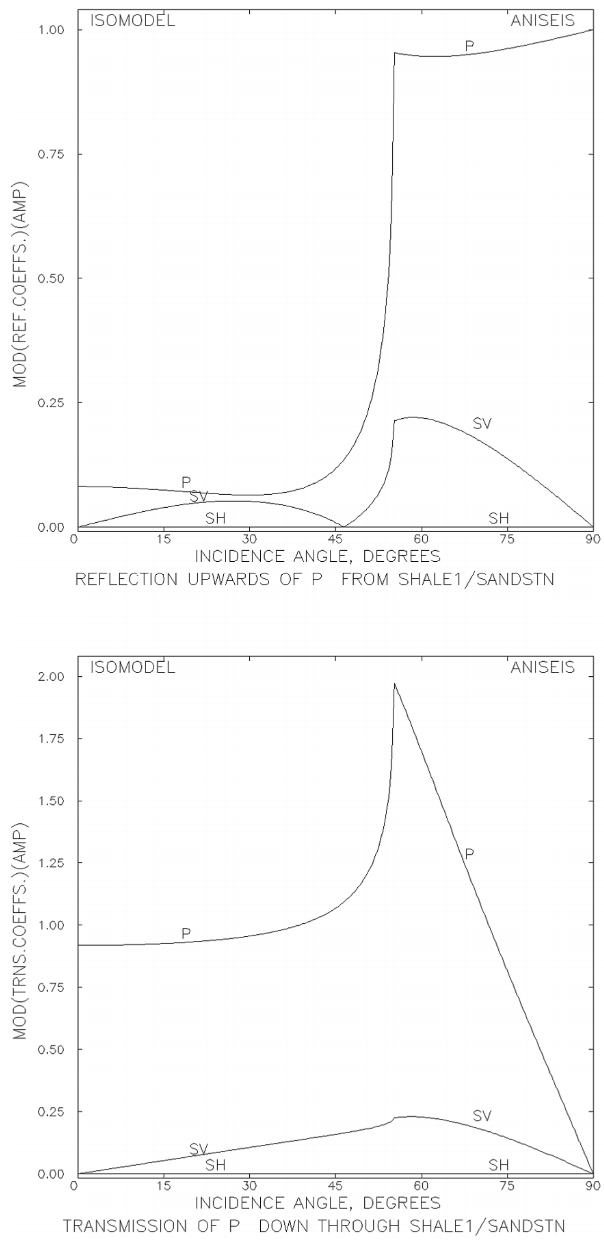

Figure 2.2. Amplitudes of reflected and transmitted P and S-waves from a P-wave incident on a solid-solid interface. The upper image shows the reflection coefficients-versus-angle of incidence. The lower image shows the transmition coefficients versus angle of incidence. This diagram was generated in ANISEIS by David Taylor, author of the ANISEIS plane layer modelling package (Taylor, 1987).

2.2 Motivation for acquiring converted wave data

> *"The combination of compressional (P) and shear (S) wave data has the potential to give more information about the subsurface than P-waves alone. The availability of P and S data are also advantageous in certain lithological settings, where P-waves alone have not been able to define fully a potential reservoir"'* MacLeod *et al.* (1999)

Some of the applications of multicomponent data are based on the use of converted waves. Imaging through gas clouds is one example (Knapp *et al.*, 2001). Gas is a fluid, and if a large amount of gas is presence in the rock pore spaces it will have a large effect on the bulk compressibility, slowing the P-waves and also reducing the P-wave reflectivity. To a first approximation S-waves travel through the rock matrix and are not affected by the presence of pore fluids such as gas. The processing of converted waves enables a clearer picture of structure previously invisible below gas-saturated pockets, to be achieved than by processing P-waves alone (Granli *et al.*, 1999; Pope *et al.*, 2000).

Imaging sand-shale boundaries can be problematical where the P-wave impedance contrasts are very low. In some cases the S-wave velocity contrast may be considerably higher. The result is that the P-SV reflection will be considerably stronger than the corresponding P-P-wave reflection. The classic recent example of this is that of the Alba field, where the P-SV data are able to image the top of the reservoir and where the P-P data are not (MacLeod *et al.*, 1999).

The one application of OBC data that benefits only the P-P data comes from the fact that both pressure and particle velocity are recorded. This vector information, coupled with the pressure data, can be used for improved multiple removal (Barr & Sanders, 1989; Soubaras, 1998), which in turn improves the P-P processed image (Kristensen *et al.*, 1999).

Finally, the full potential of the data acquired using OBC uses both the P-P and P-SV data together: flat, high-amplitude events in P-wave seismic sections known as ‘bright spots’ are associated with the presence of fluids in the rock. P-SV data can be used in combination with P-P data to check whether the amplitude anomaly is indeed a fluid effect, or simply a highly reflective lithological boundary. If the bright spot does not appear in any way on the S-wave data then the fluid is a more likely cause than if there are high amplitude reflections appearing on both P-P and P-SV sections (Garotta, 2000).

Seismic waves travel at different speeds through different materials. Their P-wave velocities alone often cannot distinguish different lithologies. When the S-wave velocity of the material is taken into account as well, the different lithologies may be resolved. Specifically cases included differentiation of sand-shale and dolomite-anhydrite (Berg, 1997; Stewart *et al.*, 2003; Engelmark, 2001).

2.3 Data acquisition

I am concerned in this chapter only with the acquisition of seismic data at sea. Seismic data are acquired on land, but the techniques and peculiarities are different. In order to record seismic waves one must first generate them, which requires an energy source. There are natural sources of seismic waves such as earthquakes, but these are not controlled or repeatable. In reflection seismology a controlled and repeatable energy source is desired and the most often used marine source is the airgun array. An airgun is an impulsive source that emits a high-pressure air bubble whose oscillations generate an acoustic wave in the water. S-waves do not travel in water, so the airgun is a purely P-wave generating source. The bulk of marine reflection data acquired since 1950 have been acquired using a ‘streamer’ containing many hydrophones towed behind the source vessel (see Figure 2.3). Energy from the source propagates through the water column and down into the rocks below the sea floor. As the waves propagate across boundaries of different elastic properties some energy is reflected back up to the surface where it can be measured by the hydrophones in the streamer. Hydrophones are transducers that convert pressure into a tiny voltages that can be measured and recorded. Hydrophones are sensitive to passing pressure waves, be they direct arrivals from the source, or energy reflected from a subsurface interface. Measurements of the pressure signal at each hydrophone group in the streamer are typically recorded every 2ms by a computer on board the survey vessel. All energy recorded using the airgun-hydrophone combination has at least a P-wave leg from the source to the sea floor and from the sea floor to the receiver. For reflected P-wave data, where energy for the whole ray path travels as a pressure wave, this is an ideal situation.

To gather shear wave information from the marine environment it would be convenient to measure the P-S-S-P mode. The P-S-S-P mode occurs where the downgoing P-wave is converted to an S-wave at the sea floor and where this S-wave is reflected as an S-wave at depth. The upgoing S-wave is then converted back to a P-wave at the sea floor and it is that P-wave that is measured by the hydrophones in the streamer. An example where this method is used with successis given by Tatham & Goolsbee (1984), however it must be noted that the area has unusually hard sea-bottom conditions-condusive to the conversion of the downgoing P-wave to a downgoing S-wave. Recording the P-S-S-P mode entails little extra acquisition cost over conventional P-P data collection. Garotta (2000) cites two reasons why this mode is not commonly used. The first is that the energy of waves that have undergone two mode conversions, one on reflection and one at the sea floor is low. That is, the returning signals have a very low amplitude on a seismic trace. The second is that current processing techniques are not sufficiently powerful to discriminate between P-P mode primary reflections, P-P multiples, and the P-S-S-P modes except in very particular conditions. To measure S-waves directly one must be in contact with a solid; at sea this means receivers must be on the sea floor. With geophones coupled to the sea bed it is possible to measure both P and S-waves directly. Geophones differ from hydrophones in that they are sensitive to particle motion, rather than pressure.

2.3.1 The OBC: acquisition geometry and data recorded

The Ocean-bottom cable or OBC is used because it is an efficient way of getting a large number of sensors in contact with the sea bed. When a survey takes place, the

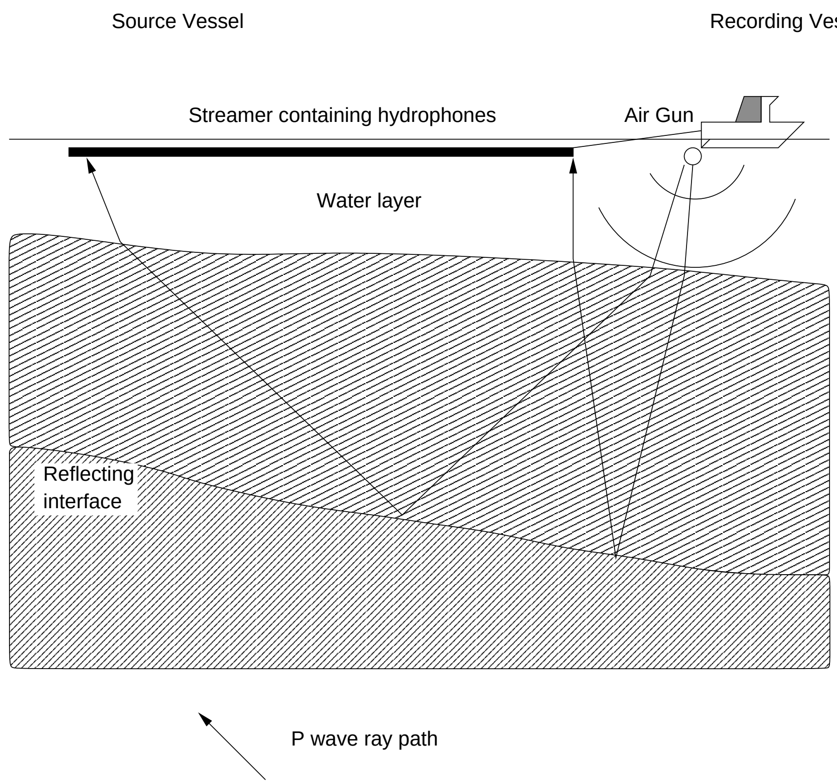

Figure 2.3. A typical streamer geometry. The survey vessel tows a streamer behind the source. The streamer typically contains a group of hydrophones, which act as a pressure sensor, every 25m of its length. The streamer might be up to 12km long.

cable is laid or dragged and dropped on to the sea bed and it remains connected to a recording ship where all the data recorded are stored. The source vessel can then sail over the cable and fire the source at intervals. Each receiver then records data for a period of time after the source is activated (Caldwell, 1999). The arrangement is shown in Figure 2.4. There are four sensors at each receiver station in the OBC cable, as shown in Figure 2.5. The hydrophone only measures pressure waves, and the geophones measure particle motion. If there is a layer of particularly low velocity immediately beneath the sea floor the upcoming waves arrive with their ray paths bent almost to the vertical (see Figure 2.6). This has the highly advantageous effect that the modes are almost separated by different sensors, the P-wave being measured on the vertical geophone and the SV wave being measured on the inline geophone. An example of the data recorded is shown in Figure 2.7: the different arrival types can be seen. The higher moveout of the arrivals on the horizontal inline geophone distinguish P-SV arrivals compared with the lower curvature of events seen in the hydrophone and vertical geophone records caused by P-P arrivals.

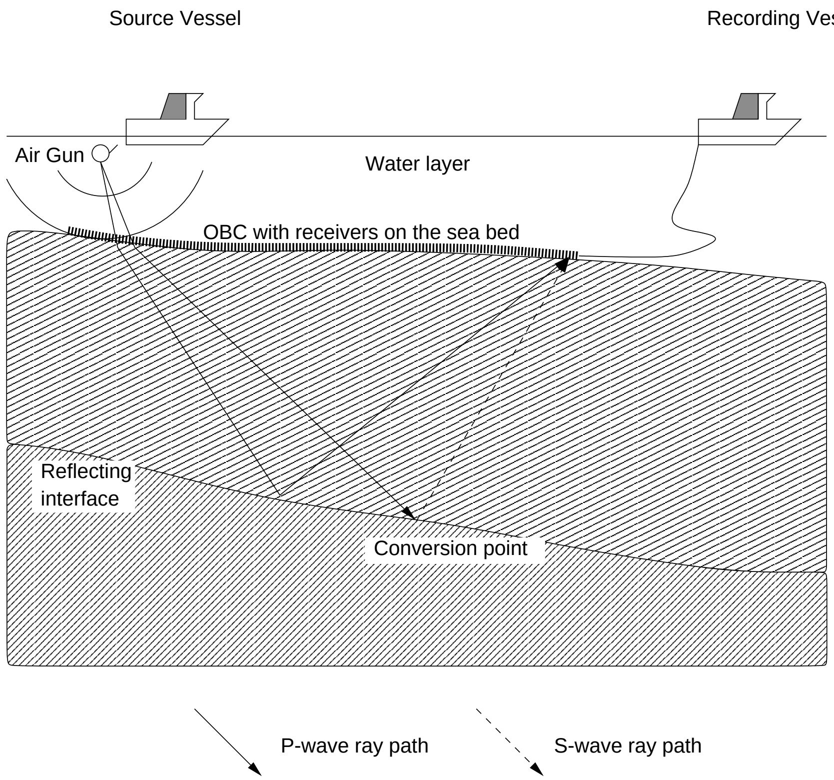

Figure 2.4. OBC acquisition geometry. For a P-wave reflected from an interface the angle of reflection is equal to the angle of incidence. Because S-waves travel more slowly through a given medium than P-waves, the angle of reflection of a mode converted shear wave is smaller than the incident angle of the P-wave. This means that the conversion point for mode converted waves is closer to the receiver than the reflection point for a P-wave travelling between the same source and receiver. The exact location of this conversion point depends on the ratio of v_p to v_s.

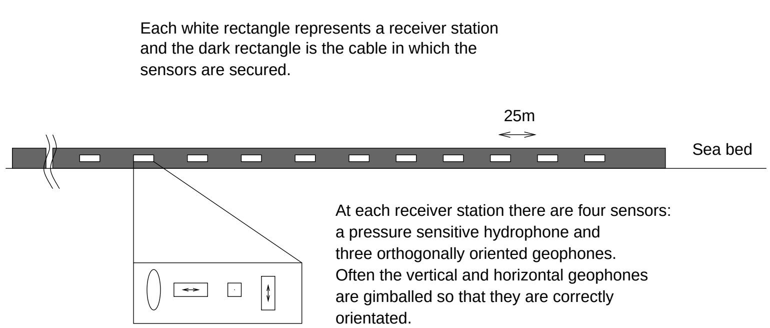

Figure 2.5. Diagram showing the different sensors in an OBC cable.

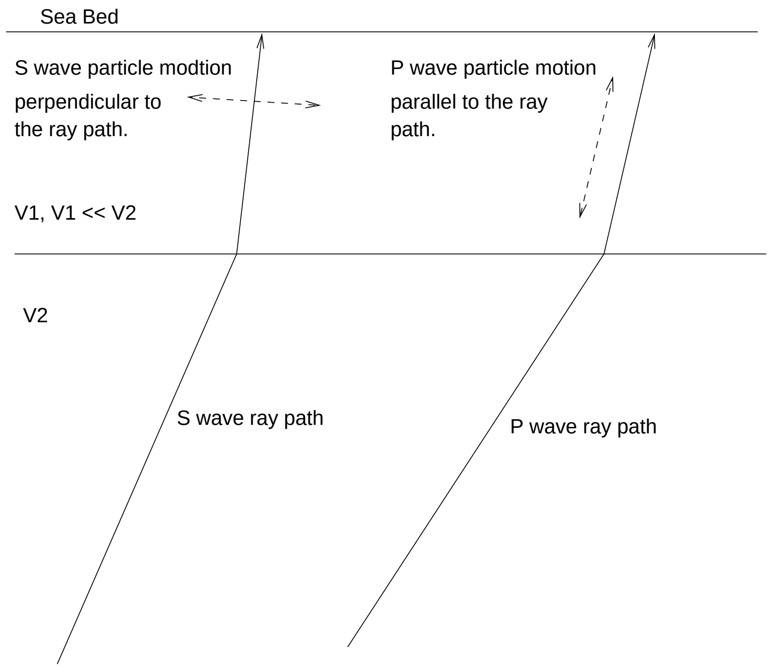

Figure 2.6. Diagram showing how P and SV waves tend to be recorded on different receivers in an OBC cable.

2.4 P-wave data processing

Once the data have been acquired, it is necessary to process them to find out seismic velocities and use these to derive a focused image of the subsurface structure. For P-waves the processing is often based on the 'Common Mid-Point' (CMP) assumption that I shall discuss further in section 2.4.1. Moveout in the gathers is used to find RMS velocities, which may then in turn be inverted to derive an interval velocity model. The inversion procedures are often based initially on the Dix inversion, which assumes straight rays in a plane horizontal earth model. Stacking is used as an important noise suppression technique. Migration is used once a velocity model has been determined to locate events correctly both laterally and in depth.

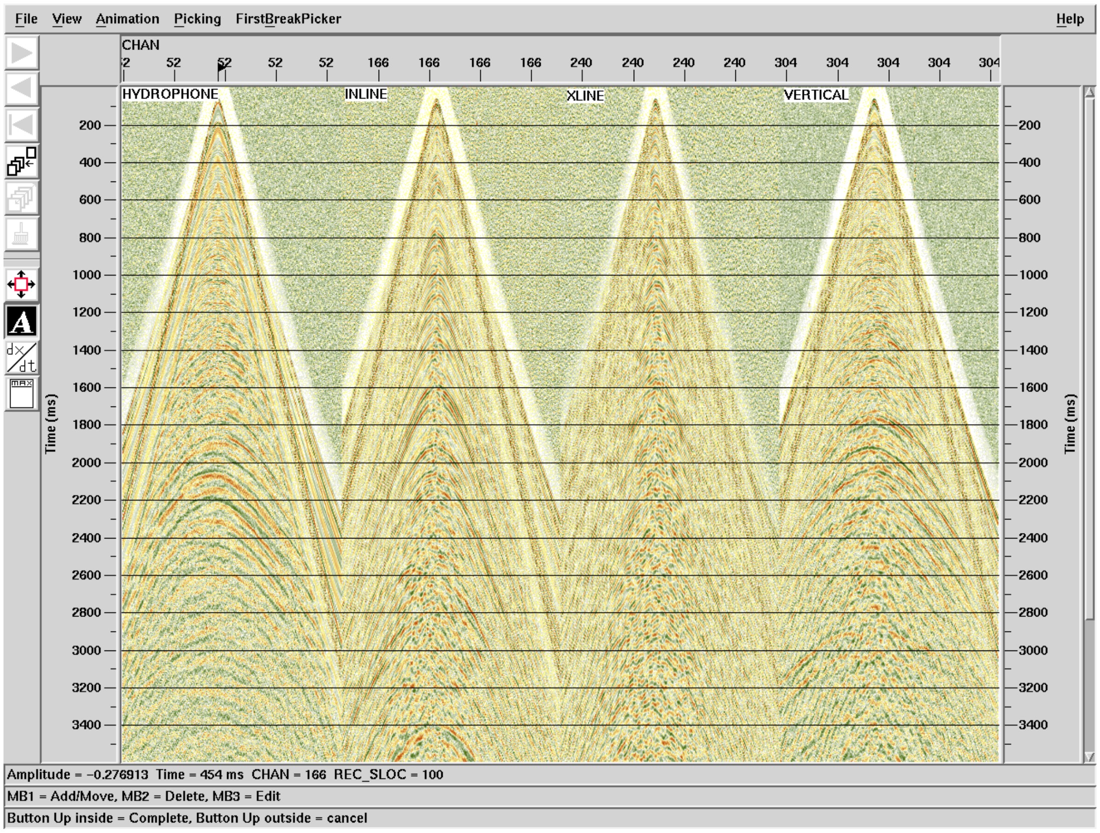

Figure 2.7. A set of receiver gathers from a common receiver station. The four components are displayed. Hydrophone measuring pressure and three orthogonal geophones measuring particle motion. Notice the flatter moveout of events on the vertical geophone and hydrophone compared with the events on the Inline geophone. A flat moveout curve is associated with high proagation velocity; P-waves travel faster than P-S converted waves. Also note the generally low coherence of events in the cross line records.

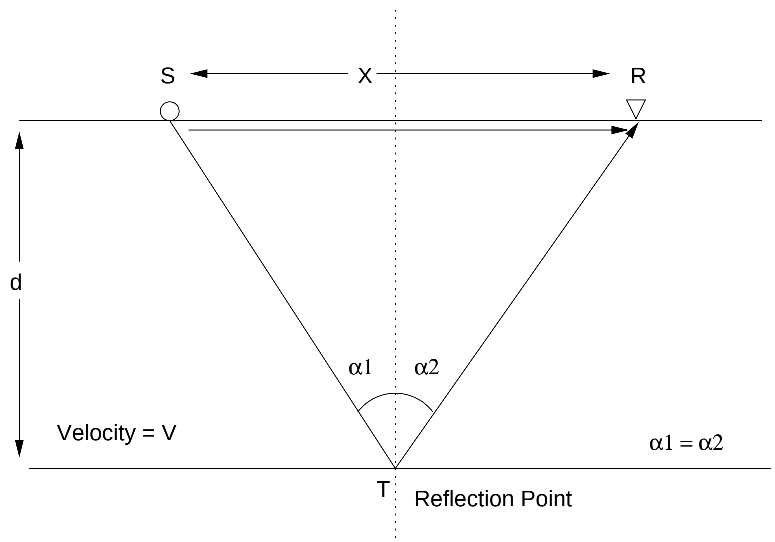

Figure 2.8. A simple model showing a source and receiver in a constant velocity medium over a single reflecting layer. S and R mark the source and receiver locations.

2.4.1 NMO and velocity analysis

Consider the response of a single receiver to a source located over a single horizontal layer as shown in Figure 2.8. In a constant velocity medium the ray paths that the waves travel along are straight lines. The first arrival at the receiver is the direct arrival, where the ray path being considered is the shortest distance between source and receiver (SR). A plot of arrival time versus source-receiver offset for a direct wave is a straight line, where offset is the horizontal distance between the source and receiver. The next ray path to consider is that of the reflected wave (STR). The angle of incidence is equal to the angle of reflection, so the reflection originates mid way between the source and receiver. As the distance SR is increased, the increase in the square of the travel time for reflected waves is proportional to the square of the offset;

$$v^2t^2 = x^2 + 4d^2, \tag{2.4}$$

where x = SR, and t is the travel time. This can be rearranged to give the well known hyperbolic equation

$$t^2(x) = t^2(0) + \frac{x^2}{v^2}, \tag{2.5}$$

where

$$t(0) = \frac{2D}{v}. \tag{2.6}$$

In equation 2.5 the first term on the right-hand side is the square of the vertical two way travel time to the interface. The second-term involves the offset x and the velocity v, and is the square of the horizontal component of the travel time from the source to the receiver. If the velocity v is estimated from travel time data using equation 2.5, it should be noted that only the horizontal component of the velocity is being estimated . Only in isotropic materials is the vertical component of velocity the same as the horizontal. A reflection event and a direct arrival are shown on the schematic diagram in Figure 2.9. For an isotropic solid the reflection event plots on a hyperbola, the equation for the curve can be used to link the seismic velocity to offset and arrival time. This geometrical effect is known as normal moveout, or NMO. A value of v can be obtained by fitting travel time data to Equation 2.5.

The basis of velocity determination for the CMP method is that the shape of the arrival time-offset curve can be related to the velocity. The methods for fitting the data vary; in the classic, but now redundant, $t^2 : x^2$ method, points of travel time vs offset are plotted on a graph and the slopes of the resulting curve are interpreted to give stacking velocity. The use of computers enables methods based on coherency calculations to fit hyperbolic curves to the data. These computer based, coherency measuring techniques are known as velocity analysis. When performing velocity analysis, value v_{stack} is found by applying the NMO correction to the traces in the CMP for different test values of v_{stack}. The picked value of v_{stack} is that which gives the highest coherence between traces of different offsets at t_0 in the CMP gather. Figure 2.14 shows a schematic example of traces in a CMP gather before and after NMO correction. The correct NMO velocity has been applied as the events are perfectly lined up in the corrected

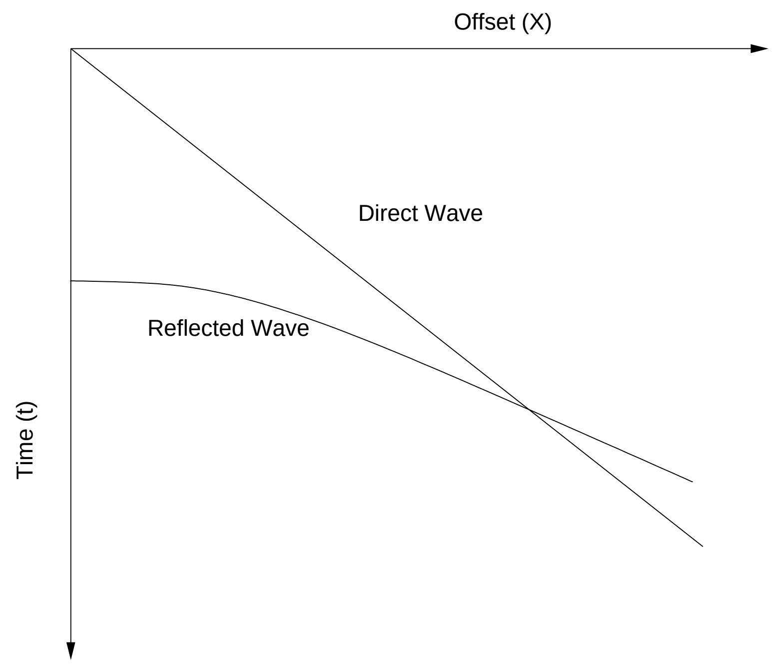

Figure 2.9. A schematic diagram showing how travel time varies with offset for a direct and a reflected wave generated in the simple model shown in Figure 2.8

gather on the right. For horizontal reflectors in an isotropic material, v_{stack} approaches the RMS velocity as the source-receiver offset approaches zero. The RMS velocity is the average velocity for the ray path being considered. It is the average speed at which the wave must travel to have the arrival time at which it appears. For parallel layers the RMS velocity is related to the interval velocity by the Dix equations (Dix, 1955).

Following Yilmaz (2000) I first define the rms velocity in a horizontally layered earth:

Consider a model made of horizontal iso-velocity layers. If the layers each have interval velocities $(v_1, v_2, v_3, ..., v_n)$ where there are n layers, Taner & Koehler (1969) propose the travel time equation as

$$t^2 = C_0 + C_1 x^2 + C_2 x^4 + C_3 x^6 + ..., \tag{2.7}$$

where $C_0 = t_0^2$, $C_1 = 1/v_{rms}$, and $C_2, C_3...$ are complicated functions that depend on layer thickness and interval velocities. The rms velocity v_{rms} down to the reflector is defined as

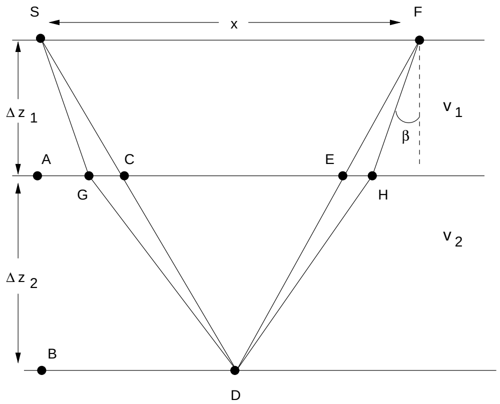

Figure 2.10. Two-layer case showing straight ray paths through C and E and minimum time paths through G and H. (after Dix (1955))

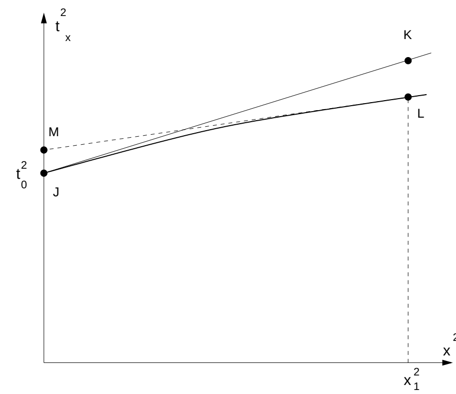

Figure 2.11. An $x^2 - t^2$ graph. The data curve, JL, with tangent line at J, JK , and tangent line at L, ML.(after Dix (1955))

$$v_{rms}^2 = \frac{1}{t_0} \sum_{i=1}^{N} v_i^2 \Delta\tau_i, \tag{2.8}$$

where $\Delta\tau_i$ is the vertical two-way time through the ith layer and $t_0 = \sum_{i=1}^{N} \Delta\tau_i$. By making the *small-spread approximation* (offset small compared to depth), the series in equation 2.7 can be truncated to leave equation 2.5 the hyperbolic travel time shown earlier.

Following the method of Dix (1955) it is possible to derive seismic velocities from surface records made over a plane horizontally layered earth made up of iso-velocity layers. When we plot t^2 as a function of x^2, if the velocity is constant, we get a straight line whose slope is $1/v^2$ and whose intercept is t_0.

Figure 2.10 is a schematic diagram of a simple two layer case with source and receiver offset by distance x. Figure 2.11 is a schematic plot. The experiment shown in Figure 2.10 is repeated for many values of x. The resulting $x^2 - t^2$ pairs define the heavy line JL in Figure 2.11. The velocity of the first layer can be determined using equation 2.5. If we caluclate the travel time for the next layer using straight paths from the source to the reflection point and from the reflection point to the receiver, say SCDEF, the $x^2 - t^2$ graph would be a straight line, say JK in Figure 2.11. But for the receiver at

F the true ray path is SGDHF, which corresponds to a shorter travel time. The true travel time is less than that calculated with a single straight ray path. The effect is smaller for smaller offsets, so that the line JK and the curve JL are tangent at J. To solve the problem of calculating the velocity in the second layer we must account for the different ray paths in the two layers. Dix inversion works by removing the effects of the overlying layer(s). First Dix states that we know

$$\frac{\sin\beta_1}{v_1} = \frac{dt_x}{dx}. \tag{2.9}$$

The tangent to the data curve at x_1 is the line LM, which has the equation

$$t_x^2 = M + \frac{1}{v_{rms_2}^2(x_1)}x^2. \tag{2.10}$$

Differentiation of equation 2.10 with respect to x gives, at $x = x_1$,

$$t_x\frac{dt_x}{dx} = \frac{x_1}{v_{rms_2}^2(x_1)}. \tag{2.11}$$

using equations 2.9 and 2.11 we get

$$\sin\beta_1 = \frac{x_1 v_1}{t_x v_{rms_2}^2(x_1)}. \tag{2.12}$$

Equation 2.12 gives β_1 in terms of the tangents[1] which can be measured. Once we have β_1 the distances and travel times associated with SG and FH can be calculated. It is then possible to calculate the time to be removed from t_x to give the travel time from G to H via D. Dix calls this time $(t_x)_r$ the reduced travel time. The distance $2AG$ can be computed, and subtracted from x to give $(x)_r$. If we now plot $(t_x)_r^2$ against $(x)_r^2$ we get a straight line whose equation is

[1]The tangents are stacking velocities which are close to v_{rms} for short offsets.

$$(t_x)_r^2 = (t_0)_r^2 + \frac{1}{v_2^2}(x)_r^2. \tag{2.13}$$

The slope gives us v_2 and the intercept gives us $(t_0)_r$. The thickness of the second layer is

$$\Delta z_2 = \frac{v_2(t_0)_r}{2}. \tag{2.14}$$

That is the basis behind Dix inversion, in a way it is a basic analytical ray tracing algorithm. It is not a completly accurate ray tracing algorithm; in an accurate ray tracing algorithm all the ray paths must all obey Snell's law all the time, not just when the direction of propagation is approximatly vertical through a plane horizontally layered medium.

Dix extends his work to be able to cope with n layers in the case of arbitrarily small x and no dip. This gives the commonly seen formulation of the Dix equation.

$$v_n^2 = \left(v_{rms_n}^2 \sum_1^n \Delta t_i - v_{rms_{n-1}}^2 \sum_1^{n-1} \Delta t_1 \right) / \Delta t_n \tag{2.15}$$

If the interval velocity for layers up to the n^{th} layer are known, the interval velocity for the $n + 1^{th}$ layer can be calculated from the RMS velocity to that layer. The assumptions inherent in Dix inversion are those of straight ray paths within layers, short offsets and plane horizontal layers. If these assumptions are violated then the results from Dix inversion can be in error to such an extent as to be meaningless. The ability of the Dix method to account for raypath bending is limited, so even if the subsurface is made up of plane horizontal layers, if the velocity changes between layers are large, the velocities from Dix inversion will be in error.

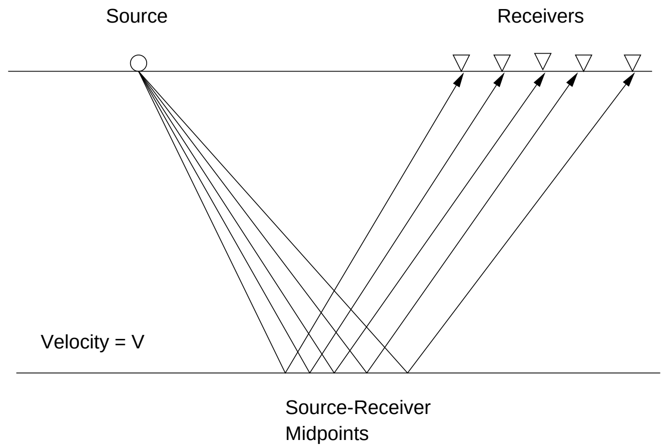

Figure 2.12. One source and a number of receivers will be able to record reflection events from a number of different subsurface locations.

For dipping layers the velocity needed to stack CMP data is higher than the velocity with which the energy travels in the subsurface, and the reflection points are no longer common (Levin, 1971). Also if the velocity is laterally variant the v_{rms} can vary substantially from the stacking velocity derived using hyperbolic moveout (Lynn & Claerbout, 1982). The apparent velocity resulting from reflection from a dipping interface can be related to the RMS velocity by the following equation:

$$v_a = \frac{v_o}{\sin \alpha}, \tag{2.16}$$

where v_a is the apparent velocity, v_o is the dip independent stacking velocity and α is the apparent dip of the interface (Levin, 1971).

2.4.2 CMP stacking

For efficiency, multi-channel seismic reflection data are recorded using acquisition systems such as the streamer or OBC shown in Figures 2.3 and 2.6. When a source is activated and the response is measured at many receiver stations, such as in Figure 2.12, the reflection response from a number of subsurface locations will be recorded.

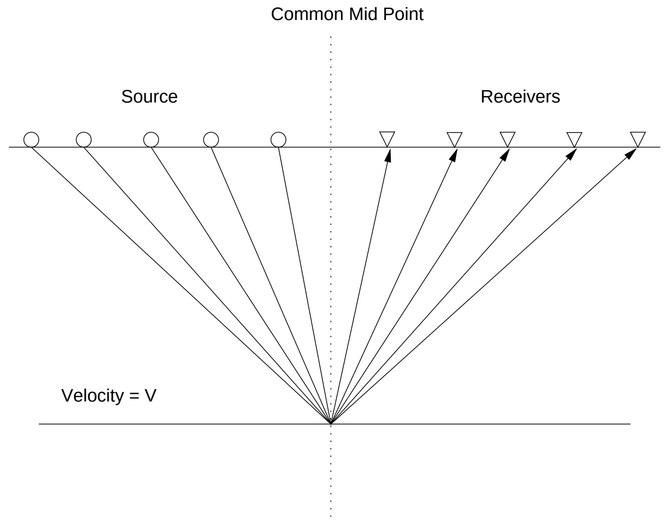

Figure 2.13. In a plane horizontally layered earth, shots and receivers spread symmetrically around the CMP record the reflection response from the same subsurface location from different offsets. Building up fold in this manner is critical to reducing noise in CMP processing

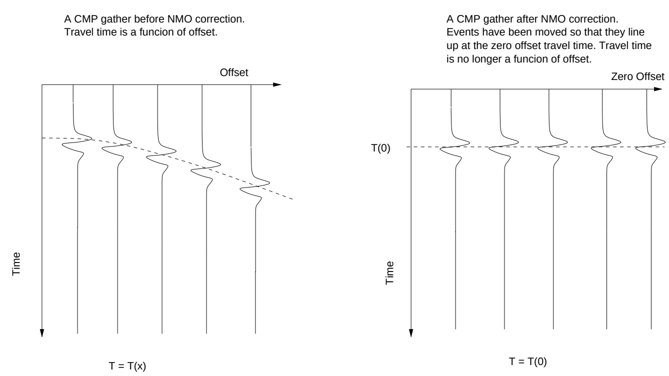

Figure 2.14. Once the best fit hyperbola has been found it can be used to line up events in the CMP gather. Traces in the gather can then be summed; this suppresses noise and reduces the number of traces in the survey.

By moving either the whole array, just the source, or both, the reflection response from many different subsurface locations is recorded. Using this method a single subsurface location or Common Mid Point (CMP) will be sampled from a number of different offsets, see Figure 2.13. The number of traces that sample a CMP is known as the fold of the CMP. High fold at a CMP is important both for finding velocity but also for suppressing a number of forms of noise.

When NMO is corrected for, the amplitude of a reflection events at non-zero offset is moved from its arrival time $t(x)$ to the zero offest travel time $t(0)$, see figure 2.14. The traces in the NMO-corrected CMP gather can be averaged and the resulting trace is said to mimic a zero-offset trace. This is known as stacking [1] and has three important effects:

- It attenuates multiple energy. Seismic velocity nearly always increases with depth. Events that have been reflected between the surface and reflecting layers a number of times spend more time travelling through the lower velocity shallow layers than primaries arriving at the same travel time. These multiple events stack with a lower velocity than the primary reflections and so when traces in a CMP are stacked, multiple energy is attenuated.
- It improves signal-to-noise ratio. The traces in a CMP gather are the result of a number of different seismic experiments, unlike the primary reflected signal, random or incoherent noise does not cerrelate between traces. When the traces in an NMO corrected CMP are averaged the random noise will interfere destructively whereas the primary signals will interfere constructively. The result is that the signal-to-noise ratio improves with the square root of the number of traces stacked.
- It reduces the number of traces to be processed. Each CMP gather is reduced to one trace, so there are many fewer traces to deal with in any further processes.

The result of the stacking process is a single trace for each CMP gather. This trace

[1] Stacking traces in a CMP is sometimes known as 'horizontal stacking'. 'Vertical stacking' is the summing of repeated signals from one source location.

is said to mimic the 'zero offset' trace. A zero offset trace is the trace that would be acquired by a co-incident source and receiver, and so it is positioned on a seismic section at the location of the hypothetical source-receiver pair. After stacking the data, each CMP is reduced to a single trace. These traces can be placed side by side to produce a 'stacked section'. We plot these traces with a vertical time axis and space as the horizontal axis. Because the earth is rarely made from plane horizontal reflecting layers, the reflection events on the stacked section may in fact be laterally shifted from their true location in space. Depth conversion is not acheived simply by scaling the time axis.The general shape of reflection events on this stacked section may reflect the subsurface geometry quite well if there is little structure. When structure or lateral velocity variation is present reflections will be mis-positioned, and some form of migration has to be used to correctly locate reflection events in space.

2.4.3 Migration

Post Stack Migration

The simplest migrations are 'Post-Stack' or zero-offset migrations. They are applied to the data after the NMO correction has been applied and the data have been stacked. At each CMP location there is a single trace, our hypothetical 'zero offset' trace. In a plane horizontally layered earth, this trace appears on the stacked section correctly located below the CMP location, as in Figure 2.15. When the reflecting interface is not one of a stack of plane horizontal reflectors, or there are lateral velocity variations, this is not true and the reflection is mis-positioned. Post Stack Migration attempts to locate dipping reflectors correctly, and to collapse the diffractions found on a zero offset section.

Dip Move Out

In areas of lateral velocity variation, or dipping structure, the CMP gather does not contain traces with a common reflection location. Two different problems arise here.

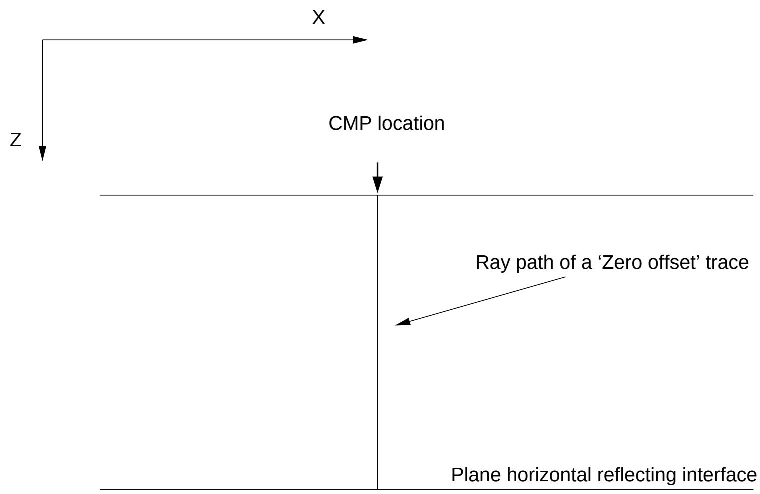

Figure 2.15. The location of the reflection point of a zero offset ray over a plane horizontal reflector is directly below the CMP. In a CMP stack section events are located at their correct lateral position.

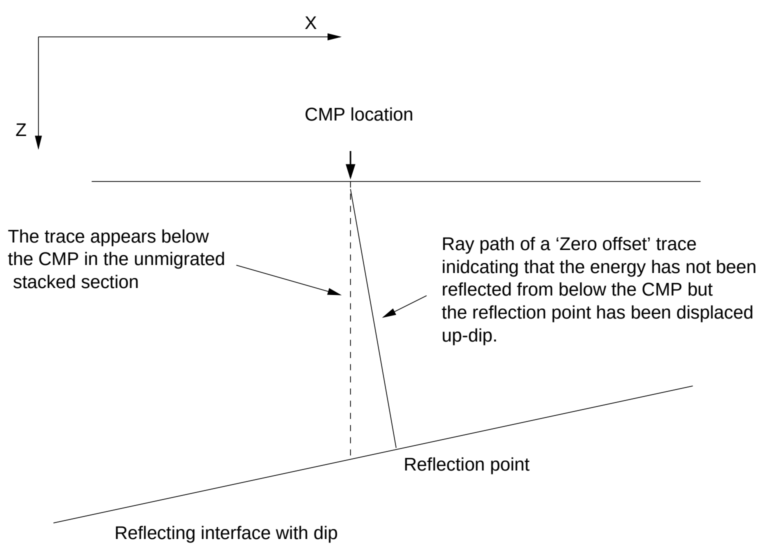

Figure 2.16. The location of the reflection point is moved laterally by the presence of a dipping reflector. In this situation the stacked section will not faithfully mirror the structure present in the subsurface.

First, the reflections do not originate from below the CMP location, and second, the traces in a CMP gather do not share a reflection location: their reflection points are dispersed along the reflecting interface (Deregowski, 1982). The smearing of reflection points even on a moderately dipping reflector is often small, but when ignored it causes a de-focussing of energy in the stacked section. A post stack migration can be used to take account of the first point, but it cannot compensate for the de-focussing caused by the reflection point dispersion. Another problem is that of conflicting dips, as the stacking velocity depends upon the dip of the reflector. If a flat reflection event is intersected by a dipping event (which can happen if there is dip out-of-plane of the section, or crossing reflectors) only one of these events can be correctly flattened when NMO is applied. So on the resulting stacked trace one of these events will appear dominant over the other. CMP stacking does not equally preserve crossing events with different dips, or stacking velocities. This is not true for a true 'zero offset' trace, where all events are present regardless of dip. A stacked section made by stacking NMO corrected CMP gathers is not the same as a zero offset section. While the best solution to this problem is to migrate the data before stack, it is often practical to apply a Dip-Moveout correction (Doherty, 1975; Sherwood *et al.*, 1978; Yilmaz, 2000).

When picking a velocity function in the presence of conflicting dips there is a problem, as two events at the same travel time require stacking with a different velocity. After correct application of DMO there is no such contradiction and the events stack with the same velocity, the effect of dip having been removed by the application of DMO. DMO is a partial migration and moves energy between CMP gathers, allowing the picking of dip-independent stacking velocities by moving traces to their correct CMP location before a second pass of velocity analysis. The stack after DMO and a second velocity analysis more closley resembles the true zero offset section. As a consequence of the partial migration effect of DMO, reflection point dispersal associated with nonzero offset recording in the presence of dip is removed. A better image will be achieved using a post stack migration, as the DMO stack more closley resembles the true zero offset section than a simple NMO corrected stack. DMO combined with zero offset migration is an often used practical solution to the problem of accounting for the effect of conflicting dips on velocity analysis. The more rigorous solution, however, is prestack time migration (PSTM) (Yilmaz, 2000). In the case of PSTM the migration step is moved up in the flow to precede the stacking step. For the case of no lateral velocity variation DMO followed by zero-offset migration is equivalent to PSTM (Hale, 1984). PSTM offers the opportunity to update the velocity model with the data closer to their correct lateral positions, and as such it is often an important step, even in depth processing flows. It must however be noted that the purpose of updating the RMS velocity field used for PSTM is to produce a more sharply focused image (in time), and not a geologically valid velocity field. I will not review the kinematics of DMO and PSTM here as our interests lie with another class of migration, where the output section is no longer in time, but in depth.

Depth Migration

All seismic traces discussed so far, and sections derived using them, have had their vertical axis in time. For the purpose of defining the structural geology this is only helpful up to a point; the earth we are exploring has vertical coordinates of depth, not time! Unfortunately conversion from time to depth is not simple; ray bending at layer boundaries, or through velocity gradients must be taken into account to generate a true depth section. Ray bending gives rise to non-hyperbolic travel time curves in CMP gathers; amplitudes and travel times are therefore distorted when hyperbolic NMO is applied. Depth migrations should therefore be applied before stack. Also we must note that ray bending can occur out of the plane of the survey, and hence true depth migration is a 3D process.

There are many different algorithms for pre-stack depth migration (PSDM) and they generally take one of two forms; Kirchhoff (Schneider, 1978) or Finite Difference (Claerbout & Doherty, 1972); the latter is also known as 'Wave Equation' migration, although there are other implementaions of wave equation migration (Berkhout, 1985). I will now outline qualitativley how both methods work. Kirchhoff migrations can be thought of as diffraction stack methods and there are two conceptually different methods of doing this. The first involves calculating the shape of diffractions originating at each sample of the subsurface and stacking the amplitudes along that diffraction curve at that image point. The second involves calculating all the possible locations that a given amplitude sample could have arrived from based on its travel time, source and receiver location, and placing a weighted version of that amplitude value at all points along the ellipse[1], this is done for all samples and the resulting image is a superposition of all the displaced (migrated) amplitude values. Amplitudes are not automatically correct after the data have been migrated, calculating the correct amplitude weighting function is an important part of Kirchhoff migration. The migration works on traces sorted by offset, and the natural output of Kirchhoff migration are image gathers sorted by offset . The traces in the image gathers must be stacked to generate the traces of the migrated-stacked section that gives an 'image' of the subsurface structure. This is the type of migration that I use exclusivley in this thesis.

Wave equation methods rely on downward continuation of the wave field; that is, back propagating the recorded wave field to a new datum within the known velocity model. At the new datum all diffractions originating from that same depth will be collapsed back to a point. This is known as the imaging condition (Claerbout & Doherty, 1972). The samples from this level are then taken to form a part of the final migrated image. This method is necessarily recursive as the output from one downward continuation step is then used as the input to the next downward continuation step. It is difficult to produce offset domain common image gathers using wave-equation migration Sava & Fomil (2003) as the offset dimension of the downward continued data shrinks with depth. An advantage of this method is that it explicity handles amplitudes correctly and accounts for all travel paths in highly complex models.

For the case of this thesis I assume that when given the correct velocity model the migration algorithms themselves will return a correctly focused image of the subsurface. This is not exactly true in some cases, in particular some implementations of Kirchhoff migration are unable to cope with multiple ray paths between points, be they source, receiver or diffraction points. For the velocity models that we come across in the thesis multipathing is not an issue. All we need to take with us is that you can do pre-stack

[1]This ellipse is only an elipse in a constant velocity medium. The shape of this 'line of equal travel times' may be highly complex in areas with a complex velocity distribution.

depth migration, and, given the correct velocity field, the result is an image of the subsurface with reflection events in their correct spatial locations.

2.4.4 Migration and Velocities

A common image gather (CIG) is the natural output of Kirkhhoff migration algorithms. It is the collection of traces that have energy reflected or difracted from the a point in space vertically below the CIG location.The horizontal axis of a CIG is offset and the vertical axis is depth a schematic diagram is shown in Figure 2.17. A very fortunate property of Kirchoff depth migration is that these CIGs provides a diagnostic for deriving an accurate velocity model. If events in the depth gather are flat it implies that imaging with that velocity model returns the same model from all offsets, and that the velocity model used for migration is correct. I use them as evidence for the accuracy of the velocity models that I generate and use to migrate data in Chapters 7 and 8. The traces in a common-image gather can be stacked to give a single trace. These single traces can then be placed side by side to form a migrated stacked section. When the correct velocity model is used for the migration the reflection events are correctly located in space.

Velocity models

The RMS velocities determined by NMO, DMO and PSTM can be used to form focused images in time. The RMS velocity fields may also be inverted to create depth velocity models that are used for depth imaging. For depth imaging we use an interval velocity field which is a seismic representation of the geological model, and so has depth as the vertical coordinate, not travel time as in an RMS velocity field. Abrupt discontinuities are allowed within the model, and where the velocity is controled by structure, the interfaces in the model must match the interfaces in the final migrated stack. In areas where a compaction gradient, or lithological changes have a significant influence on the velocities, the velocity model will not have the same structure as the geology.

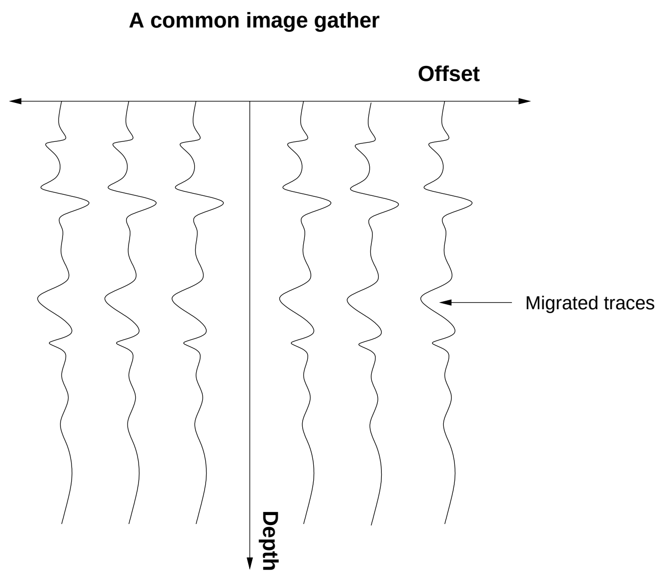

Figure 2.17. A schematic common image gather, all the traces have been migrated and are imaging the same point in space from different offsets.

Problems with depth imaging traditionally arose from a lack of computing power, but as this becomes less of an issue, depth imaging is being used in many situations by the industry. The problem of building accurate interval velocity in depth models remains. As a consequence nearly all depth processing flows are preceded by a full time processing sequence, up to and including time migration, which we have seen is needed to get an accurate RMS velocity field. The initial depth velocity model is generated using the RMS velocity field, which is converted to an interval velocity in depth field. There are a number of different ways of converting an RMS velocity field to a depth velocity field.

The most simple is Dix inversion, which assumes a 1-D velocity structure; that is, plane horizontal interfaces between iso-velocity layers. It can be implemented as a structure-independent inversion, which allows vertical gradients in the resulting velocity field. Or it can be a structure-dependent inversion, where a layer-by-layer inversion of the RMS velocity associated with layer boundaries in the earth model is performed. It is reasonably accurate for a small number of layers and has provided the backbone of velocity determination for many years. However, for an earth model with dipping boundaries and layer velocites with vertical and lateral velocity variations, more accurate methods are required.

The following are three ray-based inversions, all three can account for vertical velocity gradients and ray bending at layer boundaries.

In **Stacking velocity inversion** normal incidence ray tracing of interfaces from the stacked section is used to define an interface in depth. This is followed by modelling of non zero-offset travel times with trial constant velocities. These modelled travel time curves are then fitted with hyperbolae. The velocity at which there is a minimum difference between actual stacking velocity and modelled stacking velocity is that which is selected for use at that CMP point (Thorson *et al.*, 1987). This method is better than Dix inversion because it can correctly take acount of the effects of overlying structure. However when reflection events are not well characterised by hyperbolae such as when there are strong vertical velocity gradients the method is not as accurate as coherency inversion (Fagin, 1998).

Coherency inversion also needs time horizons from unmigrated CMP data. This method involves interaction with actual data in CMP gathers, unlike stacking velocity inversion where the RMS velocity field is used. A trial constant velocity is assigned and normal incidence time-depth conversion is applied to picks from the unmigrated time horizon. Travel times over a range of offsets are then modelled and semblance is computed within a window with the same trajectory in the CMP gather. The velocity associated with the highest semblance value is then used at that CMP. This method does account more accurately for non-hyperbolic moveout in the CMP gather than stacking velocity inversion can. Manual picking on Pre-Stack gathers is avoided with both these methods (Landa *et al.*, 1988; Yilmaz, 2001).

Tomography Complex pre-stack travel time behaviour is accounted for by finding a best fit velocity model to a large number of rays. Rays are traced through an initial velocity model which is updated until the modelled travel times match those observed in the data. The model space can be made up of layers or more usually grid squares. This method requires pre-stack picking of travel times (Bishop *et al.*, 1985). A method that does not require manual picking and has proved very sucessful on P-wave data sets is Stereotomography (Billette *et al.*, 1998).

The other group of methods may be termed **Image gather analysis.** Image gathers are the ouput product of depth migration; they contain migrated traces. With the migration algorithm that I use each trace is associated with a different source-receiver offset. When the velocity model is correct, the traces are located at their correct spatial location and the events in an image gather appear flat. If the events are not flat then the velocity model is wrong. It is possible to update the velocity model on the basis of the curvature of events in image gathers (Chauris *et al.*, 2002a,b). In the method of Stork (1992) the velocity update step uses layer tomography.

All of these velocity determination methods are rather specialised, and not widely available. The only tool I have is called Migration Velocity Analysis (MVA) implemented in the ProMAX package. MVA falls into the category of a Kirkhhoff 'Image gather analysis' method. Migrated data in Common Image Gathers (CIGs) are viewed alongside the velocity model. If the events in the gather are not flat then the velocity model needs to be updated. If reflection events 'frown' the overlying velocity model is too fast, and if the events 'smile' the overlying velocity model is too slow. In Figure 2.18 I show a CIG gather resulting from the migration of synthetic data. The migration has been performed with three different velocity models. The first is slow by 500 m/s, the second is the correct velocity model, the third is migrated with a velocity model which is 500 m/s fast. Notice that the depths of the events also change with the velocity, so a smiling event will be too shallow, and frowning one too deep. The MVA tool in ProMAX allows the user to change the velocity model and view approximately the effect this change in the velocity model will have on the migrated data, without going to the trouble of re-running the migration. The update on the migrated data is based on assuming a 1-D velocity distribution at the updated CIG locations; the change in travel time with offset in the new CIG is calculable without resorting to ray tracing.

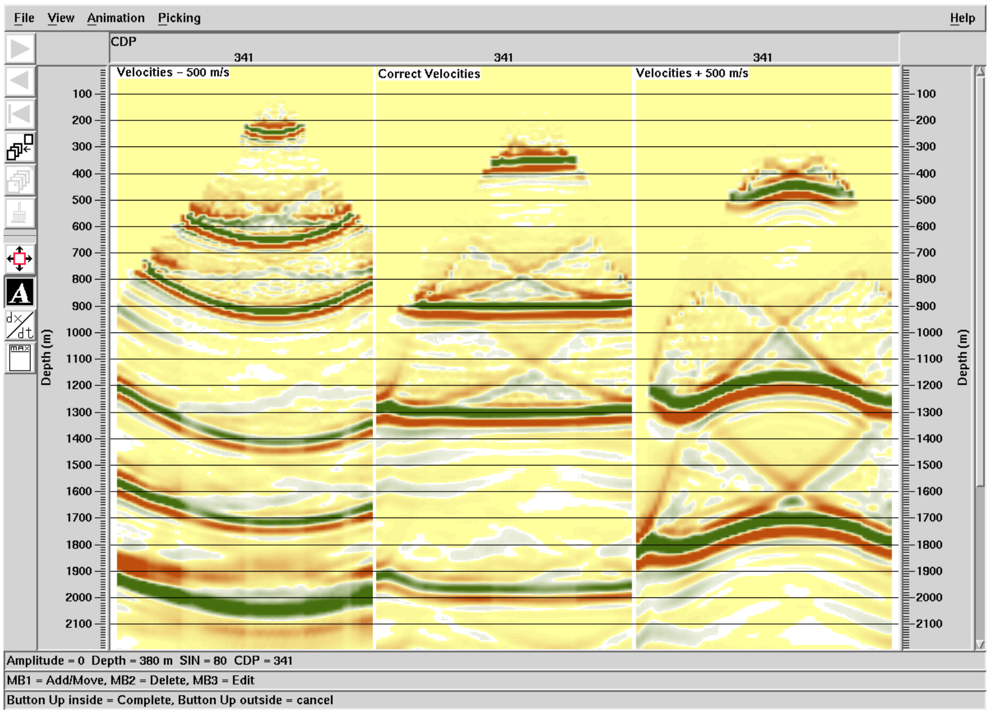

Figure 2.18. Migrated Image gathes are a diagnostic for velocity model determination. On the left, the velocity model used for migration is slow by 500 m/s, the middle gather the migration used the correct velocity model, the right hand gather used a model fast by 500 m/s. Notice that the residual moveout is different in each gather, and that when the correct model is used the events in the CIG are flat.

Migration, Modelling and Inversion

Seismic modelling and migration have always had a close relationship. It is reasonable to look at migration and inversion as the inverse process of the other. Modelling simulates the wave field that would be recorded given that model, and inversion is used to find the model given the data. Migration attempts to locate recorded data to their correct location within the model. All the 'moving about' of data is governed by the same wave equation, either operating in a forward sense (modelling), moving data away from the source, or in a reverse sense (migration), moving data from receivers back into the earth (Santos *et al.*, 2000). In Kirchhoff migration travel times between sources and receivers are often calculated by ray tracing; if so, an efficient ray tracing algorithm will be an important part of the migration code.

2.5 Converted wave data processing

Asymmetry in the travel path means the CMP assumption is not even approximately valid for P-SV converted waves. The location of the 'Common Conversion Point' (CCP) must be determined if a similar processing flow to that used for P-P data is to be followed. This is problematical, as the location of the conversion point depends on the $v_p : v_s$ ratio, the material properties one is trying to determine. The energy follows an asymmetric ray path even for plane horizontal layers, because of the difference in velocity between P- and S-waves. As the component of slowness parallel to the interface remains the same, the lower speed of the S-wave after conversion compared with the P-wave before conversion means that the S-wave travels away from the interface closer to the vertical than the incident P-wave that generated it (See equation 2.3). This means that the CMP assumption made in the standard P-wave processing discussed earlier does not hold true. Ideally the conversion point must be explicitly calculated for each trace; Zhang & Robinson (1992) describe an iterative scheme for calculation of the conversion point in isotropic media. Once the traces have been gathered into CCP gathers it is possible to mirror a similar processing flow to that used for P-P waves. A typical flow might consist of approximate common conversion point calculations,

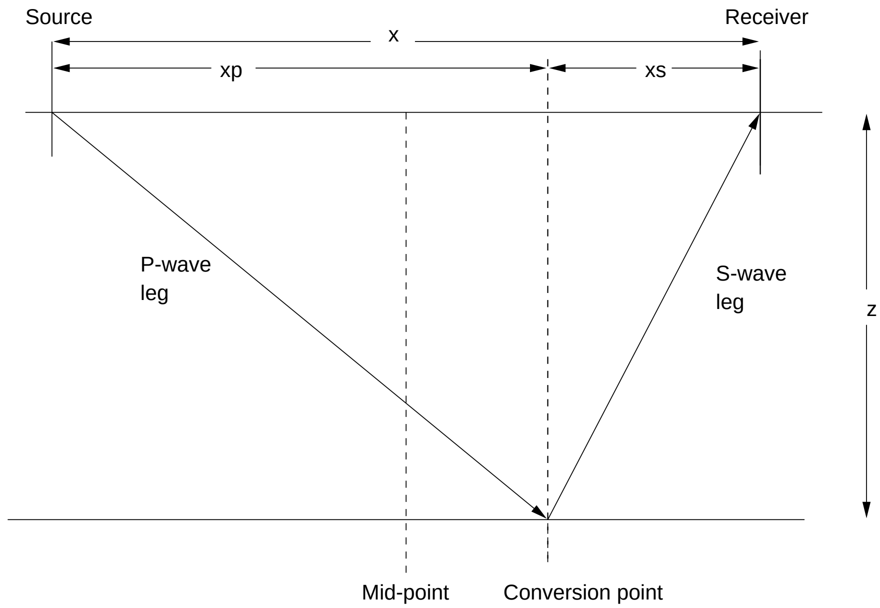

Figure 2.19. The location of the conversion point for P-SV data is not at the mid point between source and receiver, so conventional CMP processing cannot be applied.

converted wave velocity analysis, converted wave DMO, a second velocity analysis, non-hyperbolic NMO followed by stack and post-stack migration (Yuan, 2001).

Any method that requires that the data be gathered into CCP gathers needs an a-priori estimate of γ (the $v_p : v_s$ ratio).

2.5.1 Anisotropy

If the speed of propagation of a wave is the same whichever direction it is travelling through a medium, the medium, in terms of velocity at any rate, is isotropic. When the speed of propagation depends upon the direction of propagation, then the medium is anisotropic. Unless properly accounted for anisotropy will cause errors in velocity analysis, CCP binning, and correct depth imaging of seismic data. Because of this many current converted wave processing techniques incorporate the effects of anisotropy explicitly. The work that I have done for this thesis uses velocity models with isotropic velocity distributions within the layers, so I will not dwell on anisotropy and its effects

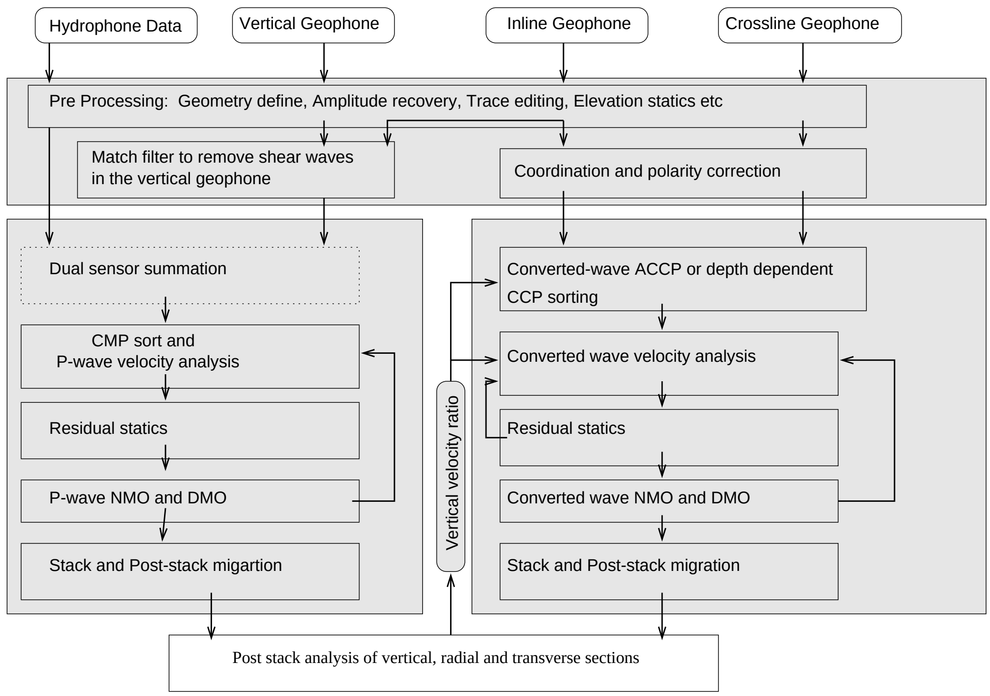

Figure 2.20. A 4-C data processing flowchart, after Yuan (2001).

at this stage other than to acknowledge that any results I show here are valid only for the isotropic case.

2.5.2 Depth velocity model building

I consider model building for joint P-P and P-SV processing in three different categories.

- Depth conversion of RMS velocity fields derived from a full time processing flow. I also place 1-D updates to the depth velocity field using migration velocity analysis in this group, as these methods do not fully account for complex ray paths (Group 1).

- Inversion methods which account correctly for the converted wave ray path through the velocity model (Group 2).

- Pure mode S-S travel times re-constructed from observations in the P-P and P-SV datasets (Group 3).

Group 1

The very simplest method of defining an initial S-wave velocity field is to divide the values in the P-wave velocity field by 2 or 2.5, and rely on effective update steps to improve the velocity field (Zhang *et al.*, 2002). The 'standard' time domain method follows a flow similar to many P-wave flows involving ACCP gathering of converted wave data, initial velocity analysis, DMO, CCP gathering, a second velocity analysis followed by non-hyperbolic NMO correction and stack. The stacking step can then be moved till after migration if prestack time migration is applied (Mancini *et al.*, 2003). The resulting RMS velocity fields (and anisotropic parameters) can then be inverted using Dix-like equations to build the depth velocity model (Yuan & Li, 1998).

Updates to velocity models can be made in the depth domain by analysing migrated gathers after PSDM. Mikhailov *et al.* (2001) find that a linear term dominates the near-offset residual moveout of migrated converted wave image gathers. This is caused by lateral mispositioning of the conversion point due to the errors in γ (the $v_p : v_s$ velocity ratio). Once the linear term has been corrected for, the curvature of events in the image gather can be used to quantify the velocity error. Both Mikhailov *et al.* (2001) and Zhang *et al.* (2002) recognise that anisotropy must be included in a complete depth imaging flow. The former use well control to get the true vertical depth of the events and derive anisotropy parameters from the mis-match between true (well) depth and an isotropic processing of the P-P and P-SV data. Using the same basic relationships Zhang *et al.* (2002) use analysis of short spread data to estimate vertical P- and S-wave velocites, and thus the vertical depth of the reflector. It is interesting to note that Zhang *et al.* (2002) suggest that analysing only the near offsets is an acceptable way of deriving vertical velocities and hence depths in anisotropic media where the anisotropy has a vertical axis of symetry. This suggests that our method might be applicable to real data from an anisotropic model if we reduce the offsets sufficiently.

Group 2

The second family are methods based in the depth domain, which can account for complex (non-hyperbolic) pre-stack travel time behaviour, hence finding true ray paths through a depth velocity model. Tomography requires travel time curves from paired P-P and P-S events, and has been shown to give good results where the data quality is high. The scheme described by Herrenschmidt *et al.* (2001) and Ehinger & Lailly (1995) uses P-wave information to get P-wave velocity and interface geometry, then the S-waves are inverted using the geometry found using the P-waves to find the S-wave velocity. Finally a joint inversion is run to retreive the P- and S-wave velocities and the interface geometry. A tomographic scheme is ideally suited to converted wave data processing as each ray is explicitly traced through the velocity model. It is straighforward enough to change the velocity model being used from the P-wave to the S-wave velocity model on reflection, thus honouring converted wave propagation through the velocity model.

Another method that I consider as part of the second group is stereotomography. It has only just been applied to P-SV data, but the method has shown great promise when applied to P-P datasets (Billette *et al.*, 1998). This method requires picking of locally coherent events in the pre-stack data. These events are characterised by their slope and travel time. The picking aspect of this method is automated. These slope and travel time data are then related to a single ray traced through a velocity model. For the inversion of P-P and P-SV data no event matching is needed. As yet, fully fledged stereotomography for PS events has yet to be implmemented.

Group 3

A third and novel aproach to the problems of processing P-P and P-SV data has been formulated by Grechka & Tsvankin (2001) where, instead of processing the P-SV data, they reconstruct the S-S travel times and process these. The S-S data can be processed using all the processing techniques developed for P-P processing on the S-S travel times to build the S-wave velocity model. This method, like ours, requires pre-stack picking of P-P and P-SV travel time curves (Grechka *et al.*, 2001). It has not yet been established whether reconstructing and processing the pure S-mode travel times is more or less work than processing the P-SV converted waves (Gaiser *et al.*, 2001).

2.5.3 P-SV migration

When applied correctly the result of migration is similar to that for P-P migration: the generation of an image of the subsurface with reflection energy located at correct reflection points and diffractions collapsed back to the scattering points that generated them. It uses, ideally, dip independent stacking velocities (Alfaraj & Larner, 1992). It is interesting that we cannot claim in this case to imitate the zero-offset wavefield when using converted wave DMO processing. We saw in section 2.1.3 that for the isotropic case there is no mode conversion at zero offset and so we would have no amplitude on our zero offset trace if we correctly mimicked the real converted wave zero offset trace. In fact we stack the amplitudes over a number of traces in the gather, and the resulting stacked trace attempts to mirror the kinematics of the zero-offset trace, but not the amplitude response. In the post-stack case a converted wave RMS velocity field can be used to focus the converted wave time image. For good results anisotropic parameters must be estimated (Mancini *et al.*, 2003). As one would expect, both P-wave and S-wave velocity fields are required for converted wave PSTM (Harrison & Stewart, 1993).

When calculating travel times for depth migration of converted wave data, the leg from source to conversion point is traced using the P-wave velocity, the leg from the conversion point to the receiver is traced using the S-wave velocity, so both P- and S-wave depth velocity fields are required.

2.6 Current shortcomings and the future

2.6.1 Event Correlation

In many processing schemes it is necesairy to tie events at the top and bottom of the interval for which we wish to derive γ. This involves picking horizons on P-P and P-SV stacked section which we believe are same. Unless there is good structure, event correlation can be ambigious, as the travel times for P-P and P-SV events are different. Event correlation is slightly complicated by the possibility that the polarity of the reflection response from a given interface can be different for P- and S-waves. Unfortunately, it is very hard to quantify the errors when doing this event correlation. Sometimes a simple vertical stretch is used to match the sections. If there is any lateral velocity variation this is not correct.

2.6.2 Conversion Point Calculation

Any processing scheme that depends on gathering the data in common-conversion point gathers has to start with an a-priori estimate of the $v_p : v_s$ ratio. This initial estimate will need to be updated further down the processing flow, as better estimates of the velocity ratios are derived. Ideally one would not want to expend time calculating conversion point locations and gathering traces in a way that will have to be revised only a few steps further down the processing flow.

2.7 Where do we go from here?

Time processing for pressure and converted wave datasets leaves us with the problem of reconciling the travel time differences between stacked sections. We find ourselves in the tricky territory of event correlation. It would be good either to quantify the error in the event correlation step or work in a system which avoids it entirely. If we could calculate the error in the event correlation it might be possible to search for a 'minimum error' match between the P-P and P-S sections. I chose to avoid post-stack event correlation. We would like to operate in an environment where we do not have to assume plane horizontal layers for even our initial velocity analyses as velocity update methods are just that, and should start from as close to the correct result as possible in order to be effective. We hope that explicitly incorporating dip will improve the initial velocity estimates. Also we should not have to make any assumptions about $v_p : v_s$ velocity ratios before we have even started our processing. This leads us to working in the common shot and receiver gathers, to avoid the estimation of velocity ratios that CCP binning requires. Working in the depth domain will make comparing P-P and P-SV sections and the corresponding P- and S-wave velocity models easier. It also has the advantage that with the correct processing the events will be correctly located in space, which is advantageous from an interpretation point of view. I am not alone in believing that the depth domain is where the future of integrating P-P and P-SV datasets lies:

> *"Processing to provide consistent images in depth and improved rock property estimates are critical to current developments"* (Stewart *et al.*, 2003) .

> *"The future is much wider (than imaging through gas clouds) and will be reached when fully compatible (depth and amplitude) P and PS depth sections are obtained, confirming structures and solving, by the way, the seismic inversion problem"* (Garotta, 2001).

Chapter 3

Vector fidelity issues in four component (4-C) sea floor data

In this chapter I introduce the real dataset on which I test our methods. The data have a problem with contamination caused by coupling between the horizontal inline and vertical geophones and in this chapter I show how this contamination is suppressed using a predictive least-squares filter.

To test our methods on real data we have a dataset from the North Sea. It is a four-component (4-C) OBC data set acquired by Geco-Prakla for Shell in 1996 over the Guillemot field. The data comprises four seismic lines, two acquired with conventional 2D shooting, and two shot with cross-spread shooting. I use only one of the 2D lines as our test dataset; it is known as 'Line 16'. The data are generally very high quality, though unfortunately the dataset shows shear (S) wave energy, usually measured only on the horizontal components, contaminating the compressional (P) wave signal on the vertical geophones. This cannot be explained by an unfavourable shallow velocity structure. Shear wave energy on the vertical geophone is a result of a coupling mechanism between the inline and vertical geophones. It can be removed satisfactorily using a least squares predictive filter.

3.1 Introduction

The term 'vector fidelity' is traditionally associated with the correct recording of the vector wavefield. Work is found often concentrating on the faithful recording of a unit amplitude on all orientations of a geophone, and corrections that can be made to orientate the records with relation to anisotropic parameters in the earth. In this case I am looking at a rather less subtle problem, in which a part of the recorded wavefield on one sensor simply shouldn't be there. The term 'vector fidelity' was coined by Leon Thomsen (of Amoco) at the 1998 I/O Sensor Technical Workshop, in a talk entitled 'Vector issues in 4C/3D OBS surveys' (Ziolkowski, *pers.com.*)

Many processing steps used on multi-component seismic data work either on P-P reflected energy or P-SV converted energy. To ensure a maximum signal-to-noise ratio the modes must be separated into P and SV types before any further processing is applied. In the case of an Ocean Bottom Cable (OBC) in the marine environment it is often assumed that the low velocity layers near the sea floor will, because of Snell's law, cause the ray paths of reflected energy to emerge very close to the vertical. P-wave particle motion is parallel to the ray path. When the emerging ray is close to the vertical the P-wave energy is recorded on the vertical geophone. For P-SV waves the particle motion is at right angles to the ray path and so the energy is recorded on the inline horizontal geophone.

Yuan (2001) has processed the same data. He showed that there was some form of contamination of shear waves on the vertical geophone, which was suppressed using a match filter. A typical common receiver gather is shown in Figure 3.1. The vertical and inline horizontal components are shown. The unexpected shear wave energy on the vertical component can clearly be seen. The P-P events are flatter and the P-SV events are steeper. In the gather on the left, data showing both steep P-SV type moveout and also data showing flatter P-P type moveout can be seen. The moveout of the unexpected energy is the same as that of the shear waves shown in the inline horizontal gather. Notice that the gather on the left shows only the steep moveout P-SV data. The contamination is not apparent in all the gathers. Badly contaminated

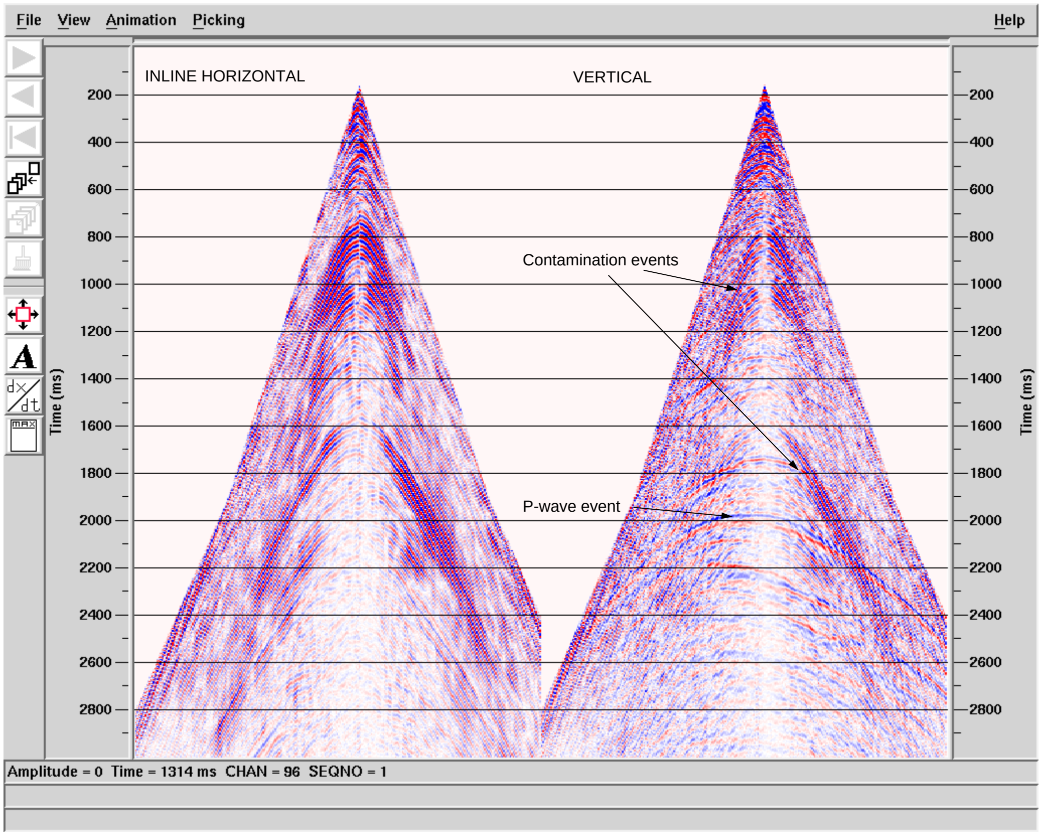

Figure 3.1. Vertical and inline component receiver gathers at receiver 30 from the North Sea data set.

gathers are all concentrated at one end of the receiver line. The inline horizontal component appears to be 'clean' showing no evidence of P-wave energy. This is the reverse of what one would expect as the P-wave ray path is the more likely to have a non-vertical emergence angle because of the of high P-to-S-wave velocity ratios near the sea bed. Hence P-wave contamination of the predominantly P-SV inline data set would be expected, not vice-versa. We would expect to see a component of the P-wave energy on the inline horizontal geophone if the particle motion is not vertical. We do not see this, so the P-wave emergence angle must be nearly vertical, and hence to S-wave particle motion must be almost perfectly horizontal, we do not expect to see S-wave motion on the vertical component geophone.

3.2 Filtering

The contamination on the vertical component occurs at travel times similar to those of the high amplitude shear wave arrivals on the inline horizontal geophone. This implies that energy orientated in the inline direction can be transmitted via the gimballing mechanism, or some other part of the sensor housing, and can then excite the vertically oriented geophone (Kees Faber 2002, pers. com.). I assume that this is the case; we can approach the problem in the following way: The seismograms recorded at a given receiver station may be considered to be a superposition of a number of different signals. The inline horizontal geophone appears to record only the inline horizontal particle motion $v_x(t)$. The vertical geophone, though, is recording not only the vertical particle motion $v_z(t)$, but also a filtered version of $v_x(t)$. Assuming that the filtering mechanism is time invariant for a given geophone, a certain proportion of the signal on the vertical geophone is predictable from the inline geophone. Thus:

$$v_{vert}(t) = v_x(t) * f(t) + v_z(t) \tag{3.1}$$

where $v_{vert}(t)$ is the total signal recorded on the vertical geophone, $v_z(t)$ is the vertical component of particle velocity, $v_x(t)$ is the inline component of particle velocity and $f(t)$ is a filter convolved with the inline component of particle velocity. The asterisk $*$ indicates convolution. The filter $f(t)$ can be estimated using Wiener Least Squares, given $v_{vert}(t)$ and $v_x(t)$. Once the filter has been derived it is then convolved with the $v_x(t)$, to calculate the predictable part of the vertical component. This is then subtracted from the vertical signal $v_{vert}(t)$, to leave us with the vertical particle motion $v_z(t)$, which is what we want.

When calculating the filter, we aim to find a single filter for each receiver which removes the contamination without distorting the amplitudes of the vertical signal. A filter can be calculated either on a trace by trace basis or on one 'super trace'. In the trace by trace method, filters are calculated and applied to individual traces.

A 'super trace' is made up of all the traces in a receiver gather placed end on end. I devised this method of arranging the data because I felt that the more data that the filter can be calculated on, the better the filter will be. I also felt that the statistics of the least-squares filter would be better at picking up a common signal than simply stacking the filters calculated from the individual traces. The 'super trace' method gives better results than those achieved by stacking individual filters in a gather, and a more even amplitude response over the whole gather than applying the one filter-per-trace. When using filters calculated on a trace-by-trace basis, high amplitude events can have a very significant effect on the resulting filter leading to odd amplitude effects in the filtered output trace. Better results can be achieved by calculating the filter over a 'window' of the data, avoiding the direct arrivals and very early times. The effect is shown in Figure 3.2 An example filter calculated on a 'super trace' is shown in Figure 3.4. When generating a 'super trace' I first applied a mute to the direct arrivals and very high amplitude early time events to avoid similar odd amplitude effects like those seen using the individual filters.

3.3 Results

The filtering is successful in removing much of the contaminating shear wave energy from the vertical component data. In some cases I found the $v_x(t) * f(t)$ part of the seismogram recorded on the vertical geophone can account for as much as 80% of the total energy recorded. Over an entire geophone gather this proportion I found to be as high as 49%. In the case of the examples at receiver 30 I found the predictable part to be 31%. We suspect that this is in fact rather a pessimistic measure; the calculations are based on the raw traces and there is significant contamination at low travel times, when the amplitudes are high. The result is that these early time high-energy events have a disproportionate amount of energy associated with them compared with their importance after geometrical spreading has been taken into account. That the contamination can be reduced remains a significant step forward in the preparation of the data for processing.

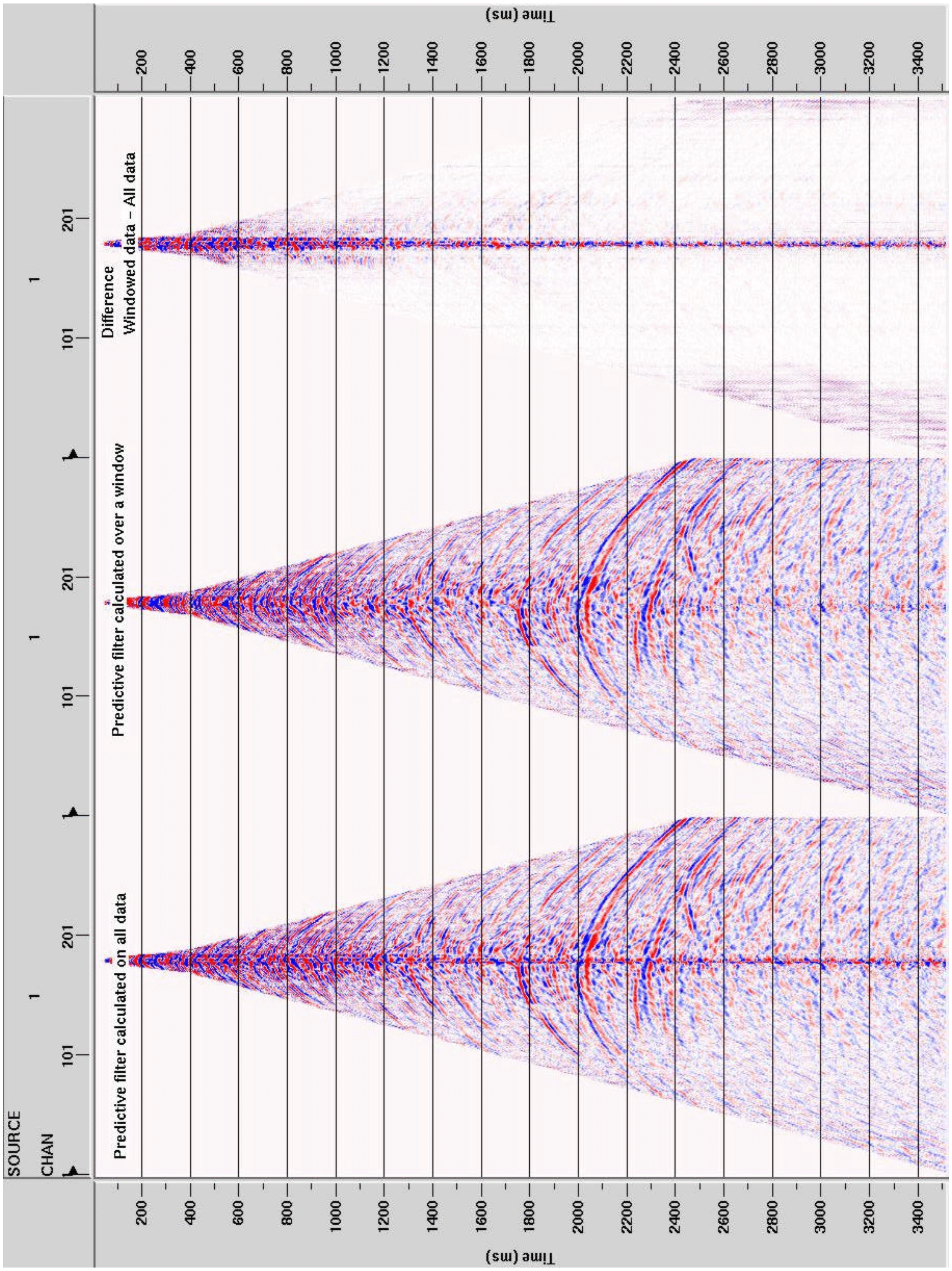

Figure 3.2. Three common-reciever gathers from receiver 1. All filtering is with individual filters. In the left-hand gather the filters have been calculated over the entire live part of the trace. In the middle gather the first sample used to estimating the filter is 20ms after the first live sample on that trace. The far right gather shows the difference between the previous two gathers, we can see that the amplitude anomaly seen at at low offsets in the first gather is indeed due to including the very high amplitude events at early times and low offsets.

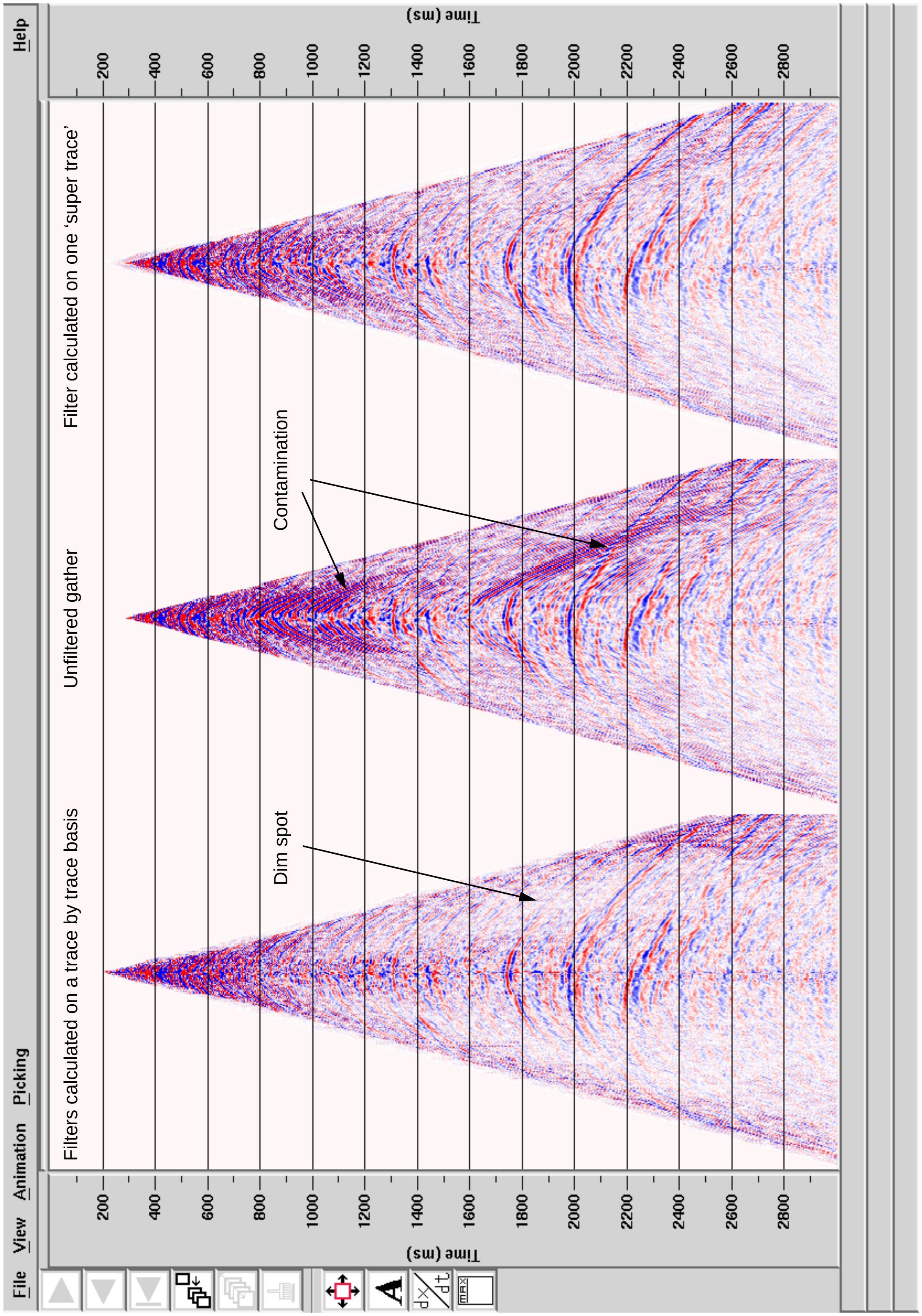

Figure 3.3. Three common-reciever gathers from receiver 30. The gather in the middle is the raw data, with no filtering applied. On the left filters have been estimated and applied on a trace by trace basis. On the right one single filter has been estimated on a 'super-trace'. Notice the low amplitudes of P-wave reflections at mid-offsets on the left-most gather. On the right-hand gather the reflections show a more even amplitude response.

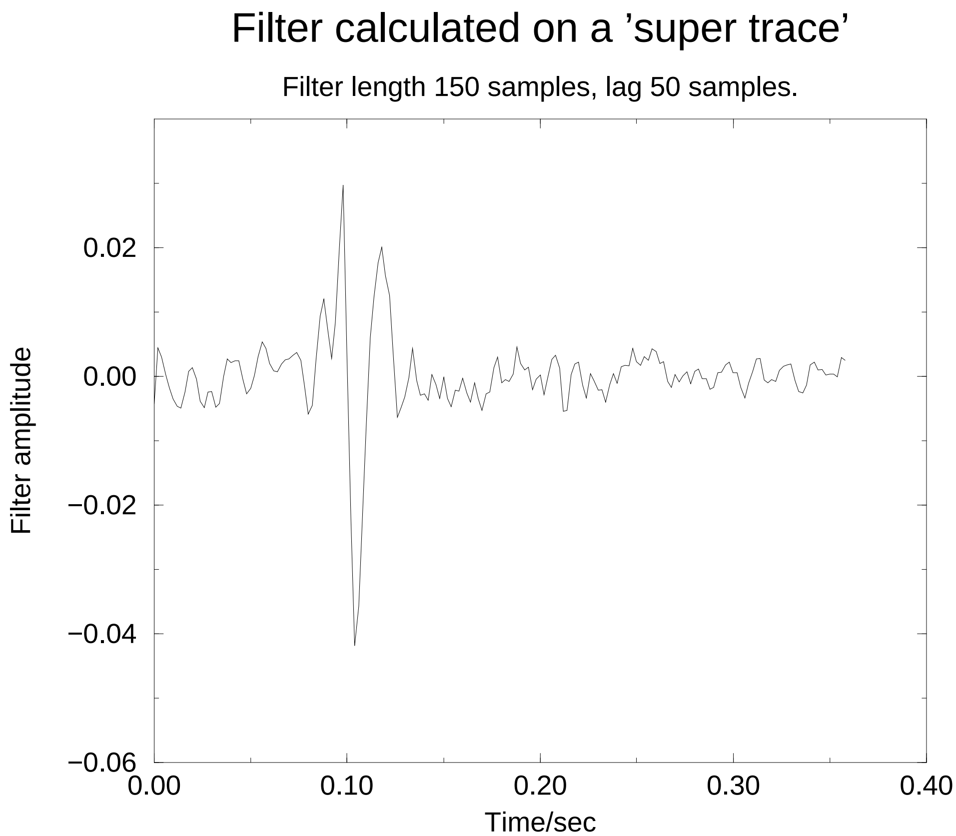

Figure 3.4. A filter calculated from all the traces in a gather placed end-on-end. Filter lag is 0.1 sec, Δt is 2ms. The filter appears to be non-causal. The generating mechanism is causal.

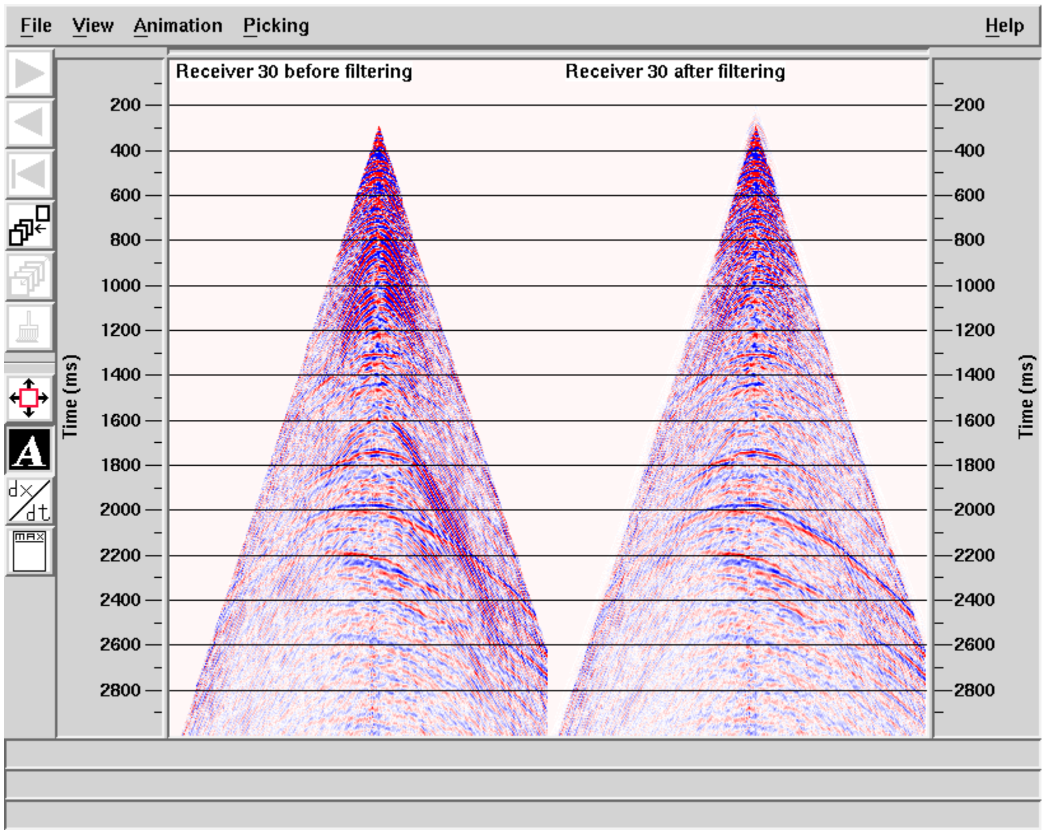

Figure 3.5. Vertical component before and after filtering, receiver 30. One filter calculated on whole gather. This is the same gather as in 3.1, although it looks slightly different because of different gain control parameters.

3.3.1 Improved stack response

For comparison, I applied exactly the same processing flow to both the filtered and un-filtered data sets. The velocity analysis was done on the filtered data, and the same stacking velocity field has been used for both data sets. Part of the final stacked section is shown below. It is possible to see an improvement in reflector coherency on the filtered dataset in Figure 3.7 over that of the unfiltered data in Figure 3.6. The filtering is not perfect, however, and some evidence of contamination does remain.

3.4 Conclusions

Some of the energy recorded on the vertical geophone displays moveout similar to that of the P-SV energy that is recorded on the inline geophone. This is the result of coupling in the geophone gimballing mechanism. Using Wiener's Least Squares method a filter can be calculated to predict and subtract contamination arising from the coupling. The preferred method involves the use of one single filter calculated on all the traces in a receiver gather, and then applied to each trace in the gather to remove the predictable contamination. Not all the contamination is removed, but a significant improvement in data quality is seen. The resulting filtered dataset gives an improved stacking response over the unfiltered data.

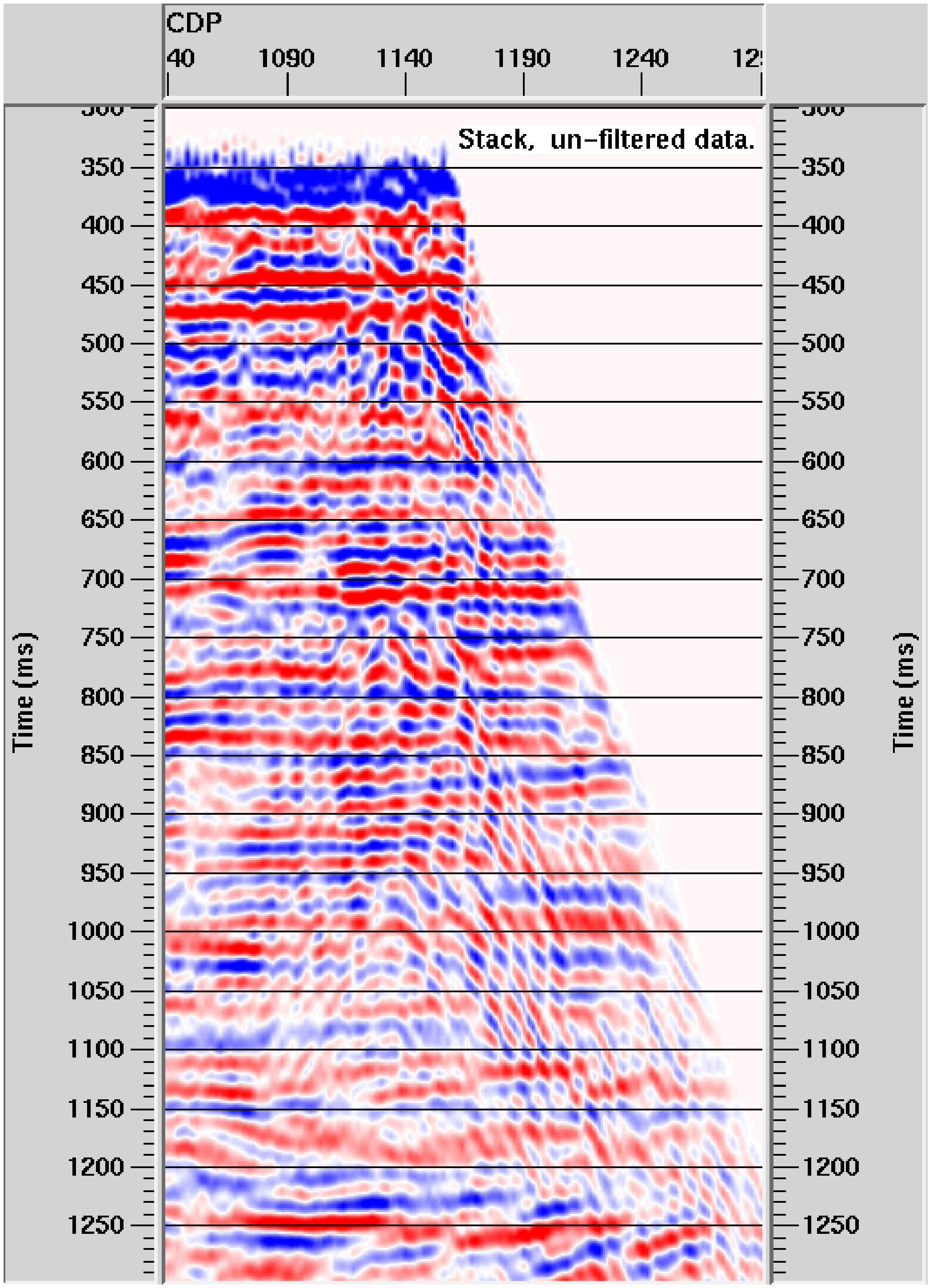

Figure 3.6. Final stack of the unfiltered data. Notice how many reflectors are cut by steeply dipping noise.

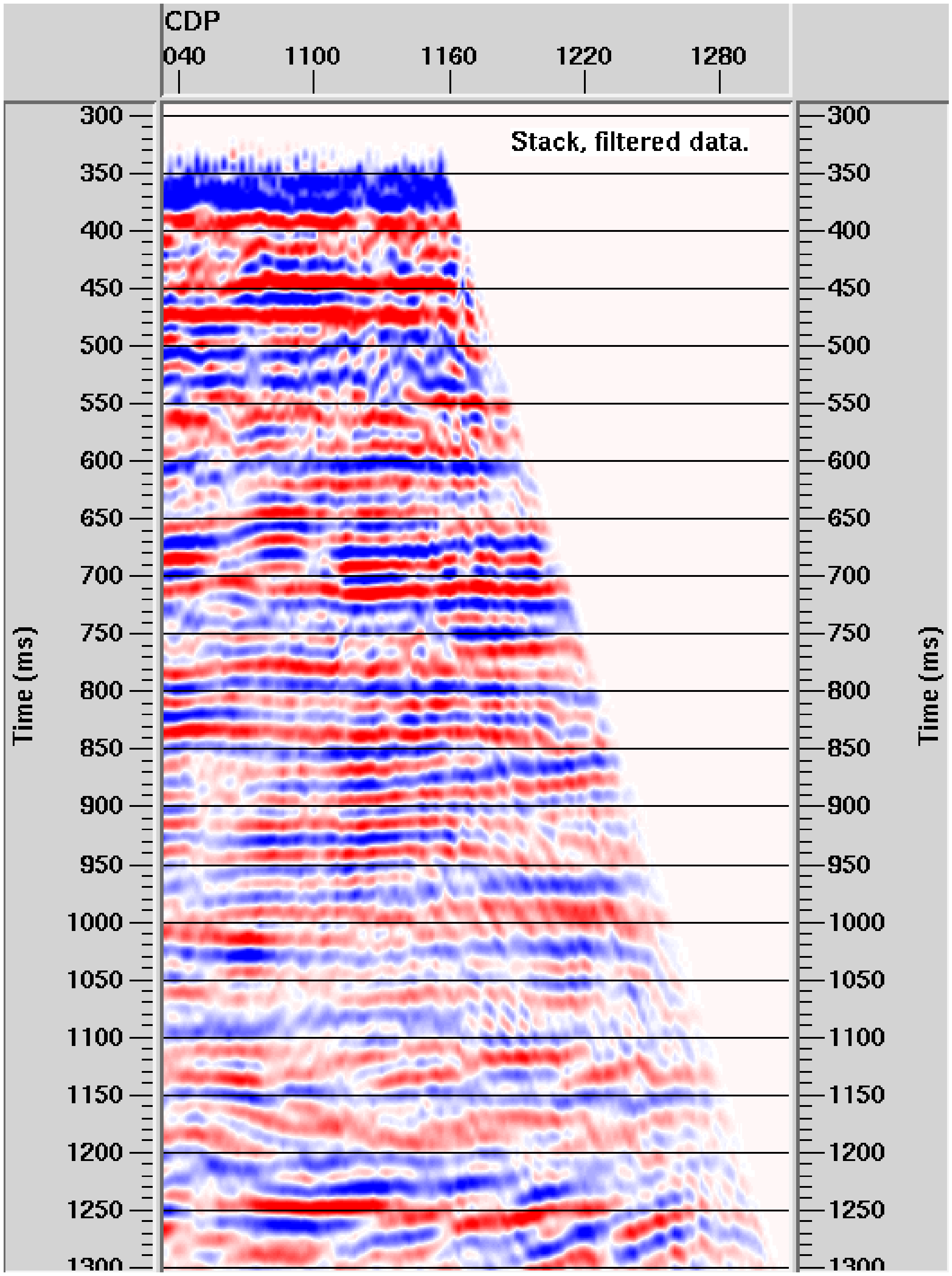

Figure 3.7. Final stack of the filtered data. Notice how the reflectors show higher coherency along their length.

Chapter 4

Travel time inversion

In this chapter I discuss the method of 2-D travel time inversion developed by Guangpin Li (Li et al.*, 2002) that is used to define a local velocity structure. The inversion initally assumes iso-velocity layers and plane dipping interfaces. The errors are unacceptably high (up to 24% in places) and we have to include interface curvature in the inversion. We then assume that interfaces can be described by a second order polynomial in x and the results are improved; average errors in velocity are reduced to less than five per cent.*

We concluded in Chapter 2 that we should like to move away from a processing scheme that is based on analysis in CMP gathers. We should like to accommodate the asymmetric ray path of the P-SV converted waves without having to guess $v_p : v_s$ velocity ratios before we start. By taking account of dip right away in the first step of inversion, we hope the velocity analysis and interface definition will be more accurate than the inversion of stacking velocites found in CMP-based time processing. In this chapter I show the application of a travel time inversion scheme which initially assumes plane-dipping reflectors. This proves to be unsatisfactory in the presence of interface curvature. Once interface curvature is included, the inversion results are improved. We compare the results achieved with CMP velocity analysis and Dix inversion and find that in this case the results are very similar.

4.1 The algorithm for plane layered inversion

The work in this section shows the application of a new inversion scheme devised by Guanpin Li of the University of Edinburgh (Li *et al.*, 2002). While I make extensive use of the inversion and its developments, I must acknowledge my deep indebtedness to Guanpin Li. He must take the credit for the design and code of the algorithms into which I pass pre-stack travel time curves and get out a local veloctiy model. Li has written down much of the detailed theory in a number of unpublished reports (Ziolkowski *et al.*, 2001a,b, 2002a,b, 2003). As these have not been widely circulated I will outline the principles. Appendix B is a draft of the paper we have submitted to Geophysics, giving more details of the P-P inversion. Li assumes that the earth can be modelled as a series of iso-velocity layers separated by plane dipping interfaces as shown in Figure 4.1. We also make the 'high frequency' approximation, that the path energy takes through the subsurface can be modelled by discrete rays. This is the simplest form of ray-based approximation, but is suitable for calculating arrival times.

The method is a ray based inversion method. Li starts by deriving an analytical solution to the problem of calculating reflection or conversion points for P-P or P-SV waves in an iso-velocity model with plane dipping interfaces. The inversion is a layer stripping inversion, determining the parameters layer by layer from the first layer down. It is designed for an OBC configuration and so assumes initially that the source is at the surface and that the receivers are at the bottom of the water layer. The equations assume a knowledge of the ray emergence angle at the receiver of the wave reflected from the i^{th} interface, this is derived from the travel time equation describing the moveout of the event in the common-shot or -receiver gather . The parameters for the $i-1^{th}$ layers and interfaces must also be known. That is, the known parameters of the model are $z_{water}, z_1 ... z_{i-1}$, the thickness of each layer, defined vertically below the shot point, the dips of the interfaces, and the velocity of P-waves, and S-waves in each layer.

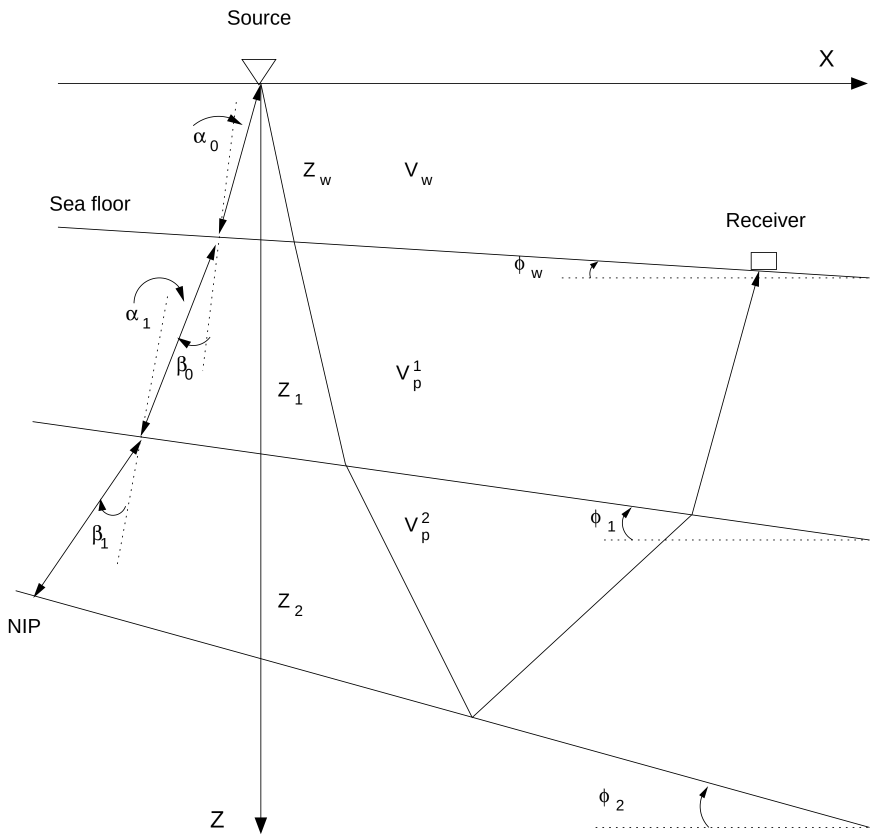

Figure 4.1. The earth model used by the plane layer inversion. The angles ϕ are dip angles of the reflecting interfaces, Z_n are the thicknesses of the layers beneath the source location. V_n are the velocitites within the layers. The angles α_n and β_n are the angles between the interfaces and the ray normaly incident on the n^{th} interface.

Assuming you know the source and receiver locations, a system of linear equations can be generated. This is solved analytically for the cases where the source and receivers are on the same interface. The exact solution for the case of an OBC geometry requires a slight modification of the equations to account for the normal ray not returning to the source, but to the interface below it. Li approximates the travel time curve of a reflected wave from the i^{th} interface as follows, using wave front curvature laws (Hubral & Krey, 1980);

$$t_{pp}(x) = t_{pp}(0) + \frac{\sin\beta_0}{v_p^1 \cos\phi_w} x + \frac{\cos^2\beta_0}{2v_p^1 R_{pp} \cos^2\phi_w} x^2 + \ldots.., \tag{4.1}$$

where $t_{pp}(0)$ is the zero-offset two-way travel time, β_0 is the emergence angle of the normal ray, ϕ_w is the dip angle of the sea floor, v_p^1 is the P-wave velocity for the first layer. R_{pp} is the radius of curvature of the normal ray;

$$R_{pp} = \frac{1}{v_p^1}\left(\frac{\cos^2\beta_0}{\cos^2\alpha_0} v_w^2 \Delta t_w\right) + \frac{2}{v_p^1}\left(\sum_{i=1}^{n} (v_p^1)^2 \Delta t_i \prod_{j=1}^{i-1} \frac{\cos^2\alpha_j}{\cos^2\beta_j}\right), \tag{4.2}$$

where v_p^i is the P-wave velocity in the i^{th} layer, Δt_i the one-way time of the normal ray in the i^{th} layer, α_j the incidence angle of the downgoing normal ray at the j^{th} interface, β_j the refraction angle of the downgoing normal ray at the j^{th} interface, v_w the P-wave velocity of water and Δt_w the one-way time of the normal ray in the water.

The squared time curve is as follows;

$$\begin{aligned} t_{pp}^2(x) = t_{pp}^2(0) &+ \frac{2t_{pp}(0)\sin\beta_0}{v_p^1 \cos\phi_w} x + \left(\frac{t_{pp}(0)\cos^2\beta_0}{v_p^1 R_{pp}\cos^2\phi_w} + \frac{\sin^2\beta_0}{(v_p^1)^2\cos^2\phi_w}\right) x^2 \\ &+ \frac{\sin\beta_0\cos^2\beta_0}{(v_p^1)^2 R_{pp}\cos^3\phi_w} x^3 + \frac{\cos^4\beta_0}{4(v_p^1)^2 R_{pp}^2 \cos^4\phi_w} x^4 + \ldots.., \end{aligned} \tag{4.3}$$

Tests with ray tracing have shown that these equations are good approximations of the travel time and squared travel time curves generated over plane dipping interfaces (Li *et al.*, 2002). Once the parameters of Equation 4.3 have been determined Li uses two further relationships to determine layer velocity. For the first layer equation 4.4 is used to find the velocity:

$$v_p^1 = \left(\frac{2\Delta t_1}{\dfrac{R_{pp} v_p^1}{\cos^2 \beta_0} - \dfrac{v_w^2 \Delta t_w}{\cos^2 \alpha_0}} + \frac{\sin^2 \alpha_0}{v_w^2} \right)^{-1/2}, \tag{4.4}$$

where $\dfrac{R_{pp} v_p^1}{\cos^2 \beta_0}$ can be obtained from the second order term of Equation 4.1, as we assume we know ϕ_w the dip of the sea bed.

For further layers the following equation is used:

$$v_p^n = \left(\frac{2\cos^2 \alpha_{n-1} \Delta t_n \displaystyle\prod_{j=1}^{n-2} \frac{\cos^2 \alpha_j}{\cos^2 \beta_j}}{R_{pp} v_p^1 - \dfrac{\cos^2 \beta_0}{\cos^2 \alpha_0} v_w^2 \Delta t_w - 2 \displaystyle\sum_{i=1}^{n-1} (v_p^i)^2 \Delta t_i \prod_{j=1}^{i-1} \frac{\cos^2 \alpha_j}{\cos^2 \beta_j}} + \frac{\sin^2 \alpha_{n-1}}{(v_p^{n-1})^2} \right)^{-1/2}. \tag{4.5}$$

Once the velocity has been determined the interface geometry can then be found: we know the arrival times and the velocity, and because the geometry of reflectors is simple the reflection and conversion points can be calculated analytically (Gangi & Yang, 1976). When the OBC geometry is taken into account the upgoing ray does not travel back through the water layer. Because of this change in the geometry, the equations are modified slightly. For the case on the left of Figure 4.2, where the source and receiver are at the same interface the normal incidence ray travels back to the source. In the right hand image in Figure 4.2 the upcoming ray is not measured at the same vertical level as the source so the receiver at which the normal ray is recorded is

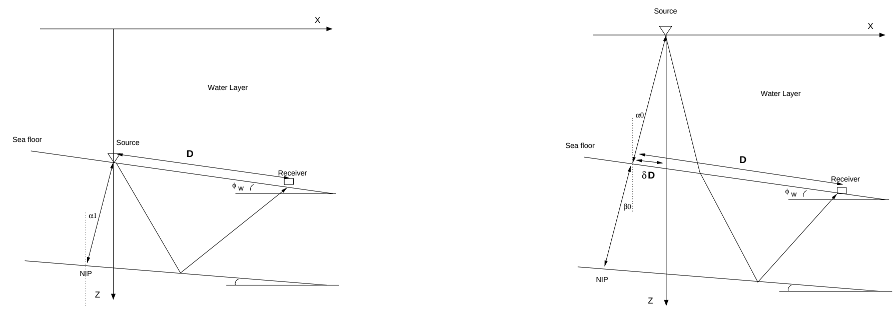

Figure 4.2. The normal incidence ray does not return to the source in the case of an OBC type geometry

displaced from the source, in this case by the distance δD. An iterative part is added to calculate precisely the effect this has on the radius of curvature of the upcoming normal incidence ray.

For the first layer the problem is solved using Equation 4.3 and some relationships derived from the radius of curvature relations Hubral & Krey (1980). Assuming we know all the parameters for the $i-1^{th}$ layer, we can then calculate the parameters for the next layer. A similar set of equations can also be derived for the P-SV case. This obviously requires both P-P and P-SV travel time curves as an input. The P-wave velocities and geometries are derived using the P-P inversion. Li *et al.* (2002) tested the algorithm on synthetic data generated by ray tracing through plane layered models. The results are very accurate, with errors reported in the order of 2% for velocities and layer thickness. Of more interest perhaps is the behaviour of the algorithm when given data from a more general model. To test this I carried out the experiment described in the following section.

4.1.1 A comparison between the inversions of Li and Dix

In order to compare the accuracy of the plane layer inversion with Dix inversion (Dix, 1955) I created a dataset that we can analyse with both methods. As Dix inversion code available in ProMAX is only applicable to P-P reflections; I do not generate or analyse any mode converted S-waves. The synthetic data are acquired over the 'Wave' model, using the ray-tracing program SEIS88 (Cerveny & Psencik, 1988). I processed the data using both Dix inversion of stacking velocities calculated on CMP gathers and the plane layer inversion on shot gathers in order to compare the results. The depth velocity models derived show that the plane layered inversion is less accurate than CMP velocity analysis and Dix inversion in the presence of curved interfaces. I conclude that it is necessary to include the effects of layer curvature to improve the accuracy of the travel time inversion.

4.1.2 The 'Wave' model synthetic data

The model has a flat seabed with water depth of 200m. Below this are two interfaces: the first is curved and the second is flat. The receiver array is 2km long with 100 receivers spaced every 20 m, located on the sea bed. The shot is located at the furthest left of the receiver array, at zero depth. The relative location of the source and receivers remains the same. Both source and receivers move up in steps of 200m between $x = 0.0$ km and $x = 6.0$ km. The model is shown in Figure 4.3. The velocity is uniform within each layer.

4.1.3 Basic CMP processing of the Wave data

In order to compare the accuracy of our method with Dix inversion, the wave model synthetic data are processed using standard CMP velocity analysis and Dix velocity-depth inversion. The average interval velocities derived from this inversion are in error by 5.0 and 3.6 percent in layers 1 and 2 respectively. There is some difference between the location of the inverted first interface and the true location of the interface, as one would expect using this inversion method over a model with curved interfaces.

4.1.4 The processing flow

The processing flow is a simple standard processing flow, resulting in an output time CMP stack and an RMS velocity field in time. The depth velocity model is found using the Dix inversion of the RMS stacking velocity field. All processing was done using

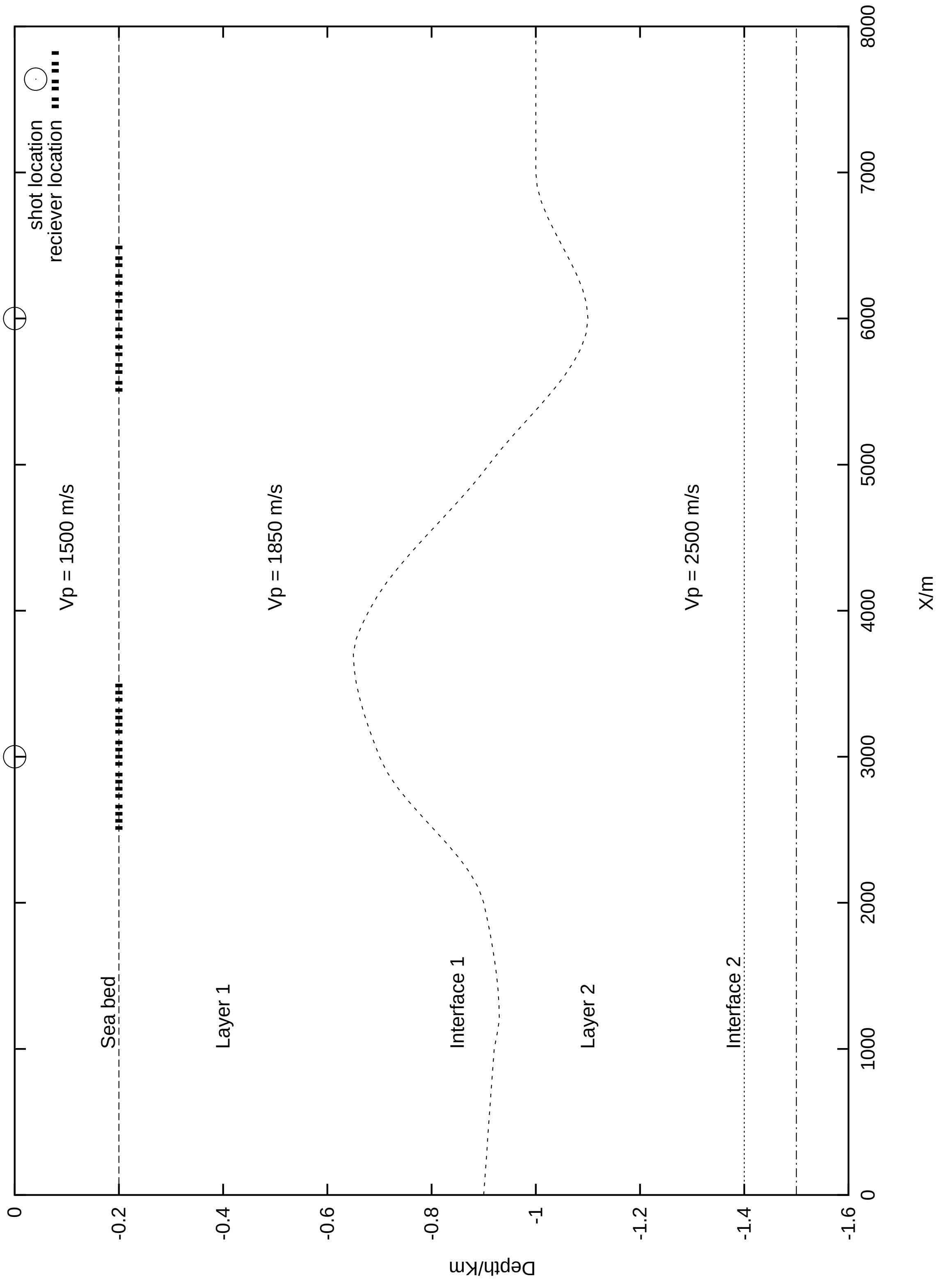

Figure 4.3. The 'Wave' model, interfaces and P-wave velocity distribution. Two example shot locations and receiver spreads are also shown.

Layer	Error of min velocity in layer	Error of max velocity in layer
Layer 1	2.86%	18.8%
Layer 2	-5.7%	12.3%

Table 4.1. Errors of maximum and minumum velocities found using Dix inversion.

Layer	$(\sum \delta v)/n$
Layer 1	6.5%
Layer 2	3.9%

Table 4.2. Errors in average layer velocity from Dix inversion.

the ProMAX seismic data processing software. The processing flow is shown in Figure 4.4. The stacked section is shown in Figure 4.5.

The velocity model resulting from the Dix inversion is shown in Figure 4.6. the velocities in each layer are seen to vary with x location. The input model we know has a fixed velocity in this layer so the average velocity is calculated within the polygon defined by the sea bed top of the velocity model and interface 1, or interface 1 and interface 2 of the velocity model. This smoothed velocity field is shown in Figure 4.7. Prior to smoothing, the velocities in layer 1 vary between 1889 m/s and 2119 m/s (+2.86% and +18.8% of true velocity respectively). In layer 2, velocities vary between 2357 m/s and 2805 m/s (-5.7% and +12.3% of true velocity respectively). The average error in velocity is shown in Table 4.2 and is 6.5% in the first layer and 3.9% in the second layer. Table 4.1 shows the errors of the maximum and minimum velocities returned by the Dix inversion of the RMS stacking velocity field, for each layer. v is the interval velocity resulting from the Dix inversion of the RMS stacking velocity, and $n = 60$ and is the number of CMPs where velocity analysis was performed.

4.1.5 Plane layer inversion of the Wave data

Using pre-stack travel time curves as an input, the inversion of Li returns subsurface layer parameters dip, depth and velocity with a very high degree of accuracy when the

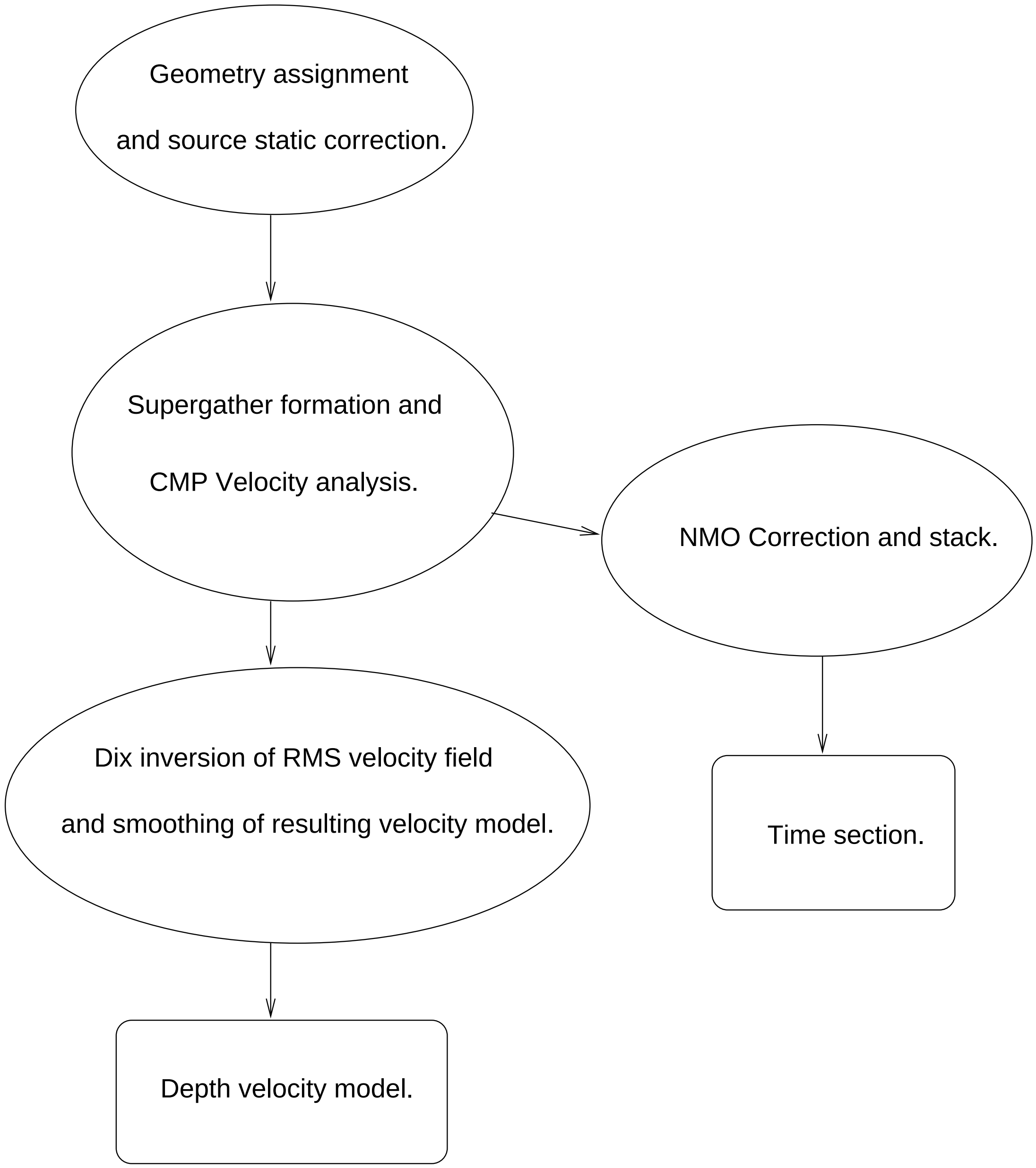

Figure 4.4. The processing flow used on the wave model synthetic data.

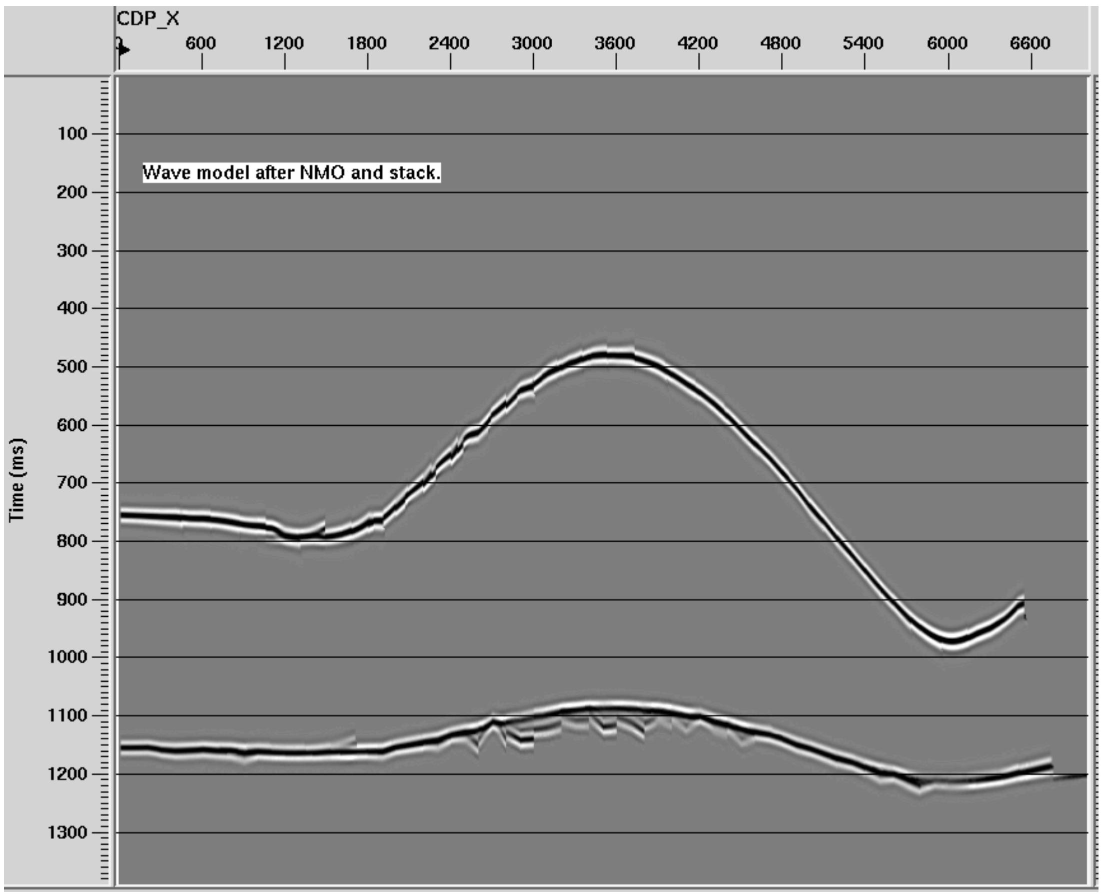

Figure 4.5. Stack after static and NMO have been applied. Vertical component of motion.

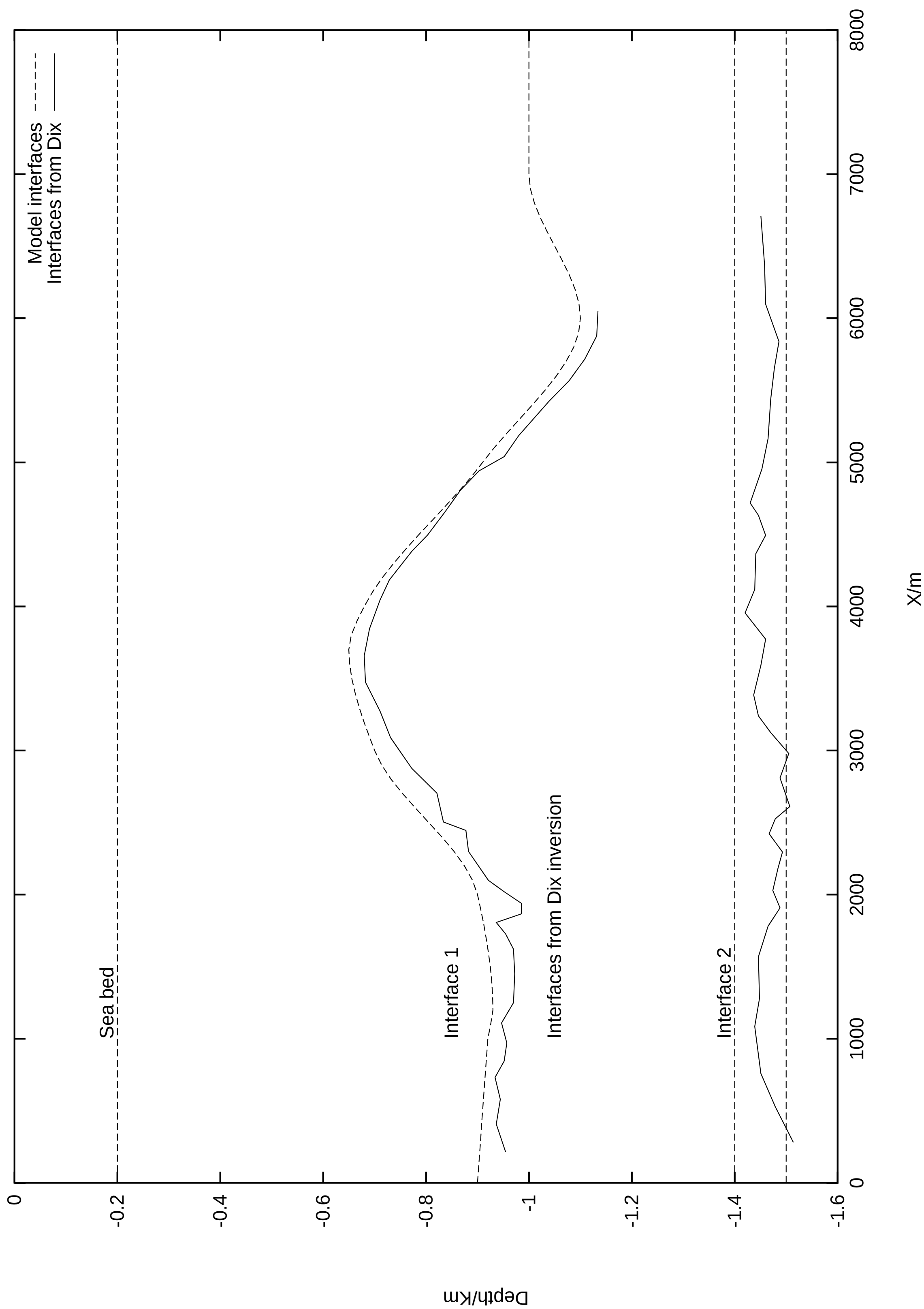

Figure 4.6. Interfaces found using Dix inversion.

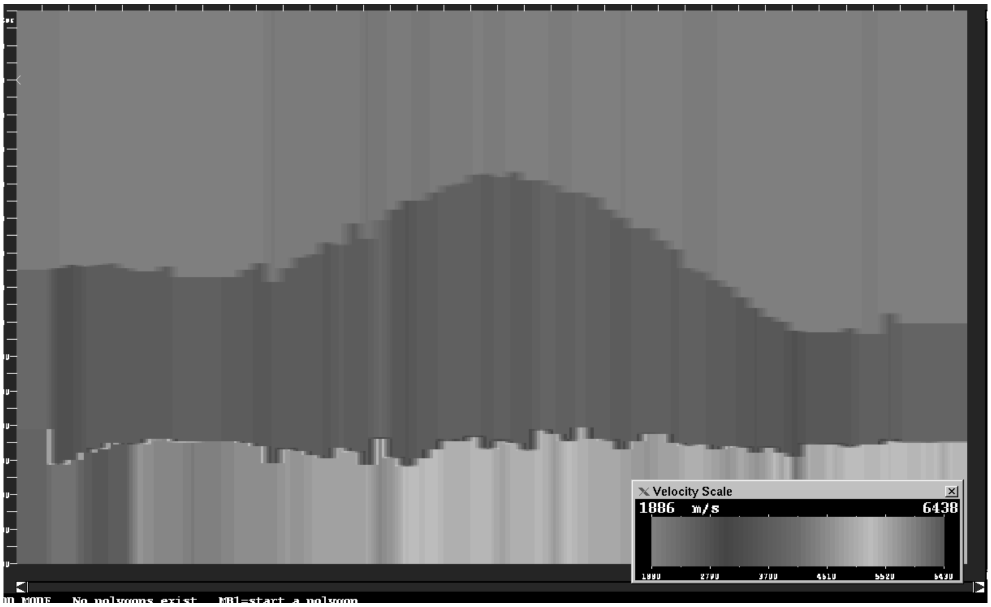

Figure 4.7. Velocity field from Dix inversion of RMS stacking velocities.

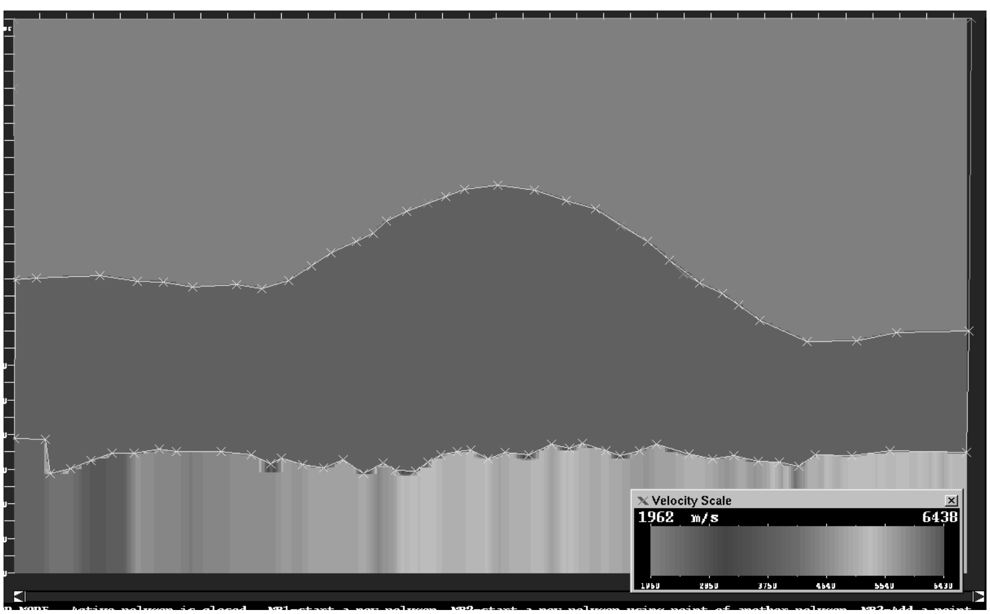

Figure 4.8. Velocity field in Figure 4.7, after averaging.

interfaces in the subsurface are plane dipping layers Li *et al.* (2002). I now test the accuracy of this method in the more general case where travel time curves are derived from synthetic data generated over a model containing curved subsurface interfaces. This is to test the assumption that an interface with a non-linear geometry can be treated as being made up of a number of plane segments. The inversion is used here to invert travel time curves derived from ray-traced synthetic seismograms, computed for the curved and plane interfaces in the 'Wave' model. The inversion results are displayed in Figure 4.9 and Table 4.3. They are of varying accuracy. While the average velocity determined for the first layer had errors less than 2%, some locations display high errors, the highest being 24%. The geometry of the structure returned by the inversion is also incorrect. The determination of the travel time curves uses a three-term polynomial, which is fitted to the seismic data using semblance (see Chapter 5 for details). In most situations the travel time curves determined using this method match those in the data well, so a large proportion of the errors must arise from the assumptions made in the inversion. The errors occur because the inversion cannot distinguish between interface curvature and a change in velocity; it must attribute the effects of curvature to velocity. There is no option in the plane layer inversion to add curvature to the interface, and hence the layer parameters, depth, dip and velocity returned by the inversion of a travel time curve over a curved interface are incorrect. The plane dipping interface assumption is not adequate in the presence of curved interfaces.

4.1.6 Results of the inversion

The inversion is valid only over a certain spatial range, depending on the layer parameters and the length of receiver array, or number of traces used for the calculation of the travel time curve. The inversion therefore returns a 'segment' of reflector. It is these segments that are used to build up a picture of the subsurface structure. The results of the inversion discussed here are shown in Figure 4.9. Table 4.3(a) shows the error in the velocity determined at each shot point, where δv is the difference between the true velocity value and the value returned by the inversion at that shot point, and n is the number of shot gathers inverted.

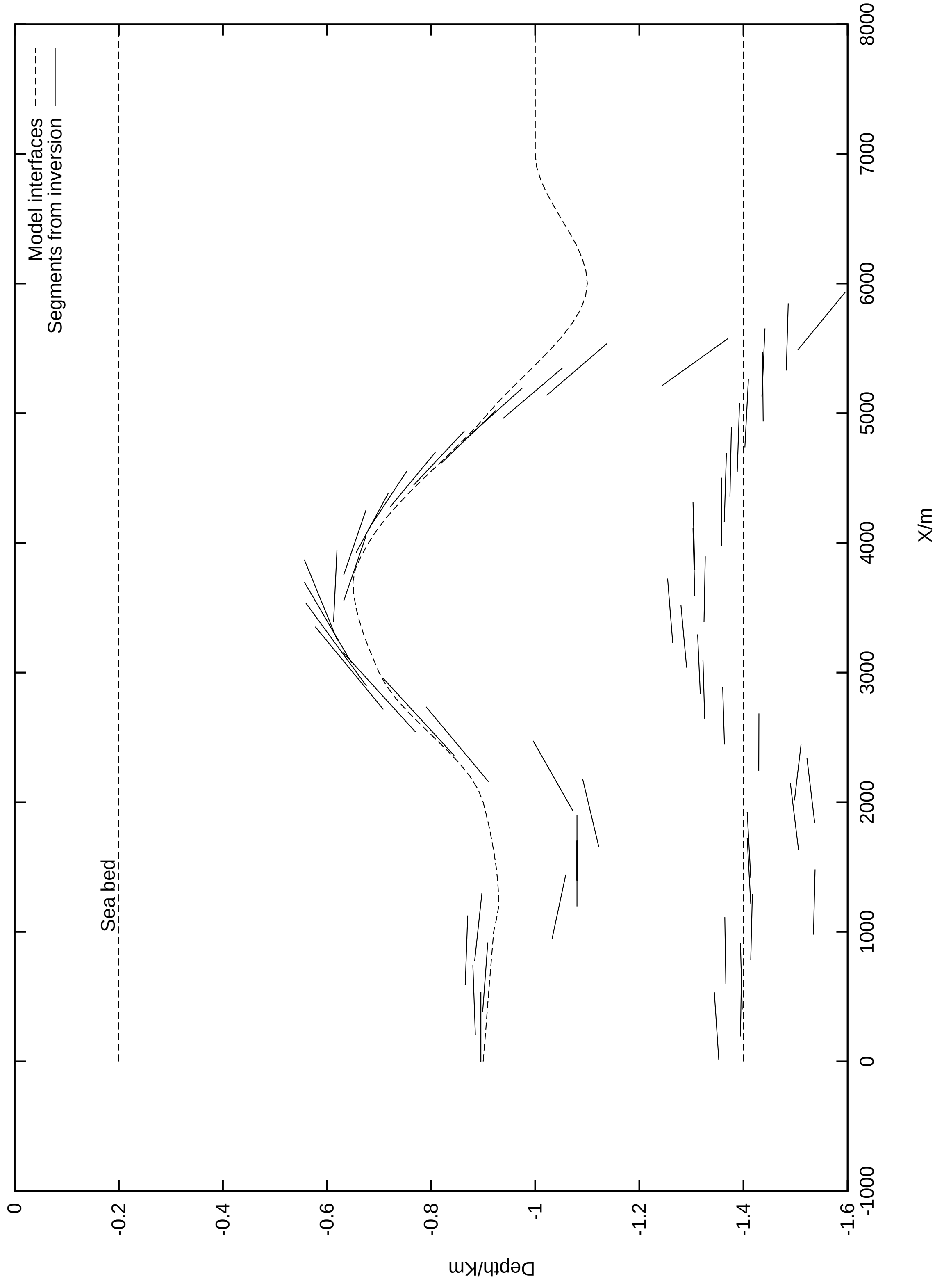

Figure 4.9. Plane interfaces returned from the inversion, overlaid on the model structure

Shot	% error in velocity, layer 1	% error in velocity, layer 2
1	-1.1	-10.0
2	-3.24	-1.0
3	-0.54	-2.4
4	-6.48	0.4
5	-5.40	7.6
6	12.4	3.6
8	-6.4	-0.4
9	23.7	-19.2
10	21.1	-8.4
11	3.7	10.8
12	-0.0	-2.4
13	-5.4	-3.6
14	-8.6	-4.8
15	-8.6	-7.6
16	-9.7	-10.8
17	-9.7	-14.0
18	-9.7	-15.2
19	-8.6	-7.2
20	-5.4	-11.2
21	-4.3	-5.2
22	-4.3	-4.4
23	-2.7	-4.0
24	-1.1	-4.0
25	0.5	-3.2
26	0.5	3.2
27	3.7	-1.6
28	8.1	0.0

(a)

Layer	$(\sum \delta v)/n$	$(\sum \sqrt{(\delta v^2)})/n$
Layer 1	1.02%	6.54%
Layer 2	4.01%	6.11%

(b)

Table 4.3. Errors in velocity from the plane dipping layer inversion.

The first column in Table 4.3(b) is the mean error value, as a percentage of the true velocity value. It is very low, but this is not truly representative of the size of the errors in the inversion. Taking the modulus of the errors reduces the tendency for errors of a different sign to cancel each other out; this figure is shown in the second column.

Figure 4.9 shows the segments returned from the inversion and how they relate to the model input to the ray tracing program. Notice the systematic errors in segment depth in relation to the curvature of the model interface.

4.1.7 Discussion of errors

In some places the reflector segment returned is a very close match to the subsurface interface at that point. However, in other areas there are large discrepancies between the model and the inverted segment. The errors in velocity at each shot point are shown in Table 4.3 above. Errors in depth can be seen in Figure 4.9, and range from almost nothing in places, to almost 170m in others. Dip is not tabulated, as it is not really meaningful in this case: we are comparing plane layer segments with a curved interface. Errors in depth are linked to the error in velocity and are very similar. Notice, in Figure 4.9, that it is at places where dip is changing quickly that the largest difference between model and inverted parameters is seen. In areas where the interface is nearly plane the segments match the model well. The average errors for velocity shown in Table 4.3(b) are comparable to those found using CMP velocity analysis and Dix inversion.

4.1.8 The effects of layer curvature

The travel time curve depends upon reflector geometry, as well as layer parameters. If an interface is curving upwards, the travel times at long offsets will be reduced when compared with a plane layer with the same layer parameters but no curvature. When the subsurface interface is concave upwards, the travel time curve appears 'flatter' than it would if the interface were plane. This has a similar effect on the travel time curves

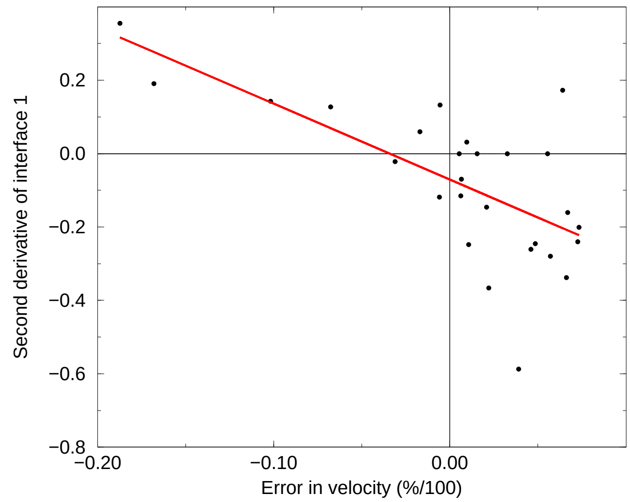

Figure 4.10. Errors in inverted velocity for the first layer versus the interface curvature immediately below the shot point. The red line is a linear regression calculated from the data points.

as would an increase in layer velocity. The result is that the velocity determined by the inversion is high, and as $t(0)$, the zero offset travel time, is fixed by the input data, the interface segment returned by the inversion is too deep. The opposite is true when the travel time curve from a convex reflector is considered: the layer velocity returned by the inversion is low and hence the reflector segment is too shallow.

Changes in interface dip or curvature within the offset range being considered add further complications. These can result in the travel time curve being complicated and having a number of gradient changes along its length. It is possible to check for the presence of 'high order terms' in the travel time curve by looking at the moveout-corrected gather to see if the selected event is flat after correction. If the travel time curve is complicated then it cannot be accurately described using a cubic polynomial. Given these two sources of error, it is possible to see the dominating effect of interface curvature on the derived velocity in the graph in Figure 4.10. Here the second derivative of the first interface (curvature) is plotted against the error in velocity returned by the plane layer inversion at the same horizontal location. The data do not all plot on a straight line, but the trend is clear.

4.2 Curved layer inversion

Following the work with the plane layered inversion, Guangpin set about updating the inversion strategy so that it would be able to cope with curved interfaces. I used the first working version of the code on the same synthetic dataset. The results for this simple model prove comparable with Dix inversion.

4.2.1 The algorithm for curve layer inversion

First of all the model is changed slightly; we allow a second order term to appear in our description of the interface, so $z(x)$ which defines the interface throughout space is defined locally as;

$$z(x) = a_0 + a_1 x + a_2 x^2, \tag{4.6}$$

where a_0 is the depth of the interface below the shot, a_1 is the dip term, and a_2 is the curvature term.

Li uses a classical approach to the inversion problem: Using ray tracing he attempts to reduce the difference between modelled and observed travel time curves by updating the model geometry and layer parameters. A linearised equation is obtained by neglecting the high order terms,

$$G\Delta m = \Delta t. \tag{4.7}$$

G is the partial derivative matrix, $\Delta m = [da_0, da_1, da_2, dv_p]^T$ is the model adjustment vector, and $\Delta t = [dt_1, dt_2, dt_3, ..., dt_n]^T$ is the travel time residual vector. For the P-SV inversion the the model adjustment vector also contains a dv_s term.

Li finds the damped least squares solution to be;

$$\Delta m = (G^T G + \lambda^2 I)^{-1} G^T \Delta t, \tag{4.8}$$

were λ is the damping factor and is updated automatically from the changing tendency of the objective function and the value of Δm. The value of the damping factor is changed for different reflectors. Selecting an appropriate value for λ is important to the success of the inversion. It is only through experience that we can find a suitable value for a given dataset. The damping factor affects the update step size Δm. Δm is the model parameter adjustment vector. If the update step is too large we can find our solution behaving erratically, and if the update step is too small and we are not close enough to the solution we might well find ourselves converging on a local minima. The stopping criteria are either when the modelled travel time curve matches the real data with a given degree of accuracy, or after a pre-determined number of iterations. We have proposed a rather 'brute force' method that we hope will avoid the problem of finding local minima, it is outlined towards the end of Chapter 6. A schematic of the problem of finding local minima is shown in Figure 4.11.

In common with nearly all inversion schemes the success or otherwise of this method depends on the starting model being a reasonable approximation of the true parameters that we are hoping the inversion will converge upon. Li has the option to use either Dix inversion, a modified Dix inversion (both re-cast in the common-shot and -receiver domains) that allows the interface to dip and the plane layer inversion described in Section 4.1, to generate the starting model. In the following case we use the plane dipping layer inversion. The plane dipping layer inversion can cope with very high dip, unlike Dix inversion, but it is more sensitive to curvature than either of the Dix

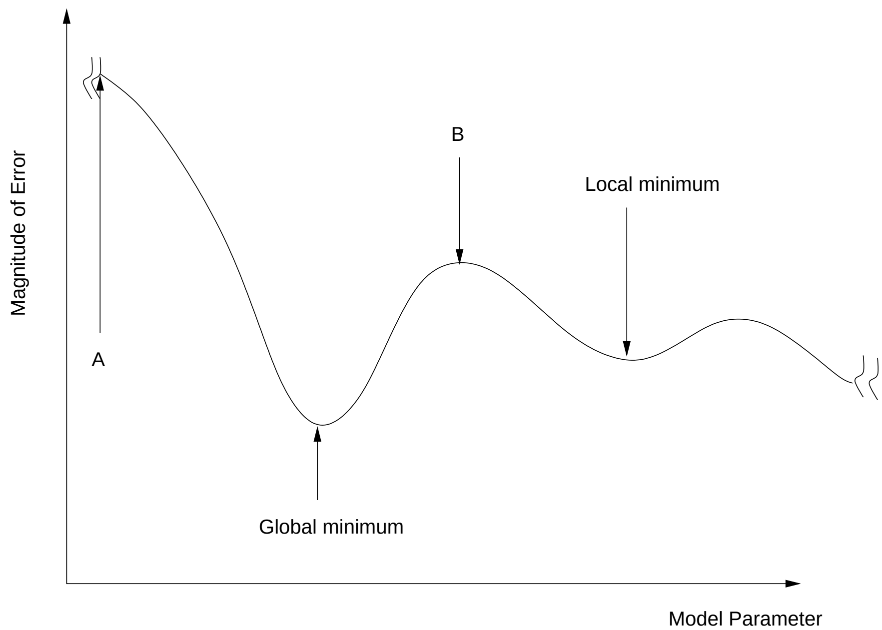

Figure 4.11. A schematic diagram of an error function. Consider a 'solution' to be a point on the curve. The correct solution lies at the point with minimum errors, that is the point marked as the global minimum. The aim is to locate this point and if we can do that the inversion problem is solved. An inversion of the sort we are using tries to move the location of the 'solution' down the slope of the error function. If the initial solution lies between A and B and the step size is correct, the inversion will indeed tend to converge on the correct solution. Problems arise if the step size in the parameter update is too large. The solution can then 'jump' out of the minima between points A and B, it may then settle on a local minimum, or carry on searching until some other stopping criteria are met. The other problem arises if the starting solution is not between points A and B; even if the step size is correct the iteration will never get away from a local minima as the solution is always trying to move down slope.

formulations *when they are applied in midpoint gathers.* The price we have to pay for moving away from mid-point and conversion-point gathers is the increased dispersal of the reflection points along the reflecting surface. The result of this is that the geometry of the reflecting surface introduces a number of unknown parameters to the inversion and this increases complication in the initial velocity determination.

4.2.2 Curved layer inversion of the Wave data

A number of the same travel time curves that had previously been inverted using the plane layer inversion code are now used as input for the curved layer inversion scheme. Table 4.4 shows errors in the velocity determined at each shot point, where δv is the difference between the true velocity value and the value returned by the inversion at that shot point, and n is the number of shot gathers inverted. The early version of the inversion code used for the tests shown in this chapter was not always very stable when it was allowed freedom in both velocity and curvature. To increase the stability I performed the inversion in two parts, fixing the velocity for the second part. I ran the inversion first to find the average velocity values and then a second time, with the velocity value fixed, to find the location of the interface segment in space. I used velocity values of $1830m/s$ for the first layer and $2400m/s$ for the second layer. The resulting interface segments are shown in Figure 4.12. As one might expect this removes the effect of systematic error caused by layer curvature and the interface segments are well positioned when compared with the model interface locations.

4.3 Conclusions

The tests on the 'Wave' synthetic data set show that the velocities returned by inversion are broadly comparable to CMP velocity analysis and Dix inversion when applied to this simple two-layer model. The interface segments from the curved layer inversion with a fixed interval velocity match the interfaces in the model very well. This is

Shot	%error in velocity, layer 1	% error in velocity, layer 2
1	-1.6	-4.8
2	-1.08	-6.4
3	-2.70	0.8
4	2.70	-5.6
5	2.16	-0.4
6	15.6	-2.4
8	10.27	-1.2
9	15.1	-2.4
10	5.40	-3.2
11	12.9	-6.8
12	2.70	-8.0
13	0.54	-7.2
14	-0.54	-7.6
15	-1.08	-7.2
16	-2.16	-11.2
17	-3.24	-13.2
18	-2.70	-12.0
19	-1.08	-4.8
20	-0.54	-8.0
21	-0.54	-5.2
22	-1.62	-2.8
23	-1.62	-4.0
24	-1.08	-0.4
25	0.0	0.8
26	1.62	-0.8
27	4.8	7.2
28	9.18	-2.4
29	29.18	-0.4
30	17.29	-1.2
31	1.08	-3.2

(a)

Layer	$(\sum \delta v)/n$	$(\sum \sqrt{(\delta v^2)})/n$
Layer 1	-3.26%	5.00%
Layer 2	4.14%	4.70%

(b)

Table 4.4. Errors in velocity from the curved layer inversion.

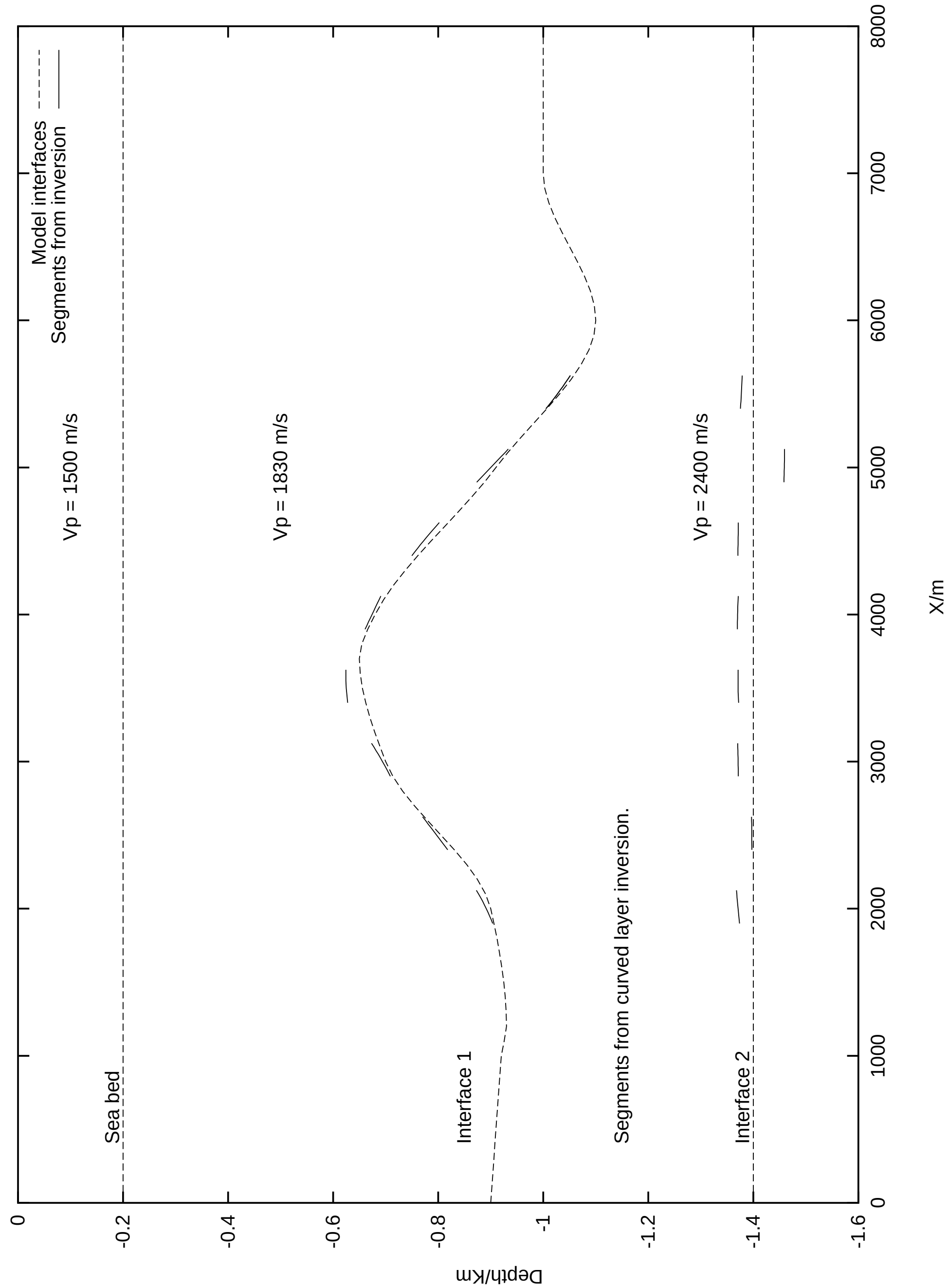

Figure 4.12. Segments returned by the curved layer inversion when performed with a fixed velocity equal to that of the mean velocity from inversion. Segments are overlaid on the actual interface geometry.

not a complete test of the inversion, as the interfaces have been derived using a predetermined velocity: the average velocity found using the inversion. A more complete test of the inversion is presented in Chapter 6, where the inversion is tested on a four layer model and both P-P and P-SV events are inverted for velocity and interface geometry. From the evidence presented so far in this chapter the inversion does not appear to be any more accurate than even the simplest implementation of the Dix inversion; so, why should we continue with this line of enquiry?

The errors atributable to ray bending seem to be small in the 'Wave' model, and so Dix inversion works well. Both Dix inversion and the curved layer inversion of Li show average errors around the 5% mark, which is acceptable for imaging purposes. There are a few points that are not well illustrated by this example but which encourage further development of a processing scheme based on the inversion:

- Dix is accurate for a small number of layers where ray bending is not a big problem.
- The inversion of Li can cope with higher degrees of dip and still return velocities and interfaces accurately.
- The inversion of Li can be extended to invert P-SV data with the problem cast in the same maner.

In Figures 4.13 and 4.14 I show a situation where the velocities found using Dix inversion are in error by over 20%. The model interfaces are described by parabolas. Using the same velocity model, but working with a shot gather rather than a CMP gather, the inversion of Li is able to derive the velocities accurately; taking the first three significant figures the errors are zero. Figures 4.13 and 4.14 were provided for me by Guangpin Li.

The velocities found using Dix inversion are shown in Table 4.5. I have not tabulated the error in velocities found by the curved layer inversion as in this case they are 0.0% for all the layers. Notice that for the first two layers the velocities found using Dix inversion are close to the correct ones in the model. It is only for the deeper, and more

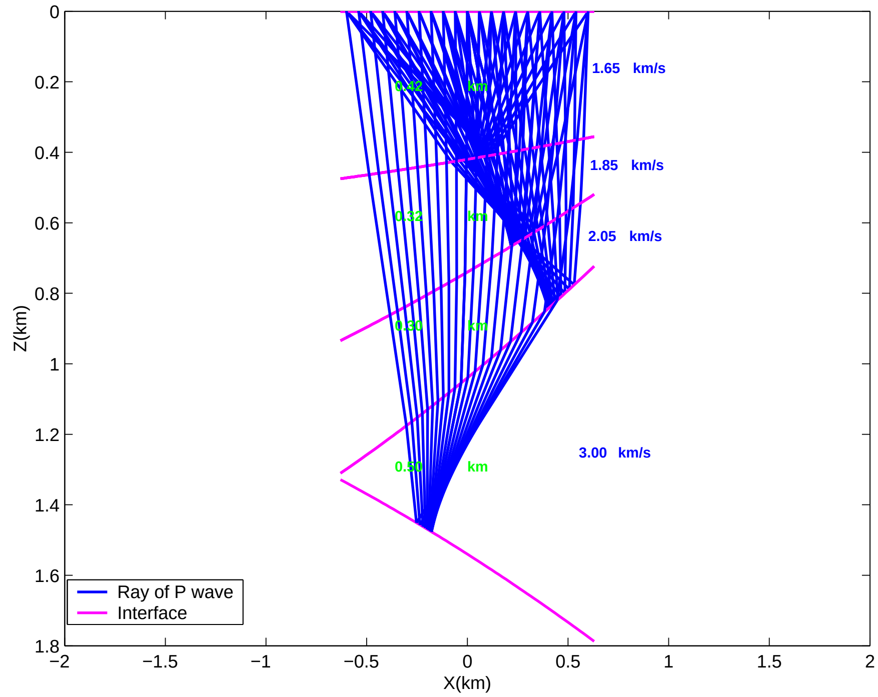

(a)

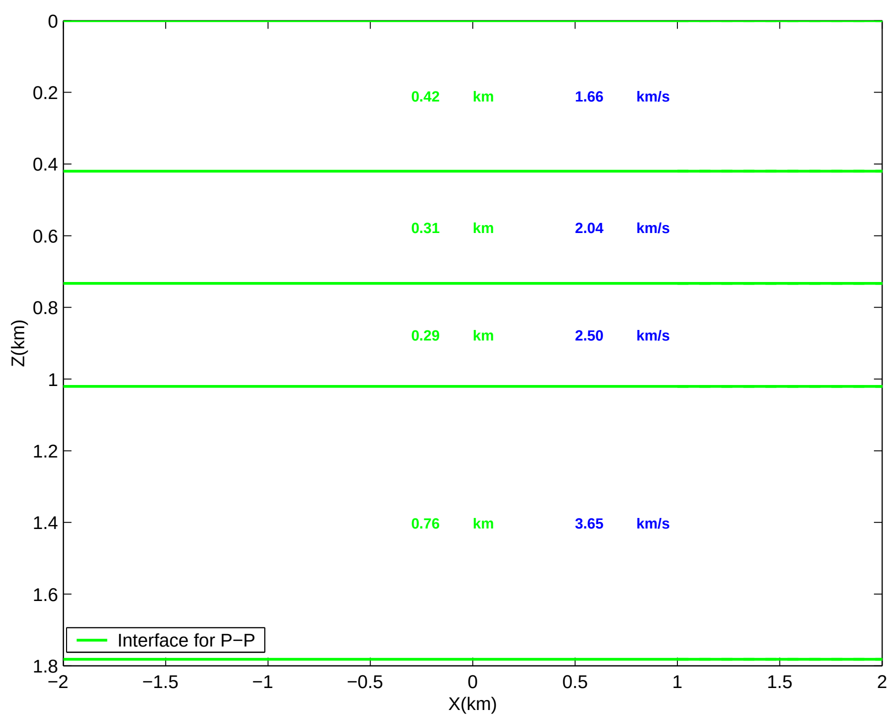

(b)

Figure 4.13. (a) Shows rays for a common mid-point gather, (b) shows the model derived from Dix inversion of the travel times calculated along the rays in (a).

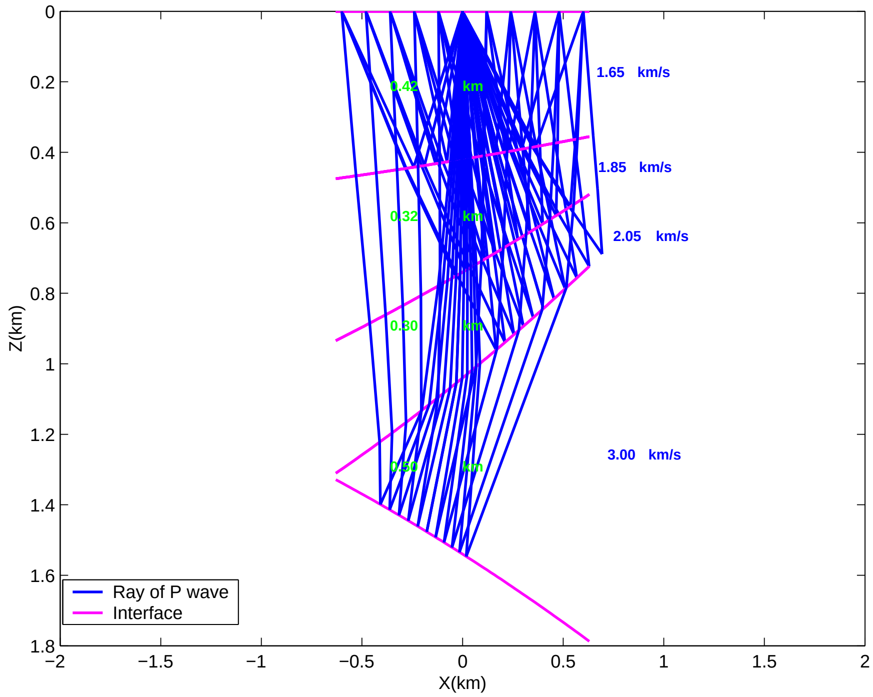

(a)

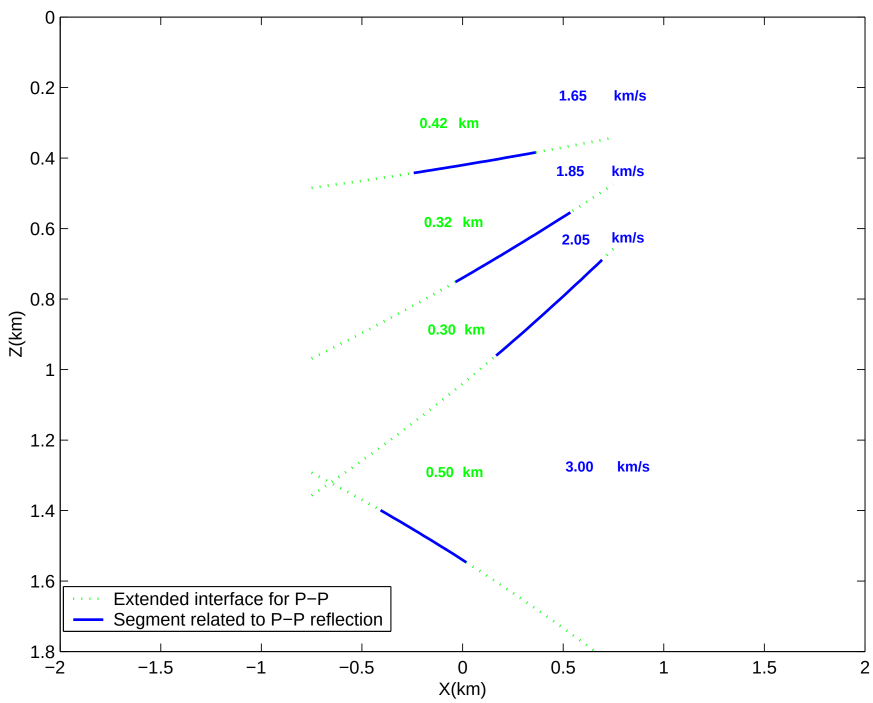

(b)

Figure 4.14. (a) Shows rays for a common shot gather. The same velocity model is used here as in Figure 4.13(a). The model found using the inversion is shown in (b) and is indistinguishable from the starting model.

Layer	Error in velocity from Dix inversion
Layer 1	0.6%
Layer 2	10.2%
Layer 3	21.9%
Layer 4	21.6%

Table 4.5. The error in interval velocity found using Dix inversion.

steeply dipping layers, that the assumptions in the Dix inversion really start to break down and affect the results bady. The inversion of Li returns the correct subsurface model in this case. That is partly a function of the interface being described by a parabola in this example and so the inversion is able to find an exact solution to the inversion problem. Even taking that into account, the example in Figure 4.14 shows that the inversion of Li has the potential to derive velocities with much greater accuracy than Dix inversion.

Chapter 5

Parameterisation of travel time curves

We saw in the previous chapter how it is possible to determine local velocity models using travel time inversion. The input data for the inversion are travel time curves and in this chapter I discuss methods of parameterising travel time curves seen in seismic data. I also discuss which events to pick, and show an example with a plane horizontal layered model where travel time inversion is used to identify the correct P-SV event to match a P-P reflection event.

5.1 Summary

The seismic data recorded using an OBC are a record of either particle motion or pressure against time; they are in the form of amplitude values at a discrete times. The data form can be visualised as the matrix as in Figure 5.1 where m receivers recorded for n time samples. The term 'travel time curve' is used to describe the changing arrival time with offset of a seismic event. In this chapter I am only interested in primary reflection travel time curves, not diffractions, direct arrivals or multiples. The inversion of Li *et al.* (2002) described in Chapter 4 requires reflection data in the form of parameterised travel time curves, as in Figure 5.2, rather than amplitude values. This chapter looks at the methods that are used to parameterise travel time curves seen in seismic data.

Extensive work has been done on finding best the fit hyperbolae to reflection events in CMP gathers, it would be usefull if some of this work can be applied to our problem. In the CMP domain travel times are often assumed to be hyperbolic and depend on two parameters, $t(0)$ and v_{stack}. These are usually found with the help of semblance. In shot gathers the travel time curves are more complicated. I find we need at least four parameters to describe travel time curves adequately for inversion. I find that on real data where there are a large number of similar events, semblance needs guidance to pick a specific reflection. This leads me to investigate a hybrid 'guided semblance' method. Computing semblance with four variable parameters is time consuming, and not always suitable for identifying individual events from within a stack of reflections. The problem of visualisation in many dimensions is another factor which leads me away from developing semblance-based methods. By examining moveout-corrected gathers I conclude that a well-picked guide function renders the semblance step redundant. I settle eventually on manual picking as a robust, if time-consuming, way of picking travel time curves. For use on real data I use a picking scheme that involves simultaneous analysis of picks from a small number of neighbouring gathers. This helps to reduce the fluctuation in travel time curve parameters between neighbouring locations caused by random noise and discretisation effects. Manual picking is only suitable because I am working on small 2D datasets. This step is currently a bottleneck in the processing flow and needs to be automated for larger datasets.

I also discuss and give examples of a method based on inversion that I use to help quantify the event correlation step. The correlation happens in the depth domain. In a plane layered environment I can pick the converted-wave event corresponding to a P-wave event with confidence.

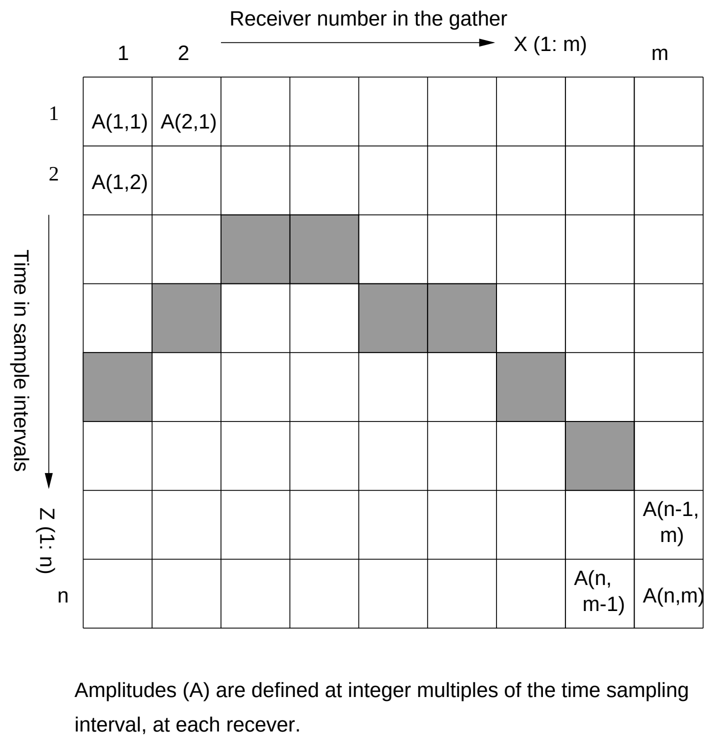

Figure 5.1. A gather of seismic traces may be considered as a matrix of amplitude values

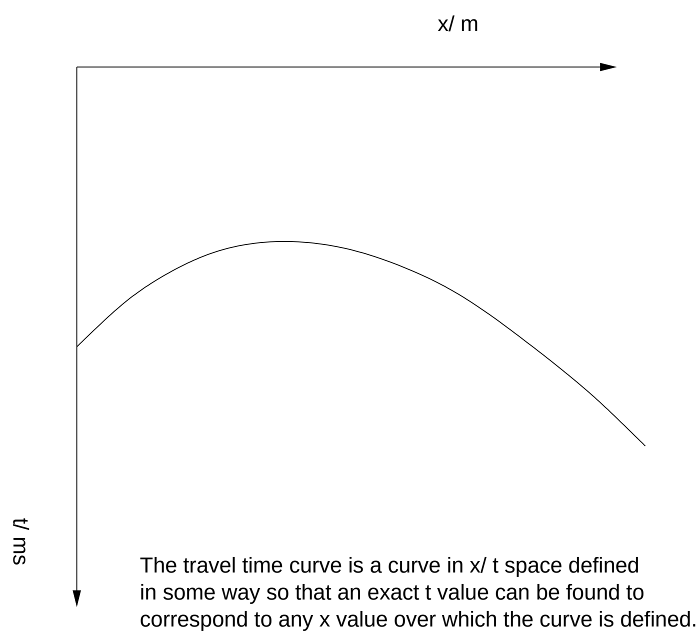

Figure 5.2. The inversion requires time curves that must be extracted from the array of amplitude values

5.2 Previous Work

In standard processing of P-P and P-SV data, travel time curves are parameterised in the CMP or CCP domain respectivley. Semblance, moveout corrected gathers, and other guides are used to find the stacking velocity. Calculating semblance values involves a search in only two dimensions; that is, the value of v_{stack} at a zero offset travel time $t(0)$. For P-wave data the hyperbola seen in Equation 5.1 is fitted to the data in a CMP gather. Both parameters $t(0)$ and v_{stack} can be altered, and for each pair a semblance value is calculated (Semblance is is a way of measuring coherency and is defined in Section 5.2.2). For converted waves a different equation is used. The parameters associated with the highest value of semblance can then be selected. The moveout-corrected gather can also be viewed and the 'flatness' of reflection events checked to see if a good fit has been made. Figure 5.3 shows an example of a semblance panel, and the corresponding moveout corrected gather.

$$t(x)^2 = t(0)^2 + \frac{x^2}{v_{stack}^2} \tag{5.1}$$

The NMO equation (5.1) is valid only for plane horizontal interfaces, and at short offsets over constant velocity media. Long offset, velocity gradient, and anisotropic corrections, which add one or more parameters to the travel time equation, have been developed by Castle (1994) and Tsvankin & Thomsen (1994). Converted waves do not display hyperbolic moveout execpt at very short offsets, Yuan (2001) shows that a non-hyperbolic equation can be used to parameterise the curvature of P-SV reflections from horizontal interfaces even beyond an offset-to-depth ratio of 2.0. By better approximating the travel time curves in the data, more traces can be used in the stack. Relationships have also been worked out to improve interval velocity determination (Thore *et al.*, 1994) and (de Bazelaire, 1988) using the derived parameters. It is debatable how far one should pursue using long offsets in the stack because of the reduced frequency content of the long offset events. This effect is called NMO stretch and is the result of greater attenuation of high frequencies over the longer travel paths

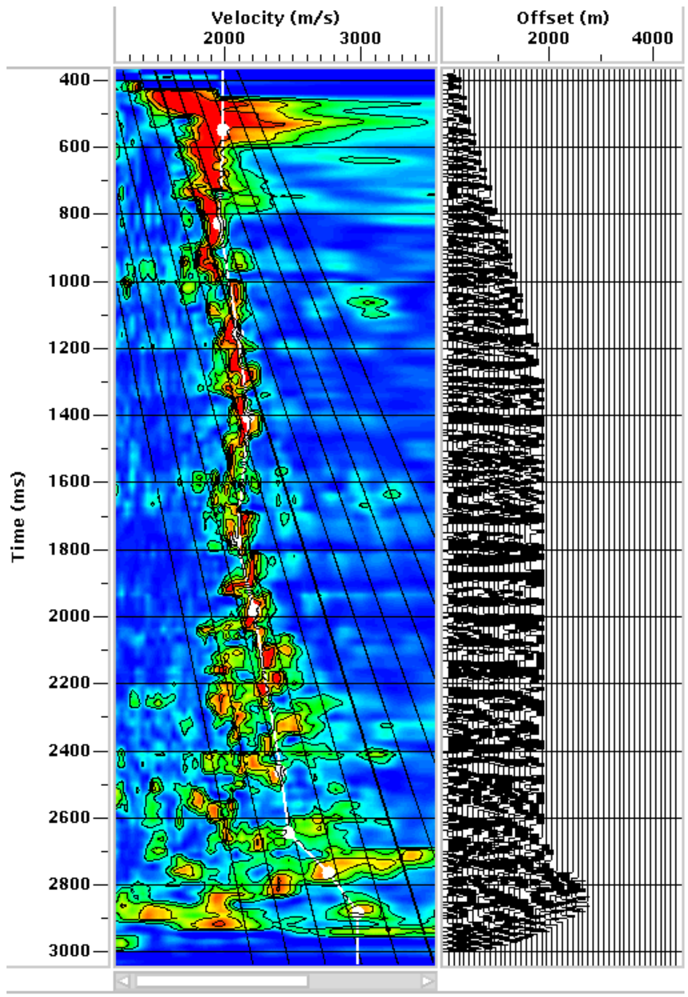

Figure 5.3. A semblance panel in ProMAX, On the left are the semblance values, and on the right is the moveout corrected gather.

associated with the further offset traces. Where improved matches in the travel time curves have been made by the addition of terms related to the effects of anisotropy (Lu *et al.*, 1998) one or two more parameters as well as the stacking velocity must be found. All of these methods require manual picking of one or more parameters, v_{stack} and a correction for offset or anisotropy. These are usually done on a semblance panel like the one in Figure 5.3, sometimes in a two-phase picking scheme; first ($t(0)$-v_{stack}) pairs are picked, then given these picks ($t(0)$-$correctionparameter$) are then picked. This picking step is time consuming as a person has to decide which semblance peak to pick.

To save time some efforts have been made to automate the velocity-picking step. None of these have yet proved to be as good as an experienced processing geophysicist. It is still worth looking at what has been achieved. Zamorouev (1999) has developed code for the automatic picking of events in pre-stack gathers. Semblance is calculated over hyperbolic windows in either mid-point or shot-point gathers. The hyperbolas need not be centered on the zero-offset trace, as is the case with standard CMP velocity analysis tools, making the picked data suitable for use with Castle's shifted hyperbola method.

Moving away from the CMP/CCP domain travel time curve determination in pre-stack shot and receiver gathers is documented. Bishop *et al.* (1985) use travel times as an input for tomography-based inversion and more recently Grechka & Tsvankin (2001) use pre-stack travel time curves for determination of ray parameters of both P-P and P-SV data which are used in a novel inversion scheme. Bishop *et al.* (1985); Mulder & ten Kroode (2001) use hand picking from a screen and both comment on the large time cost of such a picking scheme. Grechka *et al.* (2001), using the methodology of Grechka & Tsvankin (2001), use what they describe as a 'semi-automatic picker'. Sadly, the algorithm is proprietary to Schlumberger and they will not release details of the algorithm.

Interpreters use auto-picking of horizons in post stack datasets. The method used in the Geoquest software requires guide picks throughout the survey area and a user supplied value of maximum trace-to-trace dip. Picks are then identified using either a windowed correlation between two traces, or a match on amplitude and wavelength which must lie within a pre determined error window (GeoQuest, 1993). There is quite a lot of user input to the code and while it can increase the density of picks between manually picked points it is not able to identify and track events without guidance.

5.2.1 Travel time curves in shot and receiver gathers

I consider that the shot gather is a 'natural gather' as it is the domain that the data are originally recorded in; all other gathers require sorting. In the common-shot and common-receiver gathers we have some advantages and disadvantages. On the plus side, we do not need to calculate or sort on common mid-points or conversion-points. The down side is that the reflection points are more dispersed along the reflector in these gathers. Even assuming iso-velocity layers we still have to be able to handle the effects of changing reflector dip with offset. There is an infinite variety of travel time curves that can be generated by models of arbitrary complexity, and we cannot expect to match every possible travel time curve. In the case of an approximately layered earth it is possible to make some approximations as to the general shape of travel time curves that might be expected. In the case of gently dipping layers with a small degree of curvature the approximation in Equation 5.2 is very good at offsets equal to the reflector depth.

It is not possible to match all travel time curves with even very high order polynomials but through a process of trial and error I found that the cubic equation

$$t(x) = t(0) + ax + bx^2 + bx^3, \tag{5.2}$$

can be used successfully in conjunction with the parablolic layer inversion. Unlike conventional velocity analysis, where a search is made for a time and a velocity, none of the parameters in Equation 5.2 have a distinct clear physical meaning. Comparison with equation 5.3, the travel time curve for reflection over a single dipping reflector and an iso-velocity layer, sheds some light on which parameters are most highly affected by what. For a derivation of Equation 5.3 see Appendix A.

$$t_p^2(x) = t_p^2(0) + \frac{x^2}{v_p^2} + \frac{2xt_p(0)\sin(\phi)}{v_p}. \tag{5.3}$$

Equation 5.3 is an exact equation for the travel time of the P-P ray shown in Figure 5.4.

To compare the terms we must first square equation 5.2. Doing this we get,

$$t^2(x) = (t(0) + ax + bx^2 + cx^3)(t(0) + ax + bx^2 + cx^3). \tag{5.4}$$

Expanding equation 5.4 and collecting the terms up to x^2 gives

$$t^2(x) = t(0)^2 + 2t(0)ax + (2t(0)b + a^2)x^2 + ... \tag{5.5}$$

By comparing the terms in equations 5.5 and 5.3 we see that

$$a = \frac{\sin\phi}{v_p}, \tag{5.6}$$

and

$$2t(0)b + a^2 = \frac{1}{v_p^2}. \tag{5.7}$$

From Equation 5.6 we can see that the a term in 5.2 is proportional to the *sine* of the dip of the interface and inversley proportional to the velocity $1/v_p$.

Substituting for a in equation 5.7 using equation 5.6 and re-aranging we get,

$$2t(0)b = \frac{1}{v_p^2} - \frac{sin^2\phi}{v_p^2}. \tag{5.8}$$

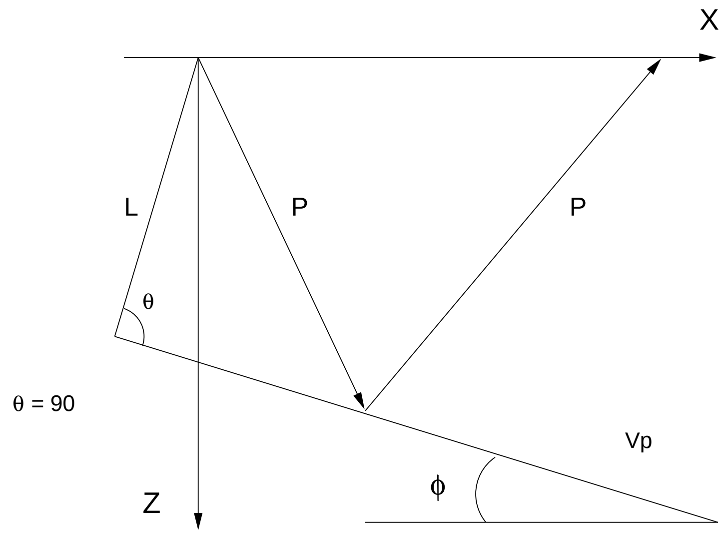

Figure 5.4. A simple dipping layer model

Introducing a length scale (see Figure 5.4) and a velocity we substitute for $t(0)$ with

$$t(0) = \frac{L}{v_p}, \tag{5.9}$$

and then re-arrange equation 5.8 to get

$$b = \frac{1}{2v_pL}(1 - sin^2\phi). \tag{5.10}$$

From this we can see that b depends on the length of L the normal to the interface, the velocity v_p, and on the square of the sin of the dip. The dip term will always have less effect on b than on a. Both terms are affected by dip and velocity although the effect of dip is greater on a than it is on b.

An interface of varying curvature and dip with a complex overlying velocity structure will yield travel time curves of great complexity. The travel time curve in this situation could be accurately described with only a very high order equation in x:

$$t(x) = t(0) + a_1 x + a_2 x^2 + a_3 x^3 + ... + a_{n-1} x^{(n-1)} + a_n x^n, \tag{5.11}$$

where n is not a small number. We do not try to fit any terms to to the data of higher order than a cubic equation, even if theoretically it might allow an inversion to get more detail about varying structure or velocity within a layer (Fagin 1998). The inversion (Chapter 4) assumes that interfaces are uniformly curved on the scale of a shot record. The inversion cannot converge if the travel time curve used as input has high order terms in it. High order terms in the travel time curve are associated with sharp gradient changes in the travel time curve, and a highly complex subsurface. We do not try to model every kink in the curve, but would like to get a good background velocity model. In real data where the actual travel time curve is not simple, using Equation 5.2 as a best fit performs a degree of smoothing. This can be helpful to the robustness of the inversion when working with real data.

5.2.2 Semblance

It is possible to measure the similarity between events in a seismic record using quantifiable measures of coherency. A reflection event is defined by the behaviour of a number of neighbouring time samples; a seismic reflection event is a wavelet with temporal extent, and is not an isolated peak. Semblance can be used to calculate how coherent the data are along a selected trajectory within a window in time and space. Neidell & Taner (1971) find that semblance has the greatest power of discrimination for determining stacking velocities from data. Although the travel time equations I use differ from those used by Neidell and Tanner, I expect that semblance will applicable in the same manner.

Semblance is the normalised output-to-input energy ratio and is defined in equation 5.12 (Neidell & Taner, 1971)

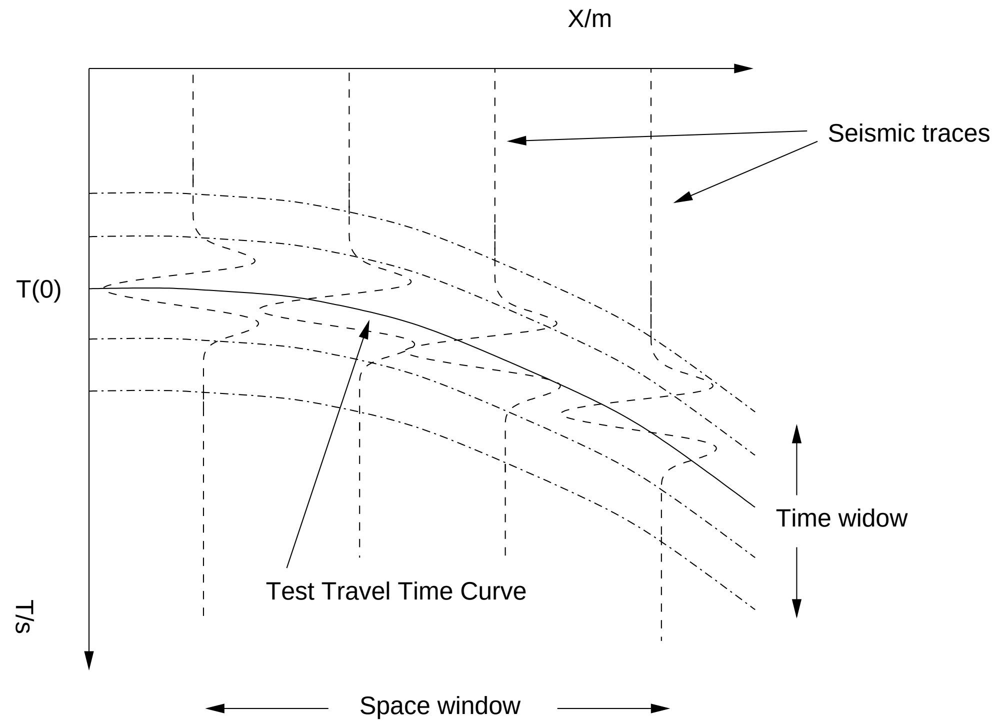

Figure 5.5. The time window over which semblance is performed is centred on the *'test travel time curve'* and covers the same number of time samples on each side for zero phase data.

$$NE = \frac{1}{M} \frac{\left\{ \sum_t \sum_{i=1}^{M} f_{i,t(i)} \right\}^2}{\sum_t \sum_{i=1}^{M} f_{i,t(i)}^2}, \tag{5.12}$$

where $f_{i,t(i)}$ is the amplitude value of the ith trace at two-way time $t(i)$, and M is the number of traces in the gather. The two way time lies along a trajectory that I call the *'test travel time curve'* (TTTC). For my purposes the TTTC is defined by the travel time equation 5.2.

The mechanics of a semblance search are quite simple: First I find the trajectory of the TTTC by calculating travel times for each trace using the trace offset and test values of the parameters $t(0)$, a, b and c . The semblance window has temporal extent and so a number of other curves which share the same trajectory, offset by a

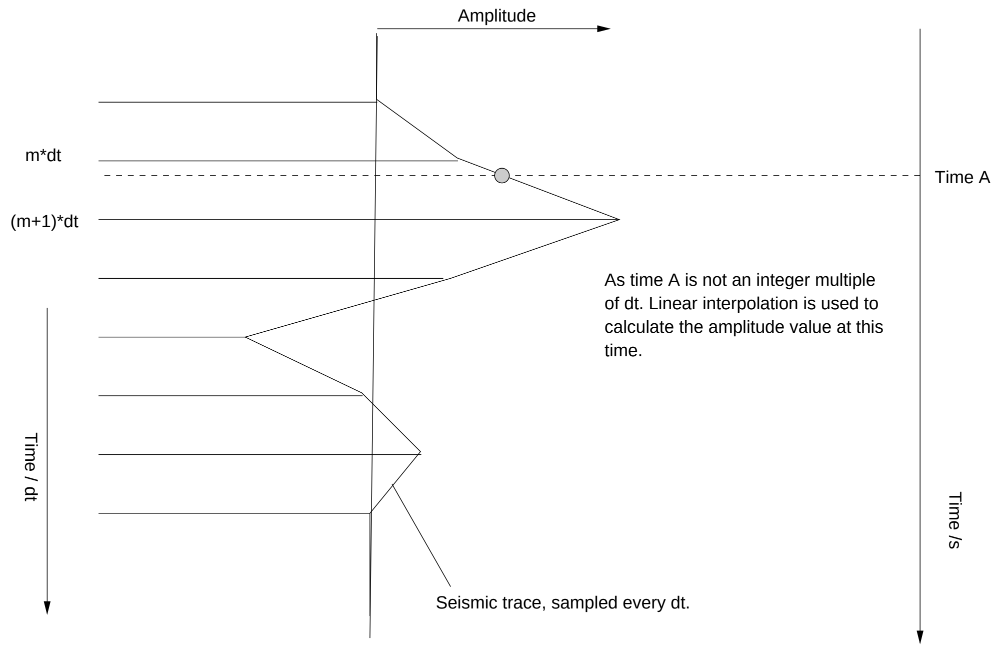

Figure 5.6. When the TTTC does not coincide with a sample location then the amplitude value for that time must be calculated, I use a simple linear interpolation.

given step size from the TTTC are also calculated, I use an integer multiple of 2ms spacing in time between the trajectories within a semblance window. The TTTC and other curves in the family usually cross the traces at times different from the sample time. The amplitude values associated with these crossing points have to be found by interpolation, see Figure 5.6. I use linear interpolation, although a more complex spline function could also be substituted. It is these interpolated amplitude values that are used in the semblance calculation. The semblance value associated with these test parameter values are calculated using the interpolated amplitude values and equation 5.12 and written to a matrix. From this matrix the location of the peak semblance value may be found. The size of the window in time is a factor that affects both the accuracy of the calculated travel time curve and the run time of the operation. A window size equal to that of the wavelet of the event gives good results, as shown in Figure 5.5.

Semblance is a maximum when events along the trajectory are most alike. In fact semblance equals 1 when the events are identical. Given a well-defined wavelet this is when the calculated travel time curve matches best that seen in the data. In the semblance search it is likely that a number of TTTCs will be a close match to the data and these are associated with the highest values in the semblance matrix. Selecting the 'peak' value can be done by taking the location of the maximum semblance value. If there are a number of locations with the same semblance value, it is reasonable to find the one nearest the middle of the 'cloud' of semblance values. Figures 5.7 and 5.8 illustrate this. To do this I specify a threshold, say 99%, of the peak semblance value, and then any location with a semblance value above this point is stored. Once all the locations with semblance values above the threshold have been found, I take the average of the a, b and c values given by these locations. This means that when there is a cloud of peak semblance values I use the middle of the cloud rather than the one with the lowest value of a, b and c.

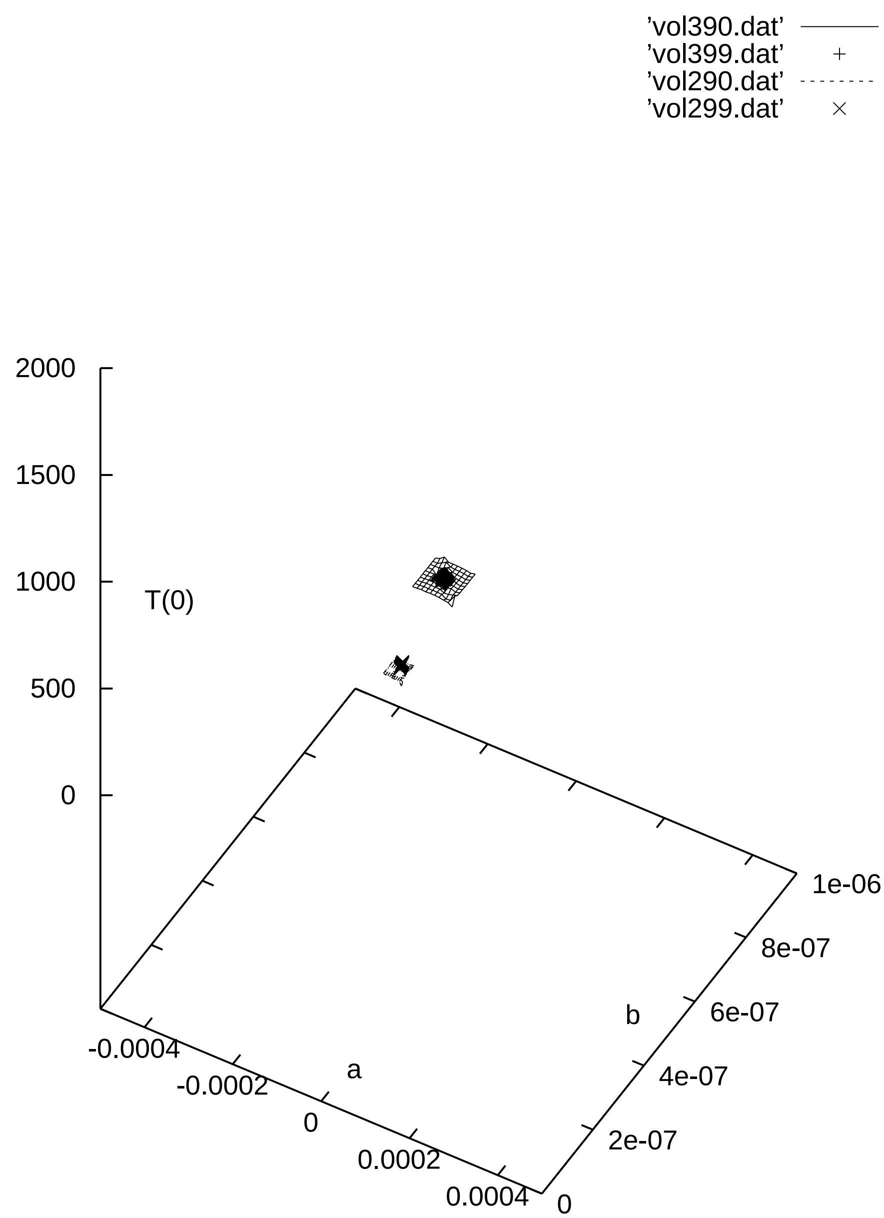

Figure 5.7. The location of the top 10% of semblance values. Semblance was run with a fixed $t(0)$ value on a synthetic P-P dataset with two reflectors.

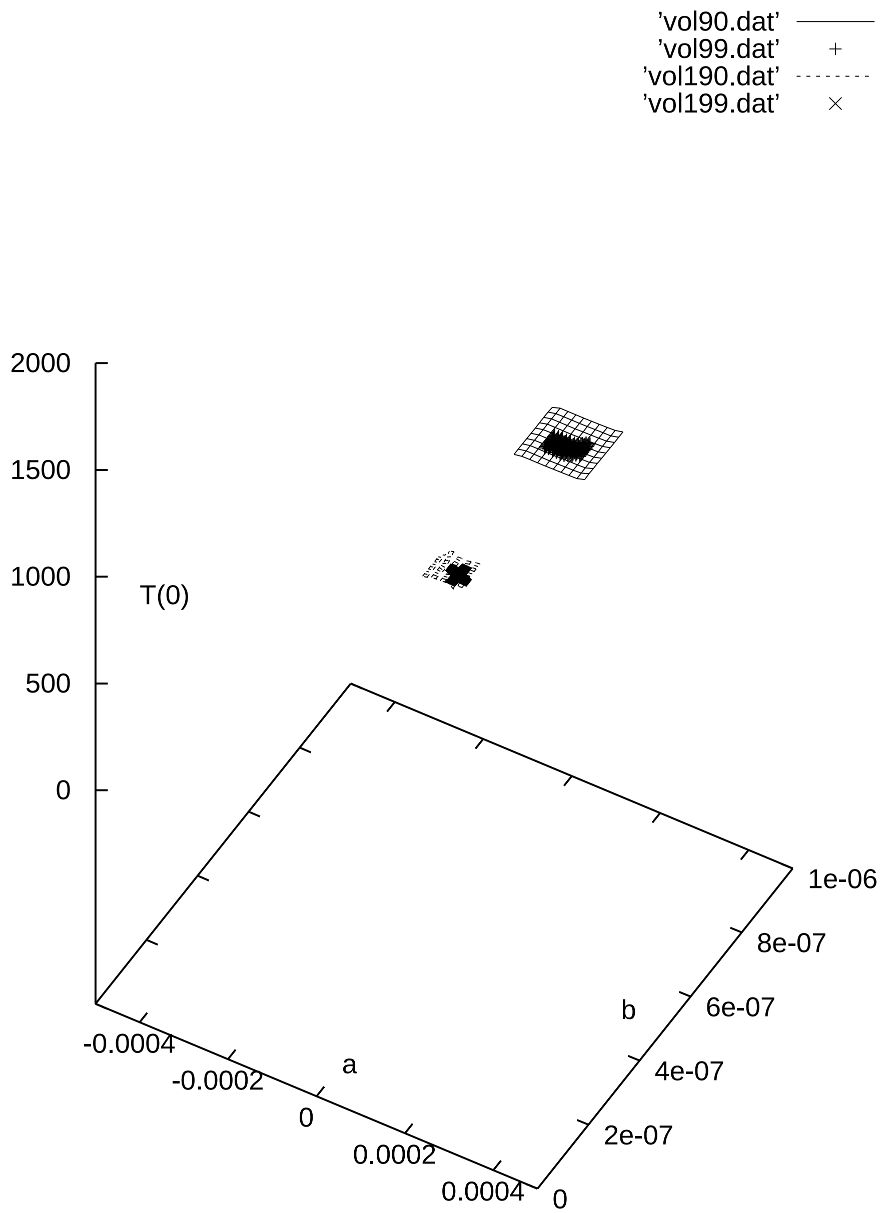

Figure 5.8. The location fo the top 10% of semblance values. Semblance was run with a fixed $t(0)$ value on a synthetic P-S dataset with two reflectors.

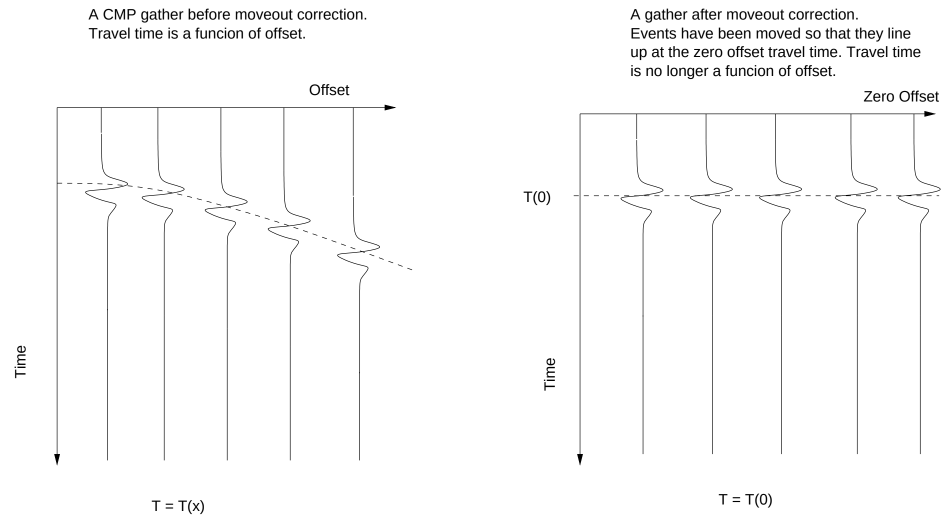

Figure 5.9. The moveout correction moves data to $t(0)$ the zero-offset travel time

5.2.3 Moveout correction as a quality contol measure.

Some of the synthetics I have used for testing purposes have been generated by ray tracing. One of the outputs from the ray tracing package Seis88 (Cerveny & Psencik, 1988) is the sequence of arrival times at each receiver, so the exact travel time curve from any given reflector is available for comparison with that determined from the seismograms using semblance. Two examples of this comparison between the exact travel time curve and curves derived from synthetic seismograms are shown in Figures 5.11 and 5.13. When finding travel time curves in real data or in finite difference synthetics, we do not know the travel time curve for the reflection events, and in this case the only check the user has is the 'flatness' of the moveout-corrected gather. To perform a moveout correction, amplitude values on traces with offset x and travel time $t(x)$ are moved in time to $t(0)$. If the events in the moveout corrected gather are flat at $t(x) = t(0)$, then the calculated travel time curve matches that seen in the data, as shown schematically Figure 5.9. Two examples of moveout performed on synthetic data are shown in Figures 5.12 and 5.14, a real data example is shown in Figure 5.15.

Tests have been performed on shot gathers over the 'Wave' model. In the 'Wave' model the curvature and dip of the first interface changes with offset. Below we show two

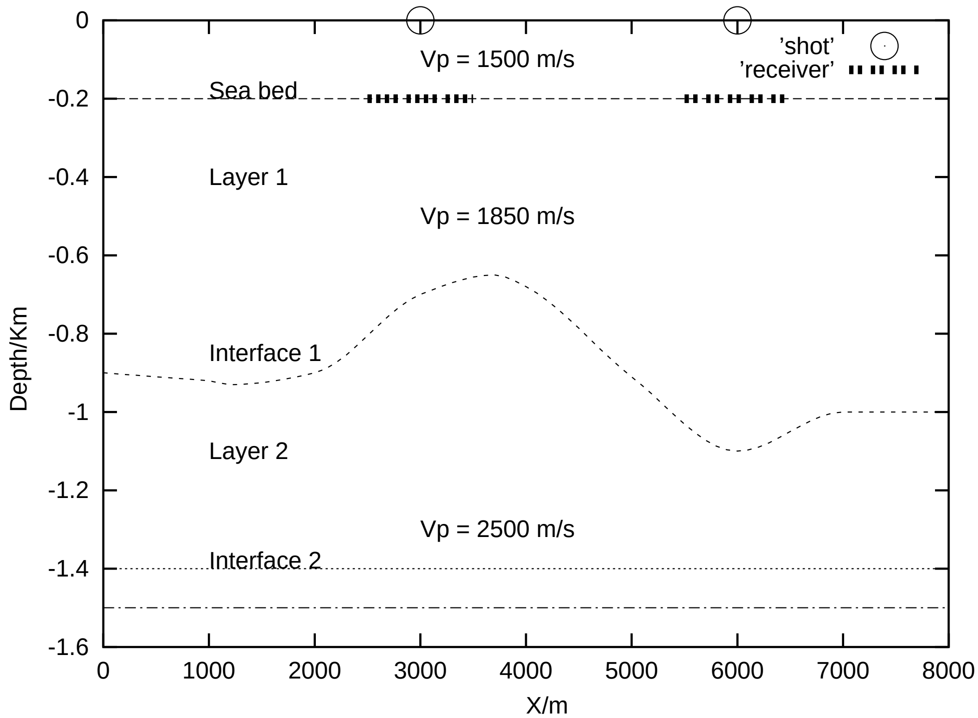

Figure 5.10. The location of source and receiver arrays over the 'Wave' structure

cases where the semblance has been calculated over a 50 trace window, and the travel time curve derived using semblance is displayed on the same plot as the exact travel time curve from the ray tracing code.

In time processing the moveout correction step is then conventionally followed by stacking, a summation step (discussed in Chapter 2). In order to preserve frequency content in the stacked traces, the flatness of the moveout-corrected gather is vitally important. In this case I will use prestack migration to take account of the effects of wave propagation. I have no intention of stacking the data in the shot or receiver gathers. The stacking step is moved down the processing sequence till after we have determined the velocity model and performed pre-stack migration. Nevertheless the 'flatness' of an event after moveout correction has been applied can still be used as a quality control check. If the event has not been correctly parameterised then it will not appear flat in the corrected gather, as shown in Figure 5.14.

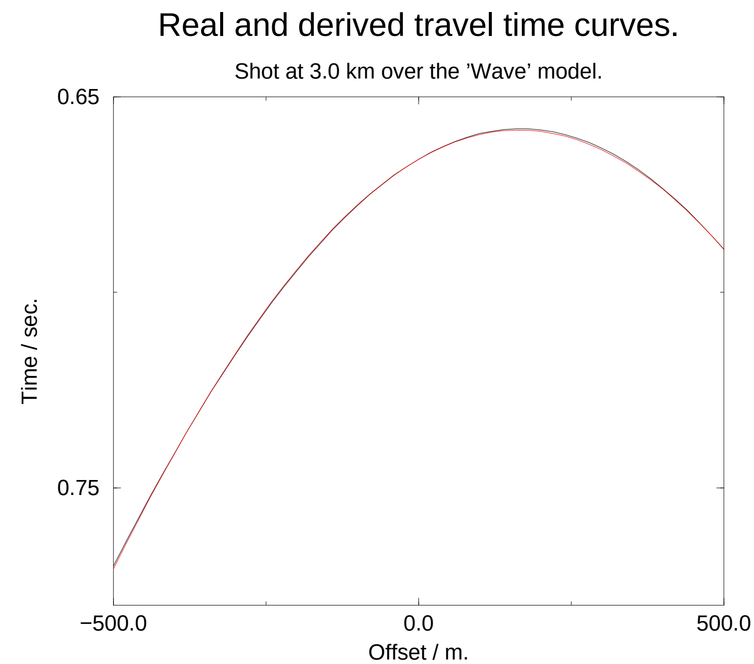

Figure 5.11. Two travel time curves plotted on the same graph. The black curve is derived from ray tracing, and the red one found using semblance. Notice how well the curve calculated using semblance matches the actual travel time curve.

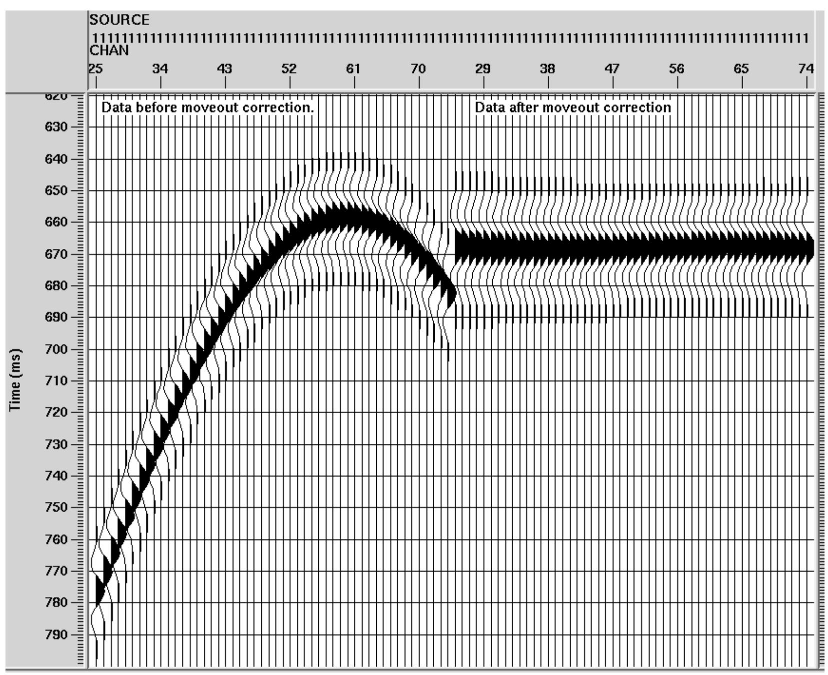

Figure 5.12. On the left are the synthetic data before moveout correction, on the right are the data after moveout correction using the cubic curve shown in the previous figure. The cubic equation is a good match and the corrected gather is almost perfectly flat.

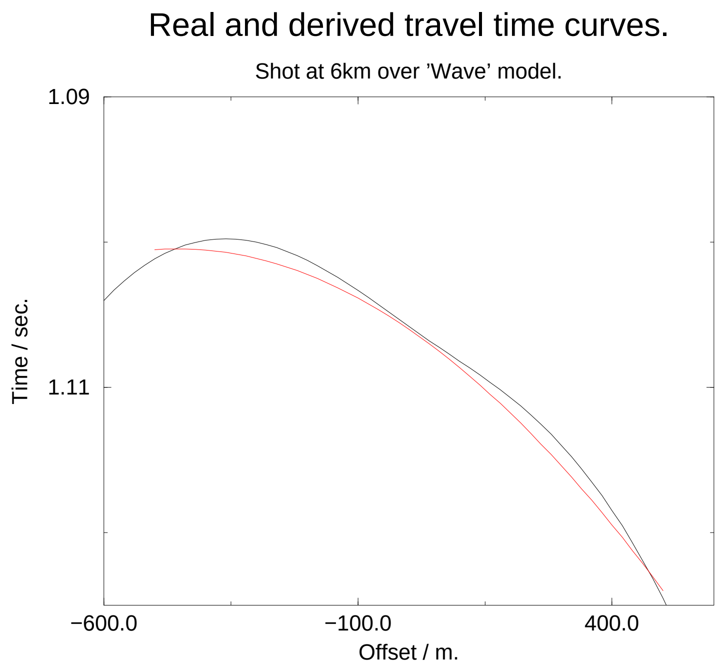

Figure 5.13. Two travel time curves ploted on the same graph. The true travel time curve plotted in black is much more complicated than the cubic curve found using semblance.

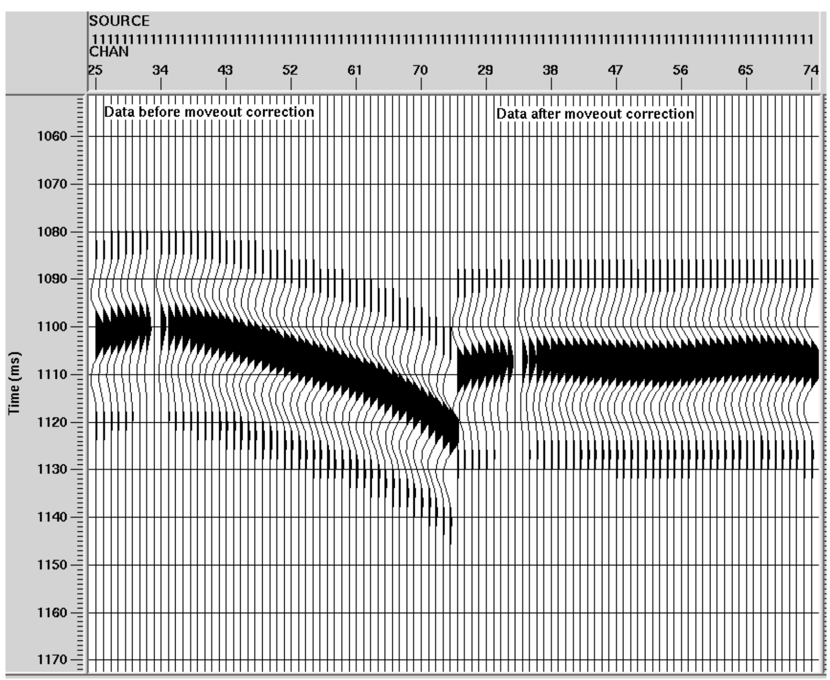

Figure 5.14. On the left are the synthetic data before moveout correction, on the right are the data after moveout correction using the curve shown in the previous figure. The user of the code can see that the travel time curve can not be described with a cubic equation in this situation.

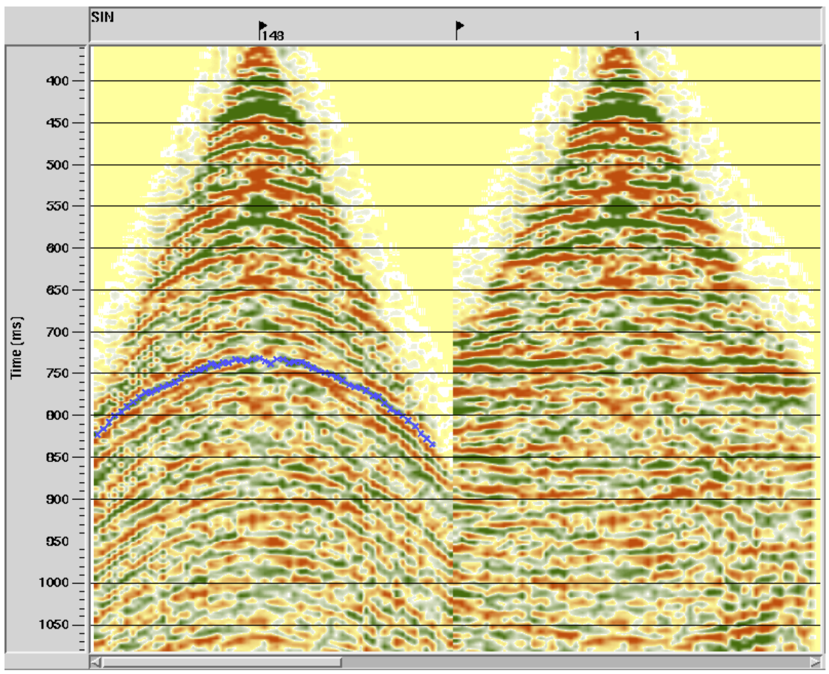

Figure 5.15. On the left panel are picks made on a shot gather, on the right are the data after moveout correction using a cubic travel time equation. The parameters for the moveout correction are found using a semblance search in a window around those derived from the manual picking. You can see that the selected event at 730 milliseconds in the right hand gather is indeed well flattened.

5.3 Findings from experience with semblance and manual picking

5.3.1 Problems with semblance

There are two major problems with the use of semblance: the large number of calculations, and the problem of visualising semblance in more than three dimensions.

With a simple search I increment each parameter by a given step size and test all combinations of parameters. This involves doing $(n_{test})^{(n_{params})}$ semblance calculations if we allow (n_{test}) test values of each parameter, of which there are (n_{params}). There are ways of speeding things up slightly and I used a two step search: first I used a 'coarse' search to get the parameters in the right sort of area, this was then followed by a search centered on the peak from the first search using a finer grid to calculate the parameters with more precision.

When picking values of v_{stack} corresponding to values of t_0 in conventional CMP velocity analysis, the semblance panel has two dimensions. This is easily visualised on a screen using a contour plot or colour scale. It is easy to locate the local maxima associated with a well parameterised travel time curve. When more dimensions are added the visualisation problem becomes hard, and then almost impossible to deal with neatly. For three dimensions one can visualise the semblance matrix as a cube with amplitude values within it, each amplitude being the semblance value associated with the test values of $t(0)$, a and b. I have plotted a very sparsely populated 3D matrix in Figures 5.7 and 5.8. With only two reflectors present it is possible to make reasonable picks on data presented in this form. For real data the visualisation problem is harder. When a large number of reflections is present, each of which would produce its own semblance peak, seeing through all the data to pick out the peaks is hard. The equation that I use for parameterising travel time curves for the inversion (equation 5.2) is a cubic equation in x, and there are four parameters that can be altered. Computationally, a 4 dimensional matrix presents no problems, but visualising this space is non-trivial and I did not attempt it. I reduced the problem to a 3D search by fixing $t(0)$, the travel time on the zero offset trace. This means that I have to make a pick from the displayed data. It is possible with modern visualisation packages to control point opacity and to see 'through' 3D data cubes. I did not attempt to make a 3D graphical display on which I could pick parameters, but instead used computer code to identify the mid point of the 3D point cloud which contains the top p percent of semblance values. The value p can be set in a prameterfile and I prefer to use a p value of 95-98%.

5.3.2 Manual Picking

The human brain has very good image processing software on board already. A human being is very good at recognising a coherent signal and I can use this to advantage. Within the ProMAX interactive trace display environment there is a semi-automatic picking tool called the 'snap to' function, which is used in conjunction with the 'Pick other Horizons' option. This enables a pick to be made on every trace in a gather very quickly. The user can roughly pick the event of interest with a mouse click on the screen. The 'snap-to' function is used to place a pick on every trace at a peak, trough, or zero-crossing, within the selected range of offsets. The picks resulting from the use of the 'snap-to' function are editable by the user, and this is sometimes necessary as the algorithm used does not always pick the peaks (etc.) of the wavelet the user had in mind. This is a simple way of picking precisely the right event over the desired offset range. The semi-automatic picker generates an output table which includes (x,t) pairs defined by the picks seen on the screen, overlaid on the seismic data.

5.3.3 Smoothing Picks

The inversion requires smooth travel time curves. Because of the time sampling of data and noise, the (x,t) pairs from the picking step tend not to fall on a smooth curve. I use a least squares algorithm (Press *et al.* (1992)) to find the parameters of the cubic polynomial which best fits the picked data. The output of the least squares fitting is a curve with parameters in $t(0)$, $a(x)$, $b(x)^2$ and $c(x)^3$.

5.3.4 Guiding semblance

Manual picking is not a flawless technique for parameterising travel time curves, as it depends on the location of only one data point per trace. The reflection event, however, has temporal extent; using semblance allows the use of data from all of the wavelet. A simple semblance search with a large number of variable parameters is very costly and does not always result in the parameterisation of the right travel time curve. In an effort to reduce the number of dimensions and the run time of the semblance search, I have had to introduce a manual interaction with the data. The first attempt involved identifying each reflector by its zero offset two way time and allowing a search on $a(x)$, $b(x)^2$ and $c(x)^3$. The travel time curves shown in Figures 5.11 and 5.13 have been calculated using this method. If the travel time curve can be accurately described using a cubic polynomial and the wavelet is well defined and isolated from other strong events, this method works well. In Figures 5.11 and 5.13 the travel time curve calculated from synthetic seismograms and the travel time curve calculated using ray tracing are superposed. In the first instance (Figure 5.11) a very good match is seen, in the second instance (Figure 5.13) higher order terms in the true travel time curve are not accurately fitted by the cubic polynomial. This is not a fault of semblance, just a result of not being able to parameterise the complicated nature of the real travel time curve with a cubic equation in x.

In quite a large number of cases, when working on real data, my semblance code does not flatten the event I have in mind and much fine-tuning of the time-window size and offset range is needed. I find that I can spend a large amount of time 'tweaking' the semblance parameters and even then can not guarantee that I have accurate parameters for the travel time curve. Noise proves to be a big problem, as the wavelets in real data are far from the idealised shapes that are seen in the synthetic data. Problems also arise from having many alike reflection events stacked close together in time. The semblance code can sometimes 'jump' between events, parameterising a mixture of one reflection event at short offset and another at long offsets. It is possible to see what the code is doing when the moveout corrected data are examined, and so re-run the code where necessary, which is very time consuming. To try and save time re-running the code because of a 'mis-pick' I can guide the semblance search by constraining the values that the parameters may take in the search. To do this I use manual picking as a guide. I manually pick the event that I would like to parameterise. The picks are then fitted with the least squares algorithm. The parameters returned from the least squares fit become the centre points for the test values of a, b, and c. In an attempt to stop the semblance code 'jumping' to another event I fix $t(0)$ using the value returned by the least squares code. This way I hope that the semblance code analyses the event I have in mind. During the quality control I view both the manually picked curve, the updated curve found using semblance and the moveout corrected data. What I find is that using the parameters from the least squares fit to the picked points results in a very well flattened gather after moveout correction. The semblance code either makes only very minor adjustments to the parameters or it still suffers from the effects of noise in the data. The resulting gather is often not as well flattened after using semblance as it was when corrected using the guide function from the manual picks.

Semblance has traditionally been used as a tool to assist in finding stacking velocity. I was interested to see if we could modify the traditional methods to suit our purposes, hence the work on semblance methods in this chapter. The way I parameterise travel time curves is rather different from the hyperbolic assumption used in CMP velocity analysis where semblance has proved to be such a powerful tool. But, because of the problems I found using semblance, I do not use it to help parameterise travel time curves any more. It may prove to be useful later on when the comunication between the inversion and the data is improved and the picking bottleneck is reduced.

5.3.5 Wavelet phase

In the real world the wavelet convolved with the earth's reflectivity series can never be zero phase (Fokkema & Ziolkowski, 1987) bcause it is causal. The peak amplitude of a wavelet in seismic data will lag the true 'arrival time' of the event. The inversion does not take account of any phase shift and assumes that the travel time curve used as an input is the true travel time curve which represents the time taken for energy to travel between the source and receiver. The source wavelet should be replaced by a zero-phase

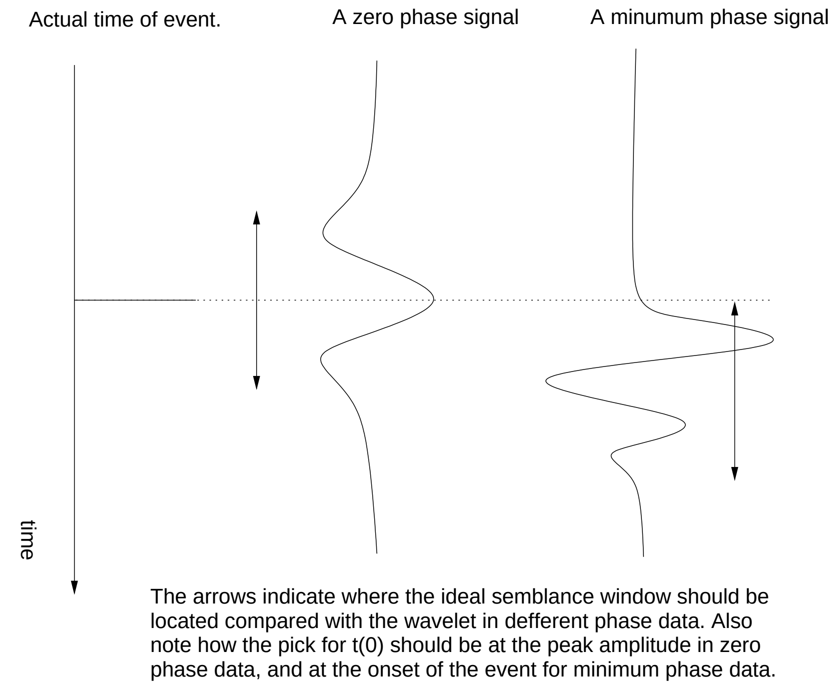

Figure 5.16. The phase of the wavelet in the data affects both the picking of $t(0)$ and the location of the semblance window compared with the TTTC.

wavelet for optimum travel time curve determination. This requires measurement of the source signature (Ziolkowski, 1991). If the picks are made on the peak amplitude in data that do not have a zero phase wavelet the resulting travel time curve will be in error.

To find out how the inversion reacts to a delayed travel time curve I used Seis88 to create a dataset with a delayed wavelet. In Seis88 only zero phase wavelets can be modelled. However a delay between the onset of the wave and the peak energy of the wavelet can be applied. I used this delay to model a wavelet whose peak amplitude occurred later than the true onset of the event, as is the case in a real non zero phase data. The wavelet was delayed by 20ms, and the resulting change in the inversion result was small. The travel time curves picked on the true and lagging arrivals are shown in Figure 5.17. The shot was located at x=3.0km over the wave model, analysing only the first layer a difference in velocity of 30m/s and a change in depth of 10m between the results obtained by inverting the shifted and un-shifted curves. I conclude that

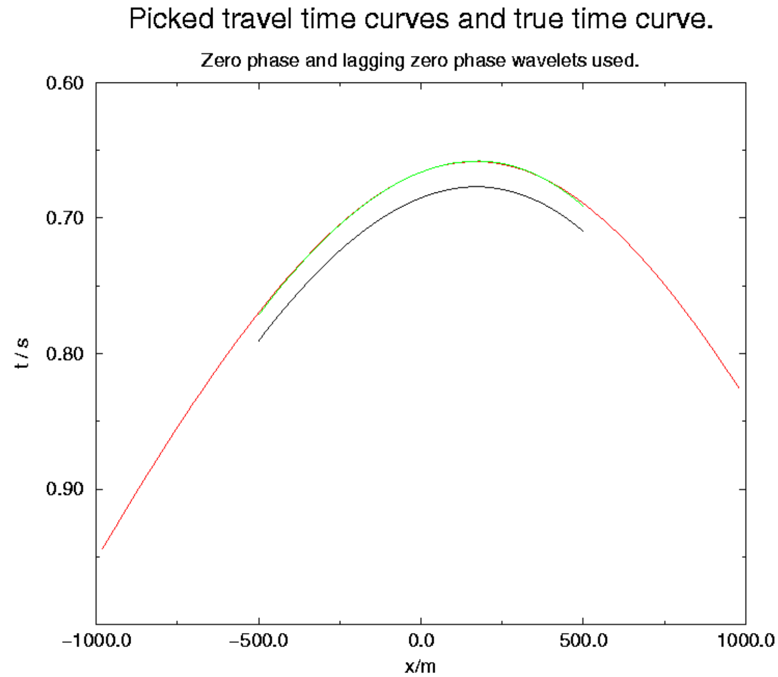

Figure 5.17. Travel time curves, the one present over all offsets is calculated by ray tracing, the other two are calculated from the synthetic seismograms generated by the ray tracing package. The curve that overlays the exact travel time curve was derived from seismograms with a zero phase wavelet. The travel time curve that is seen at a later travel time was calculated on a wavelet that lagged behind the true arrival time of the event.

while this will have an effect on the determination of true interval velocity, the effect is small compared with other potential sources of error.

5.3.6 Offset range

Here we come to one of the places where the inversion and the picking really interact. There are contradictory needs caused by a desire to reduce ambiguity in velocity determination, and at the same time to satisfy the assumption that the interfaces can be locally described as a second order polynomial in x. From one point of view we should use the lowest range of offsets possible: the interface will then be most accurately approximated by a second order polynomial, even if on a larger scale it is more complex than this. On the other hand, if we use too small a range of offsets, the ability to resolve velocity accurately is reduced. Kosloff & Sudman (2002) found that the ability to determine velocity uniquely using a tomographic scheme increases with the ratio of offset to depth. I have to find a trade-off between the assumptions made in the inversion, which benefit from the use of short offsets, and the problem of uniquely determining the velocity. I found that using too short a range of offsets ($\pm 200m$) resulted in a high degree of lateral variability in the inversion results. As a result of this I now use a larger range of offsets, I try to maintain at least offset:depth=1. This helps to reduce the fluctuations in the velocity determined from neighbouring points.

Initially in Chapter 4 I picked in gathers with only positive offsets. This is not helpful to the coefficient determination; the curvature term b, which is closely associated with the layer velocity, can be incorrectly determined, particularly if the apex of the travel time curve is not sampled. The situation I have in mind can be seen in Figure 5.18 where we see that a straight line can be fitted to the flank of the travel time curve. It is an advantage to sample both positive and negative offsets in a gather, which I now do. A 'split spread' type of acquisition geometry is an advantage here, as the shot gathers contain both positive and negative offsets. If I were to process marine streamer data the negative offsets should be generated using the reciprocity principle (interchanging souce and receiver positions).

The cubic equation is not valid for all offsets. When the offset range becomes very high, particularly when dealing with converted waves, the travel time curves seen are not well parameterised by a cubic equation, see Figure 5.19(a). However, in all the situations that I present in the thesis I have found that the approximation is acceptable, see Figure 5.19(b). This is something we need to work on, posibly moving away from parameterising the travel time curves with a single function at all offsets.

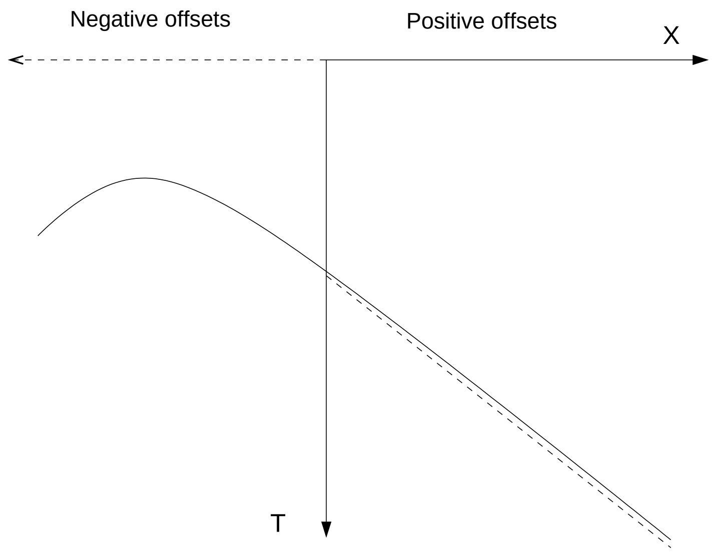

Figure 5.18. If only the positive offsets are analysed in this case the value of the second order term (which has a big control over curvature) will be much reduced below the value that correctly defines the solid curve. The dashed line is straight

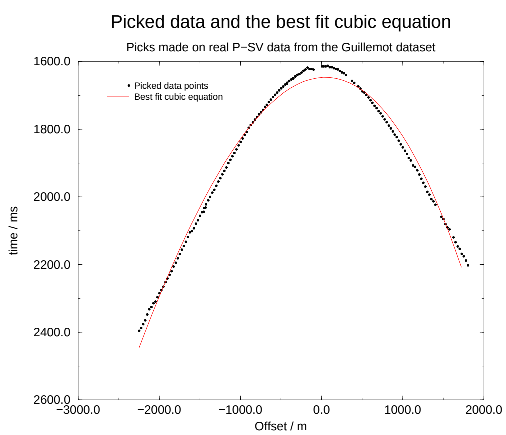

(a)

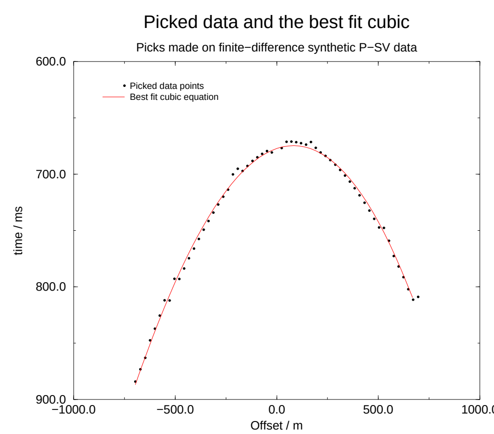

(b)

Figure 5.19. (a) Shows an example of picking on real P-SV data over a long offset range, notice that the best fit cubic equation does not match the data very well. For comparison (b), also a converted wave event, shows the degree of fit that is usually acheived when working on the data I present in later Chapters of the thesis, the cubic approximation is much better over the lower range of offsets that I currently use.

5.4 Event Selection

5.4.1 A picking scheme suitable for use on real and synthetic data

As I am trying to build velocity models over the whole extent of the survey area, it is advantageous to analyse events that are present all across the survey. Ideally, one can identify reflection events in the pre-stack gathers that correspond to the major events that are identifiable across the whole extent of the survey. If we follow this methodology we are not at liberty simply to pick the strongest coherent reflection events in a given gather. The strength of the event we are tracking throughout the survey may change, but I should still try to keep track of it. I should also like to parameterise reflection events over a range of offsets equivalent to the depth of the reflection event, and not just a small highly coherent part as Billette *et al.* (1998) do in the Sterotomography method. This limits our use of automatic methods and I find that I have to rely on the human brain's ability to identify seismic events.

The picking scheme I settle upon is made up of the following steps;

- Event Selection
- Manual Picking *(Section 5.3.2)*
- Smoothing Picks *(Section 5.3.3)*
- Quality contol measures *(Section 5.2.3)*

Most of these points have been discussed earlier in the chapter. I have not yet discussed the issues surrounding which events one should choose to parameterise but do so in the next section.

To build velocity models based on structure, we must find events in neighbouring gathers that correspond to the same reflector. The selected events should, if possible, be present across the whole extent of the survey. This is most easily checked by viewing a large number of gathers alongside one and other, so common events can be tracked by

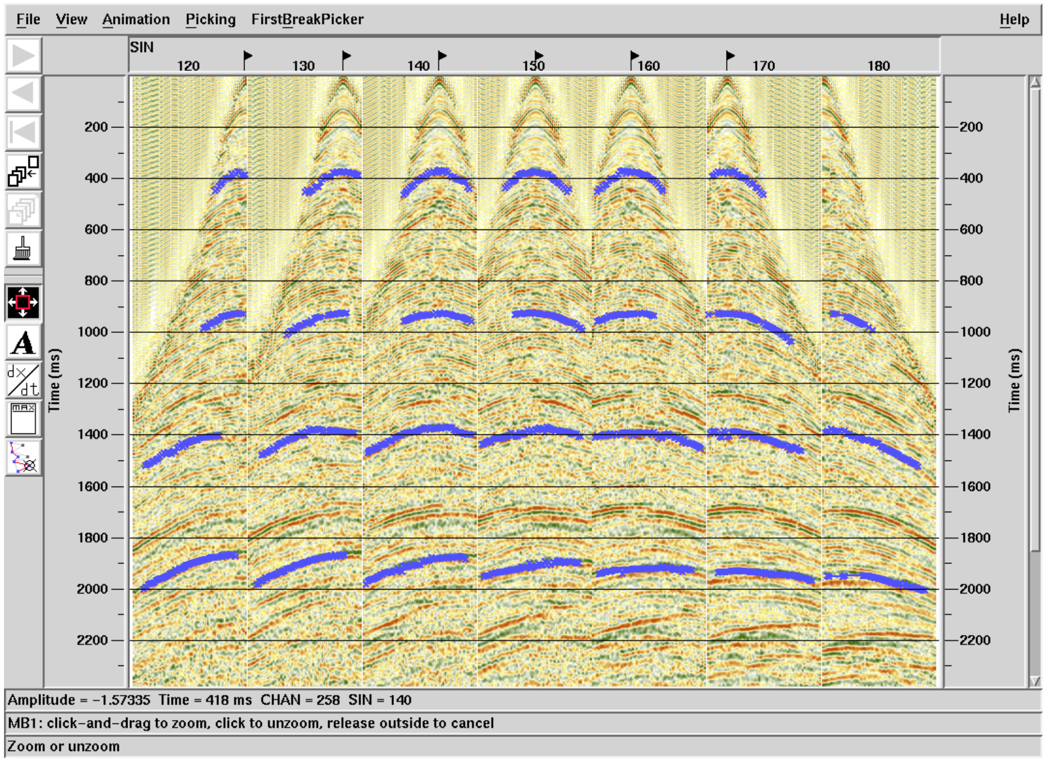

Figure 5.20. Four reflectors tracked in shot gathers across a large latteral extent of a survey. Vertical component of motion from the Guillemot dataset.

eye, as shown in Figure 5.20. It might well be sensible to use a simple stacked section to guide the selection of events for parametersiation.

The selected event should ideally have a high signal-to-noise ratio, and a wavelet identifiable over a good proportion of the traces in the gather. Crossing events, changing signal-to-noise ratio, changing wavelet character, or a discontinuous travel time curve, all cause confusion and open up possibilities for poor travel time curve determination. Multiples cannot be inverted correctly, so only primary reflection events should be analysed. Faulting can be handled to a certain extent, provided the faults are identified prior to picking. The travel time curve picking must occur only on one side or other of a fault. Attempts to interpolate over a fault, evident as a step in the travel time curve, will result in errors. It is important that the user be careful in selecting the events that are to be used for parameterisation.

5.4.2 Use of Neighbouring gathers

Initially, when using the inversion on real data, I observed variations in velocity between neighbouring locations. Neighbouring inversions might have velocities differing by as much as 500m/s. These fluctuations in the velocity model are not consistent with the idea that a large portion of the subsurface sampled by one shot is also sampled by the neighbouring shot. The change of velocity between shots should be small and smooth. The errors may be attributed to random error in the travel time curve determination and using too small a range of offsets in the inversion. In an attempt to reduce the fluctuations in the results caused by noise, I changed the picking scheme. Instead of picking in only one gather, I pick the travel time curves in a number (for instance, three or five) of gathers, and fit a curve to all of these data. If the step size between analyses is smaller than half the number of gathers analysed, there is always some data in common between neighbouring inversions. Also, using a larger range of offsets is known to reduce the uncertainty in velocity estimation and is discussed in the literature by, for example, Bickel (1990) and Lines (1993). Adopting these methods has reduced the differences between neighbouring inversions. Non-uniqueness has been cited as a problem for travel-time-based inversion schemes. Some solutions to this problem, such as imposing smooth solution criteria, or using statistics, are mentioned by Vesnaver *et al.* (1999). Combining the picks from a number of neighbouring gathers is a way of imposing a smooth solution on the model.

The method of fitting a single travel time curve to the data from a number of neighbouring shot gathers is rather simplistic. The resulting fitted travel time curve will only resemble the true travel time curve when the change in the travel time curve of the event is small from one gather to the next. To treat this problem correctly we must include the shot coordinate in the interpolation. When the travel time curves are viewed in 3 dimensions with the shot-coordinate along one axis, offset on the second and travel time on the third, as in Figure 5.21, the travel time curves produce a 'travel time surface' which can be fitted. Fitting this surface is a better way to fit the data as it is able to take account of variations in the travel time curves recorded with a different source. I have yet to implement this scheme.

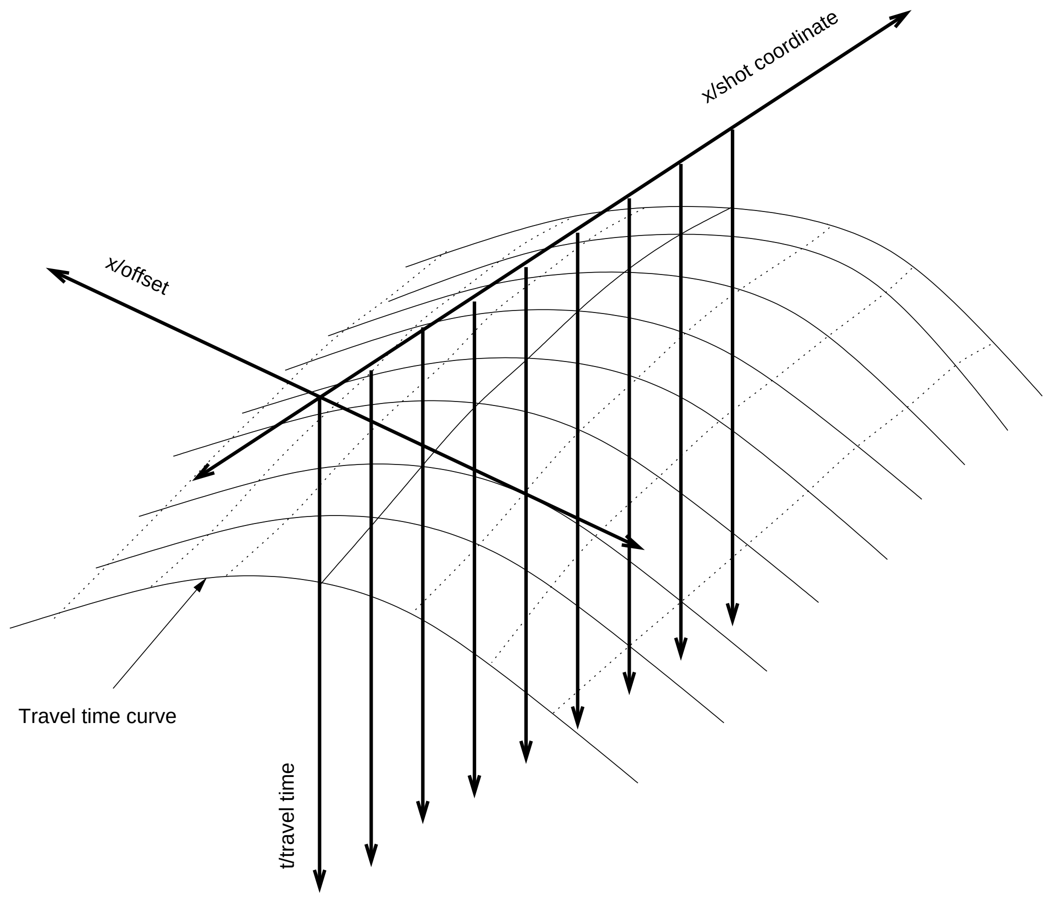

Figure 5.21. A 3-D view of a number of travel time curves. They can be seen to make a 'travel time surface'.

Layer	$(v_p)/(m/s)$	$(v_s)/(m/s)$	Thickness/m
Layer 1	1800	640	1200
Layer 2	1900	790	200
Layer 3	2000	950	90
Layer 4	2100	1050	50
Layer 5	2200	1100	60
Layer 6	2300	1210	200

Table 5.1. The model parameters for the model in Figure 5.22.

5.4.3 Which P-SV event to pick?

This remains the fundamental question in converted wave data processing. Nearly all schemes rely on event correlation to derive γ values for velocity analysis and migration (MacLeod *et al.*, 1999; Mancini *et al.*, 2003). The event correlation is subjective; it would be better to have some measure of the correlation between P-P and P-SV events. I use a method proposed by Li that uses travel time inversion to assist the event correlation. Once a P-P event has been selected and the inversion run I have the location of the subsurface interface, and values for the P-wave interval velocity. The next thing to do is to select a small number of P-SV events, say three or four, that are candidates for a match. By a match I mean that the interface at which the P-SV mode conversion takes place is the same interface that the 'matching' P-wave is reflected from. To invert the P-SV data, only the P-wave velocity from the first inversion is used, the P-SV inversion finds the S-wave velocity and a new interface location that together best match the P-SV travel time curve. The match is made when the interfaces from the P-P and P-SV inversion share the same geometry in space (ie same depth, dip and curvature). Li has developed an inversion scheme, especially for the following application. The output is two depth models, one from the P-P data, and one from the P-wave velocity and the P-SV data. I show a synthetic example below;

I consider a set of closley spaced plane horizontal layers for analysis and the aim of the experiment is to see if the travel time inversion can correctly identify the P-SV reflection event that originated from the same interface as a P-P reflection event. If I match all the reflectors correctly, then the correct model is returned from the inversion. It is

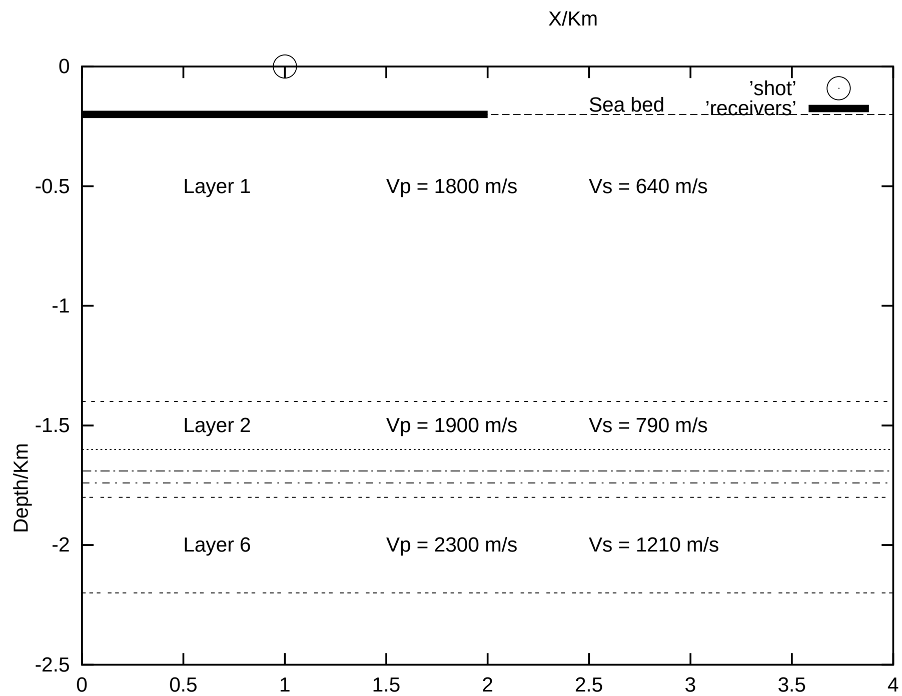

Figure 5.22. A number of closely spaced plane horizontal layers this is the model through which I performed P-P and P-SV ray tracing

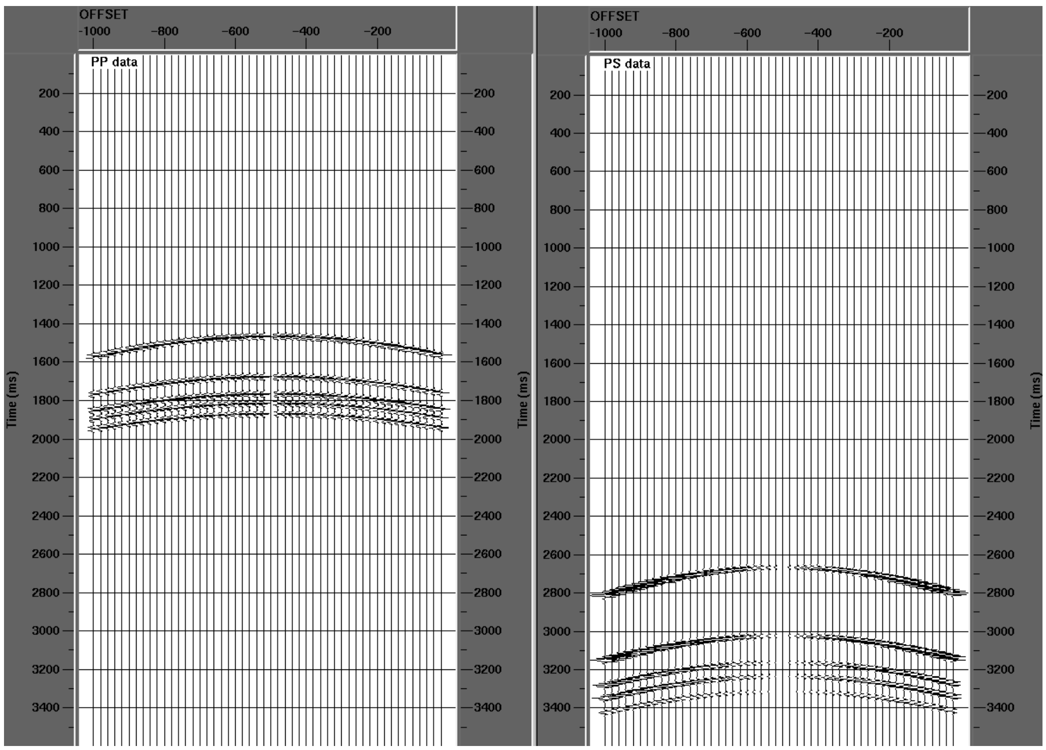

Figure 5.23. Two shot gathers from the model in Figure 5.22. On the left, P-P data and on the right P-SV data. These were generated using the ray tracing package, seis88 (Cerveny & Psencik, 1988).

Matched with P reflection 3	$(v_p)/(m/s)$	$(v_s)/(m/s)$	γ	$\Delta z/m$
S reflection 2	1926	950	2.02	50
S reflection 3	**1926**	**803**	**2.39**	**2**
S reflection 4	1926	770	2.50	30
S reflection 5	1926	660	2.91	40

Table 5.2. P-wave and S-wave velocites from inversion of matched and mis-matched P-P and PSV reflection travel time curves 5.22.

perhaps more interesting, though, to look at what happens when an incorrect match is made between P-P and P-SV reflection events. I run the inversion four times, pairing a P-P reflection event with a different one of four P-SV events originating from the stack of layers shown in Figure 5.22. I run the inversion assuming that there are two layers in the model. This requires four travel times as an input, the P-P and the P-SV travel time curves for each of the two interfaces. For the first interface the travel time curves from P-P and P-SV events are correctly matched. For the second interface I use the P-P reflection from the third interface. The P-SV travel time curve used for the second layer changes with each run of the experiment. I use in turn the second, third, fourth and fifth travel time curve from the P-SV data. This way I will be able to see if the interfaces returned from the inversion can be used to identify the P-SV reflection that originated from the same interface as the P-P reflection being analysed with it from a number of closley spaced canditate reflections.

The results of the inversion are displayed all together in Figure 5.24 and in Table 5.2. The returned interface from the four P-SV inversions are close to the location of the interface derived from the P-P data. The best matching interface is indeed returned from inverting the correctly matched travel time curves. The difference in depth between the segments returned from the incorrect matches at $x = 0$ are 50, 30 and 40m respectivley when matching the 2nd, 4th and 5th interfaces. A difference of 40m at this depth is equivalent to a 3% error in the depth location of the interface, which is not very large. This compares with a depth difference of only 2m (0.1%) at $x = 0$ for the correctly matched travel time curve pair. This is only a simple plane layered model, but the results are very encouraging.

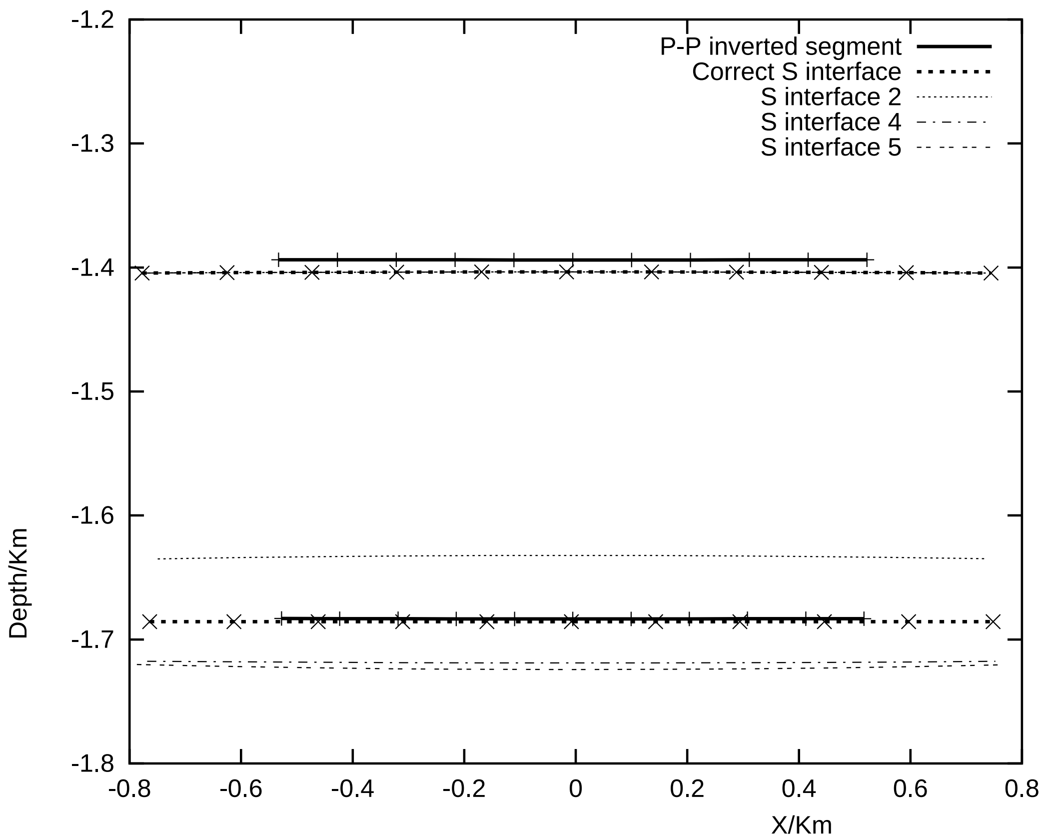

Figure 5.24. The results of the experiment described above. I have inverted four travel time curves, two P-P and two P-SV, apparently from two reflectors. I run the inversion four times, each time with a different travel time for the second P-SV reflector. This second P-SV travel time curve does not necessarily originate from the same interface as the second P-P travel time curve. Notice that only when events are paired correctly can the travel time curve be inverted to generate a co-located interface in depth. The interface geometry for the correct match is shown by the heavy black lines (P-P interface) and the heavy dashed line with the crosses (P-S interface).

5.5 Conclusions

Parameterising travel time curves in pre-stack gathers is not a trivial task. With care it is possible to derive P-P and P-SV travel time curves from real and synthetic data that can be inverted to give good results. I have shown, by comparing travel time curves derived using my methods with those generated by ray tracing, that when the travel time can be parameterised with a cubic polynomial I can retrieve the layer parameters with a great degree of accuracy. For an approximately layered earth both P-P and P-SV travel time curves are well fitted using a cubic polynomial. Initial investigations attempted to use semblance as a tool in parameterising the curves. I found that problems with event identification and visualising the four dimentional data space required of a cubic polynomial were more trouble than they were worth and so discarded semblance based picking. The preferred method of picking involves calculating the best fit parameters of t_0, a, b and c from manual picks on the data. The suppression of noise on the signal will always be an issue for picking on pre-stack data, we may find that using stacked sections as a guide will help in low signal to noise areas. When working on real data I have found that it is useful to pick the travel time curves on a number of neighbouring gathers. A better aproach would involve the effects of source location and the fitting of a surface to the travel time data.

Tests on a simple plane-layered model show that travel time inversion can help discard incorrect P-P to P-SV reflection event matches. The inverted geometry is the criteria for a match, we are working with measurable quantities in the same domain, this avoids event correlation between two incompatible P-P and P-SV time sections. Where more than one travel time curve shows the same degree of similarity between inverted interfaces and a realistic velocity ratio for the interval, the effect on velocity model building of selecting the wrong event will be small.

Chapter 6

Processing Synthetic Data

The inversion is a ray based inversion method, and up to now I have tested the method only using synthetic data generated by ray tracing. In this chapter I apply my processing methodology to P-P and P-SV data from a 2-D wave theoretical synthetic dataset generated using finite difference code. I also develop a method for joining up the results from many inversions to build a 'survey wide' velocity model out of a number of local inversion results.

6.1 Data

Two-dimensional synthetic seismic data have been generated by Taylor (2002) using the finite difference code GRIM obtained from Hamburg University. The boundary conditions have been modified by Taylor to reduce the error build-up in the corners of the grid.

The model geometry and layer velocities are shown in Figure 6.1. Receivers are on the sea floor $200m$ below the sources which are at $0m$. The model has four interfaces below the sea bottom; all but the third are curved. Each layer below the sea floor is

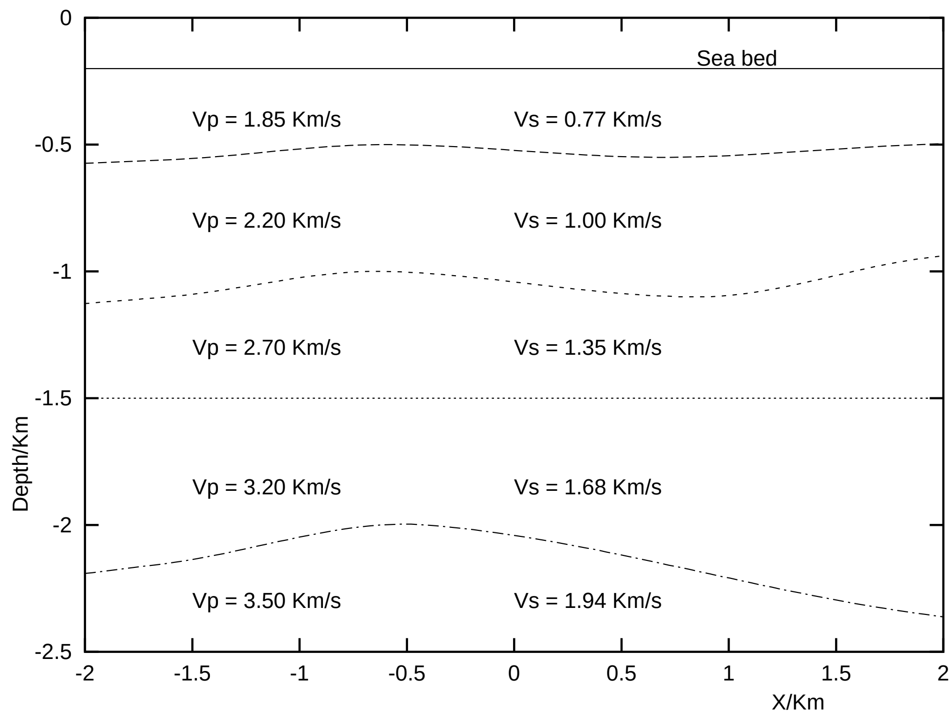

Figure 6.1. The model used for generating the synthetics data.

homogeneous and isotropic and has both P and S-wave velocites defined. The density ρ for a layer is calculated using the relationship $\rho = 1.7 + (0.2v_p)$, this relationship is taken from Cerveny & Psencik (1988) and gives physically plausible values for the density (ρ) in g/cc when v_p is in km/sec, it is not a real physical relationship. Despite absorbing boundary conditions, Taylor found that the small reflections generated from the sides of the model grid appeared in the region of interest in the seismograms with an amplitude similar to some of the weaker reflections from the model. He avoids this problem by brute force- by extending the model by 3km on each side. The sea surface has absorbing boundary conditions also, so there are no sea-surface multiples in the model, but all the other inter-bed multiples and mode conversions are present.

Vertical, and inline horizontal particle velocity and pressure data were generated. Because of the relatively high velocity of the first layer, the up coming ray paths' emergence angles are significant and hence energy from P-P and P-SV reflections within the model appear on both vertical and horizontal components. Typical seismograms from two components of motion are shown in Figure 6.2. The one on the left is the

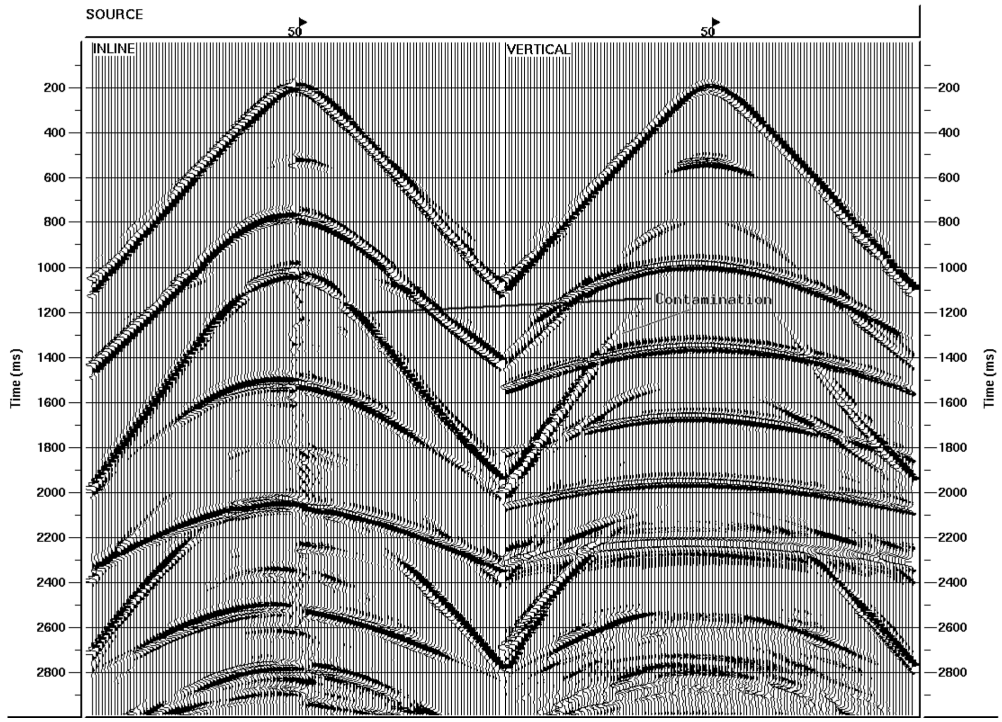

Figure 6.2. Seismograms for horizontal (v_x) and vertical (v_z) particle velocity, displayed after AGC with a 500ms time gate.

horizontal inline particle velocity and on the right the vertical particle velocity. Both P-P and P-SV reflections are evident on both gathers, although the horizontal component shows more energetic P-SV reflections, and the vertical component is dominated by P-P mode reflections. Both gathers also show an event with very linear moveout which apears with a zero offset time of about $1080ms$ and then again at $2090ms$, maked as 'Contamination' in Figure 6.2. The particle motion for this event is consistent with it being an S-wave on the upcoming leg, and the moveout is consistent with an event which has travelled more slowly than the P-SV converted waves. I think it can only be the direct wave which has undergone mode conversion to an S-wave at the sea bed. This S-wave has then been reflected normally at the first and second interfaces, and for the first reflector the zero offset travel times are consistent with this. I illustrate the suggested ray path in Figure 6.3.

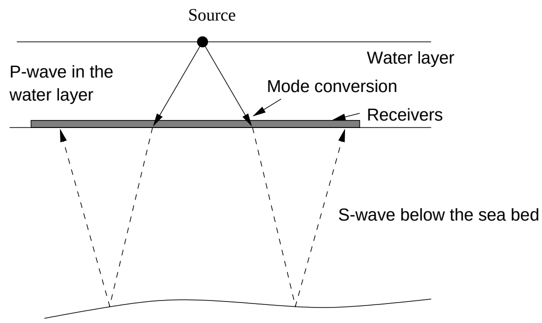

Figure 6.3. Suggested ray path for the contamination event mentioned in the text.

6.1.1 Pre-processing

Ideally I would like to separate the modes and work with two separate sections, one with only P-P reflections present and the other with only P-SV reflections. I looked into some published algorithms for separating modes in 2D and found that they were often somewhat restricted in their application. Dankbaar (1985) developed a method which requires the data to be recorded on a stress-free surface, and Amundsen & Reitan (1995) have a method which is designed for sea floor data recorded over a horizontally stratified medium. I use a pragmatic aproach to the problem. As the picking scheme I use is very much manually controlled, I can cope with a certain degree of contamination when picking events, as long as I know which events are which. For further processing after the picking, it would be advantageous to have 'clean' data. As I only have access to a P-wave migration code then I need only 'clean up' the vertical component data. To do this I remove the converted waves as if they were multiples. First I apply NMO to flatten the P-wave events in CMP gathers. In the moveout corrected gathers the P-SV events are under corrected and hence are not flat, and can then be filtered out in F-K space. Once filtered, the data are then transformed back into the time-space domain and the NMO correction is removed. The data before and after this processing are shown in Figure 6.4.

The only pre-processing I apply to the horizontal component data is to reverse the polarity of the negative offsets; that way the polarity flip across zero-offset is removed and a reflection event is characterised by either a trough or a peak across both positive

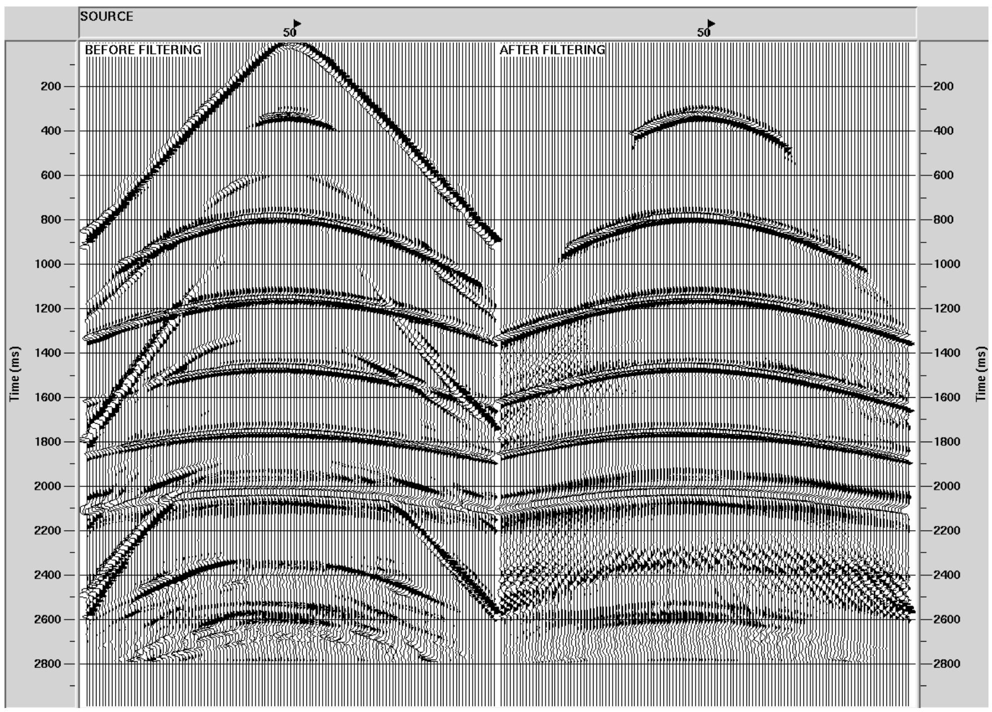

Figure 6.4. Seismograms for Vz, the left hand gather has had only a static correction applied, the right hand gather is the same as the left after NMO, an FK filter and inverse NMO correction applied.

and negative offsets. This makes picking using the 'snap to' function much easier. I also apply a static shift to both P-P and P-SV datasets, 133.3ms to account for the water depth between the source and receivers, and 66.6ms to remove a time lag introduced in the modeling code. The correct way to account for the effect of water layer is using downward continuation to move the sources from the sea surface to the sea floor. I did this, but found that I could not tune the parameters well enough to perform the operation without introducing unwelcome noise into the data. Figure 6.5 shows two gathers, they are from the same shot, the one on the left has had the downward continuation applied and the one on the right has had the static correction applied. I compared the travel time curves from the data after downward continuation with those from the data after taking acount for the sea water layer with a static correction and found that the difference was sufficiently small as to be neglected. I opted therefore to use to the data with the static correction as it is cleaner. Figure 6.6 shows two shot gathers from both P-P and P-SV datasets after all the pre-processing, with picks made on the primary reflection events.

Because the data are free from random noise, I can pick the travel times in only one gather as there is no need to suppress random noise during the travel time curve determination. I make picks approximately every ten shot points and invert the travel time curves.

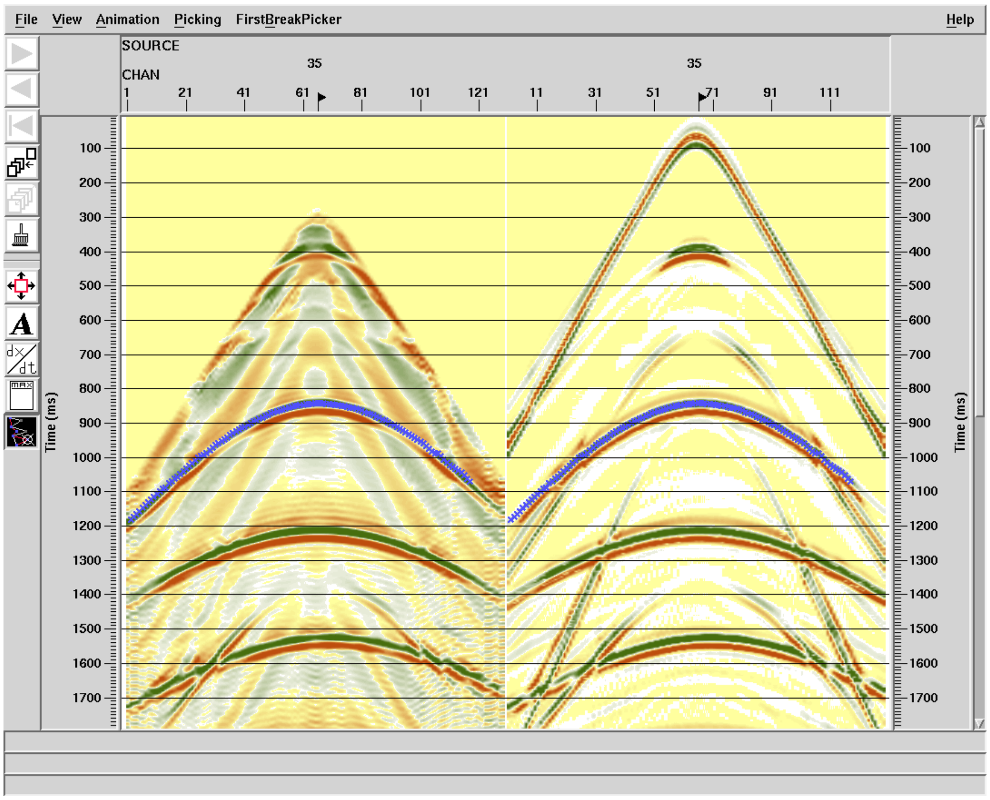

Figure 6.5. The data in the gather on the left have had the source moved to the sea floor using wave equation datuming. I have applied a static shift to the data on the right. The picked points in blue have been picked on the left hand gather and projected onto the righthand gather, note that the travel time curves in the data are apparently the same.

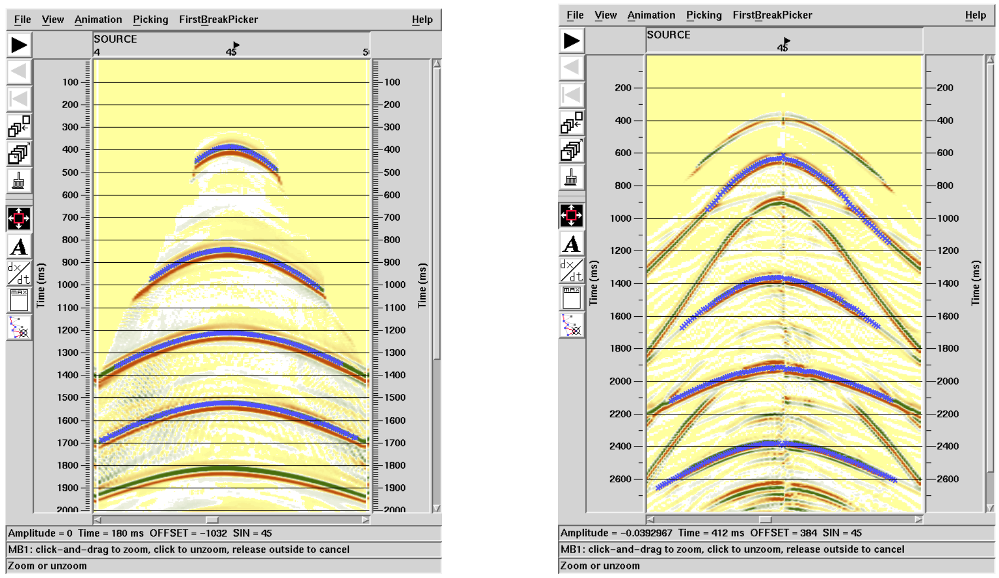

Figure 6.6. Picking of P-P and P-SV reflection events in a common shot gather. The P-P picking on the 'cleaned up' vertical geophone data are displayed on the left. The P-SV picking on the inline horizontal component data is shown on the right.

6.1.2 Defining interfaces from P-P and P-SV inversions

I show in Figures 6.7 and 6.8 how I combine the segments of interface from a number of inversions to give a single interface. First, I resample all the segments on a number of equally spaced vertical lines. There may be more than one segment defining an interface which intersect the same vertical line, suggesting that the interface is defined in two different locations at once. If this is the case an interface is defined at more than one depth on the line, I take an average value of the segments to define the position of the interface at that x location. If there are an odd number of segments crossing one vertical line I select the depth of the Median interface. If there are an even number of segments crossing the vertical line then I take the Mean depth of the two segments closest to the median. The points that are defined in this way can then be joined with either straight lines or a spline function to define the interface location across the whole extent of the velocity model.

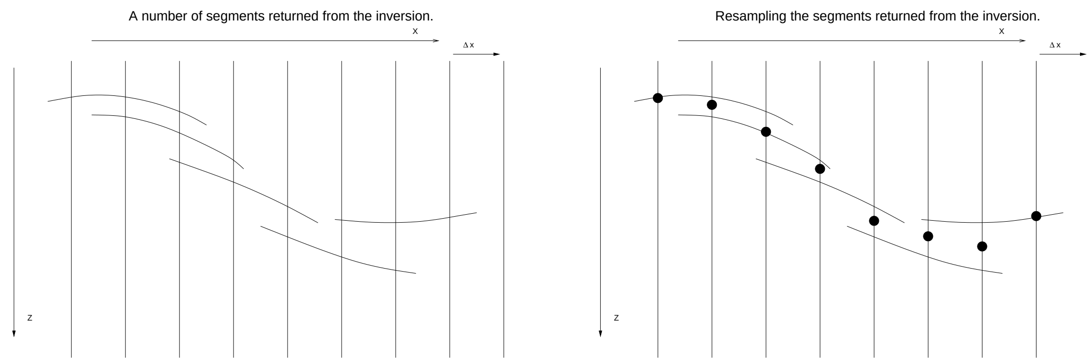

(a) (b)

Figure 6.7. (a) Shows the original segments, (b) shows the points derived from resampling the segments in (a).

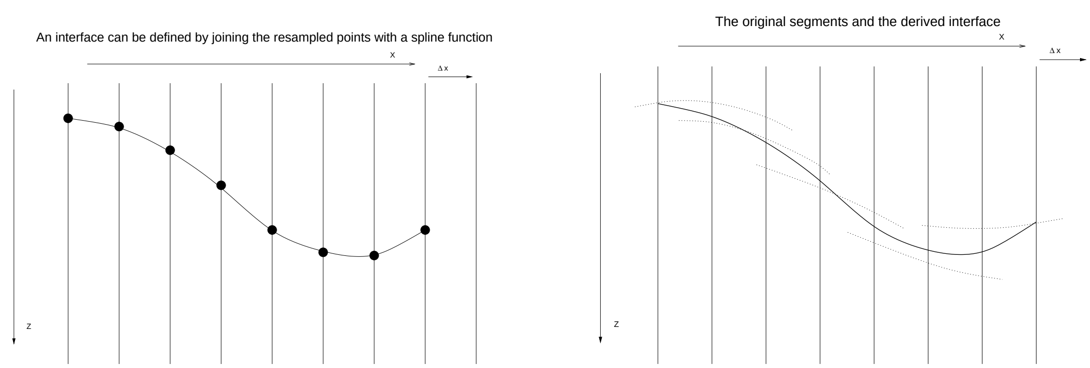

(a) (b)

Figure 6.8. (a) Shows the interface defined by the re-sampled points and (b) shows this interface alongside the original segments.

Shot	%error in velocity layer 1	% error in velocity layer 2	% error in velocity layer 3	% error in velocity layer 4
3	4.9	2.27	1.5	6.8
12	3.2	5.45	0.37	4.68
22	0.54	6.36	2.96	8.12
32	1.62	13.18	3.33	10.31
42	1.62	8.18	1.11	10.31
52	4.32	3.63	0.0	9.37
62	4.86	2.72	0.74	6.87
72	7.02	5.90	2.96	8.43
82	6.48	0.91	1.11	2.18
92	5.9	4.54	0.0	0.312
102	3.2	9.09	0.74	1.87
112	5.4	5.45	0.74	3.43
123	5.9	0.45	3.33	4.06
	Average RMS error **4.24 %**	Average RMS error **5.24%**	Average RMS error **1.45%**	Average RMS error **5.91%**

Table 6.1. A table showing the magnitude of P-wave velocity errors at thirteen locations over the model

Shot	%error in velocity layer 1	% error in velocity layer 2	% error in velocity layer 3	% error in velocity layer 4
3	6.75	1.0	5.18	11.9
12	1.35	6.0	1.48	11.3
22	4.05	5.0	2.22	2.38
32	1.35	14.0	2.22	8.33
42	4.05	11.0	0.74	11.3
52	1.35	6.0	0.74	10.7
62	1.35	1.0	0.74	8.92
72	6.75	7.0	4.44	4.76
82	5.40	4.0	3.70	5.95
92	4.05	10.0	0.0	0.59
102	2.70	11.0	0.74	1.19
112	4.05	8.0	5.18	0.59
123	4.05	9.0	2.22	2.97
	Average RMS error **3.64 %**	Average RMS error **7.15%**	Average RMS error **2.28%**	Average RMS error **6.23%**

Table 6.2. A table showing the magnitude of S-wave velocity errors at thirteen locations over the model

6.2 Results

I ran 13 inversions using both P-P and P-SV travel times. At each point first the P-P data where inverted to give both local P-wave velocity and interface geometry. The P-SV inversion was then run using the P-SV travel time curves and the P-wave velocity from the P-P inversion at that shot location. The P-SV inversion returns the local S-wave velocity and interface geometry. The results of the inversion are shown in Tables 6.1 to 6.3 and Figures 6.9 to 6.17.

	Layer 1	Layer 2	Layer 3	Layer 4
	Mean	Mean	Mean	Mean
Vp	$1.93km/s$ **4.24%**	$2.21km/s$ **0.35%**	$2.71km/s$ **0.31%**	$3.10km/s$ **-3.03%**
Vs	$0.75km/s$ **1.90%**	$1.02km/s$ **1.62%**	$1.33km/s$ **-1.48%**	$1.63km/s$ **-2.84%**
	Median	Median	Median	Median
Vp	$1.94km/s$ **4.86%**	$2.25km/s$ **2.27%**	$2.70km/s$ **0.00%**	$3.05km/s$ **-4.68%**
Vs	$0.76km/s$ **2.70%**	$1.04km/s$ **4.00%**	$1.34km/s$ **-0.74%**	$1.64km/s$ **-2.38%**

Table 6.3. A table showing the percentage error of the mean and median velocities for each layer.

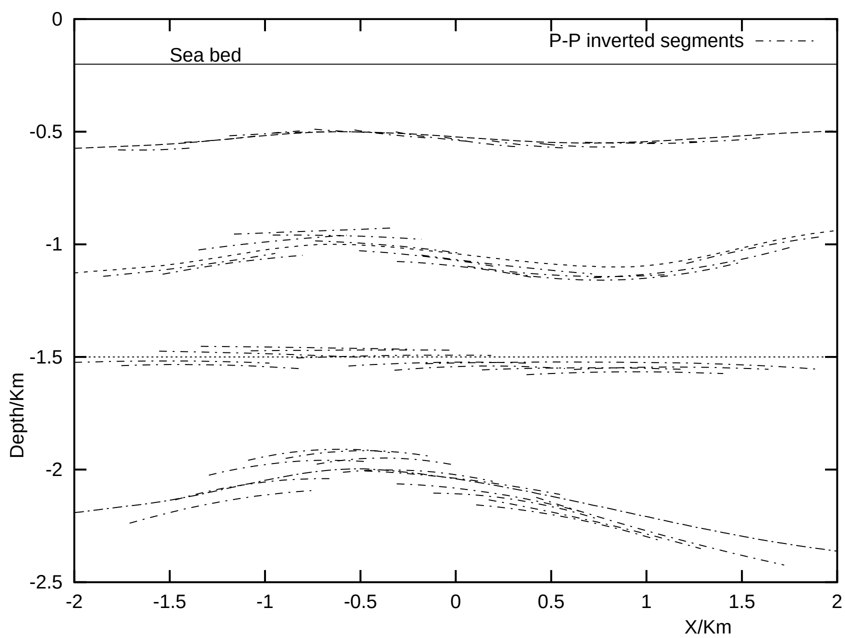

Figure 6.9. The inverted reflector segments from P-wave data

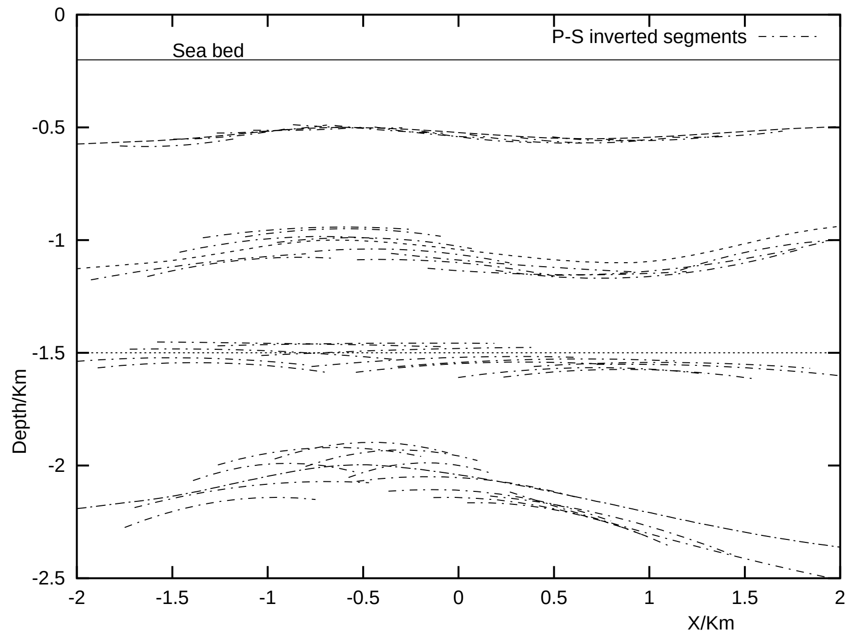

Figure 6.10. The inverted reflector segments from the inversion of P-SV travel time data, only the P-wave velocities are passed to the inversion, no interface information is passed accross

I re-sample the segments from the P-P and P-SV inversions, seen in Figures 6.9 and 6.10, on a series of equally spaced vertical lines using the method discussed in Section 6.1.2. This reduces the 13 segments into a single interface. It also allows us to compare the interfaces in the earth models obtained from the P-P and P-SV inversions, and check for the correct event matching, based on the interface geometry.

The interfaces produced by the re-sampling of both the P-P and P-SV inverted segments are shown in Figures 6.11 and 6.12. Figure 6.11 shows the points that come from the resampling routine, and Figure 6.12 shows these points joined up with straight lines to define the interfaces from both the P-P and P-SV inversions at all points in space. P-P and P-SV interface data are shown on both diagrams. A good match between the P-P and P-SV interfaces is seen. There is still evidence of a systematic error in inverted interface depth related to the interface curvature in the model.

An obvious question arises here: Could the results be improved if more locations were analysed? In order to see how the interface definition is changed when using a different

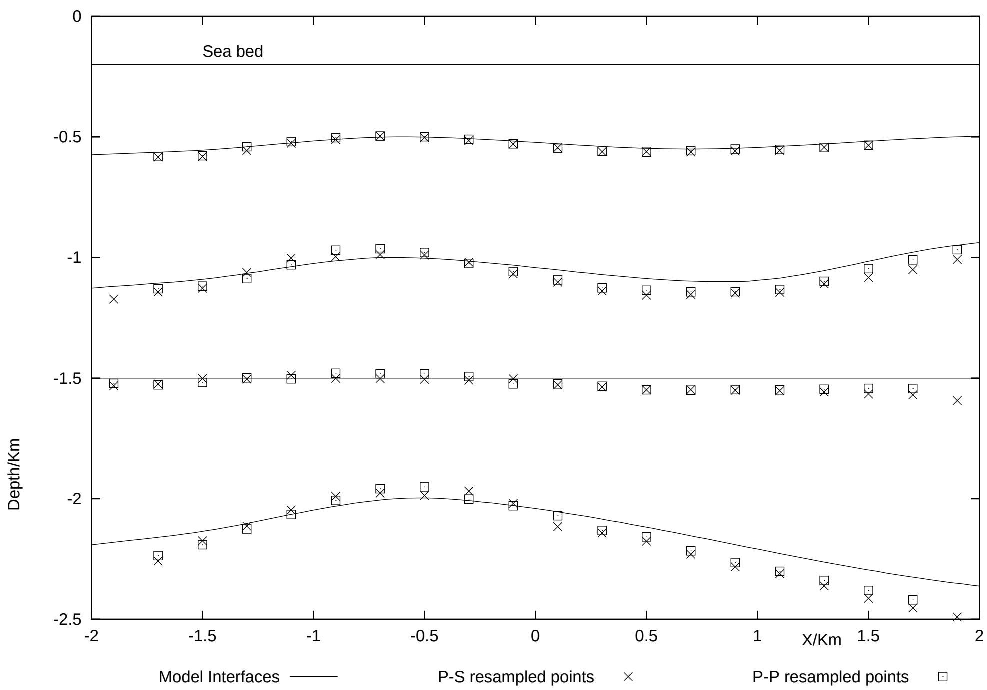

Figure 6.11. The inverted reflector segments after re-sampling, both P-P and P-SV data are shown alongside the real model.

number of the inverted segments, I have reduced the data set and run the re-sampling code again, first with half the segments present, and second with one segment in every three retained. I plot the results in Figure 6.13. The difference in the re-sampled interfaces is not really very big, and I could probably use any of the reduced datasets and still have a good model. I will however continue to use the all the interface segment data that I have generated.

Tables 6.1 and 6.2 show the magnitude of errors in the velocity returned by the inverson compared with those used in the modelling. The highest error for any layer velocity is 14%. Figures for either mean or median velocity for each layer are much closer to the true velocity in the model. The interfaces returned by the inversion are plotted in Figures 6.9 and 6.10. The most striking thing about these two figures is the systematic error in interface determination related to the curvature of the interface. The inversion is still not able fully to de-couple the effects of velocity from the influence of interface curvature. This may be an effect caused by starting with a model derived from the

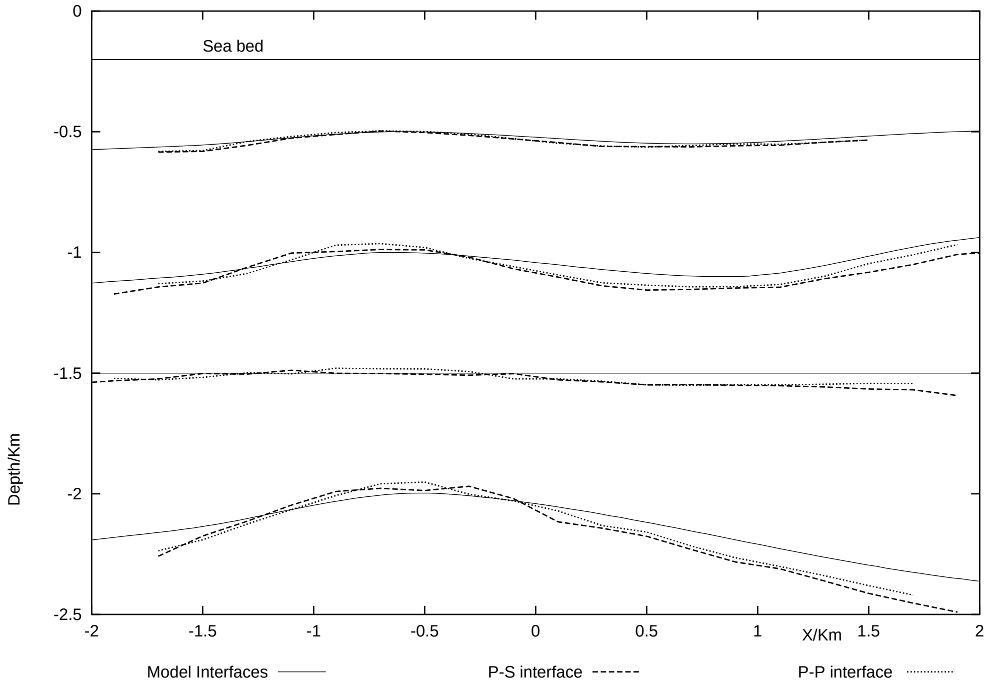

Figure 6.12. P-P and P-SV inverted reflector segments after resampling to reduce the thirteen segments to define one interface.

plane layered inversion. Velocities derived using the plane layered inversion are highly affected by layer curvature (See Chapter 4).

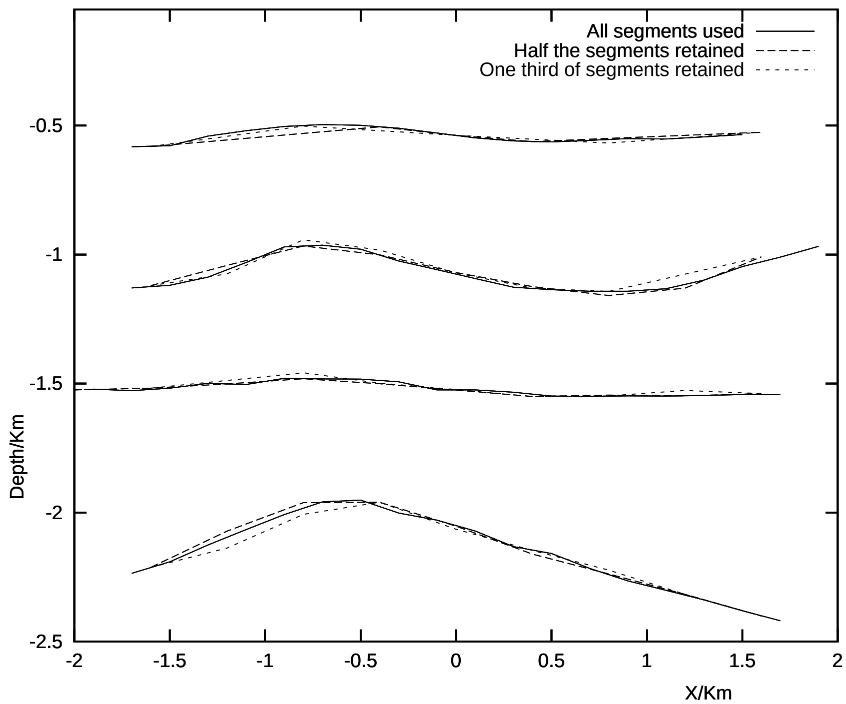

Figure 6.13. The inverted reflector segments from the P-P inversion after re-sampling. In this example interfaces are generated by applying the same resampling to different sub-sets of the data. The first sub-set of the data has every other segment removed from the dataset, the next has two in every three segments removed. I also include the version which uses the complete dataset.

6.3 Migration of the P-P data

The following section of this chapter concentrates only on the P-P data and the P-wave velocity model. I cannot migrate the P-SV data and so do not procede any further down the desired processing flow, which would involve the migration of the converted wave data using the P- and S-wave velocity models. I use the P-P interfaces shown in Figure 6.12 and the mean P-wave velocities shown in Table 6.3 as the initial velocity model for Kirkhhoff pre-stack depth migration of the filtered P-wave data. A stack and some image gathers are shown in Figures 6.14 and 6.15.

The interfaces seen on the migrated stack, shown in Figure 6.14, have been picked and are plotted on the same scale as the model interfaces in Figure 6.16. Notice how even without having precisely the same velocity model the migration returns the interfaces with remarkable accuracy, but in a different spatial location to the interface derived using the inversion . The migration result therefore shows that the inverted velocity model is not completly consistent with the data. This ability to validate the velocity model is one of the very useful properties of depth migration. The image gathers in Figure 6.15 show well flattened events, indicating that the velocity model is accurate. Some diffraction artifacts can be seen in the image gathers. It would be desirable to move the positions of the interfaces in the depth model so that they match the position of the interfaces in the migrated image in Figure 6.14. If this were done then the velocity model would be almost indistinguishable from the real model and the velocity model update - PSDM iteration can be stopped, in this case after only one update.

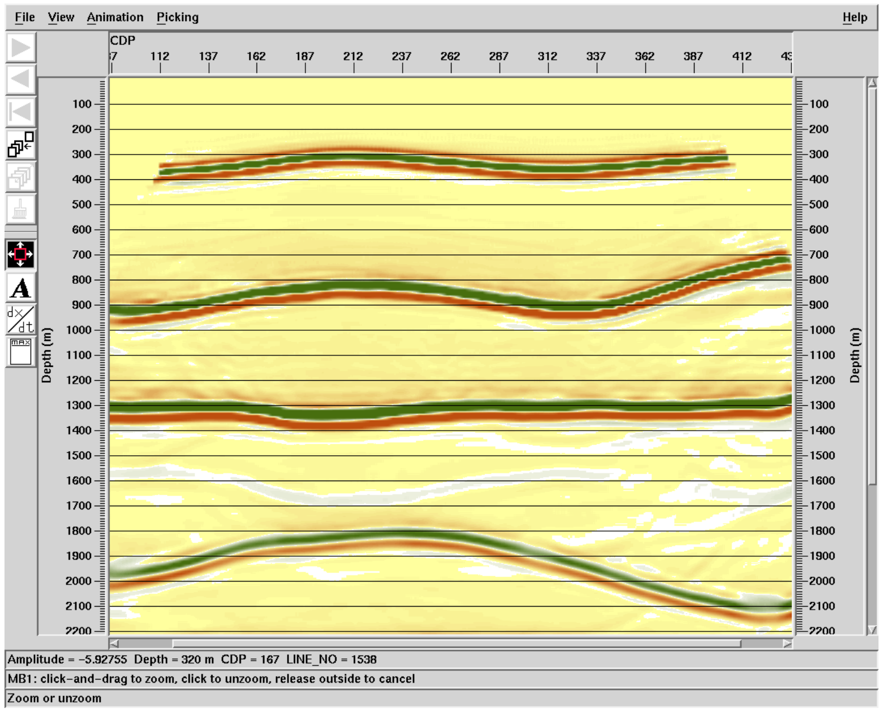

Figure 6.14. The stack after migration with the velocity field generated using the P-wave interfaces in Figure 6.12 and the mean P-wave velocites.

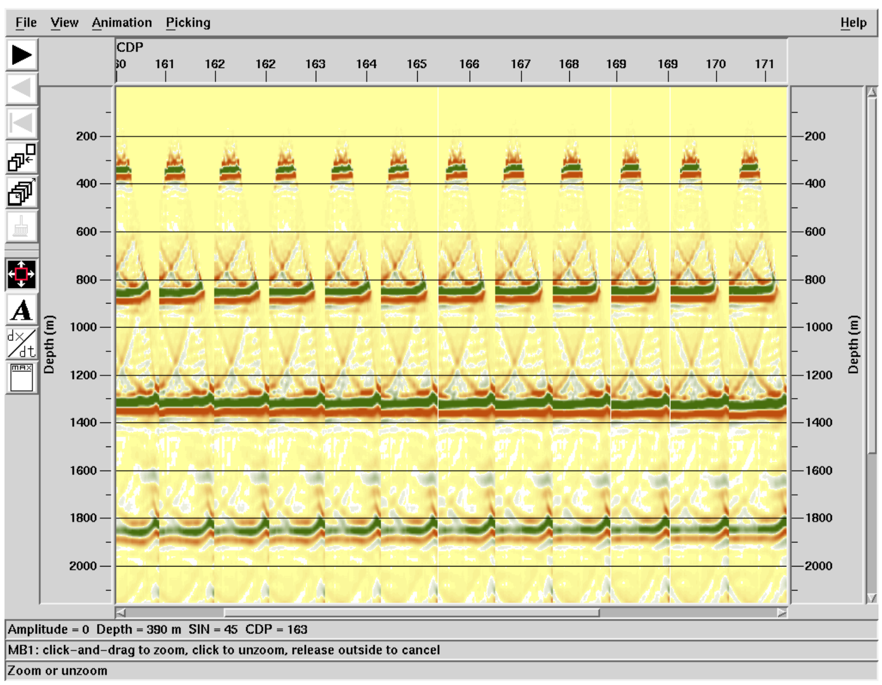

Figure 6.15. A number of Common Image Gathers from the same migrated data shown in Figure 6.14

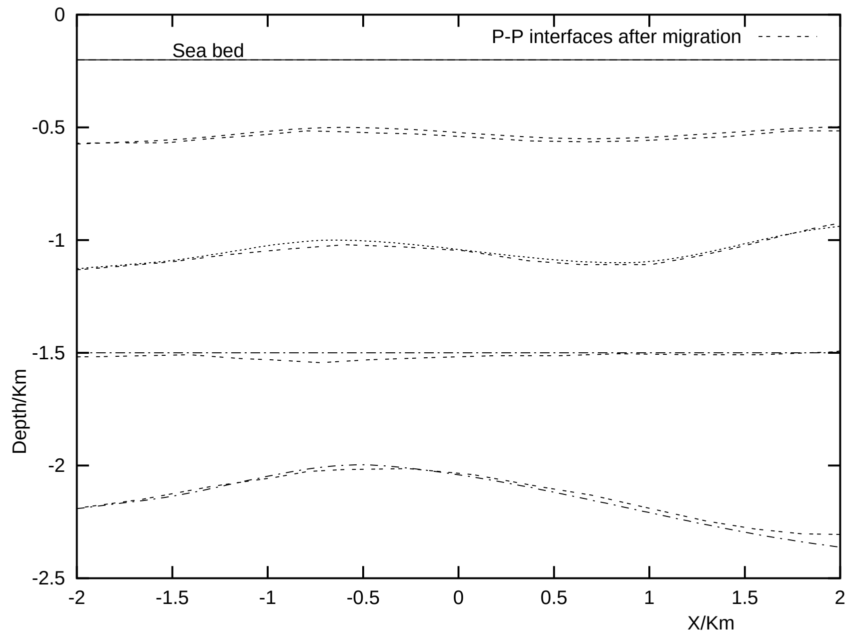

Figure 6.16. The reflectors after migration with the velocity field generated using the P-wave interfaces in Figure 6.12 and the average of all the inverted velocites

6.4 Conclusions

Looking at Figures 6.11 and 6.12 a good match between the interfaces derived from the P-P and P-SV data is seen. It is interesting to note that the interfaces match each other better than either match the true interfaces in the model. We can see in Figures 6.9 and 6.10, which show the segments returned by the inversions, that the the inversion results are still affected by the presence of curvature on the interface in the same way as the plane layer inversion seen in Chapter 4.

The velocites are found to be generally good, with the average error for the velocity returned by an inversion not exceeding 7.2% for a layer. The tabulated values for velocity returned by the inversion in Tables 6.1 and 6.2 show some locally high errors. Using model building methods which reduce the effects of these outliers, such as taking median values for interfaces and velocities, can help reduce their effect (Claerbout & Muir, 1973), see Table 6.3. However, this is only possible here because I already know that each layer is homogeneous and isotropic.

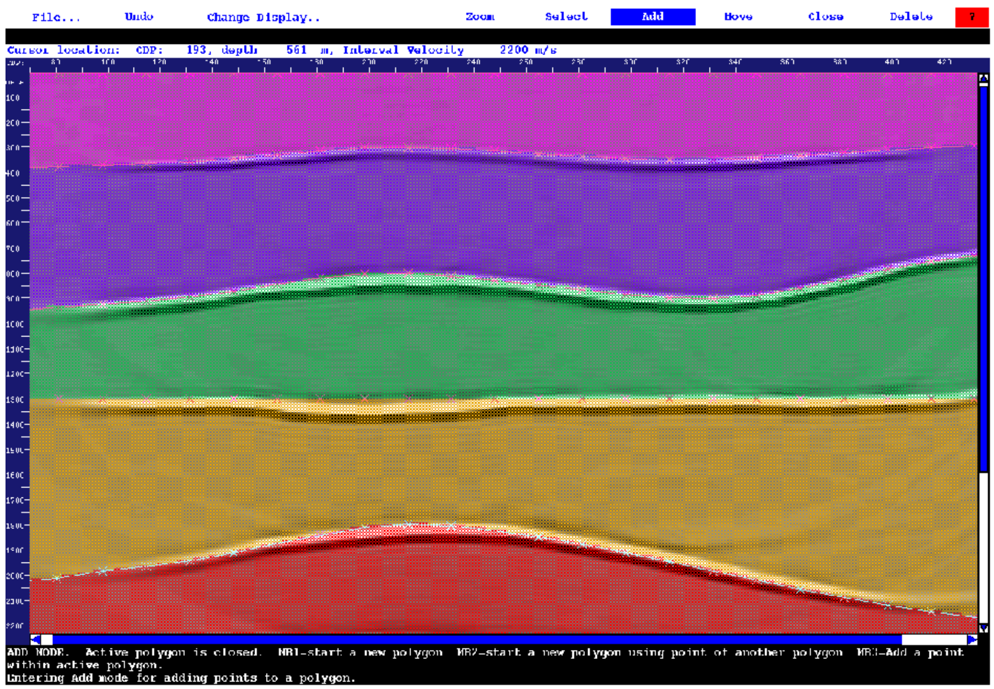

Figure 6.17. The migrated stack is shown as black and white seismic data, it is overlayed on a colour image of the velocity model used in the finite difference modeling. The different colours in the model background are because of the different velocities in each layer, and an interface exist where the colours change. Notice how the interfaces in the seismic data lie almost on top of the interfaces used in the forward modelling.

Having defined the interfaces, I use the median value of the velocity in each layer to define the velocity model for depth migration. The P-P migrated image is really quite good; the interface locations plotted in Figures 6.16 and 6.17 are almost indistinguishable from those in the true model.

The errors in the interface segments may be caused by three things: the starting model being incorrect, the problem of de-coupling the effects of layer curvature from a change in velocity of the layer, and incorrect travel time curve parameterisation. The starting model for the curved layer inversion is the plane dipping layer inversion and so the initial model used in the iteration will be faster than the true velocity over a concave interface and slower over a convex interface. The current inversion scheme does not get to the exact model from the starting point given by the plane layer inversion. In this particular example the results after taking averages are good because there is roughly the same amount of curvature in both the concave and convex sense. From an inversion point of view the problem we have is one common to almost all inversion schemes; an inability to locate the global minimum. We find a solution close to the real solution and the curved layer inversion is definitely a huge improvement over the plane layer inversion alone, but not, as we can see from the results presented in this chapter, the true solution. The travel time curves in this dataset are well parameterised by a cubic equation in x. I don't think that a large proportion of the errors arises from incorrect travel time curve parameterisation.

There is a possible solution to this problem. As the travel time curves in our simple models are affected both by velocity and reflector geometry, we must find a way of de-coupling the effects of reflector geometry from interval velocity. To do this we propose the use of a rather brute force method where a large number of inversions are run with a fixed velocity (within a range of probable solutions) after each inversion a number of diagnostic values are saved, such as the residual between the modelled and true travel time curves. Once a large number of inversions are run, the function described by, say, the travel time residuals can be examined and the minimum value selected. This way we test a large number of values of velocity and do not risk getting stuck in a local minimum. The inversion for interface geometry when the layer velocity is fixed is very robust, so I expect this method to be suitable for use on real data.

Chapter 7

Processing real data using travel time inversion and PSDM

Up till now all the tests using the picking, inversion and model building have been applied to synthetic data of one sort or another. In this chapter I show the application of our methodology to the real dataset that was first introduced in Chapter 3.

The inline horizontal component suffers badly from a receiver statics problem, caused by a thin layer of low S-wave velocity near the sea bed. I had hoped that the inversion would be re-cast in the common-receiver domain and work on travel time curves picked in common-receiver gathers. This I anticipated would avoiding having to find a receiver-statics solution for the P-SV data. Because of this I processed only the P-P data to start with, which does not suffer from the same statics problem, and travel time curves picked in common-shot gathers can be inverted with confidence . When it became apparent that the inversion would not be re-cast into the common-receiver domain I set about finding a solution to the problem of the static shifts in the inline-horizontal component data. This then allowed me to proceed with the joint inversion of P-P and P-SV data using the inversion of travel time curves picked in common-shot gathers.

Because of these two different attempts at processing real data the chapter is split into two parts:

- In the first part I build only a P-wave velocity model. I use a slightly modified velocity model building method to construct a velocity model down to a depth of 2400m. I refine the velocity model using MVA in an atempt to overcome some of the limitations imposed by the assumptions in the inversion.

- In the second part I show the application of the joint inversion scheme to both P-P and P-SV parts of the data set. The event matching between pre-stack P-P and P-SV reflection events is performed in depth and guided by travel time inversion. This method is stable for the first three selected reflection interfaces, up to a depth of 1400m.

The quality of a depth migration can be judged by flatness in the final migrated image gathers. I do not have access to a converted wave pre-stack depth migration and so have not attempted to migrate the converted wave data. The results shown in this chapter show that the inversion can be used successfully to generate good initial P-wave interval velocity-depth models. The interfaces analysed appear flat in the Common Image Gathers (CIGs) after migration with a smoothed version of the velocity field.

I pick, where possible, prominent reflectors assuming that they coincide with changes in acoustic impedence, and therfore, probably, velocity. Between the picked reflections there may be other changes in velocity. The model used in the inversion assumes homogeneous isotropic materials between the interfaces, the inversion cannot cope with changes in velocity within the layers. I can reduce the errors in the P-wave velocity model caused by this using curvature of events in the migrated image gathers to guide a velocity update step. In Part 1 the final P-wave velocity model shows a low velocity zone over the crest of the structure that I speculate may be a gas induced.

7.1 PART 1: Inversion of real P-wave data

7.1.1 Method

Travel time curve picking on real data

I pick the travel time curve manually. I use the 'snap to' function in the ProMAX *interactive trace display* so that a peak, trough or zero crossing is picked. As well as calculating the coefficients of the best fit cubic to the travel time curve, I record the offset range, as this parameter is also used by the inversion. No semblance is used in this process. The raw data and the fitted curve are displayed as a quality control check to ensure that the curve is a good match to the picked data. On a more general note, any code that successfully picks events on prestack data could be used at this stage. The data would then have to be fitted with the cubic polynomial required by the plane dipping layer inversion.

7.1.2 Use of Neighbouring gathers

In an attempt to reduce the influence of random noise on the inversion I pick the travel time curves in five gathers, and fit a curve to all of these data. This means that there are always some data in common between neighbouring inversions. This is also a way of imposing a smooth solution on the models returned by the inversion. This is not the correct way to handle the data, as the changing position of the shot should be taken into account. A better method involving parameterising 3-D travel time surfaces is discussed in Chapter 5, but this has not yet been implemented.

7.1.3 Adjustments to the velocity model building

For this real data set I have modified model building techniques shown in earlier chapters. In previous tests, I have assumed the models have homogeneous isotropic layers, and so the previous model building methods allowed for averaging of velocities within the layers, either by selecting a mean or median for the layer velocity. In the real world I expect lateral velocity variation to be present, and so must use a model building technique that allows for this. In ProMAX the x-coordinate of a point in a model is referenced by CDP number. This is simply a way of knowing where a point is within the model and does not imply any knowledge of the subsurface. The velocity field database stores depth and velocity pairs, using the CDP header as the x-coordinate reference. I use each inversion result to define a one dimensional blocky velocity structure at the CDP closest to the location of the shot (see Figure 7.1). The velocity is defined at the shallowest and deepest extent of the layer. In this way the location of an interface is implied by the velocity contrast between the points that define adjacent layers. Before migration, the velocity model is smoothed using two passes of a trapezoidal filter, one in each dimension (Advance, 1995) . This should reduce the effects of migrating with a blocky velocity model in this area where a velocity gradient is more likely to characterise the change in velocity with depth. Given that the model is smoothed, the exact locations of interfaces are rather less important than if we were to use a blocky model. This is why I pay rather less attention to the interfaces returned by the inversion than in the model building method in Chapter 6. This simple model building is only really possible because of the very high sampling density in the x direction. An inversion has been performed at every shot location, that is, every 25 m. That means that the interfaces are in fact defined at each of these points and the velocity model does come over as almost blocky, with some lateral variations. This high sampling density allows me to perform smoothing to the velocity model without worrying too much about the result not resembling the input data in any way, which can happen with a sparse data set.

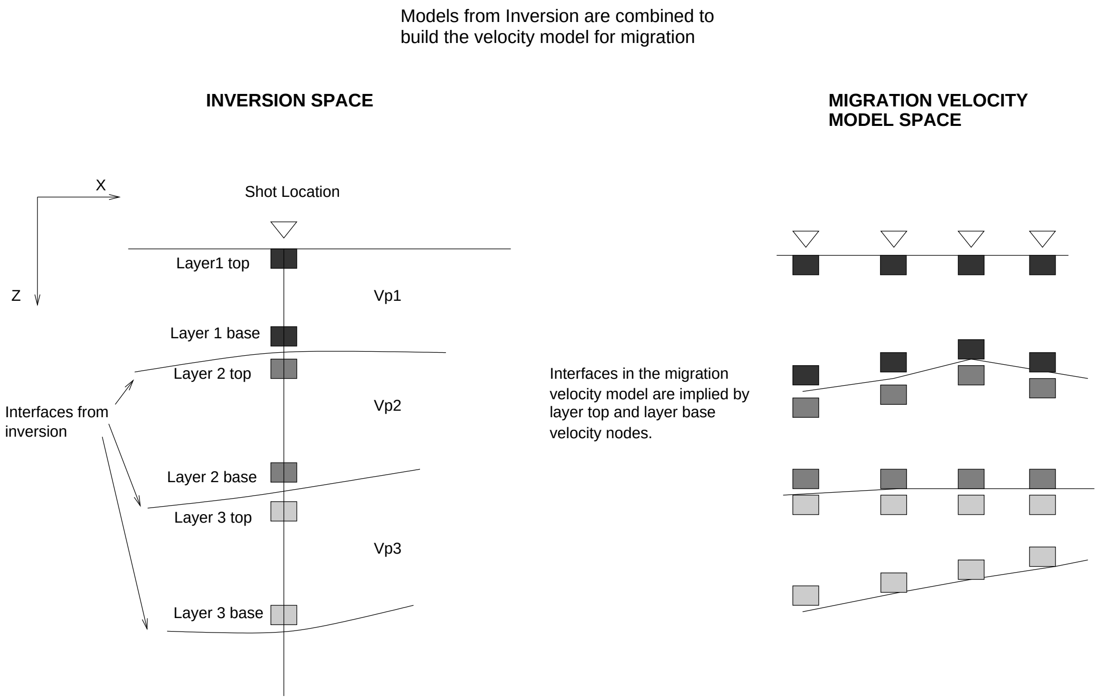

Figure 7.1. Simple velocity model building, no interface information is explicitly used as the velocity model will be smoothed prior to use.

7.1.4 Processing the P- wave data, using the inversion

The picking inversion and model building methods described in the previous chapters are applied here to the real OBC data acquired over the Guillemot field in the North Sea. There is evidence that the conversion point of the P-SV data is at the reflector, so we should be able to apply the algorithms developed for this geometry (Yuan, 2001). One of the things that indicates that the seismic energy has undergone conversion on reflection is from the source and receiver statics. In the common-shot gathers the reflection events apear wavy, see Figure 7.2. This 'wavyness' is not seen in the common-receiver gathers, the cause of this is discussed in Section 7.2.2.

The basic flow I apply is show in Figure 7.4, and a more detailed flow is shown in Figure 7.5, in Part 1 I only process the P-wave data, and so only follow the left hand side of the flow shown in Figure 7.5. It is worth noting that it can be thought of in three simple steps; picking, inversion and model building. This is very simple compared with other routes to an interval velocity in depth model. If depth modelling using

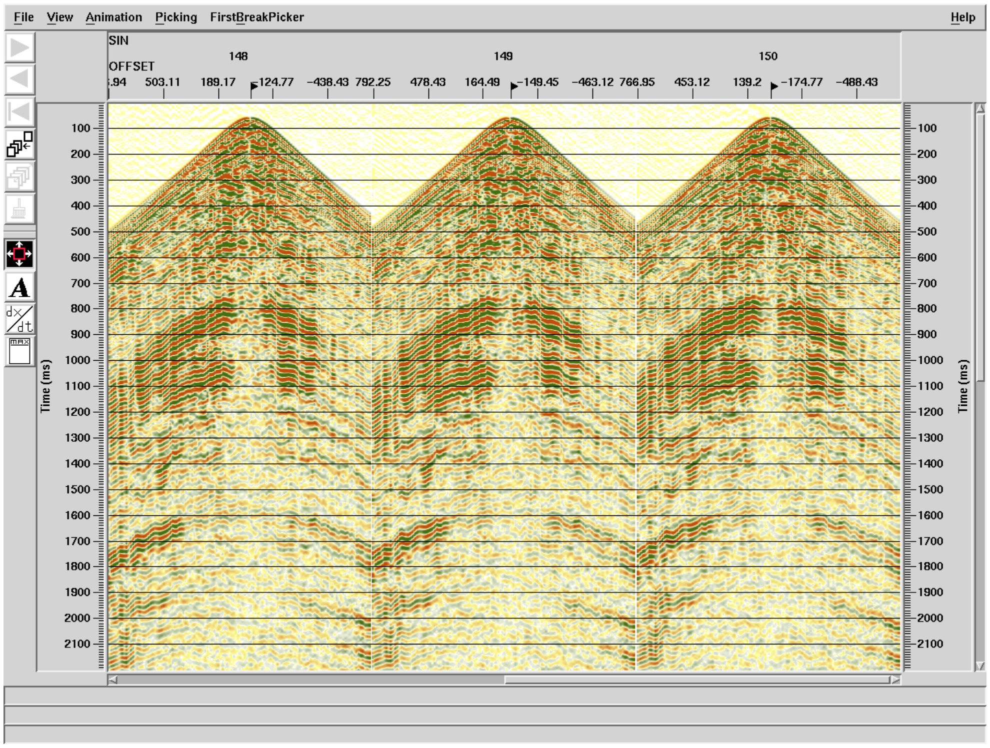

Figure 7.2. Common-shot gathers of the inline horizontal component. Notice that the main reflection events exhibit a pronounced 'wavyness'.

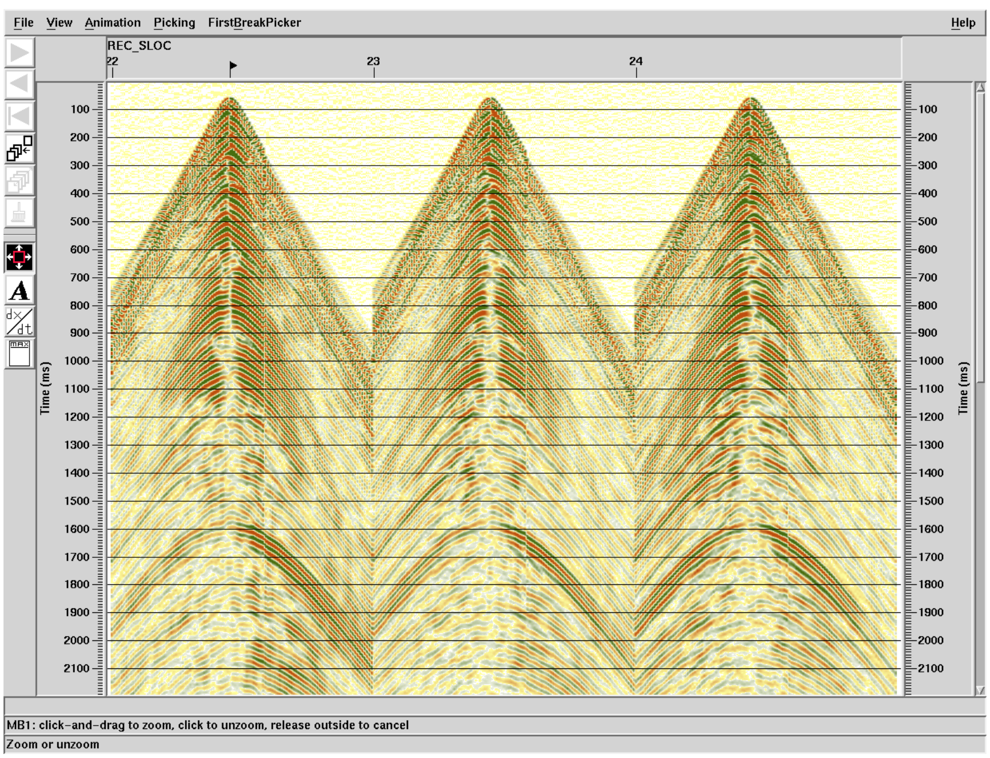

Figure 7.3. For comparison with Figure 7.2, here are three common-receiver gathers of the inline horizontal component. Notice that the main reflections display very even moveout.

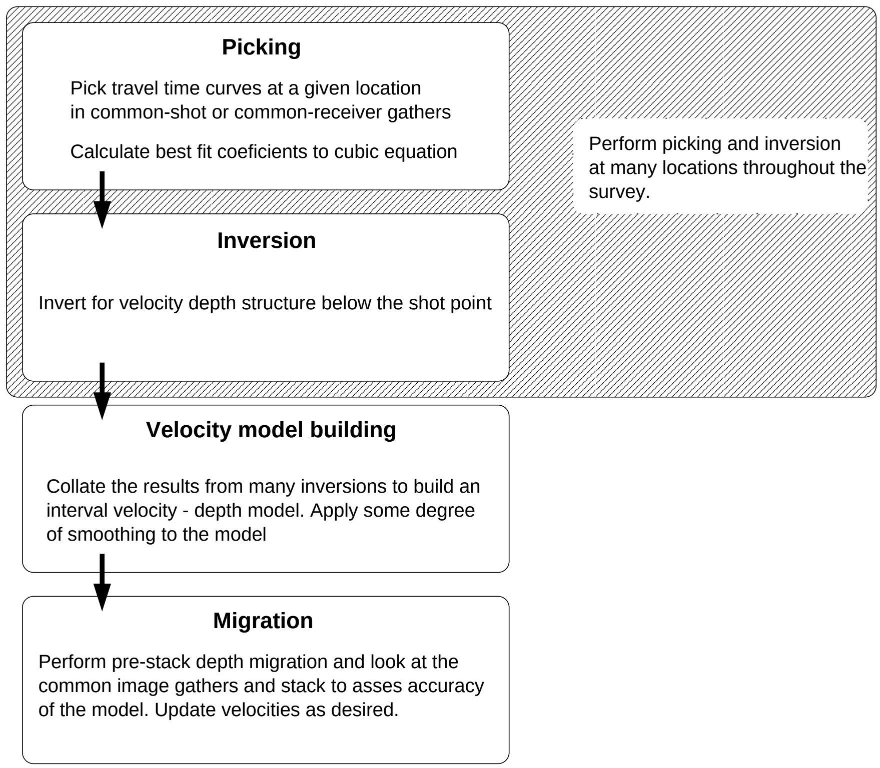

Figure 7.4. An overview of the processing flow, from picking to migration.

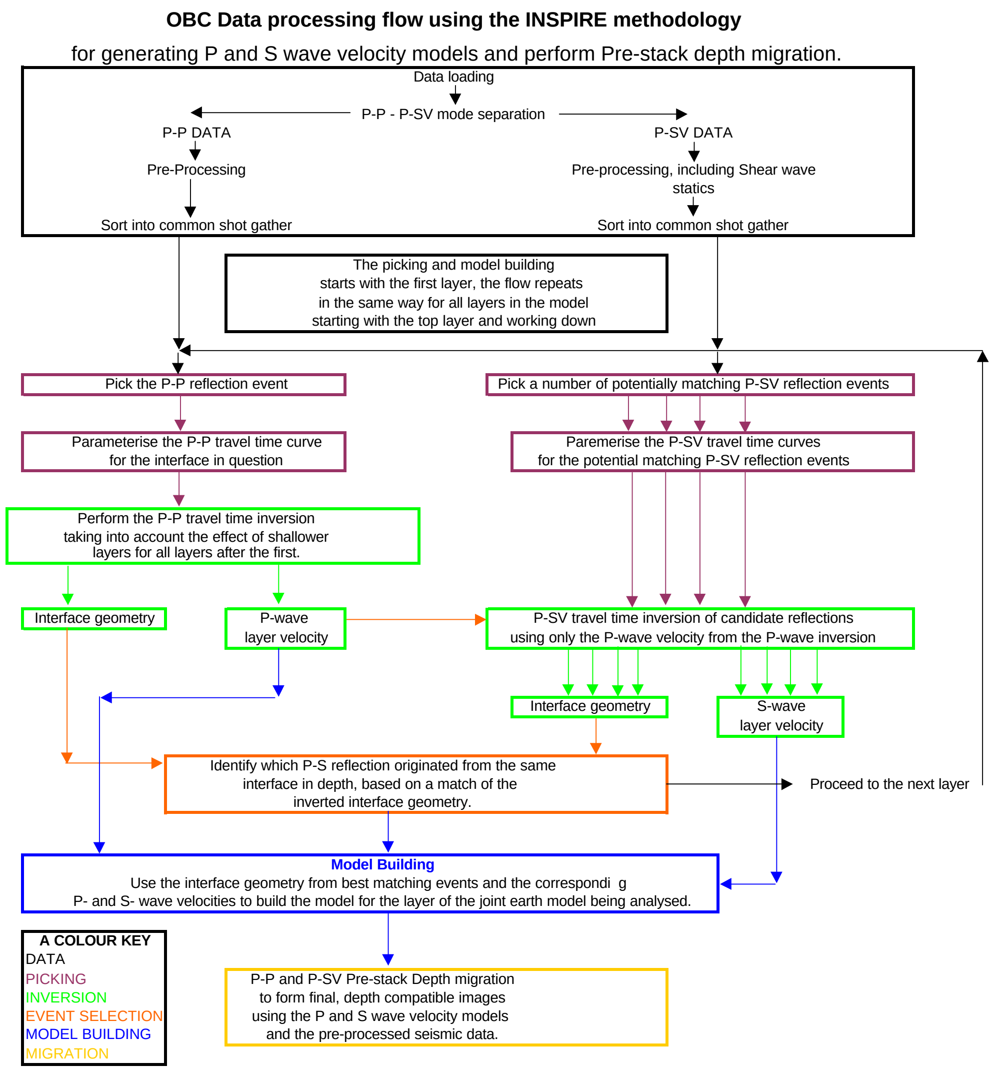

Figure 7.5. A more detailed look at the processing flow, from picking to migration.

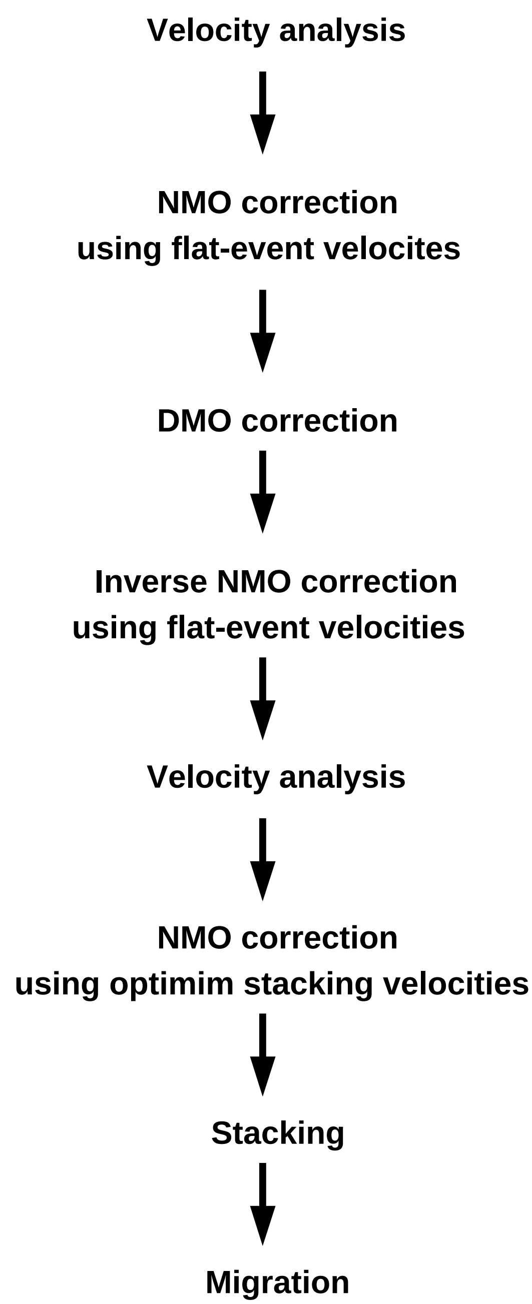

Figure 7.6. A DMO processing flow, from velocity analysis to migration, after Yilmaz (2000).

standard processing is to use dip-independent stacking velocities any inversion and model building must be preceeded by at least a DMO processing flow; an example is shown in Figure 7.6. In some cases the velocities from pre-stack time migration are used. Below I show a list of the steps required for a common-offset pre-stack time migration, taken from Yilmaz (2000):

- Perform velocity analysis at sparse intervals
- Apply NMO correction using these flat-event velocities.
- Sort data into common-offset planes and apply DMO.
- Migrate each common-offset section using a zero-offset migration algorithm and the flat-event velocities.
- Sort the common-offsets data back into CMP gathers, and apply inverse NMO correction using the flat-event velocities.
- Perform velocity analysis at frequent intervals to derive an optimum stacking velocity field
- Apply NMO correction using the optimum stacking velocity field.
- Stack the data and perform inverse migration using the flat-event velocity field.
- Finally, remigrate the result from the previous step using the optimum velocity field calculated on the migrated data

The list above and Figure 7.6 are included to give some idea of how many steps are required to get acceptable velocites when we start by assuming plane horizontal layers in the inital velocity analysis. Our flow needs only picking, inversion and model building and we are ready for PSDM.

In the example I describe below picking is performed at every shot point along the survey. The depth model consists of four layers, the first starting at the sea bed. When calculating the travel time curve at one reflector, the same event is picked in four other gathers, two gathers on either side of the location in question. Data from these five gathers are used to calculate the coefficients of the travel time curve. Some pre-processing has been applied to the data before picking; shear wave contamination

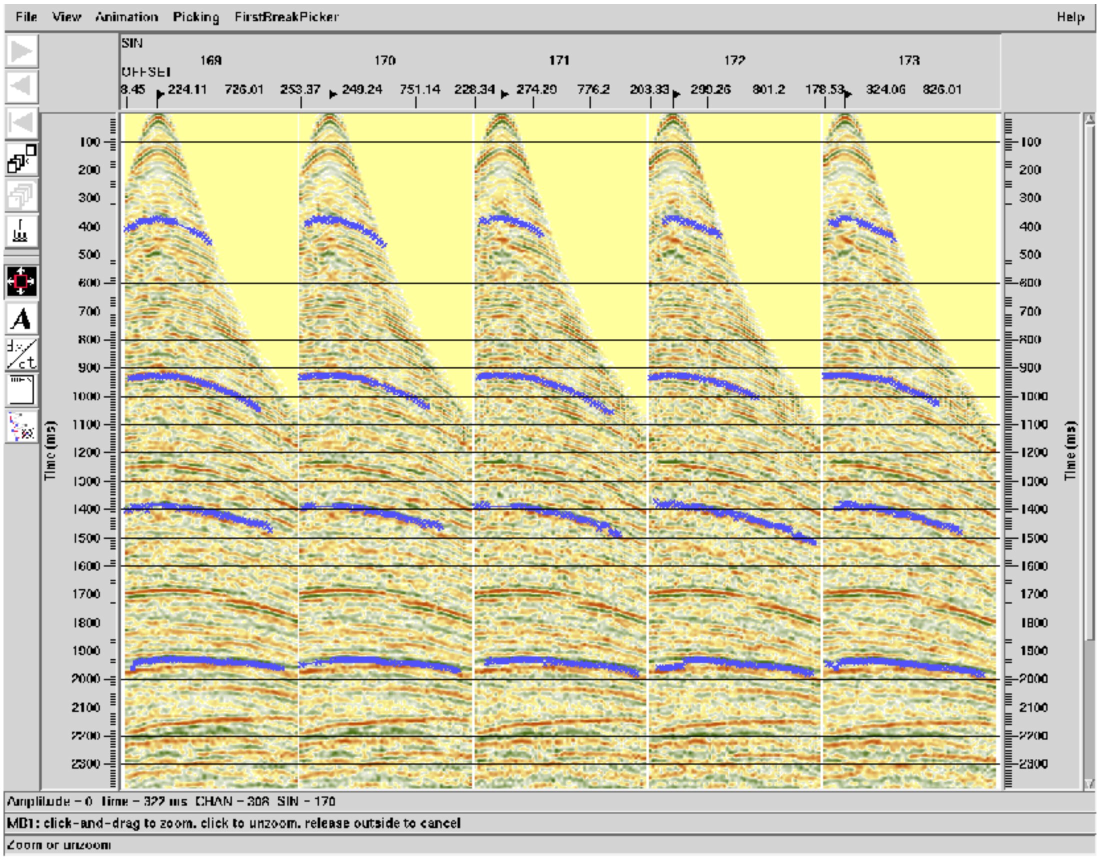

Figure 7.7. Data and picks as seen by the user during picking.

has been removed (see Chapter 3), and the source has been lowered to the sea bed using downward continuation.

Figure 7.7 shows an example of picks made on five common shot gathers and Figure 7.8 shows the cubic polynomial fitted to the data using least squares.

The next stage of the operation is to invert the picked travel time data and to store the model; the result of one such inversion is shown in Figure 7.9

The picking and inversion are performed at each shot location between shots 120 and 180. Shots outside this range have only positive or negative offsets present in the gather. Travel time curve determination does not work very well unless both positive and negative offset traces are present in the gather. The raw data from the inversion are shown in Figure 7.10, along with manually picked polygons showing the location of the interfaces implied by the many inversion results. In Figure 7.11 the same data

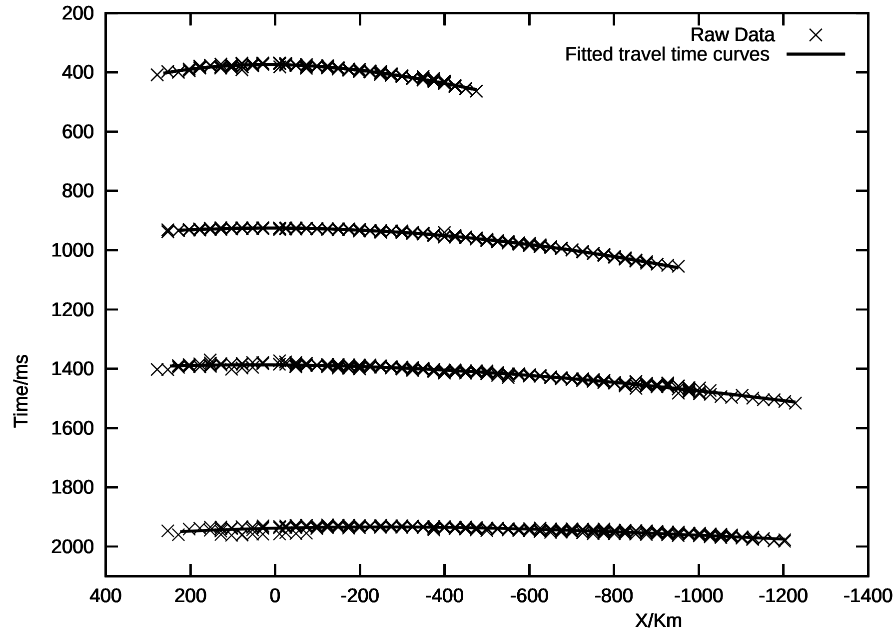

Figure 7.8. Picked data as crosses and fitted travel time curves as solid lines.

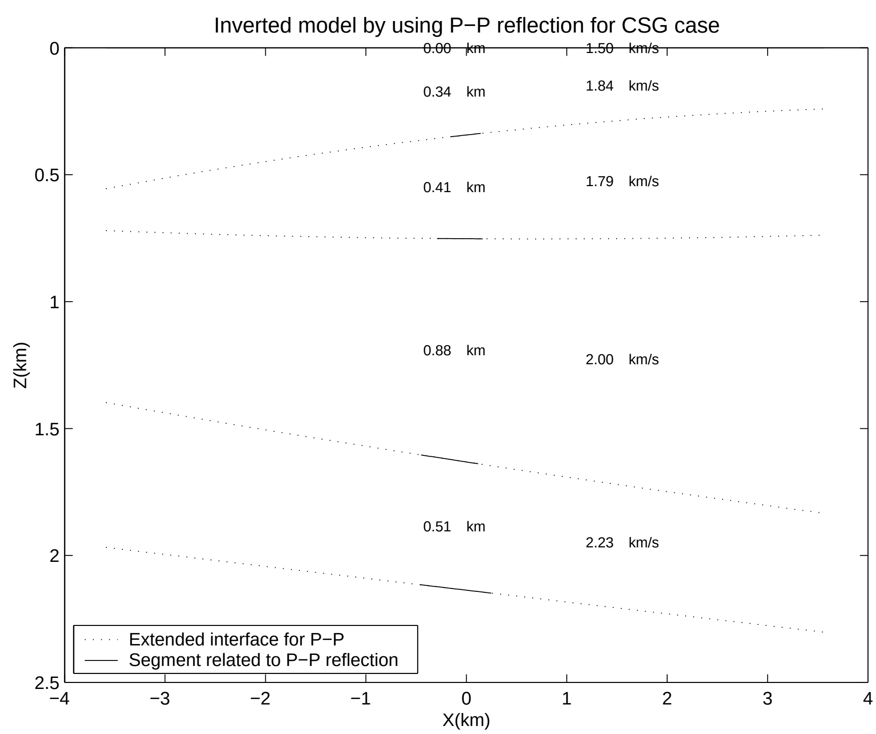

Figure 7.9. Output model from the inversion of data from a single shot gather.

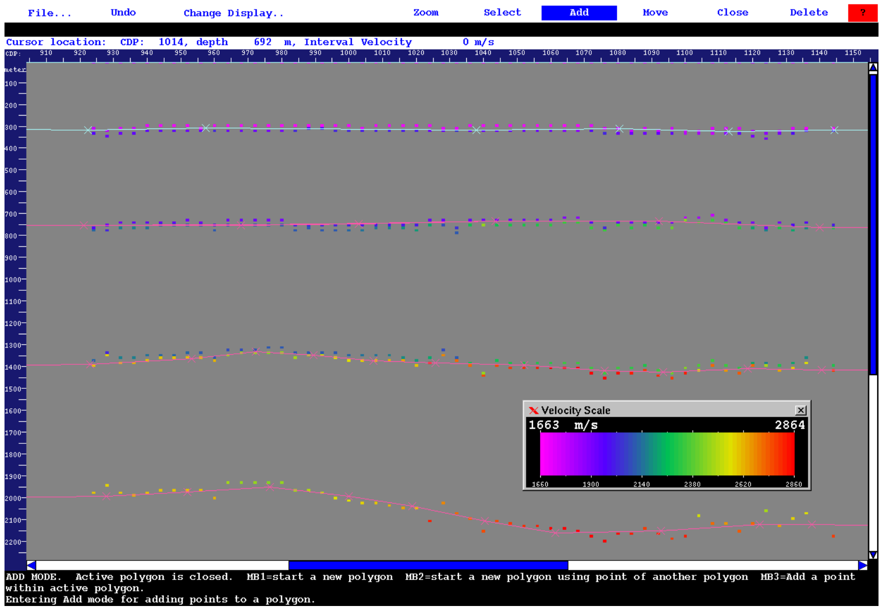

Figure 7.10. Step 1 of model building; the raw data, compare this figure with Figure 7.1 it is not a velocity model itself, but a step in building the model in Figure 7.11

are shown, only the display is interpolating between defined points, so this defines the velocity field at all points in space within the model. The vertical striping is caused by the slightly different results of the inversion at different locations.

Before using the model for migration I apply some smoothing to the velocity field shown in figure 7.11.

After migration with a correct velocity model all the events in the Common Image Gathers (CIG) will appear flat, so the 'flatness' of events in these gathers gives a good indication of how accurate the velocity model is (see Chapter 2 for more details on common image gathers). The migration with the initial velocity model is not perfect (Figures 7.13 and 7.14); however, the events analysed are generally well flattened, indicating that the inversion does a reasonable job of account for the kinematics of the event, given the assumptions made in the inversion. Overall, the initial model (Figure 7.12) is a good starting model, and can be updated as necessary. I have used one pass of migration velocity analysis to update the model and the updated model is shown in Figure 7.15, the stack of data migrated using this velocity field is shown in Figure 7.17.

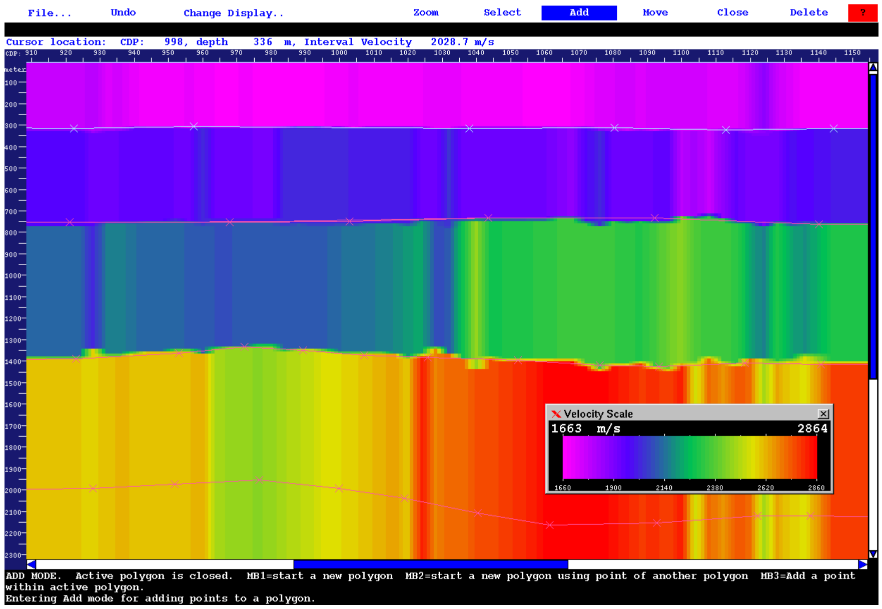

Figure 7.11. Step 2 of model building; the initial velocity model with no smoothing.

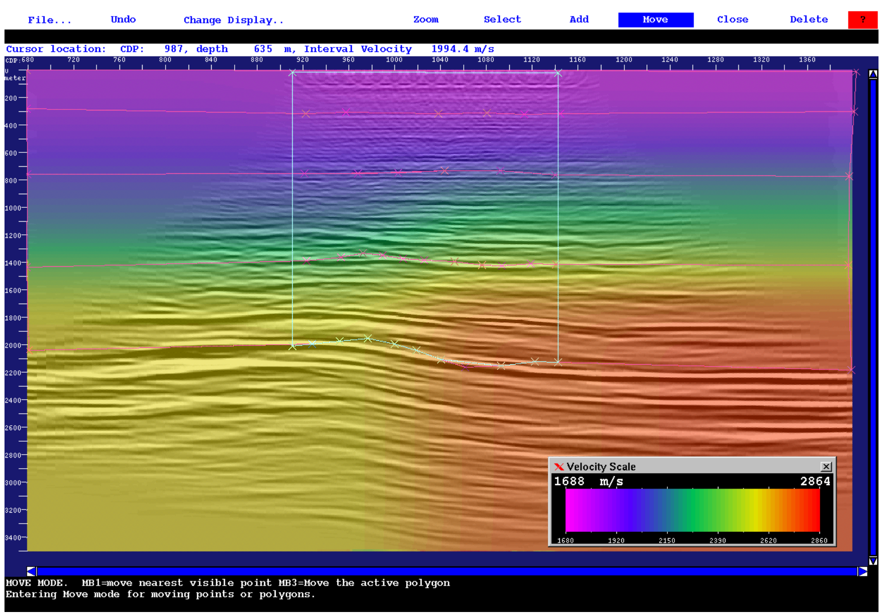

Figure 7.12. Step 3 of model building; the smoothed velocities overlaid on a migrated stack. Only the area within the pale blue polygon (between CDP 920 and CDP 1145) have been analysed, the edges of the model are simply filled with the velocities from the end analyses.

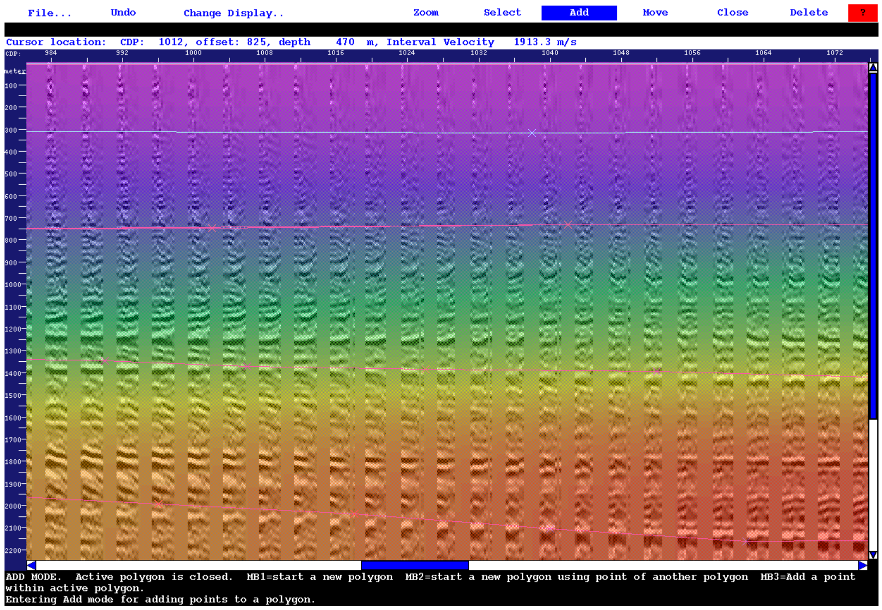

Figure 7.13. Common Image Gathers displayed in their correct spatial location overlaid on the velocity field. The interfaces analysed are shown by the coloured polygons. Notice that events close to the interfaces are well flattened.

The CIGs in Figure 7.16, after the update step, are more consistently flat throughout the model, indicating that it is an improvment over the previous velocity field shown in Figure 7.12. What is interesting to note is that the velocity structure shows three main zones of different velocities, plus a small low velocity zone, possibly caused by the presence of gas over the crest of the structure at 2km depth. This possible gas zone can be seen in Figure 7.15 as the darker green / blue (lower velocity) zone betewen 1200-1800m depth, to the left hand side of the image. This brings to light an important point that, in picking in the pre-stack domain, I choose events which are the boundaries of the isotropic layers in the velocity model without knowing where the major natural boundaries in velocity regime are. The result is that the interval velocity coming from the inversion will not optimally focus the events within the layer. This is a limitation of the way we have chosen to parameterise the earth.

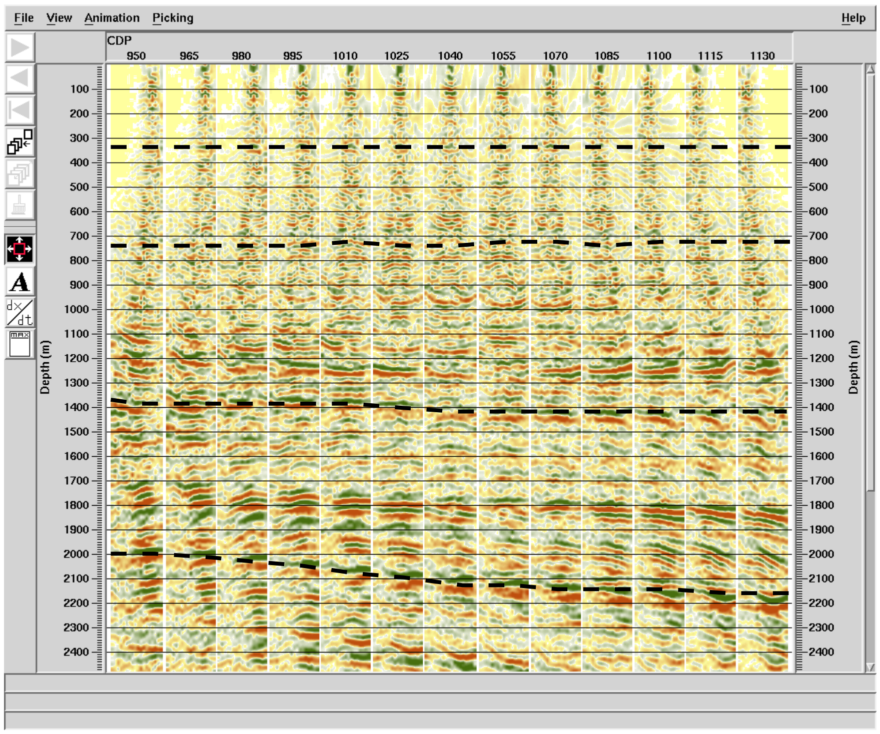

Figure 7.14. Common Image Gathers after the data have been migrated with the initial velocity model shown in Figure 7.12. The dashed lines show the interfaces analysed. Notice that events close to the interfaces are well flattened.

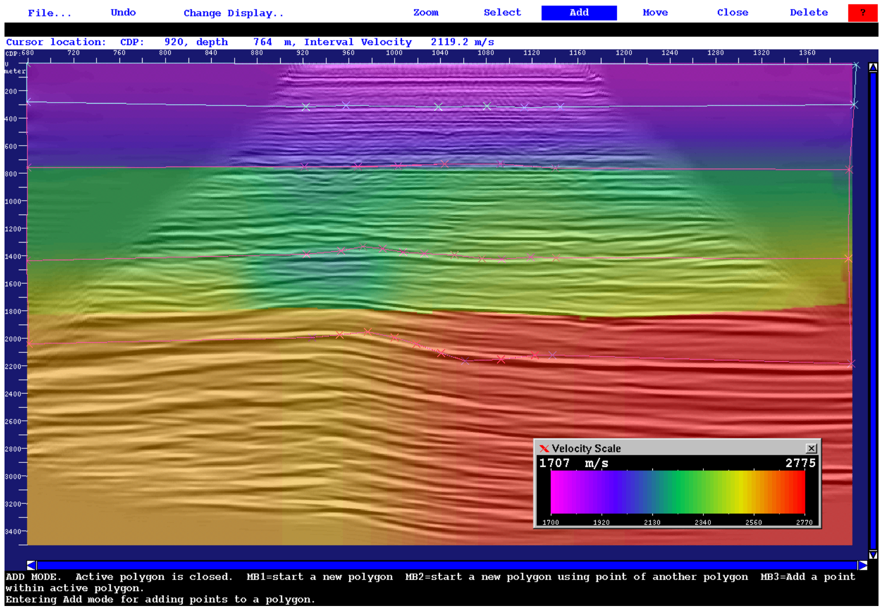

Figure 7.15. The velocity model after updating using migration velocity analysis to flatten the image gathers. Compare this velocity field with the initial velocity field in Figure 7.12. Notice the low velocity zone left of center between 1200 and 1800m depth.

7.1.5 Limitations of the assumptions

This problem of picking events that do not coincide with the natural changes in velocity regime in the subsurface is a natural one which derives from the way we parameterise the earth. In the model building and inversion we make a number of assumptions, these are:

- 2-dimensional earth,
- Isotropic velocity regime within layers,
- No lateral or vertical velocity variation on the scale of a shot record,
- Locally parabolic continous interfaces,
- Velocity is related to structure.

There is plenty of evidence to suggest that the earth is not like this and in fact the velocity regime is better modelled if we take into account the effects of:

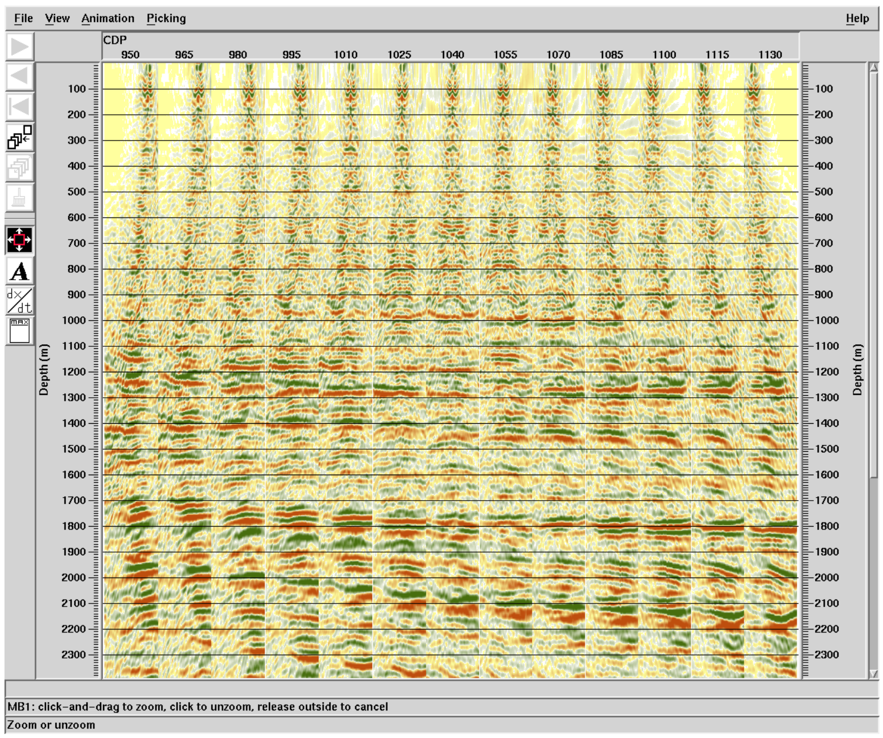

Figure 7.16. Common image gathers after migration with the updated velocity model shown in Figure 7.15

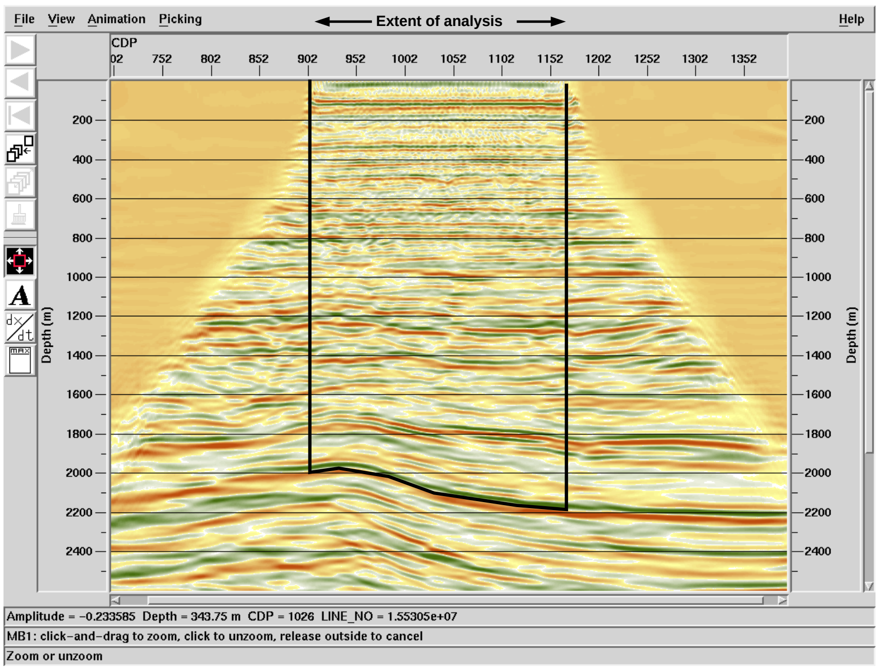

Figure 7.17. Stacked data migrated using the updated velocity model. This is the final and best stacked section I have produced. The black box overlaid on the seismic data shows the spatial extent of inversion locations, and the depth to the deepest reflector analysed.

- 3-dimensional earth,
- Anisotropy,
- Horizontal and vertical velocity gradients,
- Discontinous interfaces; ie faulting,
- Non-layerd structures, like salt bodies,
- Velocity regimes that are not related to structure.

These shortcomings are of a type common to nearly all inversion problems. We can not model all the complexities of the real world, so we make certain assumptions about it and, given these assumptions, we do the best job we can to match the data that we observe. We have chosen a model which includes the effects of dip and interface curvature in the assumptions. This is the main difference with the conventional approach to model building.

7.1.6 Seismic Velocites

When considering a single isotropic layer, the inversion of Li *et al.* (2002) leads to the correct interval velocity and depth location of the reflector. The straight ray aproximation is correct in this environment (Li, 2002). When several layers are considered and analysed as if they were a single layer (such as the stacking velocity used in CMP velocity analysis), the velocity is called an RMS velocity. If layered media are considered, with varying velocity in each layer, the ray paths through a number of layers are not straight. In our case the inversion will treat the travel time curve as if it had been derived from a single isotropic homogeneous layer, using straight ray paths. The inversion matches the travel time curve from the layered media with that from a single thicker iso-velocity layer. This means that the 'interval velocity' for a thick layer, which is in fact made up of many thinner layers, is more like a 'pseudo RMS' velocity for that block. Using straight rays the inversion has found the closest match to the real traveltime curve seen in the data.

7.2 PART 2: Joint inversion of real P-P and P-SV data

7.2.1 Summary

The inversion of multicomponent seismic data for determination of P- and S-wave interval velocities requires the correspondence of P-P and P-SV reflections to be known. In this Section I use travel time inversion to guide event matching in pre-stack gathers. In the resulting four layer P- and S-wave velocity models the first three interfaces have almost exactly the same geometry. Pre-stack depth migration of the P-wave data using the P-wave velocity model generates well flattenend common-image gathers, indicating a reasonably accurate velocity field.

Until now I have conducted tests of the joint inversion scheme only on synthetic data. In order to process the P-SV component in common-shot gathers I have had to apply receiver static corrections, Section 7.2.2 discusses the calculation of the statics correction. Following the application of static corrections to the data I then use the inversion to identify the P-P and P-S events that can be inverted to give a common interface geometry. I find that the inversion apears to discriminate well between closely spaced reflectors. Once I have selected the reflection events of interest, picking, inversion and model building procede in the way described in Chapter 6. I show the results of inverting travel times, picked at six locations, and the subsequent P- and S-wave velocity model building.

7.2.2 Receiver Static Corrections

At the sea floor there is a very thin layer of poorly consolidated muddy sediment. This has a small effect on the propagation of P-waves, but not much, as the layer is very thin and the mud velocity is at least as fast as water. For S-waves this layer, although thin, has a very large effect because the S-wave velocity is reduced to a high degree as the mud is quite 'fluid-like'. The presence of a low velocity layer is not a problem in itself, as the effect is simply to add a time delay proportional to the thickness and

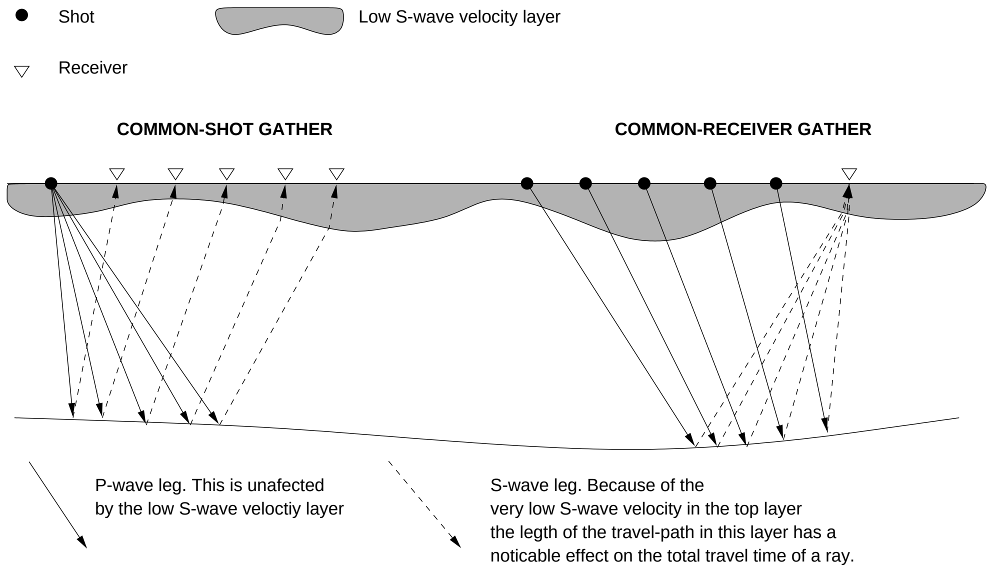

Figure 7.18. In the common shot gather on the left, the rays going to the receivers all travel through a different thickness of low S-wave velocity layer. In the common-receiver gather the rays travel through almost the same thickness of low S-wave velocity layer, and so the static shift is almost the same for all the traces in a common-receiver gather.

inversely proportional to the velocity in the layer. Problems arise when the layer is laterally variant in either thickness or velocity; when this happens the time shift caused by the slow layer is spatially variant, as illustrated in Figure 7.18 . In a common shot gather, the effect is to add a different time shift on to each trace according to receiver position, causing easily visible 'wavyness' in the reflection events, as shown in Figure 7.19.

In order to remove the effect of this we should ideally like to find out the properties of this thin low velocity layer and include them in all our modeling. However this is hard to do, and we have come up with a rather more pragmatic aproach.

7.2.3 What datum?

The problem is that it is easy to see that the travel time curve of a P-SV reflection event (in this case simply the inline horizontal component geophone record) is wavy, but, wavy compared with what? If the answer to that question is; 'compared to the travel time curve without the effects of the low velocity layer' I have, somehow, to define the corrected travel time curve in order to calculate the difference between it and the real data. This is not an ideal situation, as the whole point is that I don't know the shape of the travel time curve without the static shift.

I can make a few assumptions that will allow me to procede with a pragmatic method to determine and remove the static shifts occurring on each trace. First I assume that the static shift should be the same at a given receiver for different shots, i.e. one time shift value is associated with each individual receiver. Second I assume that the static shifts have no long wavelength spatial trend, i.e. it is not all positive on one part of the survey and negative in an other, but fluctuates between being positive and negative over quite a small spatial range.

These assumptions allow me to fit a smooth function through reflection events picked on the un-corrected data to define the datum.

I pick a number of travel time curves in different shot gathers. These do not have to be the same reflector but the reflectors should all be quite shallow, I use ones with less than 1.2 seconds two-way-time. I then fit the picked points with a cubic equation. This gives a smooth line that defines the datum from which the static shift can be calculated. This is repeated at a number of locations so that some average value of the static shift required at each location can be calculated. An example of the raw picks and the datum curve is shown in Figure 7.20 and the static correction is shown in Figure 7.21.

There is a danger here that the static shift does not fluctuate very quickly, in which case this will be reflected in the fitting of the 'datum' and will bias the calculated static shift. Another problem comes from fitting the picks with a cubic equation, as this approximation is not valid for all travel time curves (although it appears to work well here). The other source of error comes from local, or random noise, which can affect the exact time value of the picks made on the seismic data, and hence the calculated static shift associated with that receiver. Increasing the number of shots and reflectors analysed will help to address the issue of local random noise in the data (I show some average values of the static corrections found using different shots and reflectors in Figure 7.22). It may not, however, help if there is bias in the static estimation caused by using a cubic equation to define the datum.

To address the latter problem I also analysed the data in common-offset sections. At zero offest no energy is converted from P to S mode, so I used sections with offsets around 200-300m, as here the reflections are quite energetic. Again I picked a common reflection event and fitted these data with a cubic equation calculated using least squares to define the datum. The reflectors appear essentially flat in the common-offset sections at the picked times, but nevertheless I fitted them with a cubic equation. A running mean method could have been used to calculate any large scale trends to the data, but the least squares code was convenient. The procedure is exactly the same as for the picks in the common-shot gather. After calculating the datum curve, I then find the time shift between the picked points and the datum. The resulting time differences are the static shifts for each trace. I compare the static corrections found using both common-shot gathers and common-offset gathers in Figure 7.23.

These static corrections are then combined with those derived from the shot gathers to give an average static shift for each receiver location. The various estimates of the static shift and results of applying them are shown in Figures 7.21 to 7.27 below. I find that using the median of all the calculated static shifts (both from shot gathers and common offset sections) results in the best looking data. Data corrected using these values are shown in Figures 7.25, 7.26 and 7.27.

These results improve the data quality suficiently to enable picking and inversion of these data. They are not a physical static correction in that they are not related to a shallow velocity structure, such as statics calculated using refraction data or borehole measurments might be, however, they do diminish of the waveyness that can cause problems in the pre-stack picking.

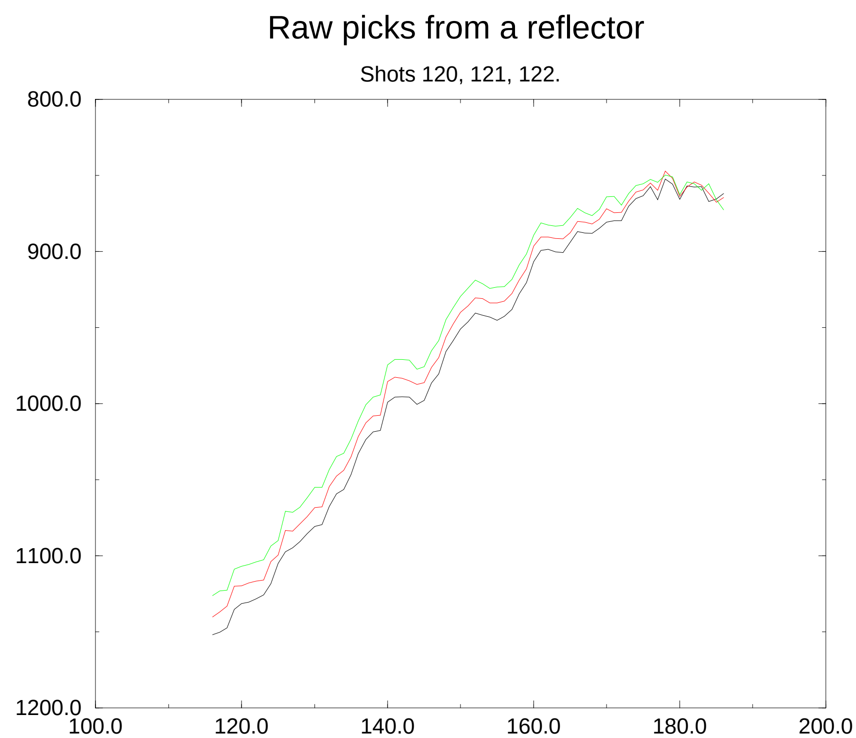

Figure 7.19. A number of picked travel time curves from different shot gathers. The horizontal axis is receiver number; notice that the wobble is systematic with receiver number.

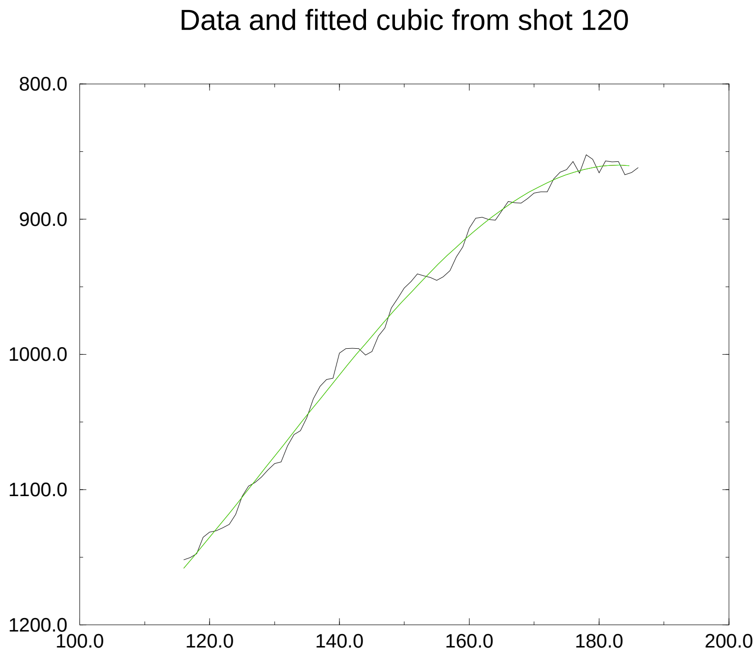

Figure 7.20. A picked travel time curve and its best fit cubic equation; time is on the vertical axis and receiver number on the horizontal.

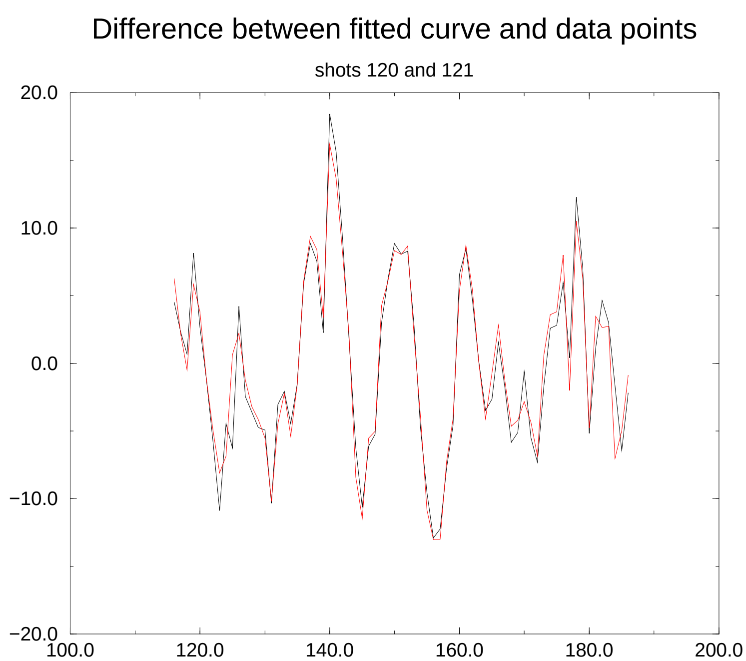

Figure 7.21. For the same reflector picked in next-door shot gathers, the difference between the fitted cubic curve and the picked data is very similar at each receiver location. Time in milliseconds is on the vertical axis and receiver number on the horizonal axis.

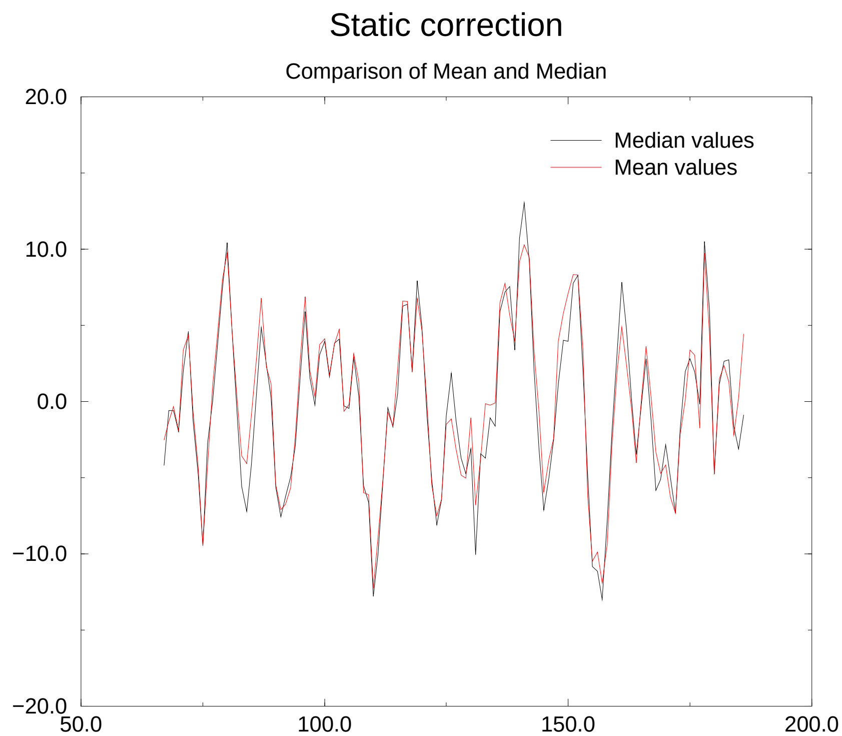

Figure 7.22. I measured the difference between picked data points and the best fitting cubic for different reflectors in different common-shot gathers (nine data sets in all). Here I compare the mean and median values of the nine different estimates for the static correction at each receiver location. The vertical scale is the time in milliseconds and the horizontal scale is receiver number.

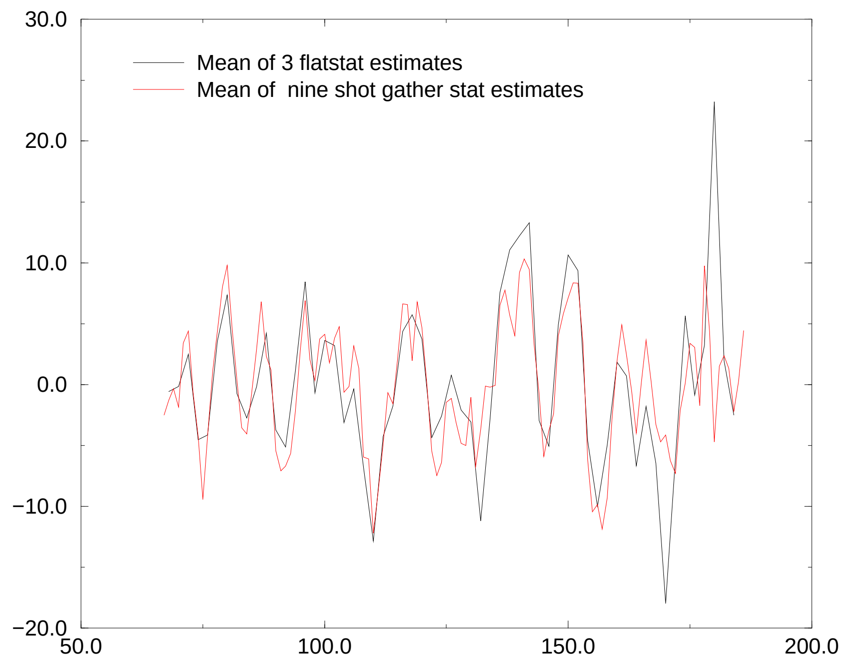

Figure 7.23. The static estimates labeled 'Flatstat' come from estimating the static corrections in the common offset domain. Here they are compared with the mean value for the static corrections estimated in the common-shot gathers. The vertical scale is the time in milliseconds and the horizontal scale is receiver number.

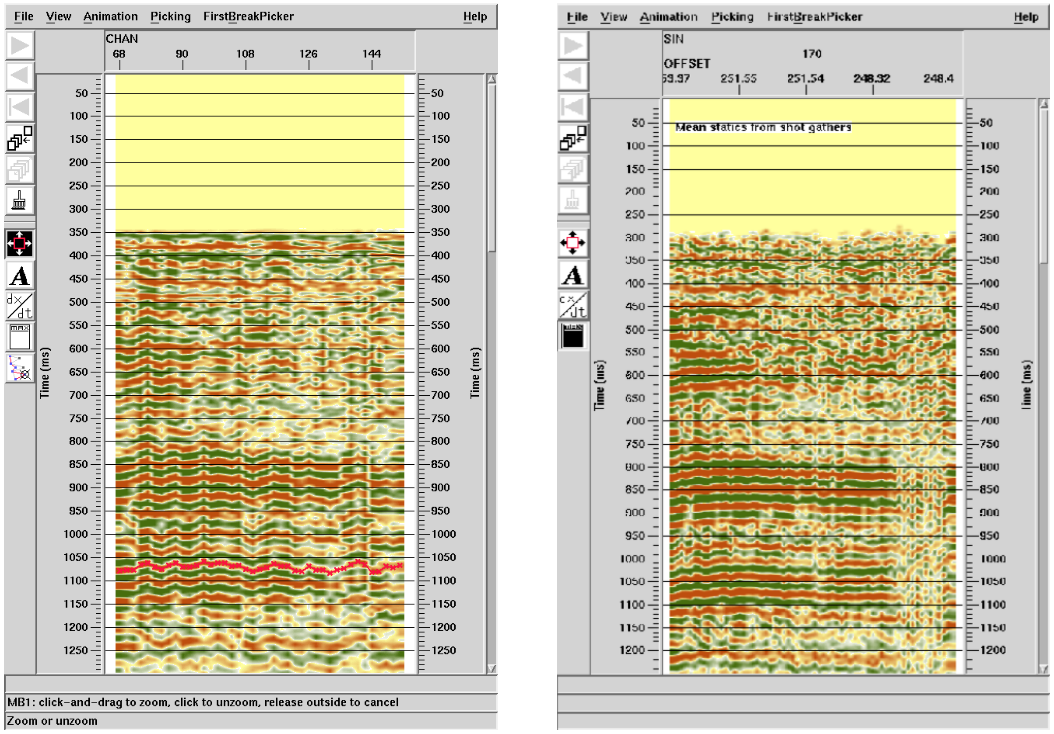

Figure 7.24. A common-offset gather, on the left with no static correction applied, and on the right with the mean static correction calculated from the common-shot gathers only.

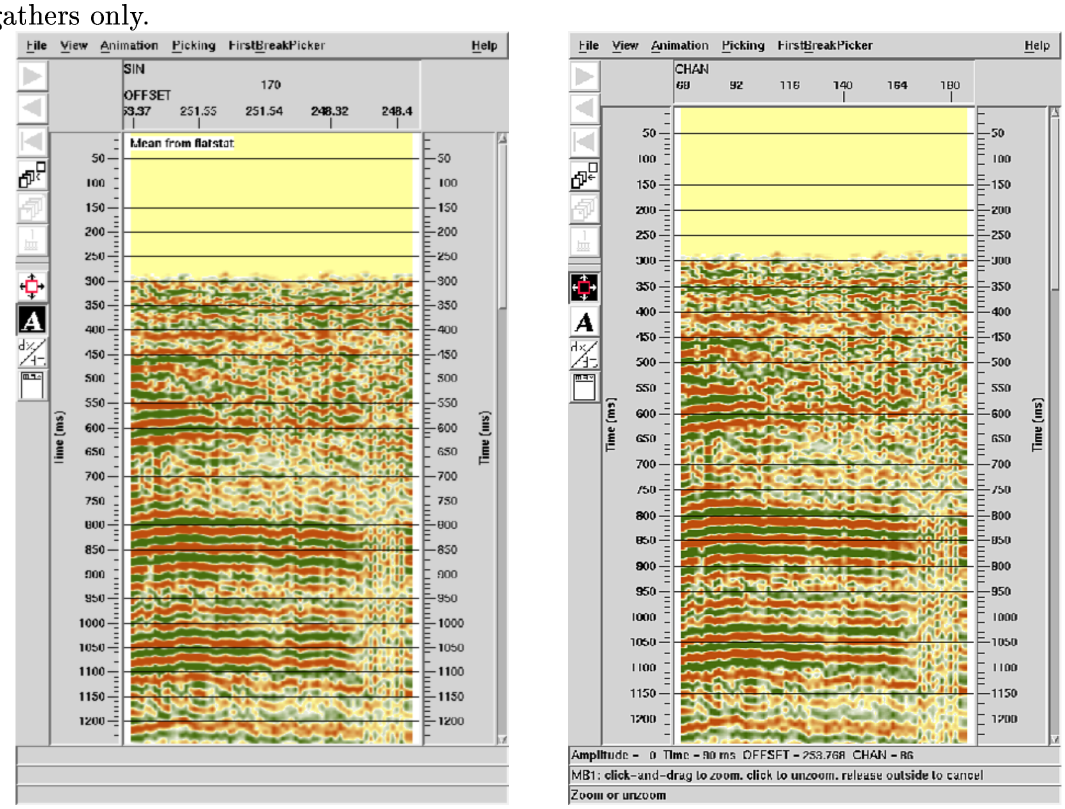

Figure 7.25. The same common-offset gather with receiver static corrections applied. On the left the static corrections have been calculated only in the common-offset gathers, and on the right the median of static corrections calculated from shot and offset gathers is applied.

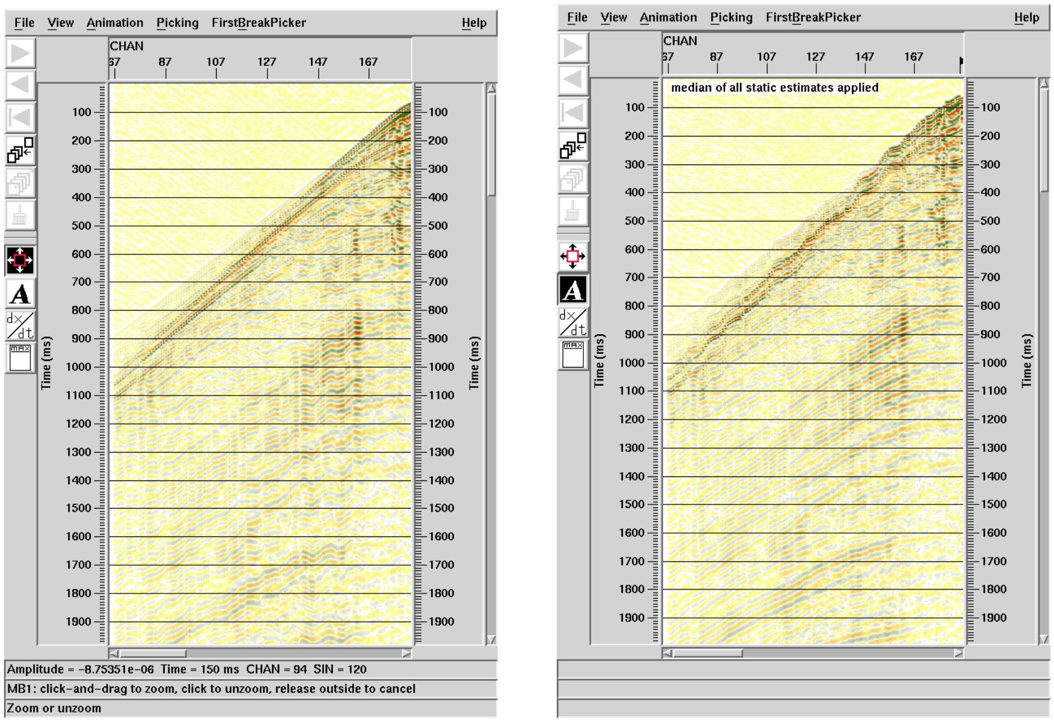

Figure 7.26. A common shot gather, before (left) and after (right) the application of receiver static corrections, 'best static estimate' applied.

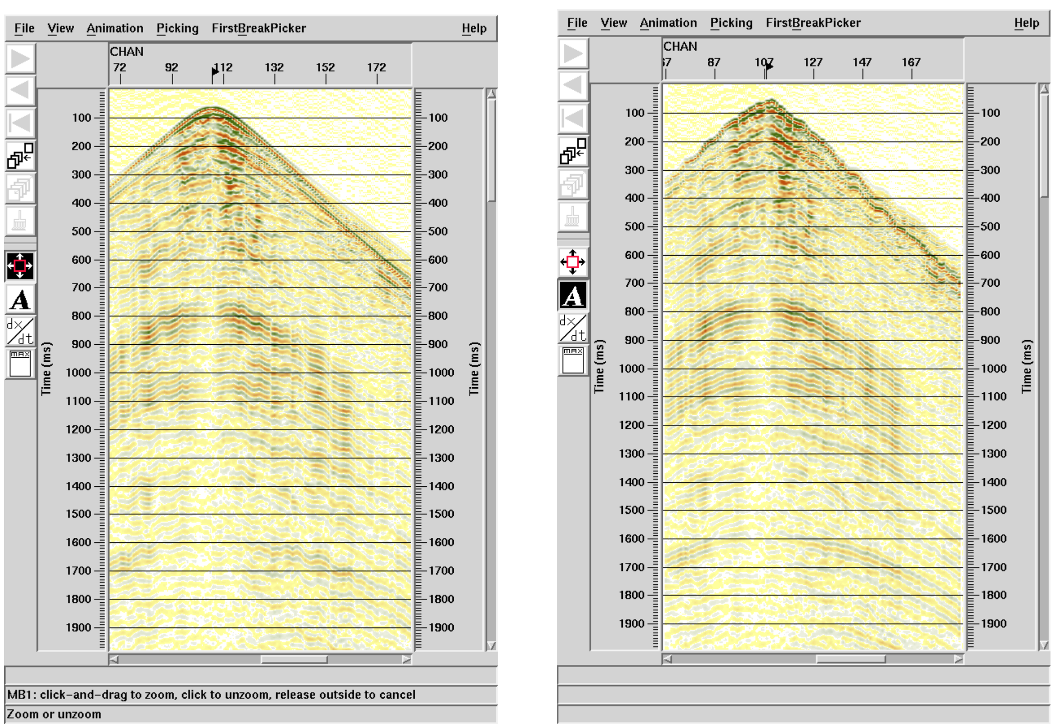

Figure 7.27. A common shot gather, before (left) and after (right) the application of receiver static corrections, 'best static estimate' applied

7.2.4 Event Selection

Following the application of the static corrections, it is now possible to pick travel time curves for inversion from both the filtered vertical and inline horizontal datasets, these are records of P-P and P-SV data respectively.

I start by doing a detailed analysis at one shot location to determine the correct match between P-P and P-SV events. Once this is done I then pick and invert the same reflectors at different shot locations throughout the survey area. I use shot 140, near the middle of the survey, for the event selection procedure. Figures 7.28 to 7.31 illustrate the data and results obtained at this stage.

Starting at the top of the model I pick a P-P reflection event, and a number of candidate P-S reflection events. I invert these to find out which give the most consistent interface geometry. Figure 7.29 shows the inverted interface geometries from the first layer for shot 140, and Figure 7.31 shows the selection for the second layer.

Figures 7.28 to 7.31 are illustrative of the ideal picking scheme. After I had done the tests shown in Figures 7.29 and 7.31, I changed the picking tactics slighty. Instead of picking lots of horizons and hoping that I had the right one somewhere within that picked set, I chose to use one test horizon for the P-S picking. I changed which P-S reflection event I picked until I found the closest match to the P-P interface. I picked the events in three neighbouring gathers to reduce noise, using the method described in Chapter 5. When moving on to deeper layers, the event matches for the layers above are fixed, and the model builds down from the top. The fourth layer was a bit troublesome as there is only one strong converted wave reflection event in the P-SV data, so I had to use this event for the P-S travel time curve. I then had to find the matching P-P event. I did this by changing the picked P-P reflection event until I found the smallest difference between the inverted models from the P-P and P-SV travel time curves. The best fitting picks are shown in Figures 7.32 and 7.33. The interfaces resulting in the inversion of these four travel time curves are shown in Figure 7.34.

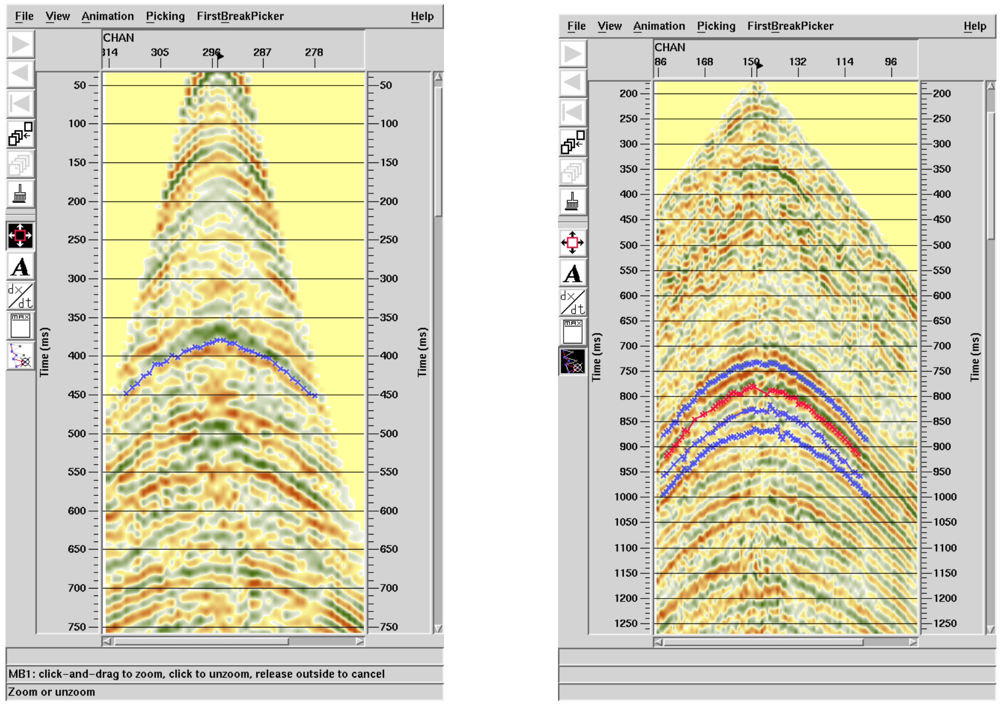

Figure 7.28. P-P and P-S travel time curves for event selection of interface 1. For the sake of illustration I show picked events on one P-P and one P-SV gather. For the determination of the travel time curve parameters, I pick and analyse reflection travel times on three neighbouring gathers.

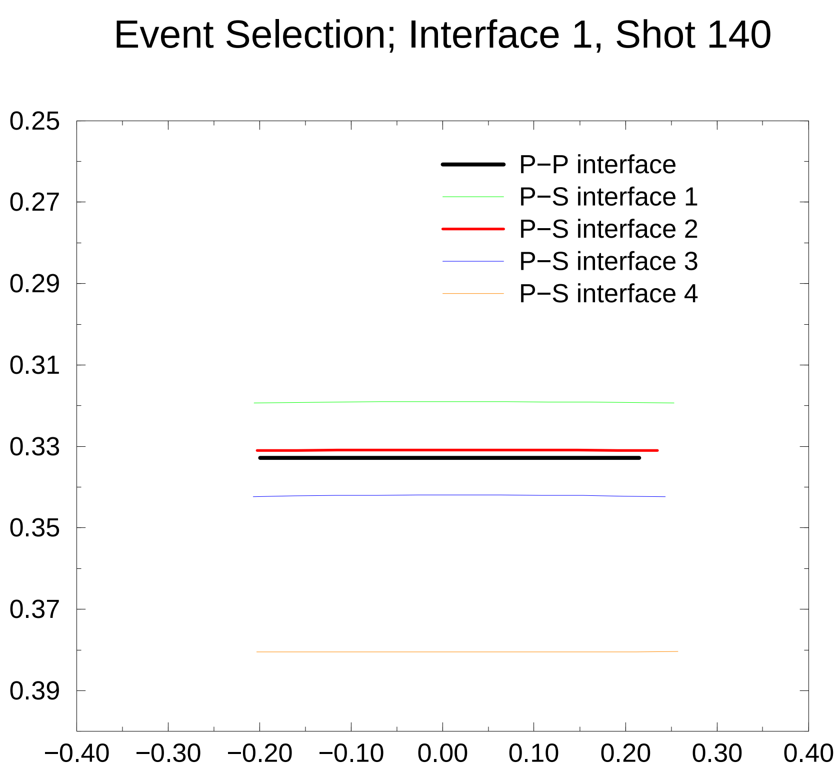

Figure 7.29. The inverted models from P-P and P-SV inversions, evidently the second P-S interface gives the best match.

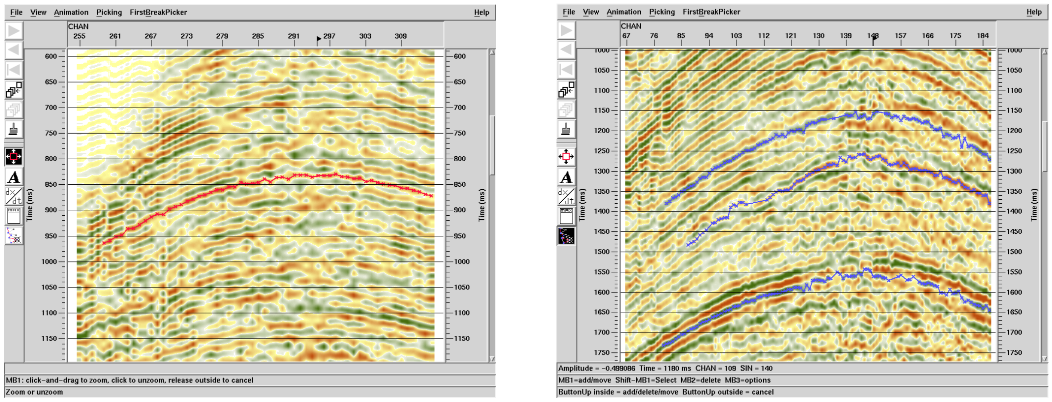

Figure 7.30. P-P and P-S travel time curves for event selection of interface 2.

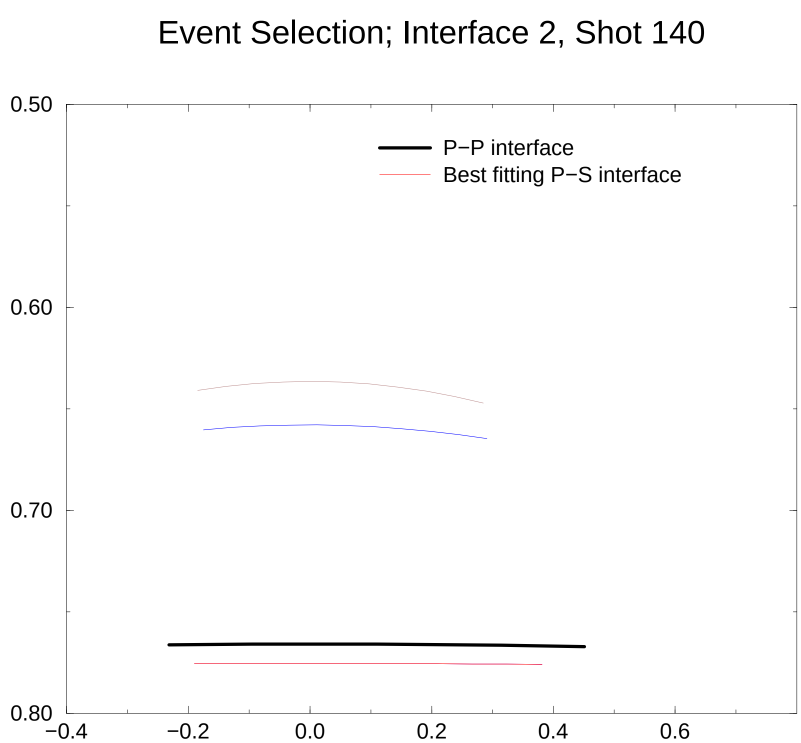

Figure 7.31. The inverted models from P-P and P-SV inversions, evidently the second P-S interface gives the best match.

In Figures 7.35 to 7.37 I show the inverted segments derived from every 10th shot across the survey. There are only three present in the data for shot 120 as the inversion proved to be unstable and gave a meaningless result. I have not yet investigated the cause of this. The interfaces tend to agree very well, although less so for the fourth layer and possible reasons for this are discussed in Section 7.3.

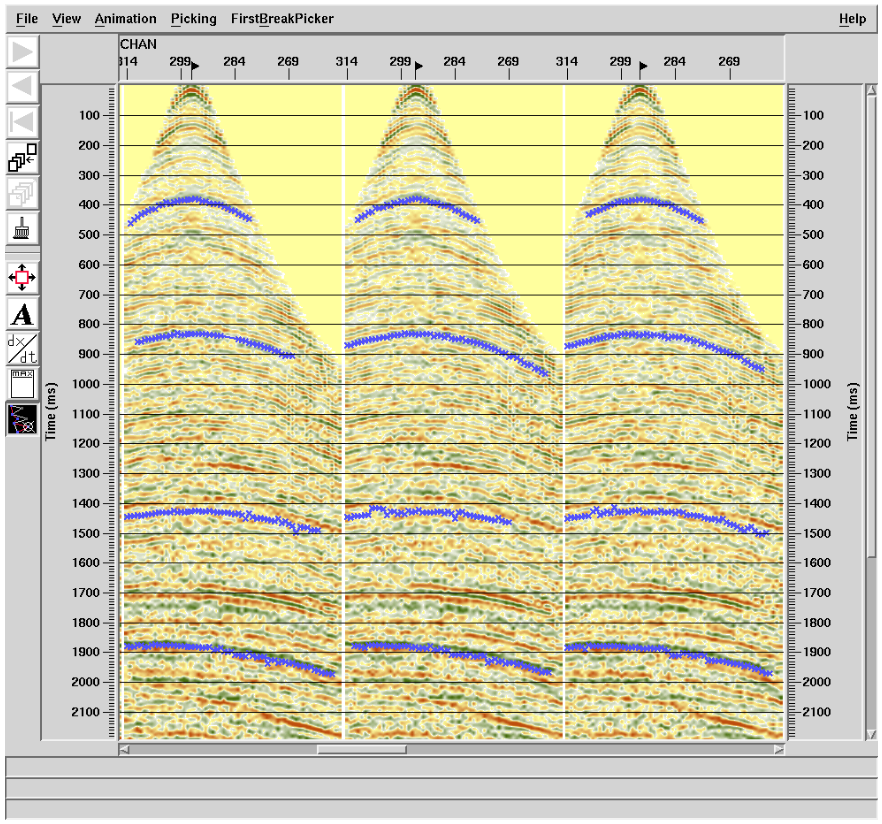

Figure 7.32. Inversion of the matched reflectors gives these well matched interfaces.

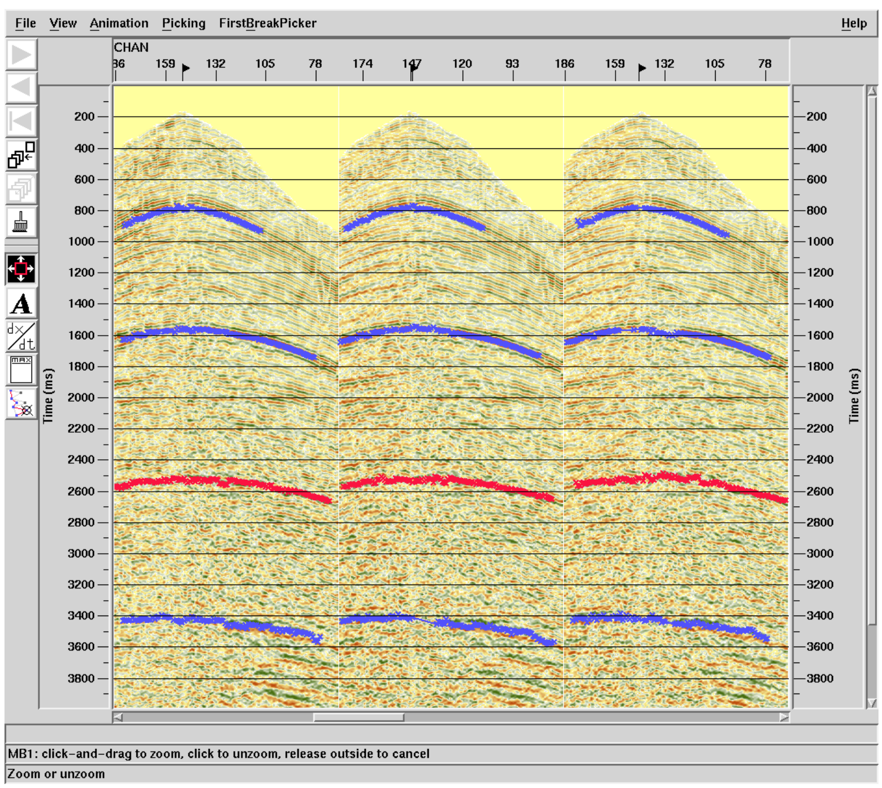

Figure 7.33. Inversion of the matched reflectors gives these well matched interfaces.

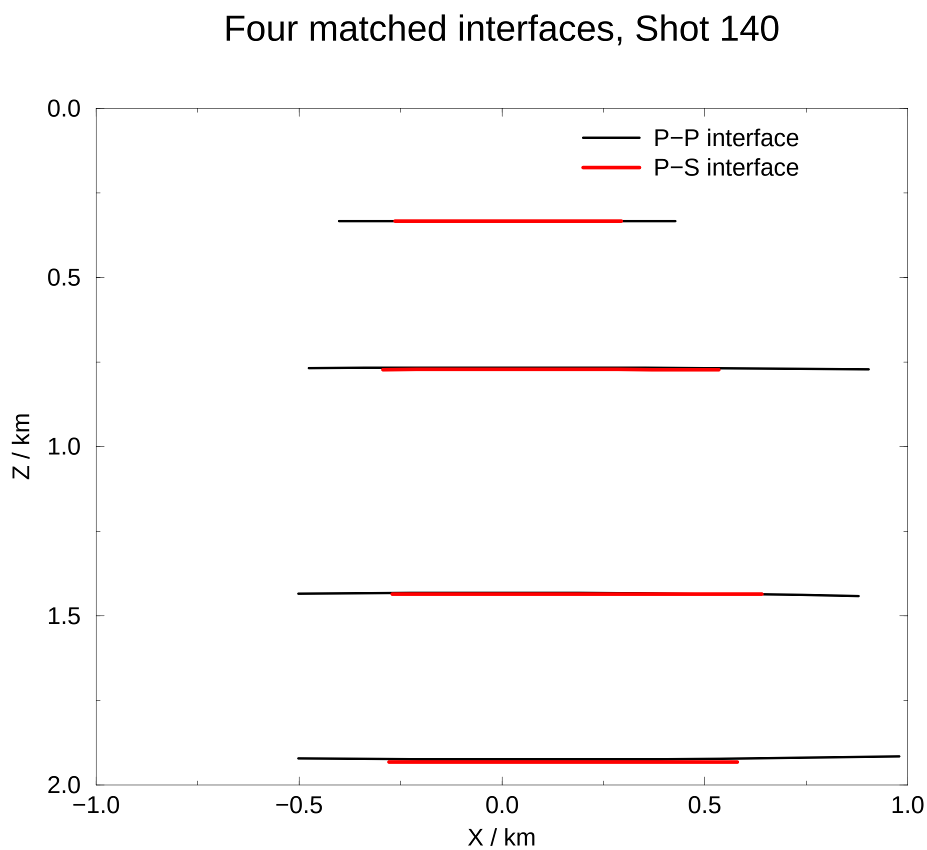

Figure 7.34. Inversion of the matched reflectors gives these well matched interfaces.

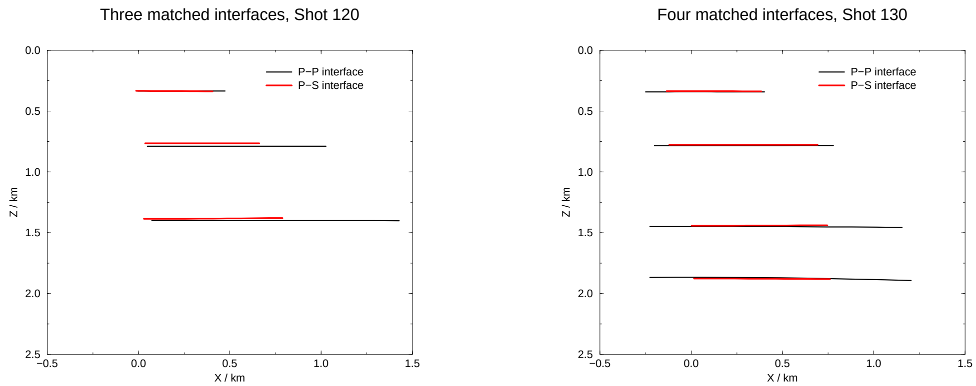

Figure 7.35. Interfaces from inversion, shots 120 and 130

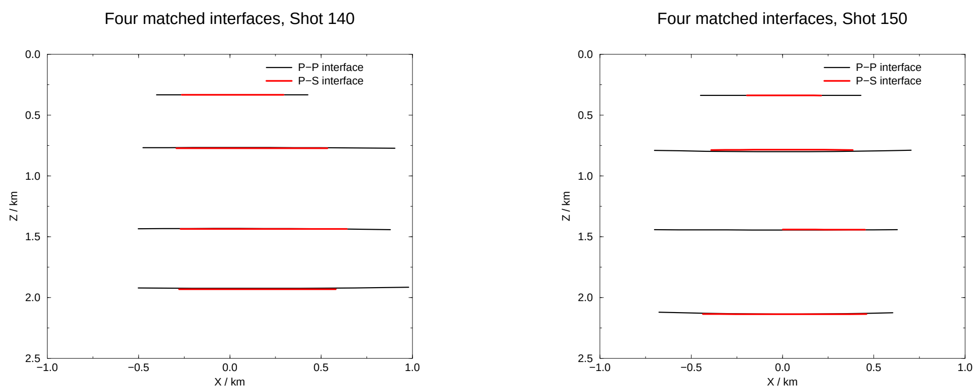

Figure 7.36. Interfaces from inversion, shots 140 and 150

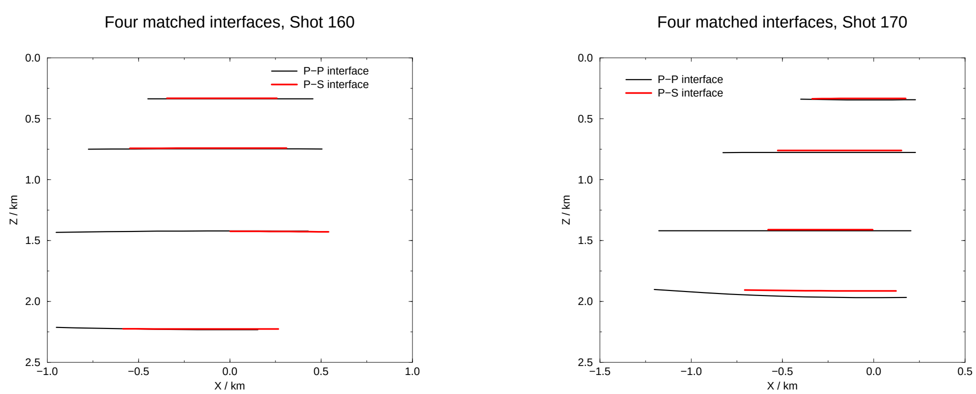

Figure 7.37. Interfaces from inversion, shots 160 and 170

Layer	$vp : vs$ ratio
Layer 1	3.1
Layer 2	2.6
Layer 3	2.3
Layer 4	2.2 to 3.2

Table 7.1. Typical values of the $vp : vs$ ratios for each of the four layers. We are not completely confident with the results for layer 4.

7.2.5 Model building

Having done the event selection I then proceeded to pick and invert for a four layer model across the survey between shots 120 and shot 170. I analysed only every 10 shots, as time was a factor in getting this test completed. This gives six inversion results with which to build the model. The raw data used for re-sampling are shown in Figures 7.38 and 7.39.

Re-sampling the segments using the method described in Chapter 5 results in the interfaces shown in Figure 7.40. The P- and S-wave velocity models shown in Figures 7.41 and 7.42 I derive using the same velocity model building that we used to build the P-wave velocity field in Section 7.1. This is not really suitable for this sparsely sampled dataset and in future the interface data shown in Figure 7.40 would be included. I have not applied smoothing to the velocity field in the fourth layer as we do not yet have much confidence in this part of the velocity field. Some typical values for the $vp : vs$ velocity ratios are shown in Table 7.1.

7.2.6 P-wave migration

I use the velocity model built using the inversion to perform pre-stack depth migration of the vertical component data. Only the upper part of the model, down to 1.5 km is migrated as at present I am not confident with the deeper part of the model. The velocities are defined only at six points throughout the model (this is about 10 times less than in Section 7.1) and so I have applied a higher degree of smoothing to the

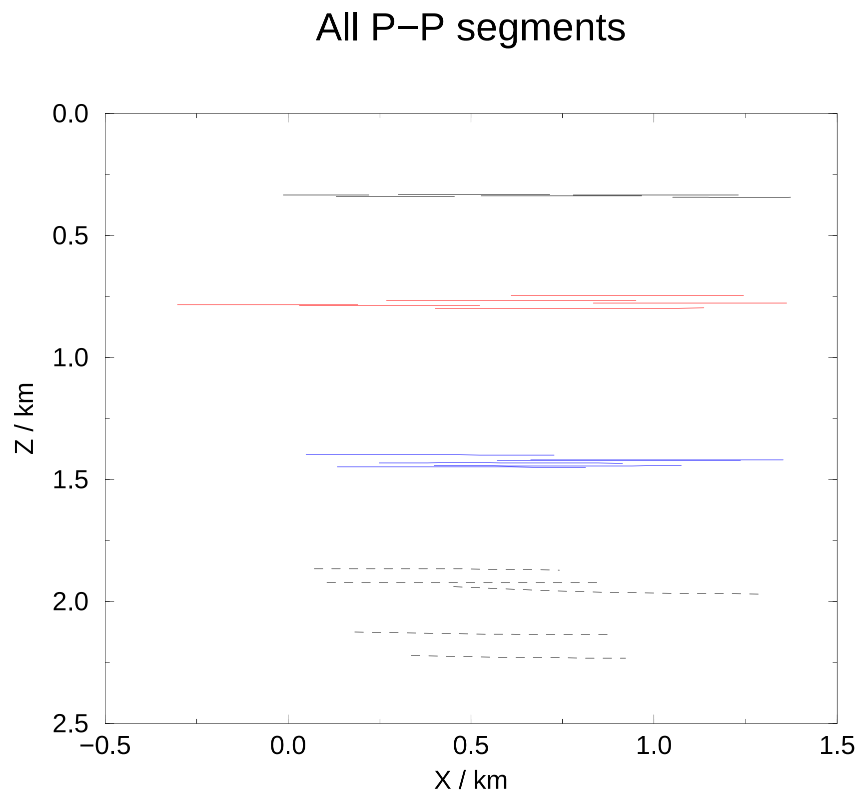

Figure 7.38. Segments from the P-P inversion

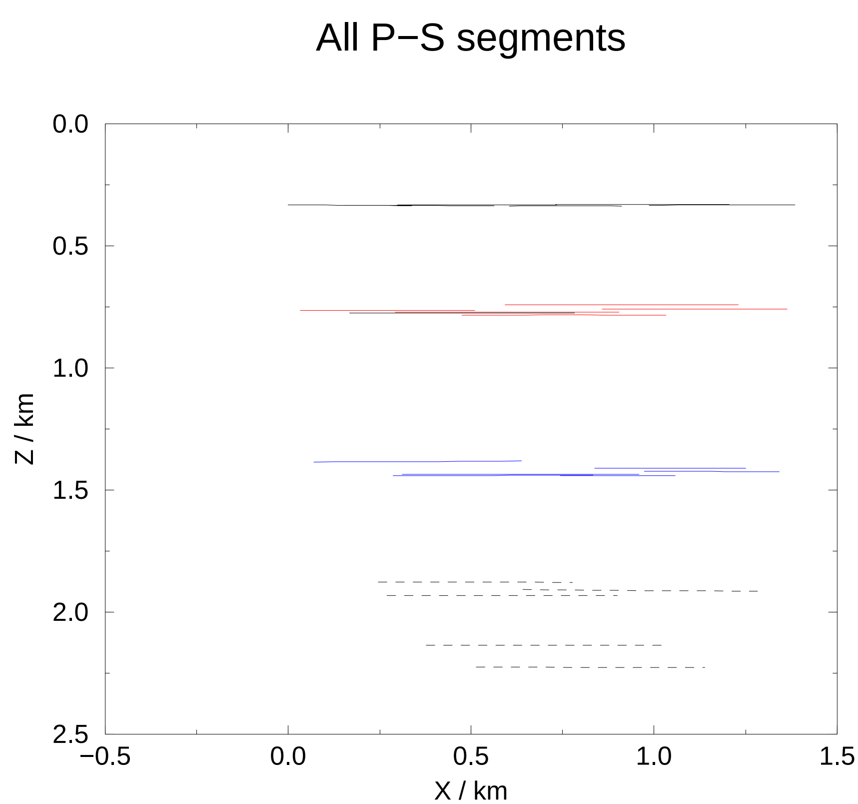

Figure 7.39. Segments from the P-S inversion

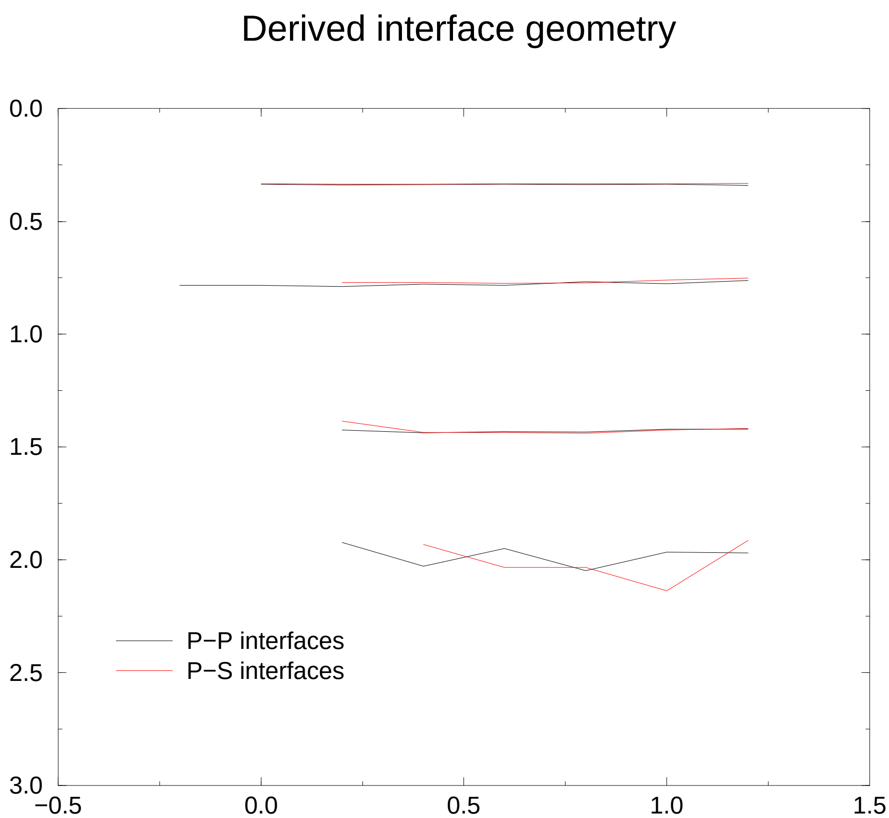

Figure 7.40. Re-sampled interfaces in depth

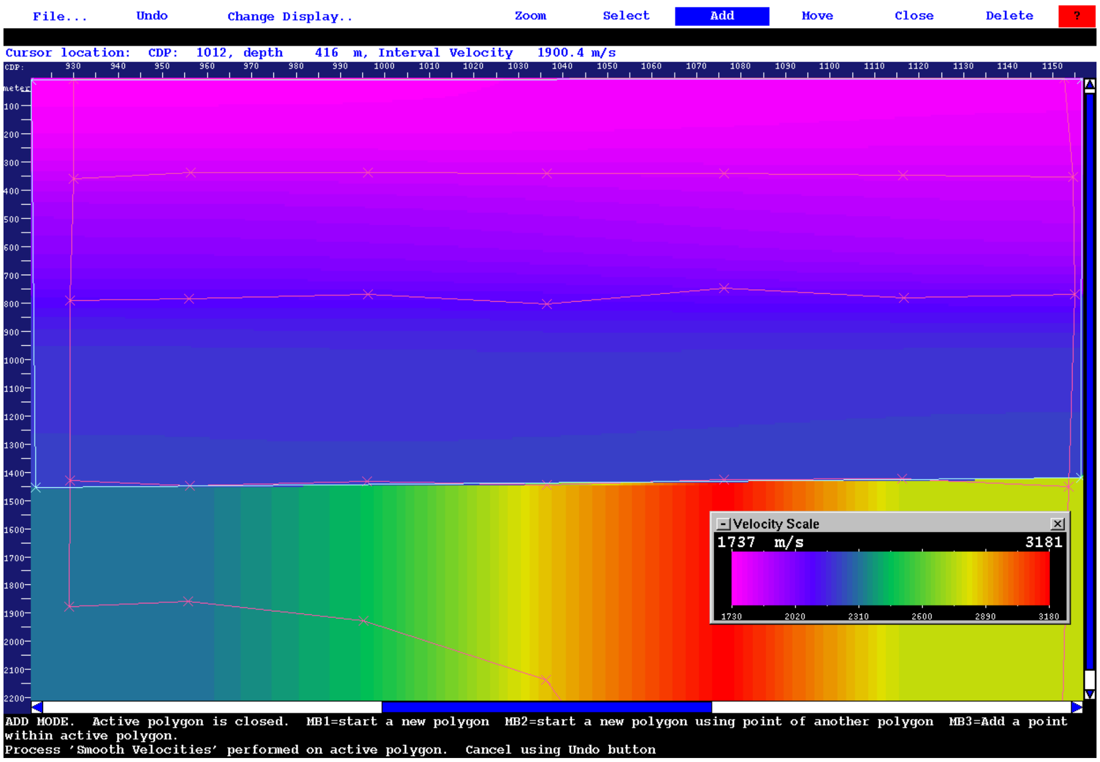

Figure 7.41. Smoothed P-wave velocities

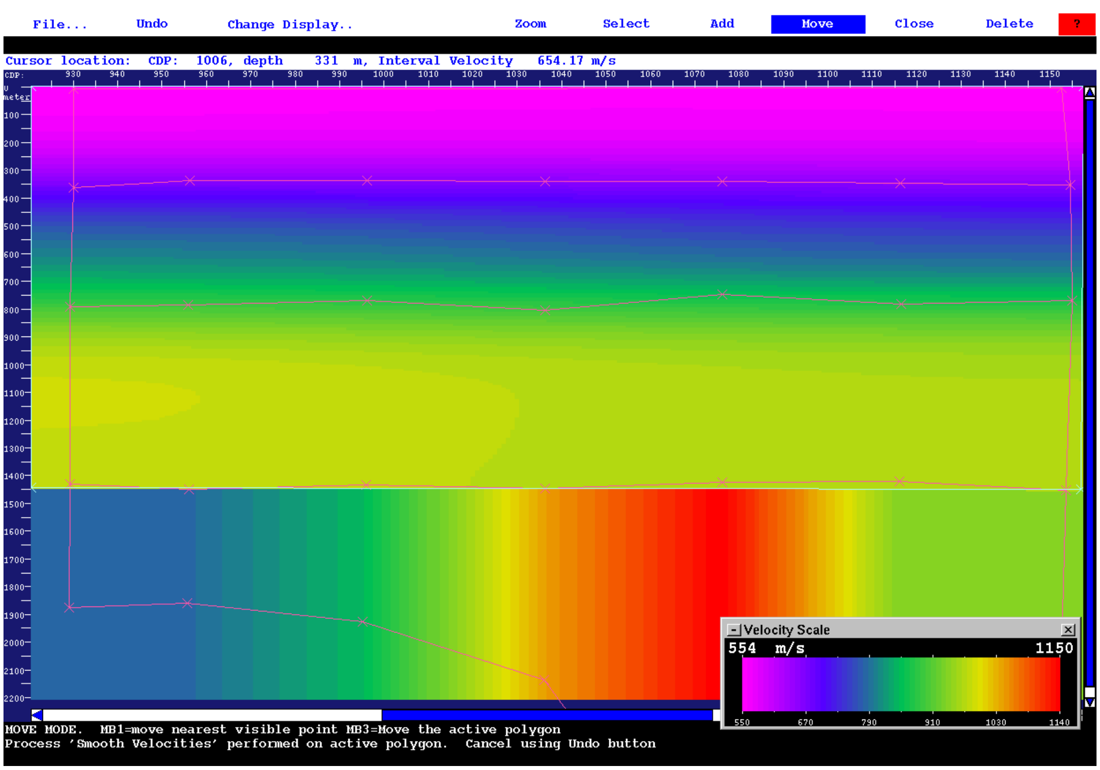

Figure 7.42. Smoothed S-wave velocities

model prior to using it as an input for the migration. The image gathers shown in Figure 7.44 are well flattened and the stack in Figure 7.43 is well focused.

7.3 Conclusions

Conclusions from Part 1

Using picking and inversion I have succeeded in making the processing scheme suitably robust for use on real data which contains some noise. When applied to the Guillemot data I am able to build an initial interval velocity-depth model. Analysis of the CIGs after migration shows that the initial model is not perfect, but is none the less a very good starting point. The events analysed using the inversion are generally well flattened. The initial model can be improved as much as one wants using a suitable update method. I update the velocity field using the ProMAX *Interpretational Migration Velocity Analysis* tool and the data output from Kirkhhoff PSDM, I find I can improve the focusing of the image. This is evidence that there are certain limitations in the way we parameterise the earth when trying to find the velocites. I find a low velocity zone, possibly caused by gas, over the crest of a structural high point at 2km depth (See Figure 7.15). Looking at the new updated velocity model one possible flaw in the method becomes apparent: the imposition of boundaries at arbitrary places within the depth model, caused by picking events which do not necessarily coincide with the major discontinuities in subsurface velocity. This flaw may be remedied to a certain extent by allowing a vertical velocity gradient within the layers. With this proviso, given that we have made the assumption of iso-velocity layers, the results are probably as good as can be expected.

Conclusions from Part 2

I have demonstrated the potential of our inversion to identify matching P-P and P-S reflection events from within a stack of almost featureless horizontal layers. The

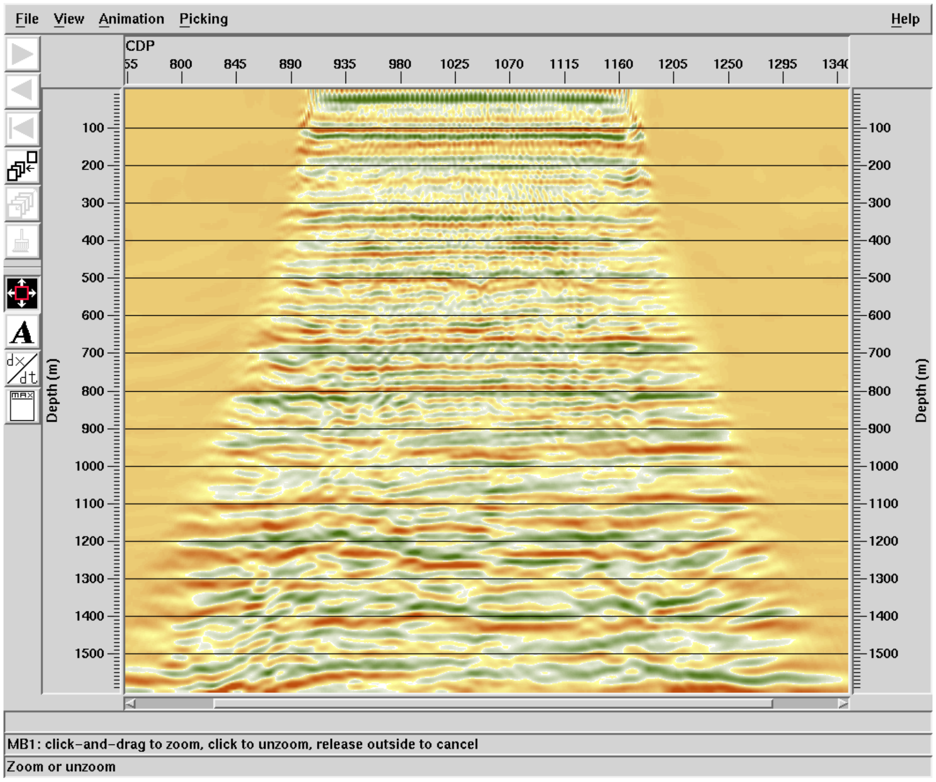

Figure 7.43. Stack from the migration

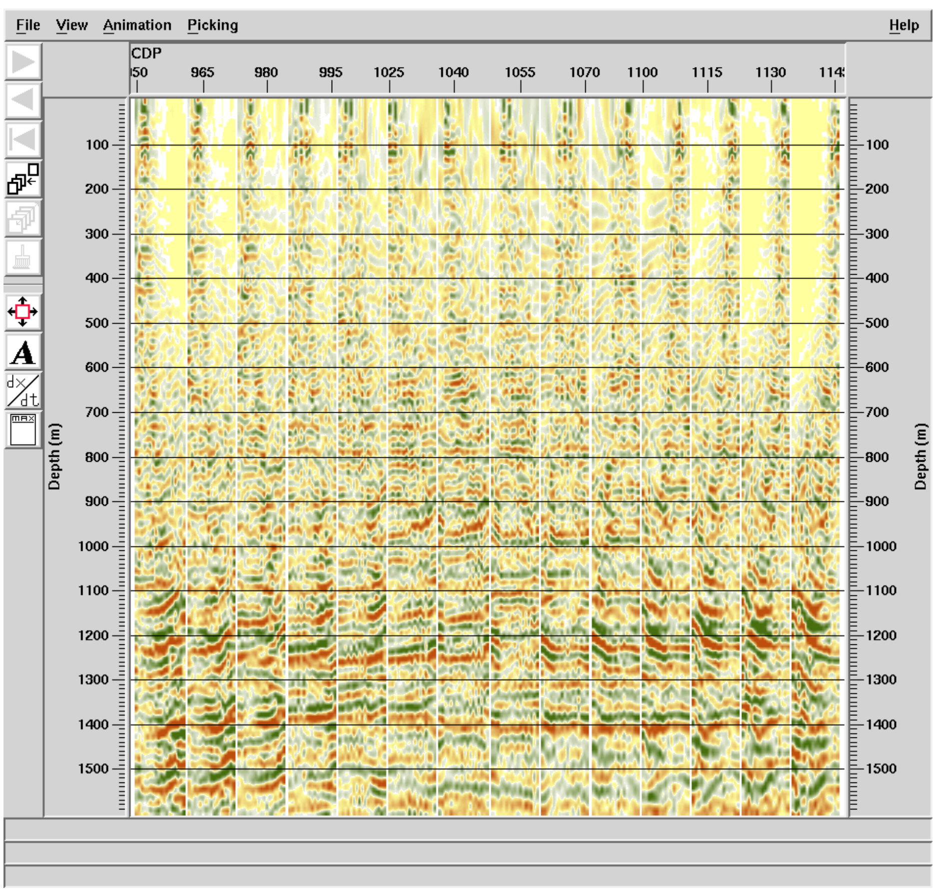

Figure 7.44. Image gathers from the migration using the P-wave velocity model

shallow part of the resulting velocity field has been used to migrate P-wave data. I need P-SV pre-stack depth migration code in order to assess the validity of the S-wave velocity field.

The event selection procedure allows me to select reflection events which, when inverted, give rise to an isotropic velocity model that comes very close to sharing interface locations for the first three interfaces. For the fourth interface things are more complicated and I do not yet trust the velocity model. This is partly due to being forced to pick an event that we would not otherwise have picked (I think this is an unconformity; as I move through the survey, reflections from this and nearby interfaces interfere with each other), but have had to because it was the only reflection event visible on the P-SV data in an otherwise poorly reflective part of the data. The migration of the top part of the P-wave model gives good results.

Forcing event correlation

When selecting the events to match, we move the picks down through the column of available- pickable reflection events. I have tended to move from peak to next peak and so on, and then have fine tuned the closest fitting initial pick until I have an almost exact match in depth. This sometimes means pairing a trough with a peak or a peak with a zero-crossing. The inversion is not 100% accurate all the time, because of the various limitations of the assumptions that we make in the inversion. We might, therefore, expect that even if the P-P and P-SV events are correctly paired the inversion might not return an exact match between the interfaces in depth. Picking different parts of a wavelet until I get an exact match in depth leads, I beleive, to unrealisticaly low errors. It would be better to develop rules for picking, but this needs considerable thought, as this is related to the reflection coeficient for both P- and S-wave reflections at each interface. This is one issue that I have yet to resolve and I beleive this is a non-trivial problem.

Noise issues

In this particular dataset the signal-to-noise ratio of the converted waves at times beyond 2 seconds is very poor and picking was particularly challenging. I do not know if this is a problem unique to the Guillemot dataset, but it has hampered my attemps at joint inversion by forcing me to pick the only strong P-S reflector at depth. Unfortunately this event originates at what I think is an unconformity and is not ideally suited to inversion.

Chapter 8

Conclusions

Here I conclude that it is possible to use travel time inversion to process seismic data. The models we can invert are not very complex yet, but in a stratified earth with moderate dip and curvature the route from data to a depth model suitable for migration is simple. Picking reflection travel times is a bottleneck which takes too long at present. An efficient picking routine is required. Further work includes improving the picking and travel time parameterisation, the comunication between the data and the inversion and reducing the effects of layer curvature on velocity determination.

8.1 Summary of important new work

I have shown that it is possible to use the new inversion scheme of Li to build velocity models for both P-P and P-SV data. For the case of isotropic homogeneous layers and smoothly curving interfaces the models returned by the inversion are a reasonable match to the models used to generate the data. I have shown using the Guillemot dataset that the P-P velocity models provide a reasonable starting point for pre-stack depth migration over a simple geological structure.

Nearly all current converted wave processing flows rely at some stage on event correlation between P-P and P-SV sections, my method is no different in to most others in this respect. Instead of using Post-stack event correlation, I have used the travel time inversion to help match reflection events in the pre-stack data. This method apears to work well in geoplogy that is dominated by plane horizontal layers. This is exactly the sort of regime in which post-stack event correlation based on structural features is hardest. A usefull application of this method, which seems to struggle with complex geology, is in tying down the P- and S-wave velocity ratios in areas dominated by plane layers.

8.2 Recomendations for further work

In order to prove the method, tests of the P-SV model building and the event selection technique must be made on more real data in a situation with well control over the depths. Recasting the inversion in the common-receiver domain might be advantageous as we would not need to apply the static correction before travel time curve picking. In fact we could possibly even use the inversion to solve the near surface problem. Other improvments include the handling of anisotropic effects, velocity gradients, and the extension of the inversion and picking scheme into three dimentions. Including these things will allow us model the earth more accuratly.

Picking

Here there are two big issues, the first is automation of the event recognition and parameterisation, the second is how we choose to parameterise the travel time curves. The cubic that we use to parameterise the travel time curves is not valid over all offsets and in some situations it is not a very good fit to the real travel time curves in the data. As we progress to more complicated models the cubic fit will become a greater constraint on the potential accuracy of the method. While plane layer inversion does require the parameters of the best fit cubic to the travel time data, more general inversion is hampered by this requirement. The greatest advantage in terms of potential accuracy can be gained by removing any picking step at all and work with the data itself, rather than a representation of parts of the data. The advantages of reducing the number of data used in the inversion are lost if one has to spend an inordinate amount of time finding these parameters. The potential for high degrees of accuracy are also lost as smoothing inevitably removes some signal as well as noise.

In the interim good automatic surface fitting code could prove very usefull in extending this method to allow better parameterisation of the travel time curves, and also possible extention into three dimentions.

Inversion

The biggest step forward will be to reduce the effect of the initial model on the final result. Currently this is still affected by interface curvature. We need to improve the inversion by de-coupling the effects of reflector geometry from interval velocity.

There is a possible solution to this problem. As the travel time curves in our simple models are affected both by velocity and reflector geometry, a way must be found to de-coupling the effects of reflector geometry from interval velocity. To do this I propose the use use of a rather brute force method where a large number of inversions are run with a fixed velocity (within a range of probable solutions) after each inversion a number of diagnostic values are saved, such as the residual between the modelled and true travel time curves. Once a large number of inversions are run, the function described by, say, the travel time residuals can be examined and the minimum value selected. This way we test a large number of values of velocity and do not risk getting stuck in a local minimum. The inversion for interface geometry when the layer velocity is fixed is very robust, so I expect this method will be suitable for use on real data.

This method needs to be tested and implemented. To make the inversion scheme applicable in more situations than the approximatly layered earth with isotropic homogenious layers velocity gradients and non-layered structures need to be included in the modeling.

Generating more finely layered models, and being able to include sub-spread length velocity variation would obviously be useful to improve the accuracy and applicability of the method. I suspect that the limitations imposed by starting with a plane layered earth model and using common shot gathers for the inversion may be something that we cannot overcome by improving latter parts of the inversion processing. The errors in the starting model propagate to the curved layer inversion and, so far, it has not been possible to de-couple the effects of layer curvature and velocity determination and converge on the correct solution in all but the most simple cases. The primary cause of these errors in the inital estimation of velocity and geometry is the result of analysing the data in the common shot domain. This results in a high degree of reflection point dispersal along a surface with unknown and possibly complex geometry. This is, in my opinion, the source of the most serious problems of this method. Ironically the use of common-shot gathers for this method is a strong point when it comes to its application to converted waves; we do not have to estimate the velocity ratios before sorting data into common-conversion point gathers.

Interaction between the model space and data space

This is where another significant restriction lies at the moment, neighbouring inversions are done 'cold' there is a slight interaction between some neighbouring gathers when their travel time curves are smashed together, but they really should know more about what is going on arround them. The results of one inversion should have some influence over the inversion at a next-door location. It might be possible by using a way similar to a layer-tomographic type aproach where one looks for a smooth solution which satifies all the data, not just the data at one, or a few local points. If I parameterise the travel times from a reflecting interface as surfaces, once the fitting has been performed, then the whole volume of travel time surfaces should be available to the inversion. That way the inversion will have all the data that will ever be available ready in one data volume. As mentioned in the section on Picking it would be event better for the inversion to interact directly with the seismic data. Coherency Inversion measures semblance along a ray traced travel time trajectory, and this aproach might be adaptable for use with this inversion method.

Model Building

I expect that it would be interesting to experiment with structure independant velocity model building. This may well be important for more challenging structural areas were the geology is not easily aproximated by a layered model.

References

Advance (1995). *ProMAX Reference Manual*. Landmark Graphics Co, version 6.0 edn.

Alfaraj, M. & Larner, K. (1992). Transformation to zero offset for mode-converted waves. *Geophysics*, **57**, 474–477.

Amundsen, L. & Reitan, A. (1995). Decomposition of multicomponent sea-floor data into upgoing and downgoing P- and S-waves. *Geophysics*, **60**, 563–572.

Barr, F.J. & Sanders, J.I. (1989). *Attenuation of water-column reverberations using pressure and velocity detectors in a water-bottom cable*, 653. Soc. of Expl. Geophys.

Berg, E. (1997). 4c-2D or 3D sea bed seismic methodology. In *Proceedings of IIR Forum on Acquisition, Processing and Interpretation of Marine Seismic Data*, 1274–1282, London.

Berkhout (1985). *Seismic Migration Imaging of acoustic energy by wave field extrapolation*. No. 14 A in Developments in solid earth geophysics, Elsevier, 3rd edn.

Bickel, S.H. (1990). Velocity-depth ambiguity of reflection traveltimes. *Geophysics*, **55**, 266–276.

Billette, F.J., Podvin, P. & Lambare, G. (1998). *Stereotomography with automatic picking: application to the Marmousi dataset*, 1317–1320. Soc. of Expl. Geophys.

Bishop, T.N., Bube, K.P., Cutler, R.T., Langan, R.T., Love, P.L., Resnick, J.R., Shuey, R.T., Spindler, D.A. & Wyld, H.W. (1985). Tomographic determination of velocity and depth in laterally varying media. *Geophysics*, **50**, 903–923.

Caldwell, J. (1999). Marine multicomponent seismology. *The Leading Edge*, **18**, 1274–1282.

Castle, R.J. (1994). Theory of normal moveout. *Geophysics*, **59**, 983–999.

Cerveny, V. & Psencik, I. (1988). *Numerical modelling of seismic wave fields in 2d structures by the ray method*. Institute of Geophysics, Charles University. Prague.

Chauris, H., Noble, M., Lambare, G. & Povdin, P. (2002a). Migration velocity analysis from locally coherent events in 2-D laterally hetrogeneous media, Part I: Theoretical aspects. *Geophysics*, **67**, 1202–1212.

Chauris, H., Noble, M., Lambare, G. & Povdin, P. (2002b). Migration velocity analysis from locally coherent events in 2-d laterally hetrogeneous media, Part II: Applications on synthetic and real data. *Geophysics*, **67**, 1213–1224.

Claerbout, J.F. & Doherty, S. (1972). Downward continuation of moveout-corrected seismograms. *Geophysics*, **37**, 741–768.

Claerbout, J.F. & Muir, F. (1973). Robust modeling with erratic data. *Geophysics*, **38**, 826–844.

Dankbaar, J. (1985). Separation of P-wave and S-waves. *Geophys. Prosp.*, **33**, 970–986.

de Bazelaire, E. (1988). Normal moveout revisited - inhomogeneous media and curved interfaces. *Geophysics*, **53**, 143–157.

Deregowski, S. (1982). Dip-moveout and refloctor-point dispersal. *Geophysical Prospecting*, **30**, 318–322.

Dix, C.H. (1955). Seismic velocities from surface measurements. *Geophysics*, **20**, 68–86.

Doherty, S. (1975). *Structure indipendent velocity estimation*. Ph.D. thesis, Geophysics, Stanford University.

Ehinger, A. & Lailly, P. (1995). *Velocity model determination by the smart method, part 1: Theory*, 739–742. Soc. of Expl. Geophys.

Engelmark, F. (2001). Using 4-C to characterize lithologies and fluids in clastic reservoirs. *The Leading Edge*, **20**, 1053–1055.

Fagin, S.W. (1998). *Model-Based Depth Imaging*, 173. Soc. of Expl. Geophys.

Fokkema, J. & Ziolkowski, A. (1987). The critical reflection theorem. *Geophysics*, **52**, 965–972.

Gaiser, J., Moldoveanu, N., Macbeth, C., R., M. & Spitz, S. (2001). Multicomponent technology: the players, problems, applications, and trends. *The leading edge*, **20**, 974–977.

Gangi, A.F. & Yang, S.J. (1976). *Traveltime curves for reflections in dipping layers*, vol. 41, 425–440. Soc. of Expl. Geophys.

Garotta, R. (2000). *Shear Waves from Acquisition to Interpretation*. No. 03 in Distinguished Instructor Serise, Society of Exploration Geophysicists.

Garotta, R. (2001). 4C-ing the future - a word from the 'gurus'. *The leading edge*, **20**, 978–980.

Garotta, R., Granger, P.Y. & Dariu, H. (2002). Combined interpretation of pp and ps data provides direct access to elastic rock properties. *The Leading Edge*, **21**, 532–535.

GeoQuest (1993). *3D/2D interpretaion training manual*. Schlumberger GeoQuest.

Granli, J.R., Arntsen, B., Sollid, A. & Hilde, E. (1999). Imaging through gas-filled sediments using marine shear-wave data. *Geophysics*, **64**, 668–677.

Grechka, A., Pech, A. & Tsvankin, I. (2002). Multicomponent stacking-velocity tomography for transversley isotropic media. *Geophysics*, **67**, 1564–1574.

Grechka, V. & Tsvankin, I. (2001). *PP + PS = SS*, Session: P111. Eur. Assn. of Expl. Geophys.

Grechka, V., Bakulin, A., Tsvankin, I. & Hansen, J. (2001). *Joint inversion of PP and PS reflection data for VTI media: a North Sea case study*, 2112–2115. Soc. of Expl. Geophys.

Hale, D. (1984). Dip-moveout by fourier transform. *Geophysics*, **49**, 741–757.

Harrison, M.P. & Stewart, R.R. (1993). Poststack migration of P-SV seismic data. *Geophysics*, **58**, 1127–1135.

Herrenschmidt, A., Granger, P.Y., Audebert, F., Gerea, C., Etienne, G., Stopin, A., Alerini, M., Lebegat, S., Lambare, G., Berthet, P., Nebieridze, S. & Boelle, J.L. (2001). Comparison of different strategies for velocity model building and imaging of pp and ps real data. *The Leading Edge*, **20**, 984–995.

Hubral, P. & Krey, T. (1980). *Interval Velocities from Seismic Reflection Time Measurements*, 203. Soc. of Expl. Geophys.

Knapp, S., Payne, N. & Johns, T. (2001). *Imaging through gas clouds: A case history from the Gulf of Mexico*, 776–779. Soc. of Expl. Geophys.

Kosloff, D. & Sudman, Y. (2002). Uncertainty in determining interval velocities from surface reflection seismic data. *Geophysics*, **67**, 952–963.

Kristensen, A., Amundsen, L., Rogno, H., Lanfranchi, P., Aarmot, A. & Oxnevad, G. (1999). *A 3D/4C OBC survey at the Statfjord field*, Session:6041. Eur. Assn. Geosci. Eng.

Landa, E., Kosloff, D., Keydar, S., Koren, Z. & Reshef, M. (1988). A method for determination of velocity and depth from seismic reflection data. *Geophys. Prosp.*, **36**, 223–243.

Levin, F. (1971). Apparent velocity from dipping interface reflections. *Geophysics*, **36**, 510–516.

Li, G. (2002). Inversion of P-SV reflections for 2-D curved layers. *Processing 4-Component Sea-Floor Seismic Data*, Paper 2, Report 4.

Li, G., Ziolkowski, A., Taylor, D. & Hall, G. (2002). *An approach to determine subsurface structure using P-P and P-SV reflections.*, P006. Extended Abstracts, 64th conference and exhibition, EAGE.

Lines, L. (1993). Ambiguity in analysis of velocity and depth (short note). *Geophysics*, **58**, 596–597.

Lu, L., Chen, J.J. & Chen, W.D. (1998). *Anisotropic velocity analysis and moveout: a practical approach*, 1487–1490. Soc. of Expl. Geophys.

Lynn, W. & Claerbout, J. (1982). Velocity estimation in laterally varying media. *Geophysics*, **47**, 884–897.

MacLeod, M.K., Hanson, R.A., Hadley, M.J., Reynolds, K.J., Lumley, D. & McHugo, S. (1999). *The Alba field OBC seismic survey*, Session:6025. Eur. Assn. Geosci. Eng.

Mallet, R. (1848). On the dynamics of earthquakes; being an attempt to reduce their pbserved phenomena to the known laws of wave motion in solids and fluids. *Trans. Roy. Irish Acad.*, **21**, 50–106.

Mancini, F., Li, X., Ziolkowski, A. & Pointer, T. (2003). *Anisotropic parameter estimation*, Anual Meeting and Exhibition. EAGE.

Michelena, R.J., Donati, M., Valenciano, A. & D'Agosto, C. (2001). Using multicomponent seismic for reservoir characterization in venezuela. *The Leading Edge*, **20**, 1036–1041.

Mikhailov, O., Johnson, J., Shoshitaishvili, E. & Fraisier, C. (2001). Practical approach to joint imaging of multicomponent data. *The leading edge*, **20**, 1016–1021.

Mulder, W. & ten Kroode, A. (2001). *Automatic velocity analysis by differential semblance optimization*, 893–896. Soc. of Expl. Geophys.

Neidell, N.S. & Taner, M.T. (1971). *Semblance and other coherency measures for multichannel data*, vol. 36, 482–497. Soc. of Expl. Geophys.

Pope, D., Kommedal, J. & Ohansen, J. (2000). Using 3D-4C to drill beneath the Lomond gas cloud. In *62nd Ann. Mtg. Extended Abstracts*, L–01, EAGE.

Press, W., Teukolsky, S., Vetterling, W. & Flannery, B. (1992). *Numerical Recipes in FORTRAN*. Cambridge University Press, 2nd edn.

Santos, L., Schleicher, J. & Tygel, M. (2000). Seismic modeling by demigration. *Geophysics*, **65**, 1281–1289.

Sava, P. & Fomil, S. (2003). Angle-domain common-image gathers by wavefield continuation methods. *Geophysics*, **68**.

Schneider, W. (1978). Integral formulation for migration in two and three dimensions. *Geophysics*, **43**, 49–76.

Sheriff, R. & Geldart, L. (1995). *Exploration Seismology*. Developments in solid earth geophysics, Cambridge University Press, 2nd edn.

Sherwood, J., Schultz, P. & Judson, D. (1978). *Equalizing the stacking velocities of dipping events via Devilish.*. Soc. Expl.Geophys.

Soubaras, R. (1998). Multiple attenuation and P-S decomposition of multicomponent ocean-bottom data. In *68th Ann. Internat. Mtg*, 1336–1339, Soc. of Expl. Geophys.

Stewart, R.R., Gaiser, J., Brown, R.J. & Lawton, D. (2002). Converted-wave seismic exploration: Methods. *Geophysics*, **67**, 1348–1363.

Stewart, R.R., Gaiser, J., Brown, R.J. & Lawton, D.C. (2003). Converted-wave seismic exploration: Applications. *Geophysics*, **68**, 40–57.

Stork, C. (1992). Reflection tomography in the postmigrated domain. *Geophysics*, **57**, 680–692.

Taner, M.T. & Koehler, F. (1969). Velocity spectra - Digital computer derivation and applications of velocity functions. *Geophysics*, **34**, 859–881.

Tatham, R. & Goolsbee, D. (1984). Separation of s-wave and p-wave reflections offshore western florida. *Geophysics*, **49**, 493–508.

Taylor, D. (1987). Double countour integration for transmission from point sources through anisotropic layers as used in ROCPAC* software. *Geophys. J.R astr. Soc*, **91**, 373–381.

Taylor, D. (2002). 2-D finite difference modelling. Inspire Report 4, Centre for Reservoir Geocience, University of Edinburgh.

Thomsen, L. (1999). Converted-wave reflection seismology over inhomogeneous, anisotropic media. *Geophysics*, **64**, 678–690.

Thore, P.D., de Bazelaire, E. & Ray, M.P. (1994). Three-parameter equation: An efficient tool to enhance the stack. *Geophysics*, **59**, 297–308.

Thorson, J.R., Gever, D., Apsel, R., Swanger, H.J. & Hadley, D.M. (1987). *A model-based approach to interval velocity analysis*, Session:S3.3. Soc. of Expl. Geophys.

Tsvankin, I. & Thomsen, L. (1994). Nonhyperbolic reflection moveout in anisotropic media. *Geophysics*, **59**, 1290–1304.

Udden, J. (1920). Suggestions of a new method of making underground observations. *Bull AAPG*, **4**, 03–85.

Vesnaver, A.L., Bohm, G., Madrussani, G., Petersen, S.A. & Rossi, G. (1999). Tomographic imaging by reflected and refracted arrivals at the north sea. *Geophysics*, **64**, 1852–1862.

Yilmaz, O. (2000). *Seismic Data Analysis*, vol. 01, 1000. Soc. of Expl. Geophys.

Yilmaz, O. (2001). *Seismic Data Analysis*, vol. 02, 1001–2027. Soc. of Expl. Geophys.

Yuan, J. (2001). *Analysis of Four-component Seafloor Seismic Data for Seismic Anisotropy*. Ph.D. thesis, University of Edinburgh, Department of Geology and Geophysics.

Yuan, J. & Li, X.Y. (1998). *A new approach for converted-wave moveout in transversely isotropic media*, 1495–1498. Soc. of Expl. Geophys.

Zamorouev, A. (1999). *Automatic picking of seismic events*, 1158–1161. Soc. of Expl. Geophys.

Zhang, Y. & Robinson, E.A. (1992). *Stacking P-SV converted wave data with raypath velocity*, 1214–1217. Soc. of Expl. Geophys.

Zhang, Y., Min, L. & Pham, D. (2002). *Velocity update via joint velocity inversion for anisotropic depth migration*, 141–144. Soc. of Expl. Geophys., 72nd edn.

Ziolkowski, A. (1991). Why don't we measure seismic signatures? *Geophysics*, **56**, 190–201.

Ziolkowski, A., Taylor, D. & Li, G. (2001a). Processing 4-Component Sea-Floor Seismic Data. Tech. Rep. 1, Centre for Reservoir Geocience, University of Edinburgh.

Ziolkowski, A., Taylor, D., Li, G. & Hall, G. (2001b). INSPIRE Processing 4-Component Sea-Floor Seismic Data. Tech. Rep. 2, Centre for Reservoir Geocience, University of Edinburgh.

Ziolkowski, A., Taylor, D., Li, G. & Hall, G. (2002a). INSPIRE Processing 4-Component Sea-Floor Seismic Data. Tech. Rep. 3, Centre for Reservoir Geocience, University of Edinburgh.

Ziolkowski, A., Taylor, D., Li, G. & Hall, G. (2002b). INSPIRE Processing 4-Component Sea-Floor Seismic Data. Tech. Rep. 4, Centre for Reservoir Geocience, University of Edinburgh.

Ziolkowski, A., Taylor, D., Li, G. & Hall, G. (2003). INSPIRE Processing 4-Component Sea-Floor Seismic Data. Tech. Rep. 5, Centre for Reservoir Geocience, University of Edinburgh.

Zoeppritz, K. (1919). Uber reflexion und durchgang seismicher wellen durch unstetigkerlsflaschen. *Uber Erdbebenwellen VII B, Nachrichten der Koniglichen Gesellschaft der Wissenschaften zu Gottingen, Math. Phys.*, **K1**, 57–84.

Appendix A

Travel time over a single plane dipping layer.

For the simple case shown in Figure A.1 I derive the travel time equation for the case of non-zero source-receiver offset. I thank Guanpin Li for his assitance with this derivation.

Using geometry we find that

$$z = \frac{z_n}{\cos\phi}. \tag{A.1}$$

The P-wave velocity is v_p , so the zero offset travel time is given by

$$t_0 = \frac{2z_n}{v_p}. \tag{A.2}$$

If we reflect the ray path from the source to the reflection point using the reflector as the axis of reflection we get a single straight ray path from s^1 to the receiver whose length is the same as that from the source via the reflection point to the receiver.

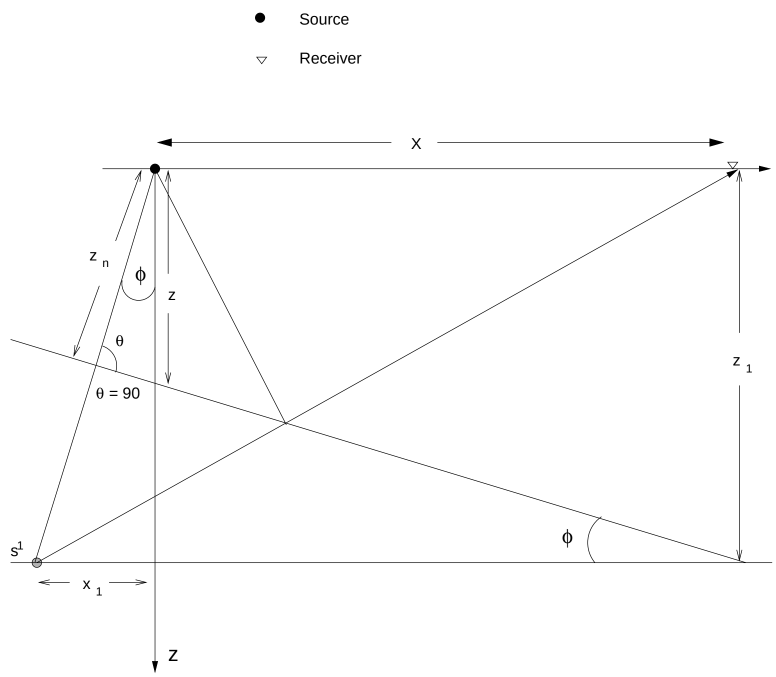

Figure A.1. A simple iso-velocity plane dipping layer model.

Again using geometry we find that

$$x_1 = 2z_n \sin\phi, \tag{A.3}$$

and that

$$z_1 = 2z_n \cos\phi. \tag{A.4}$$

We now know the total travel path of the ray, dividing this by the P-wave velocity v_p we get the travel time, to save on using the square root we square the whole expression to give:

$$t^2 = \frac{(x + 2z_n \sin\phi)^2 + (2z_n \cos\phi)^2}{v_p^2}. \tag{A.5}$$

Expanding the brackets in equation A.5 we get:

$$t^2 = \frac{x^2}{v_p^2} + \frac{4z_n^2}{v_p^2}\sin^2\phi + \frac{4xz_n\sin\phi}{v_p^2} + \frac{4z_n^2}{v_p^2}\cos^2\phi. \tag{A.6}$$

As $(sin^2\phi + cos^2\phi) = 1$,

$$t^2 = t_0^2 + \frac{x^2}{v_p^2} + \frac{4xz_n\sin\phi}{v_p^2}. \tag{A.7}$$

Re-aranging and substituting equation A.2 we get,

$$t^2 = t_0^2 + \frac{x^2}{v_p^2} + \frac{2xt_0\sin\phi}{v_p}, \tag{A.8}$$

which is the equation shown in Chapter 5.

Appendix B

Paper submited to Geophysics .

The following is a paper that has been submited to the journal of the Society of Exploration Geophysics.